UNIVERSITY OF OKLAHOMA

GRADUATE COLLEGE

CHEMICAL LOOPING OXIDATIVE COUPLING OF METHANE AND CO_2-H_2O SPLITTING FOR SUSTAINABLE ETHYLENE AND SYNGAS PRODUCTION AT INTERMEDIATE TEMPERATURES

A DISSERTATION

SUBMITTED TO THE GRADUATE FACULTY

in partial fulfillment of the requirements for the

Degree of

DOCTOR OF PHILOSOPHY

By

Hafiz Ahmad Hassan

Norman, Oklahoma

2026

CHEMICAL LOOPING OXIDATIVE COUPLING OF METHANE AND CO_2-H_2O SPLITTING FOR SUSTAINABLE ETHYLENE AND SYNGAS PRODUCTION AT INTERMEDIATE TEMPERATURES

A DISSERTATION APPROVED FOR THE

SCHOOL OF AEROSPACE AND MECHANICAL ENGINEERING

BY THE COMMITTEE CONSISTING OF:

Dr. Pejman Kazempoor, Chair

Dr. Ramkumar N. Parthasarathy

Dr. Wilson E. Merchan Merchan

Dr. Hamidreza Shabgard

Dr. Reza Faudazi

Acknowledgments

First and foremost, I would like to express my deepest gratitude to my advisor, Dr. Pejman Kazempoor. His guidance, support, patience and mentorship throughout my doctoral journey have been invaluable. His encouragement and advice have contributed significantly to my growth as an independent researcher and to my professional development. I am sincerely thankful for his belief in my potential.

I would also like to sincerely thank my committee members, Dr. Ramkumar N. Parthasarathy, Dr. Wilson Merchan-Merchan, Dr. Hamidreza Shabgard, and Dr. Reza Foudazi, for their valuable time, thoughtful feedback, and service on my dissertation committee. Their expertise and constructive suggestions have helped improve the quality, clarity, and direction of this work. I would also like to express my sincere appreciation to Dr. Canan Karakaya of Oak Ridge National Laboratory for her vital guidance and support in the CFD modeling aspects of this study and Dr. Chuancheng Duan of University of Utah for his support with pilot-scale experimental data.

I am deeply grateful to my parents (Farkhanda Kauser and Zulfiqar Ahmad), wife (Alnaz Ahmad), brother (Ali Hassan) and sister (Fatima Usman), nephews and nieces (Ibrahim, Umamah, Ahad and Minha) for their continuous love, prayers, encouragement and support. Their belief in me have been the foundation of my academic and professional journey. I am profoundly thankful to all for their constant support, patience and the many sacrifices they made to support me throughout my studies.

I would also like to thank all of my team members at the Sustainable Energy and Carbon Management Center of the University of Oklahoma. I would like to acknowledge the individual contribution of Dr. Abu Yousuf to this dissertation, particularly for his support with the life-cycle assessment of the proposed integrated technology.

Furthermore, I would like to express my sincere gratitude to my school teachers (the late Mr. Shafqat Ali Tahir and Mr. Muhammad Arif). Their guidance and example taught me the true value of hard work, a lesson that has remained with me throughout my life.

To all those facing oppression, poverty and hardship around the world, I sincerely pray for peace, prosperity and a future where your children can grow with dignity, receive an education and have the same opportunities that I was blessed to receive.

To my little daughter, (Emaan Ahmad):

You have been my constant source of happiness, strength, purpose and hope. Your presence made every challenge throughout my Ph.D. journey into an effortless task. I pray that you grow with confidence, compassion and the knowledge that you are deeply loved.

Table of Contents

List of Figures

List of Tables

Abstract

The rising global warming concerns have prompted research in the direction of greenhouse gas (GHG) mitigation technologies. Amongst all of the GHGs, methane (CH_4) and carbon dioxide (CO_2) gases are the most abundant ones and their conversion to valuable chemicals holds significant value. The discovery of shale gas reserves has further encouraged the development of direct methods for methane conversion into valuable chemicals, offering an alternative to indirect approaches that involve an energy-intensive intermittent syngas production step, leading to high CO_2 emissions. Amongst the direct methods, the oxidative coupling of methane (OCM) is a potential pathway to reduce CO_2 emissions and which can produce commodity chemicals such as ethylene, a chemical regarded as central to the petrochemical industry. Even though OCM has been studied for over four decades, the technology still has not found commercial applications. Though there are many challenges regarding industrial deployment of OCM, the most significant one is the requirement of a high ethylene yield of 30% which is currently reported to be around 20%. Moreover, the highly exothermic nature of the process and controlling the carbon selectivity over oxides of carbon (COx) is the heart of the problem. Numerous researchers have presented promising results in terms of catalysts, reactor designs and feeding strategies for OCM. However, due to lack of inclusiveness in the results, none of the combinations of catalysts, reactors and system optimizations have been able to bring about its industrial viability. Integration of OCM which another catalytic process which occurs at intermediate temperatures can increase the profitability of the overall process. One such catalytic process is the chemical looping (CL) CO_2-H_2O splitting process that produces valuable syngas.

Integrating OCM with CO_2-H_2O splitting allows efficient energy utilization, yield improvement and minimal heat losses and pollutant emissions to the environment. The current dissertation presents an extensive review of the noteworthy attempts to achieve industrial targets for OCM. Similarly, a comprehensive review of the CL CO_2-H_2O splitting process is presented and a novel system of integrated CL OCM/CO_2-H_2O splitting process is introduced and assessed. Moreover, a comprehensive set of benchmarks is presented which highlights the desired end-state for the industrial deployment of CL OCM/CO_2-H_2O splitting technology. Furthermore, the dissertation includes a multiscale packed bed reactor model for CL OCM developed using a Computational Fluid Dynamics (CFD) commercial tool. CFD tools help analyze spatial gradients within the reactor to deeply understand the diffusion of species, mass and heat transfer phenomena. Furthermore, challenges associated with scaling up such as hot spot formation and parametric sensitivity are addressed without having to expend on costly experiments. The CFD model includes two scales i.e., macroscale for catalyst bed and microscale for individual pellets. Moreover, a chemical kinetic model based on 10 gas-phase reactions is integrated with the CFD model. An additional surface reaction for the formation of gas-phase oxygen from catalyst surface is added to account for the absence of feed oxygen. The model is calibrated against experimental results. The calibrated model captures trends in CH_4 conversion, C_2 selectivity and C_2 yield within a ±4.35% range across a temperature range of 700-900ºC. Moreover, model fidelity is evaluated by varying key parameters such as mesh resolution and time step size. The model is also verified by varying the inlet methane concentration and the gas hourly space velocity (GHSV) and comparing the results with literature.

Based on the CFD model, a parametric study is also conducted to optimize the reactor performance which includes parameters such as GHSV, inlet methane concentration, oxygen availability and reactor diameter across temperature range of 700-900ºC. Results from the parametric study suggest that the C_2 yield is increased from 19.15% to 20.4% as the CH_4/O_2 ratio is decreased to 1.71 at 1125 mL/hg GHSV and 825ºC. However, the C_2 selectivity drops to 44.6%. Conversely, a remarkable C_2 selectivity of 76.8% is achieved at a CH_4/O_2 ratio of 8.9, 2500 mL/hg GHSV and 800ºC. However, the yield drops to ~10%. Furthermore, increasing the diameter/length ratio of reactor, at constant volume constant, reduces the hot spots while maintaining the C_2 yield.

A techno-economic assessment (TEA) based on an industrial-scale, system-level model is also conducted for the CL OCM/CO_2-H_2O Splitting. The system-level model is developed using optimized performance metrics from the CFD parametric study. Furthermore, the effect of different recycled methane content on the levelized cost of products (LCOP) has also been studied. The original case from the parametric study had a C_2 yield of 10.76% and selectivity of 72% at a temperature of 800ºC. The inlet flow rate of feed gas has been adjusted to obtain 1 million tonne/year C_2 products. Results suggest significant improvement in C_2 yield and LCOP with methane recycling at the studied operating condition. The C_2 yield improved by 15.87 percentage points with 60% recycled methane. The LCOP is also close to the threshold value of 1000 $/tonne with 60% recycled methane. However, at this high recycled percentage, hydrogen concentration is more than the flammability limit which can cause safety issues because of hydrogen combustion. Therefore, a methane recycle percentage of 40% is recommended with hydrogen

concentrations lower than the flammability limit. The LCOP with this recycle percentage becomes competitive to conventional ethylene production technologies at lower methane feedstock prices projected for future. Furthermore, a sensitivity analysis is conducted which suggests that the integrated technology can produce further lower LCOPs given the lower methane and CO_2 feedstock prices.

A cradle-to-gate (CtG) life cycle assessment (LCA) is also conducted in SimaPro 8.1 using Ecoinvent v3.6 background data and the ReCiPe 2016 (H) midpoint and endpoint impact assessment methods. CL OCM/CO_2-H_2O achieved the lowest global warming potential (GWP) at 0.38 kg CO_2-eq/kg C_2H_4, compared with 1.93 kg CO_2-eq/kg C_2H_4 for ethane steam cracking (950 °C) and 2.84 kg CO_2-eq/kg C_2H_4 for naphtha steam cracking. Endpoint results show 96–97.5% lower human-health impacts (2.12 mPt vs. 55.74–86.13 mPt) and 96.4–97.6% lower ecosystem damage (1.25 mPt vs. 34.64–51.92 mPt) relative to conventional routes, while resource depletion is slightly higher.

Overall, this dissertation demonstrates that the integrated CL OCM/CO_2-H_2O splitting process is a promising technology for methane and CO_2 valorization while producing ethylene and syngas with improved economic and environmental performance. The combined CFD, system-level modeling, TEA and LCA results show that methane recycling accompanied by reactor optimization can substantially reduce LCOP relative to conventional steam cracking. Although challenges remain in hotspot control, hydrogen safety and long-term catalyst stability, the proposed framework provides a practical foundation for advancing the technology toward industrial deployment. These findings

establish CL OCM/CO_2-H_2O splitting as a potentially competitive and low-carbon alternative for future ethylene production.

Graphical Abstract

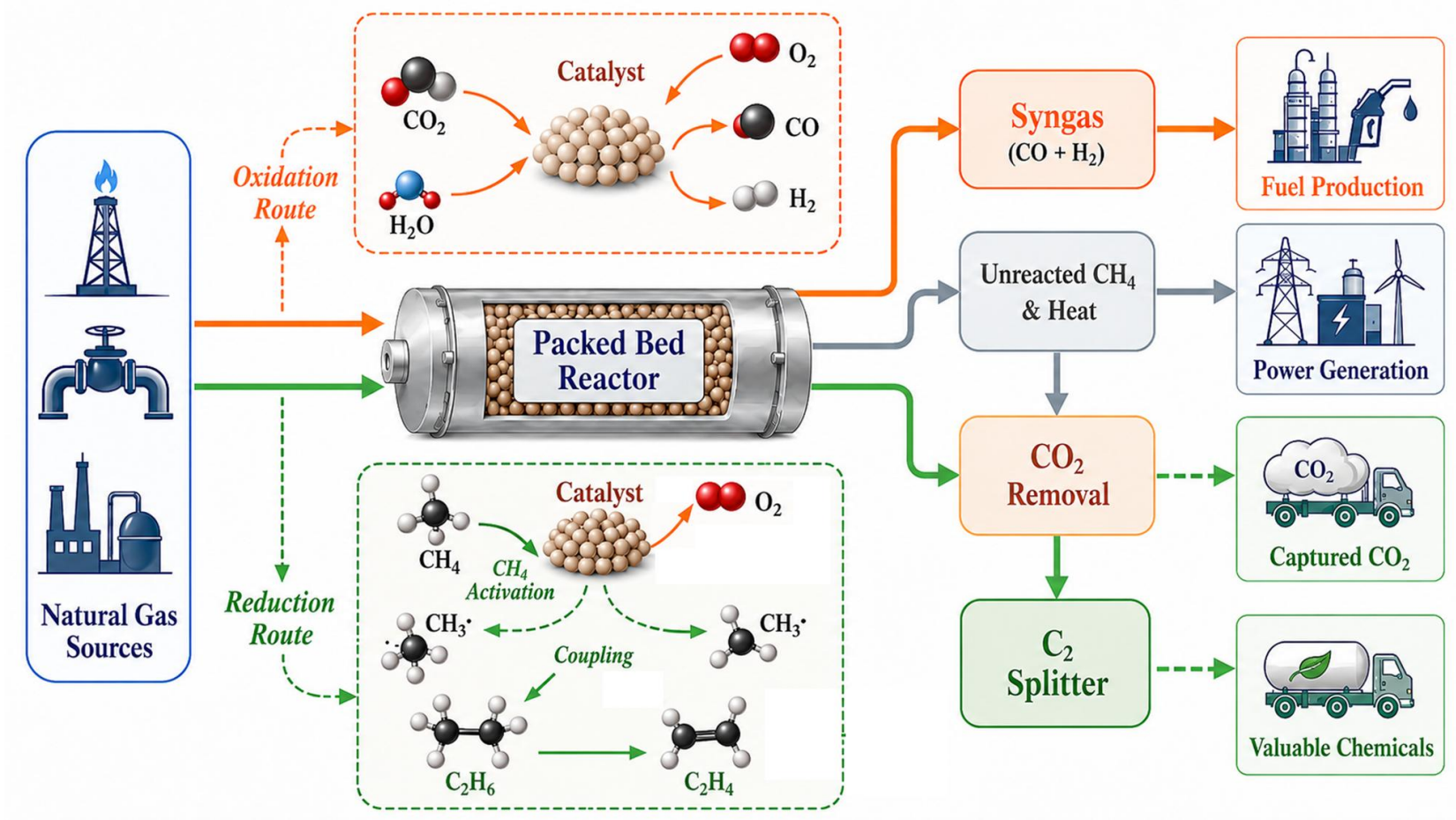

Chapter 1. Introduction

The recent discovery of shale gas reserves has expanded the application of natural gas (NG) as a source of fuels and chemicals [1-7]. Methane (CH_4) is the main constituent of NG, biogas and is also found in crystalline hydrates at the continental slopes of many oceans and in permafrost areas [8, 9]. As a pollutant, it is 25 times more harmful than carbon dioxide (CO_2) over a century long span [10].

Since the transportation of methane from remote sites is economically inviable and the conversion of methane to easily transportable chemicals is difficult, it is common to burn off methane which results in pollutant emissions such as oxides of carbon (COx) [1, 2]. Majority of methane in natural gas is burned for cooking, heating and, electricity transportation instead of being used as an economical feedstock [8]. Moreover, the amount of natural gas which is flared is almost 3.5% of the total natural gas produced [11]. Only 6% of the global natural gas consumption includes its use as a chemical feedstock in the petrochemical industry [12]. The reason for such a small utilization of natural gas in petrochemical industry is related to economic difficulties associated with its transportation. Since NG has three orders of magnitude less mass and energy density compared to oil, it becomes difficult to handle its transportation through tankers [8]. This emphasizes the conversion of NG/methane to liquids that can be easily transported from the wellheads. Moreover, profitable methane conversion to valuable chemicals would reduce the transportation costs as well since the methane could be converted at the consumer site.

Therefore, there has been a recent quest for conversion of methane to valuable chemicals while keeping in check its environmental impact. Figure 1 shows total publications and citations from the year 2014 to 2024 related to methane conversion technologies and oxidative coupling of methane (OCM) which are testament to increased global interest in OCM and methane conversion in general [13].

The C_2 hydrocarbons such as ethylene are considered the backbone of chemical industry as they are used as raw materials for polyethylene, vinyl chloride, ethylene oxide and ethylbenzene. As ethylene is one of the most widely used raw materials in the chemical industry, it can be used to assess the production level of a country's petrochemical industry [4, 10, 14, 15]. Currently, the global production of ethylene is from 150-200 million tons per year [16, 17]. For the production of ethylene, steam cracking plants of ethane or naphtha are utilized. However, the discovery of shale gas and reduced NG prices have driven ethylene production to a fuel switching case where the conventional ethane/naphtha cracking plants would be accompanied by diverse methods, potentially the oxidative coupling of methane (OCM) process [18].

The conversion of methane can be performed by either direct or indirect methods. In the direct methods, methane is converted to value added chemicals without the formation of any intermittent products whereas, the indirect methods require the intermediate step for the formation of syngas ($CO + H_2$) which is then converted to valuable chemicals via Fisher-Tropsch synthesis (FTS) [1, 6]. Moreover, syngas can be converted to methanol which can be further converted to gasoline, olefins or aromatics [1].

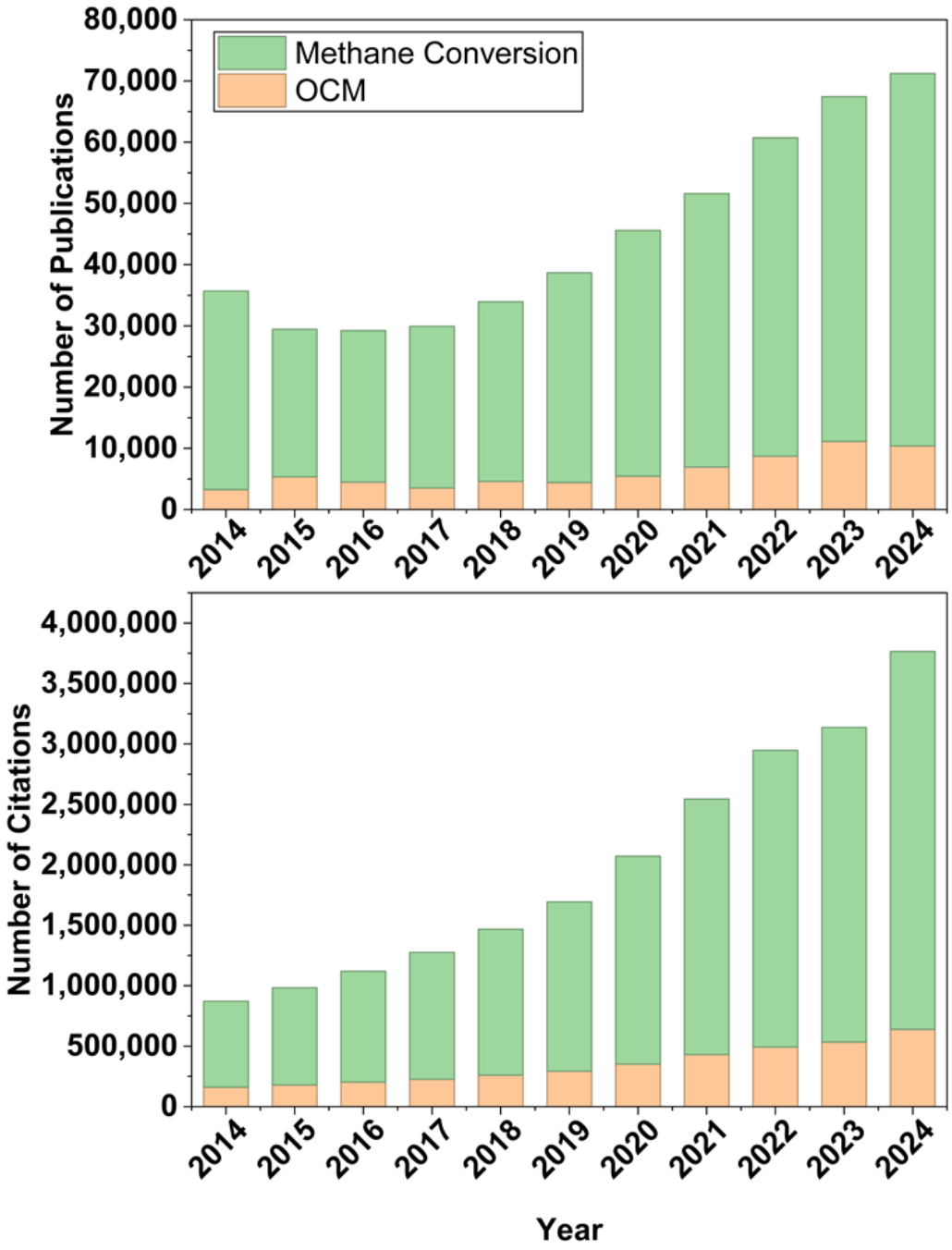

Figure 1. Publications and citations on methane conversion technologies and OCM adapted from Dimensions [13].

1.1. Problem Statement and Research Objectives

Methane and CO_2 are two of the most abundant carbon-containing gases with significant relevance to the global energy and chemical industries. Methane is the primary component of natural gas and represents a major feedstock for fuel and chemical production, while CO_2 is the dominant greenhouse gas associated with fossil fuel utilization and industrial processes. Simultaneous conversion of methane and CO_2 into valuable chemicals offers an attractive path for improving carbon utilization, reducing emissions and producing important products such as ethylene and syngas. However, the commercial implementation of methane conversion technologies, particularly OCM, remains limited due to several technical and economic barriers, including low single-pass C_2 yield, poor selectivity at high methane conversion, catalyst deactivation, high operating temperatures, heat management challenges, and scale-up limitations. The chemical looping (CL) design (redox cycle design) for OCM is promising in terms of improving process selectivity however, it suffers from downtimes required to oxidize the catalyst. This downtime can be monetized if replaced by an oxidation cycle of another intermediate temperature technology such as CL CO_2/H_2O splitting.

In parallel, CO_2/H_2O splitting through CL provides a promising route for converting CO_2 and H_2O into CO and H_2 using lattice oxygen (i.e., oxygen build into the solid metal oxide structure). When integrated with OCM, this approach has the potential to improve

overall process efficiency by coupling methane conversion with oxygen carrier regeneration and syngas production. Nevertheless, the integrated CL OCM and CL CO_2/H_2O splitting (CL OCM/CO_2-H_2O splitting) process introduces additional challenges related to reactor design, reaction–transport coupling, process integration, product separation, energy efficiency, and environmental performance. Therefore, a systematic investigation is required to evaluate the technical feasibility, economic competitiveness and environmental benefits of this integrated process compared with conventional ethylene production technologies.

Accordingly, this dissertation addresses the following research questions:

➢ **RQ1:** Why is it important to convert CH_4 and CO_2 into valuable chemicals, and what are the major challenges associated with these conversion pathways?

➢ **RQ2:** What are the technical challenges preventing the commercial viability of OCM and how can these challenges be addressed?

➢ **RQ3:** What performance benchmarks must the CL OCM/CO_2-H_2O splitting achieve to compete with conventional technologies?

➢ **RQ4:** How can a reactor be designed to optimize the performance of the CL OCM process?

➢ **RQ5:** How can the plant operation be optimized to improve process efficiency and economic performance?

➢ **RQ6:** How can the environmental impact of the integrated system be minimized?

Overall, given the growing need for sustainable chemical production and effective carbon utilization, this dissertation aims to develop and evaluate an integrated CL process for the co-conversion of methane and carbon dioxide into valuable products. The primary goal is to advance the modeling, optimization, techno-economic assessment (TEA) and life-cycle assessment (LCA) of an integrated CL OCM/CO_2-H_2O splitting process for low-carbon ethylene and syngas production. To achieve this goal, advanced lab-scale reactor modeling, system-level modeling and TEA/LCA are employed. These approaches are used to identify the key performance limitations of the system, determine optimal operating conditions, evaluate scale-up potential, and assess the economic/environmental viability of the proposed process. To accomplish the main goal of this dissertation, the following research objectives, along with their corresponding research questions and tasks, are proposed.

➢ **Objective 1: Literature review and identification of major challenges in methane conversion, OCM and CO_2-H_2O splitting technologies (RQ1 and RQ2)**

Approach: A comprehensive literature review is conducted to evaluate the current progress, limitations and opportunities in methane conversion, OCM and CO_2-H_2O splitting technologies. Special attention is given to the challenges associated with OCM, CO_2-H_2O splitting, catalyst performance and stability, C_2 (ethane and ethylene) selectivity, reactor operation, and commercial scalability.

New knowledge: A detailed understanding of the current state of methane conversion, OCM and CO_2-H_2O splitting technologies, their technical limitations and the opportunities for integrating OCM with CO_2-H_2O splitting for low-carbon chemical production.

➢ **Objective 2: Establishment of performance benchmarks for integrated CL OCM/CO_2-H_2O splitting (RQ3)**

Approach: Performance benchmarks are identified to evaluate whether the proposed integrated process can compete with conventional ethylene production technologies. Important performance indicators include methane conversion, C_2 selectivity, C_2 yield, catalyst stability and process economics. These benchmarks are used to define the minimum performance requirements needed for the integrated process to become technically and economically competitive.

New knowledge: Identification of critical performance targets and benchmark metrics required for CL OCM/CO_2-H_2O splitting to become a viable alternative to high energy intensive conventional ethylene production routes.

➢ **Objective 3: Development and optimization of a reactor model for CL OCM (RQ4)**

Approach: A lab-scale reactor model is developed to investigate the coupled reaction, transport, and heat-transfer behavior of the chemical looping OCM process. The model is used to study the effects of operating parameters such as temperature, inlet methane concentration, gas hourly space velocity (GHSV), oxygen availability and reactor diameter on methane conversion, C_2 selectivity and C_2 yield. The reactor design is optimized to

improve product formation while minimizing unwanted combustion and deep oxidation products such as COx.

New knowledge: Insight into the reaction–transport interactions controlling OCM performance and identification of optimized reactor operating conditions that enhance C_2 yield and selectivity in a CL environment for OCM.

➢ Objective 4: Process design and system-level optimization of the integrated CL OCM/CO_2-H_2O splitting system (RQ5)

Approach: A system-level process model on an industrial scale is developed to evaluate the integration of CL OCM with CL CO_2-H_2O splitting, product purification and separation, methane recycle, CO_2 recycle and syngas production. Process simulations are performed to assess the influence of recycle ratios and energy integration on the overall plant performance. Optimization is conducted to improve ethylene production, energy efficiency and economic viability.

New knowledge: Development of an integrated plant configuration for low-carbon ethylene and syngas production, along with an understanding of how process integration, recycle operation and separation strategies influence system-level performance.

➢ Objective 5: Techno-economic and environmental assessment of the integrated CL OCM/CO_2-H_2O splitting process (RQ5 and RQ6)

Approach: A TEA is performed to estimate the capital cost, operating cost and economic competitiveness of the proposed integrated process with conventional technologies. Sensitivity analyses are carried out to determine the effects of key economic parameters including feedstock cost and capital expenditure on the overall process feasibility.

New knowledge: Understanding of the economic and environmental viability of the integrated CL OCM/CO_2-H_2O splitting process, including the key parameters that control cost and efficiency.

In summary, this dissertation provides a systematic framework for evaluating the integrated conversion of methane and CO_2 into valuable chemicals through CL OCM/CO_2-H_2O splitting. By combining reactor modeling, process optimization and TEA/LCA, the study addresses key technical and practical challenges that currently limit the commercialization of OCM-based methane conversion technologies. The outcomes of this work are expected to provide important insights into the design and optimization of low-carbon chemical processes that can improve methane conversion and support more sustainable production of ethylene and syngas.

1.2. Dissertation Structure

The current Ph.D. dissertation is organized into eight chapters. The dissertation follows a sequential structure beginning with the introduction section which provides the motivation and technical background, followed by technology benchmarking, CFD reactor

modeling and optimization, system-level modeling, TEA/LCA and final conclusions with recommendations for future research.

Chapter 1 provides the introduction to the dissertation. This chapter presents the motivation for converting methane and CO_2 into valuable chemicals. Detailed description of the end-state Approach in the context of proposed technology is presented. It also provides the challenges and opportunities associated with methane conversion technologies. The research gap, research questions, objectives, scope of the study and overall dissertation structure are also presented in this chapter.

Chapter 2 provides a comprehensive literature review of OCM and CO_2-H_2O splitting technologies. The chapter discusses the current state and challenges associated with each technology and the potential benefits of combining them. Technical limitations that have prevented the commercial deployment of OCM are also discussed. This chapter establishes the scientific and technical foundation for integrating CL OCM with CL CO_2/H_2O splitting for low-carbon and sustainable ethylene and syngas production.

Chapter 3 presents the evaluation strategy for the integrated CL OCM/CO_2-H_2O splitting technology. This chapter presents the critical performance benchmarks required for the proposed technology to compete with conventional ethylene production technologies so it can be competitive at industrial scale.

Chapter 4 presents the computational fluid dynamics (CFD) model for the CL OCM reactor. The chapter describes the governing equations, reaction kinetics, heat and mass transfer used to simulate the reactor.

Chapter 5 presents the CFD parametric study based on the CL OCM reactor model presented in Chapter 4. The chapter evaluates the effects of major operating and design parameters, including temperature, GHSV, inlet methane concentration, oxygen availability, CH_4/O_2 ratio and reactor diameter/length ratio. The results are used to identify optimized operating conditions that enhance the reactor performance.

Chapter 6 presents the system-level model for the CL OCM and TEA of the CL OCM/CO_2-H_2O splitting process. This chapter develops the overall plant configuration for the process, including the reactor, separation and purification stages, recycle streams, heat integration and utility requirements. The TEA evaluates the influence of integrating CL OCM and CL CO_2-H_2O splitting and methane recycling on the capital cost, operating cost and energy consumption.

Chapter 7 presents the LCA of the integrated system. This chapter evaluates the environmental performance of the proposed process by quantifying the associated life-cycle impacts, including greenhouse gas emissions and other relevant environmental indicators. The analysis examines how the CL OCM/CO_2-H_2O splitting technology compares with conventional ethylene production technologies in terms of environmental impacts.

Chapter 8 summarizes the main conclusions of the dissertation and outlines the road for future directions. It highlights the key scientific and technical contributions of the work and discusses the remaining challenges that must be addressed before the CL OCM/CO_2-H_2O splitting process can be further developed toward practical implementation. Recommendations for future research are also provided. The complete structure is shown in Figure 2.

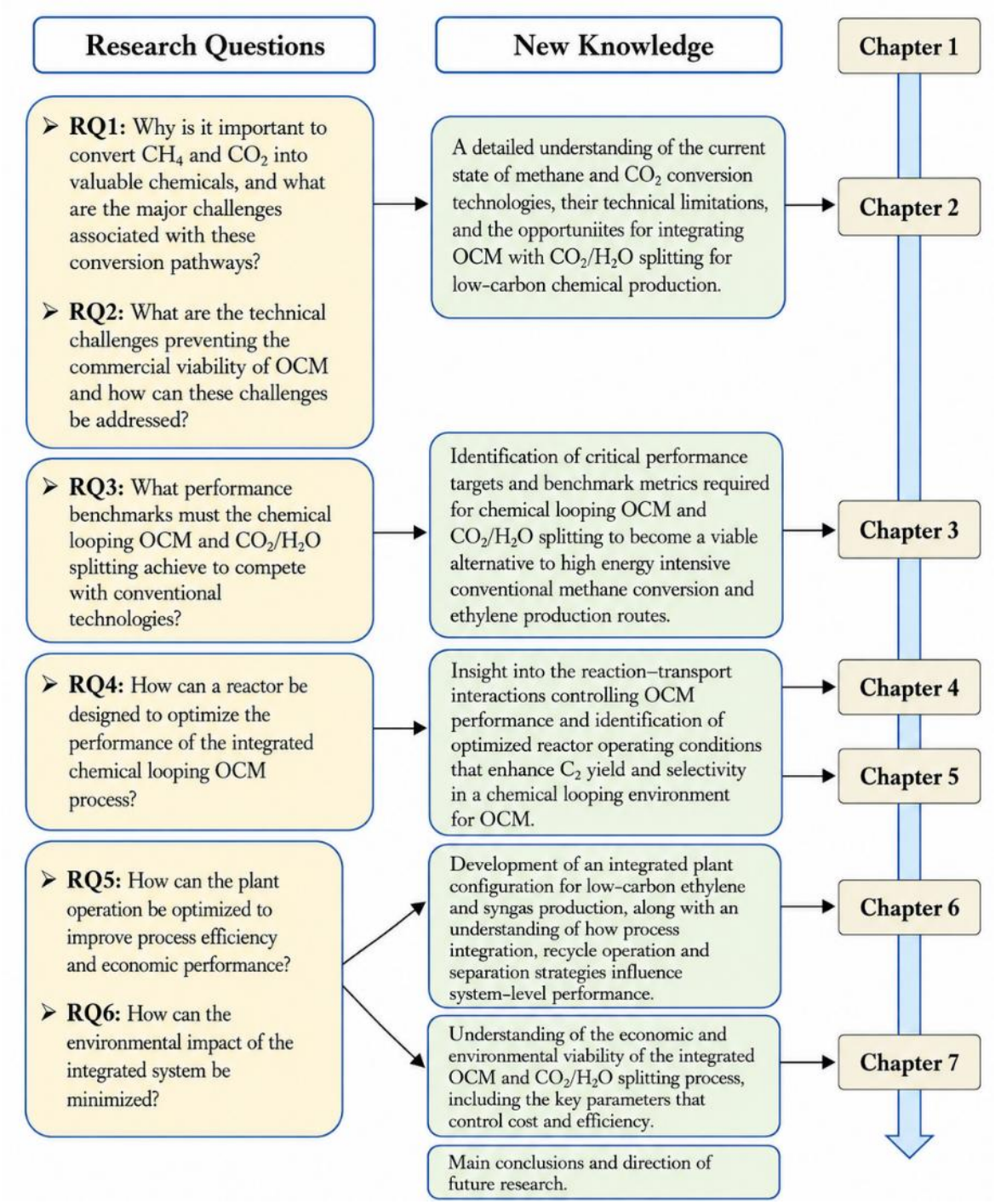

Figure 2. Dissertation structure.

1.3. End-State Approach for Technology Development and Evaluation

For this dissertation, an end-state approach is adopted for the development and evaluation of the integrated CL OCM/CO_2-H_2O splitting process. This approach, also referred to as a technology development roadmap or target-state architecture, is a structured planning methodology where the desired final state of a technology is first established, and then the required technical, economic and environmental milestones are identified by working backward from that targets [19, 20].

For the current research, the desired end-state for the development of an integrated CL OCM/CO_2-H_2O splitting technology consists of sustainable production of ethylene and syngas with improved carbon utilization, reduced environmental impact and competitive economic performance. This framework is suitable for emerging technologies because commercialization does not only depend on high reactor performance, but also on meeting broader economic and environmental targets.

1.3.1. Initial and End-State Establishment

The first step in this end-state approach is the establishment of the initial and final states. The initial state represents the current state of development of the OCM technology, i.e., what are the highest performance metrics achieved to this day, including the C_2 yield, methane conversion and catalyst stability. Whereas, the end-state represents a practically viable set of targets in which methane is selectively converted to C_2 products during the

OCM cycle of the proposed integrated CL OCM/CO_2-H_2O splitting technology at a reasonable cost and low environmental impact. Defining this end-state provides a clear set of performance targets for the industrial deployment of the technology. Establishment of initial and end-states provides a clear gap between the state-of-the-art and required goals for the technology and provides input data and performance targets for the modeling processes.

1.3.2. Reactor Modeling and Optimization

Following the definition of the initial and end-states, reactor modeling and optimization serve as the next major component of the end-state framework. Since the reactor is the core unit, reactor understanding is essential for determining whether the proposed process can meet the desired technical benchmarks. In this study, reactor modeling is used to investigate the effects of operating conditions such as temperature, inlet methane concentration, GHSV, oxygen availability and reactor geometry on the performance of the CL OCM process. The reactor model also provides insight into reaction–transport interactions, heat-transfer limitations, and the formation of undesired products such as CO_2. Therefore, reactor optimization directly supports the research objectives related to improving C_2 yield, enhancing selectivity and identifying operating conditions that move the technology closer to the desired end-state.

1.3.3. System-Level Modeling

After reactor-level optimization, system-level modeling is employed to evaluate how the optimized reactor can be integrated into a complete chemical process. This step is

necessary because high reactor performance alone does not guarantee overall process feasibility. The process must also include product separation, methane recycle, CO_2 recycle, heat integration and overall plant operation. System-level modeling allows the effect of recycle ratios, separation efficiencies, operating pressures, product recovery strategies and energy integration to be evaluated on a plant-wide basis. The end-state approach ensures that the proposed technology is assessed as a complete process rather than as an isolated reactor concept by connecting reactor performance with downstream processing and recycle operations.

1.3.4. Techno-Economic Assessment

The TEA represents the next stage of the end-state approach and is used to determine whether the proposed integrated process can become economically competitive with conventional technologies. Even if the integrated CL OCM/CO_2-H_2O splitting process demonstrates strong technical performance, its commercial viability depends on capital cost, operating cost, energy consumption, product yield, equipment size, feedstock cost and the cost of product separation. Therefore, TEA is used to estimate key economic indicators such as total capital investment, operating expenses and sensitivity of the process economics to major end-state targets. This step helps identify the most influential cost drivers and establishes whether improvements in reactor performance, recycle strategy or process integration can reduce the cost of ethylene and syngas production. In this way, the TEA connects the technical objectives of the dissertation with the practical requirements for future scale-up and commercialization.

1.3.5. Life-Cycle Assessment

Finally, the LCA is incorporated as the environmental evaluation component of the end-state approach. Since the motivation for integrating CL OCM with CL CO_2-H_2O splitting is not only to produce valuable chemicals but also to improve carbon utilization and reduce environmental impact, it is essential to quantify the sustainability benefits of the proposed system. LCA can be used to evaluate greenhouse gas emissions, energy intensity, carbon efficiency, and the environmental trade-offs associated with feedstock use, utility demand and product separation. This analysis provides a broader perspective on whether the proposed process can offer environmental advantages compared with conventional ethylene and syngas production routes.

Overall, the end-state approach provides a structured framework for achieving the research objectives of this dissertation. This methodology links technology development across multiple levels, beginning with the identification of current challenges and ending with the assessment of commercial and environmental feasibility. The approach ensures that each objective contributes to the final goal: the development of a technically feasible, economically viable and environmentally beneficial process. Therefore, the end-state approach serves as the foundation for the organization of this dissertation, from the selection of assessment methods to defining the milestones required to advance the proposed technology toward practical implementation. Figure 3 represents the complete flow diagram for the end-state approach developed for this dissertation.

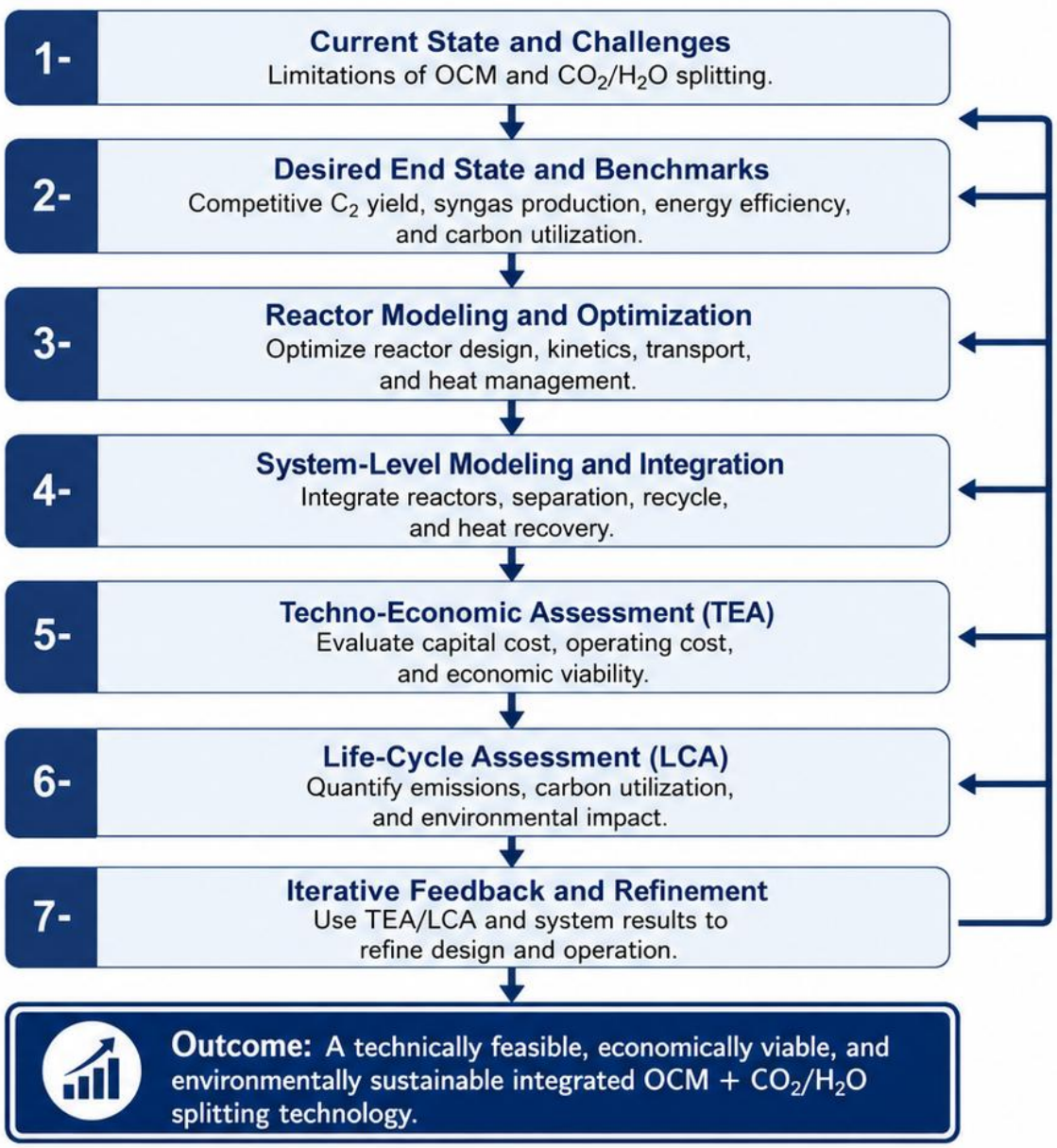

Figure 3. End-state approach for the integrated CL OCM/CO_2-H_2O splitting.

1.4. Methane Conversion Technologies

This section provides an overview of major methane conversion technologies, including both indirect and direct conversion pathways. Although these technologies offer important opportunities for improving carbon utilization and reducing dependence on conventional petrochemical feedstocks, they also face several technical challenges. These challenges include high operating temperatures, catalyst deactivation, coke formation, low single-pass conversion, poor product selectivity and difficulties in process scale-up. Therefore, understanding the advantages and limitations of each methane conversion pathway is essential for identifying practical, efficient and economically viable routes for future methane valorization.

Some of the methane conversion technologies are shown in Figure 4. Methane is the one of the most stable molecules. It consists of a central carbon atom which is surrounded by four hydrogen atoms. All four C-H bonds are highly stable with ($\Delta_d H = 440\ kJ/mol$). Methane is resistant to nucleophilic attacks and acid/base catalysis [21]. The most simplistic way to activate methane is the C-H bond cleavage and hydrogen atom transfer to a radical as the reaction partner.

Regardless of the method chosen for methane activation, high temperatures and aggressive reactants decrease the selectivity of the process [8]. The conditions required for methane activation also favor activation of other molecules which result in undesired products [8].

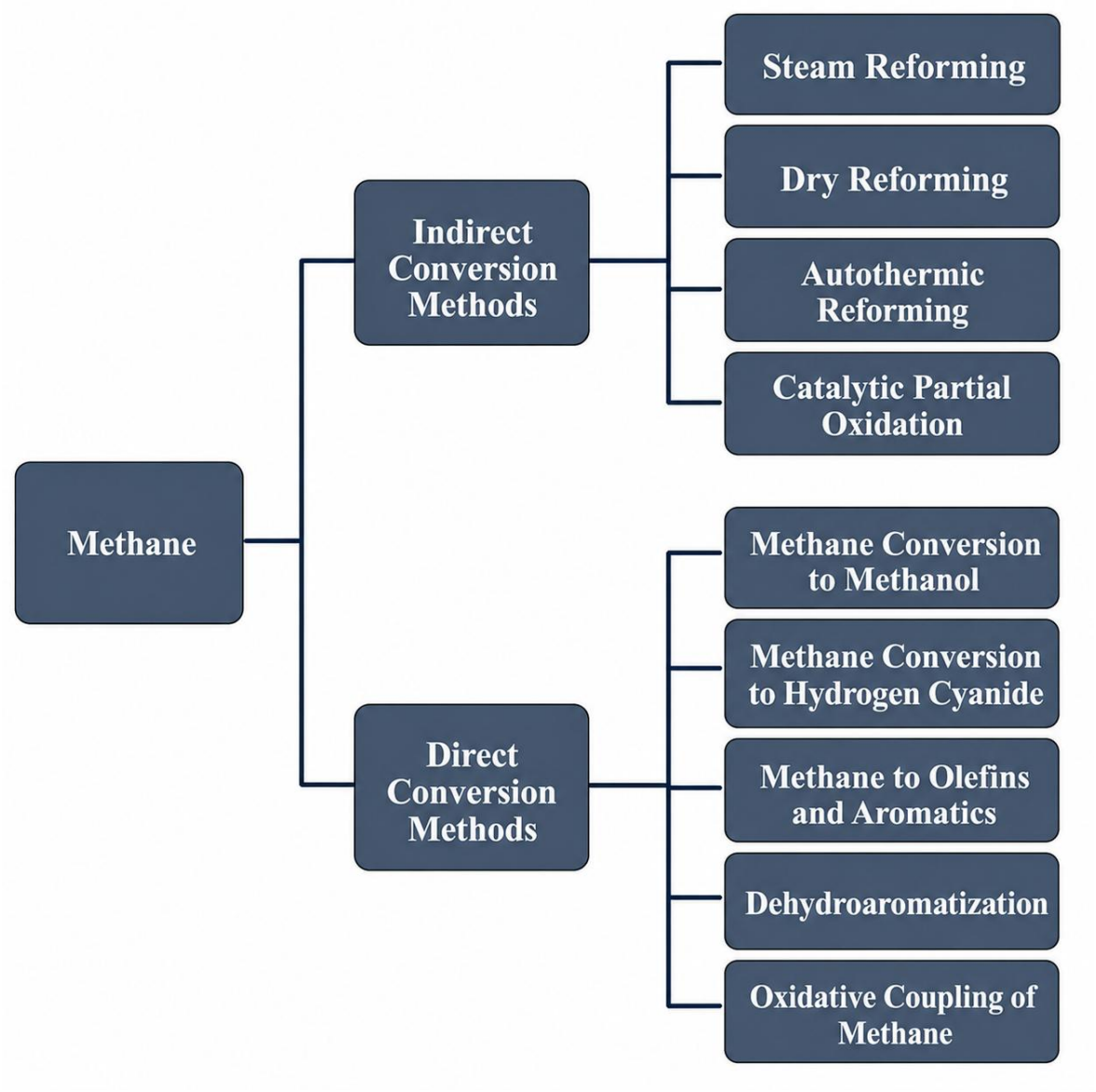

Figure 4. Methane conversion methods.

1.4.1. Indirect Methane Conversion Technologies

Indirect methane conversion technologies involve the transformation of methane into an intermediate product, most commonly synthesis gas (syngas), before it is further

converted into fuels, chemicals, or other value-added products. These methods are widely studied and commercially important because syngas can serve as a flexible platform for producing hydrogen, methanol, ammonia, liquid fuels and various hydrocarbons. Common indirect methane conversion methods include steam reforming, dry reforming, autothermal reforming and catalytic partial oxidation.

Although these processes can achieve high methane conversion performance, they often require high operating temperatures and significant energy input. In addition, challenges such as catalyst deactivation, carbon deposition, heat management and process integration must be carefully addressed. Therefore, understanding the principles, advantages and limitations of indirect methane conversion technologies is essential for evaluating their role in efficient and sustainable methane utilization. Some of the indirect methane conversion technologies and the challenges associated with them are briefly discussion in the following subsections.

1.4.1.1. Steam Methane Reforming

Indirect methods, such as methane reforming, are currently dominating the industry for the methane conversion [22, 23]. However, they are energy intensive as they require high temperatures and pressures and also produce high carbon dioxide (CO_2) emissions [24-29]. In methane steam reforming, methane reacts with water to form CO, H_2 and some CO_2. The reaction is endothermic and limited by equilibrium [30, 31]. The major challenge faced by steam reforming is the deactivation of the catalyst by sintering, carbon blockage and poisoning by S, As, Pb, P, SiO_2 and other alkali metals [30, 31].

1.4.1.2. Dry Methane Reforming

Dry reforming is beneficial as it converts two greenhouse gases, i.e., methane and CO_2, to valuable syngas while absorbing heat (endothermic reaction). Moreover, it produces lower ratios of H_2/CO compared to steam reforming which is desirable if long chain hydrocarbons are the target product [8]. The main challenges include a high activation barrier, low sticking coefficient and a high hydrogen kinetic isotope effect on transition metal surfaces for CH_4 and CO_2 activation and reactions [32]. Moreover, at reaction temperatures for dry reforming, the CO_2 molecule dissociates to CO and O while CH_4 dissociates to CH and H. CH and O then form CHO which splits off the H atoms. In terms of catalyst, the biggest challenge is also catalyst deactivation by carbon blockage. To avoid carbon blockage, temperatures higher than 1000 K are required with excess CO_2 [30].

1.4.1.3. Autothermic Reforming

In an Autothermic Reforming (ATR) process, sub-stoichiometric feed of natural gas, steam and oxygen (H_2O/C = 0.5-3.5, O_2/C = 0.4-0.6) is burned at high temperature of almost 2773 K in a burner [8]. Moreover, it consists of a combustion chamber where homogeneous gas-phase reactions like CO oxidation, steam reforming, water gas shift and pyrolysis occur and a catalyst zone where methane is steam reformed. The challenges faced by ATR are related to reactor/burner design, minimizing pressure drop and optimizing catalyst pellet shape [8].

1.4.1.4. Catalytic Partial Oxidation

Catalytic Partial Oxidation involves premixing of methane and oxygen which is then converted to H_2 and CO in a reactor. The side products are H_2O and CO_2. The challenges in industrial deployment include pressures as high as 50 bar for downstream processes [8]. These high pressures can lead to safety issues. Moreover, air separation for pure O_2 is costly. In terms of catalyst, highly coke formation brings about the deactivation of catalyst [8].

Furthermore, the processing of FTS include the following challenges.

- The FTS requires H_2 or CO in syngas to reduce CO which decreases the carbon-utilization efficiencies to values below 50% [33].
- The H_2 used for CO reduction is obtained from naphtha cracking, a process which generates high CO_2 emissions [34, 35].

1.4.2. Direct Methane Conversion Technologies

The direct conversion methods aim to transform methane directly into higher-value products such as ethylene, methanol, hydrogen cyanide, olefins, aromatics, and other chemicals. In contrast to the indirect methods for methane conversion, the direct methods are cheaper and simpler because of the absence of intermittent syngas formation [30, 31]. The direct methane conversion methods are further divided into two categories i.e., oxidative and non-oxidative.

1.4.2.1. Oxidative Coupling of Methane (OCM)

As a direct pathway, OCM is more economically viable and can occur at wider operating conditions and lower temperatures than steam reforming [21]. The OCM was discovered in the 1980s by the pioneering work of Keller and Bhasin [36] and has been researched on ever since. The OCM process converts methane directly into ethylene (C_2H_4) [30]. Moreover, OCM can propel the chemical industry towards a less CO_2 emitting path to produce valuable chemicals [31].

1.4.2.2. The Direct Oxidation of Methane to Methanol and Formaldehyde

The direct oxidation of methane to methanol and formaldehyde has not yet found industrial application despite extensive research. The reason for this is that the methanol and formaldehyde yields are only a few percent [8]. The formaldehyde yields are within the range of 3-4%. The conversion of methane to methanol takes place because of partial oxidation shown in Equation 1.

$$CH_4 + 0.5O_2 \rightarrow CH_3 \quad \Delta H_{298K} = -30.4 \text{kcal/mol} \qquad (1)$$

The reaction can take place in gas-phase or liquid-phase. However, there are some challenges faced by the reaction. In gas-phase, the reaction occurs at 30-200 bar pressure and 473-773K temperatures with catalysts. In liquid phase, the reaction proceeds with methane oxidation by super acids [33]. Zhang et al. [37] showed that a methanol yield of 30-40% was achievable but at high pressures (30-60 bars) and low methane conversion rates (5-10%) [38]. Despite the impressive yield, the methane conversion to methanol still hasn't

achieved commercial deployment because of poor conversion efficiency, slow reaction rates and because these reactions are highly energy intensive [38].

1.4.2.3. Formation of Hydrogen Cyanide

Formation of Hydrogen Cyanide can be obtained from methane either with or without oxygen. The process without oxygen is termed as BMA process whereas with oxygen is called Andrussow process. The BMA process is endothermic and requires temperatures of 1473 K [8].

1.4.2.4. The Non-Oxidative Direct Methane Conversion Methods

The non-oxidative direct methane conversion methods have several benefits. Since there is no reagent required, these processes can take place in remote areas close to the natural gas sources. Moreover, the absence of oxygen eradicates explosion risks and COx formation. However, there are some drawbacks associated with these processes as well. The methane to olefins, aromatics and hydrogen process requires high temperatures and can occur within narrow range of operating conditions. Dehydroaromatization process faces issues with catalyst stability, coke formation and low methane conversion rates [32].

Chapter 2. Background and Literature Review of Chemical Looping OCM and CO_2-H_2O Splitting

In this chapter, the concept of CL reactor design and the integration of CL OCM and CL CO_2-H_2O splitting technologies is explained in detail. First, a detailed literature review is presented for both OCM and CO_2-H_2O splitting including the technology background and previous studies and advancements. Then the concepts of CL OCM and CL CO_2-H_2O splitting reactor design and integration of OCM and CO_2-H_2O splitting is presented.

Both processes are beneficial as they convert major GHGs i.e., CO_2 and CH_4 to valuable fuels and chemicals [39]. OCM is beneficial as it converts methane to ethylene, a chemical which is considered the backbone of petrochemical industry. Splitting of CO_2 and H_2O produces syngas which can be transformed to liquid through FT synthesis and easily transported [40, 41]. Additionally, CO_2 splitting allows for conversion of CO_2 where its capture and storage in not suitable [42].

2.1. Oxidative Coupling of Methane (OCM)

2.1.1. Introduction and Challenges

In the OCM, methane is activated heterogeneously on the surface of a catalyst producing methyl free radicals. These radicals are coupled to form ethane (C_2H_6) which is then dehydrogenated to form ethylene (C_2H_4) [4, 5, 43, 44]. However, the formation of ethylene is not a straightforward process. The overall yield of ethylene is shortened by the

reactions of free radicals with oxygen and surface to form carbon monoxide (CO) and CO_2. A schematic diagram of the OCM reaction is shown in Figure 5. Apart from Figure 5 reactions, there can be non-selective surface reactions that can form COx. OCM is an exothermic reaction (ΔH = -280 kJ/mol) which produces heat, ethylene, water, CO and CO_2. The reaction usually occurs at high temperatures i.e., 750-950 ^oC [3].

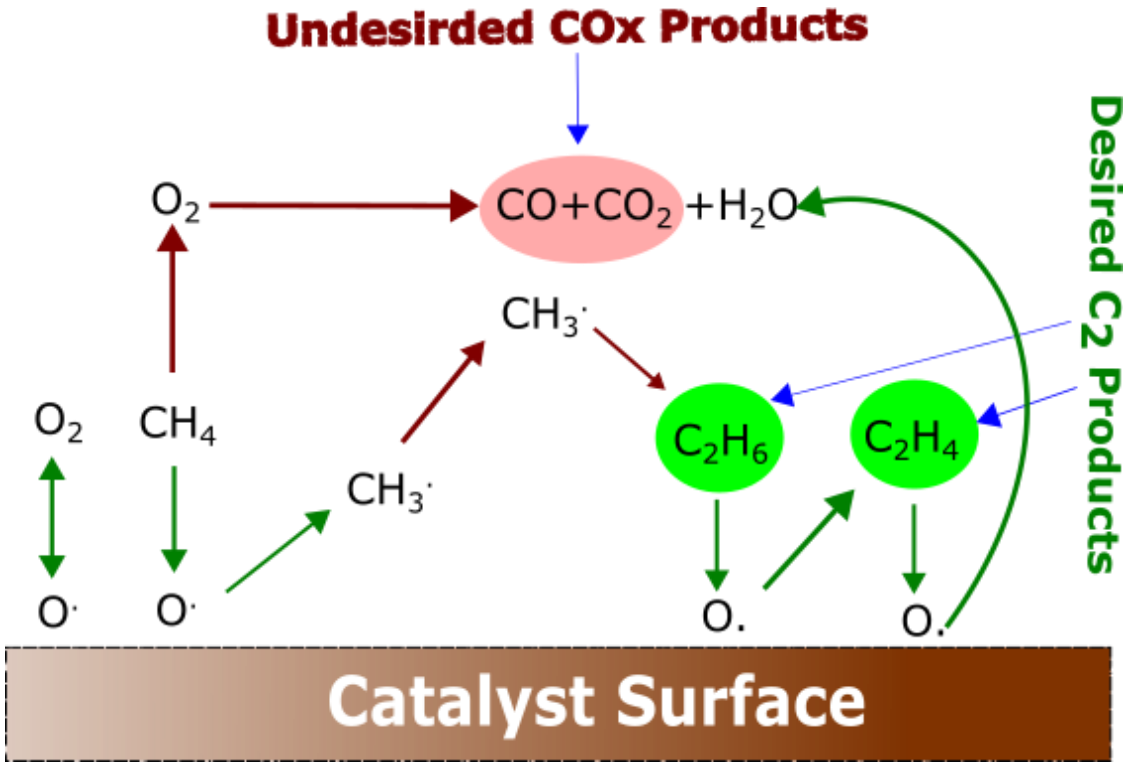

Figure 5. OCM reactions [32] (green arrows = surface reaction, brown arrows = gas-phase reaction).

Though there are many advantages of OCM as an excellent ethylene production process, some drawbacks have hindered its industrial deployment. At first, the CH_4 molecule has a bond dissociation energy of 439.3 kJ/mol at room temperature which makes it the most

stable molecule in nature [10]. Therefore, the CH_4 activation is challenging for the OCM process and requires elevated temperatures [45].

However, at high temperatures (i.e., above 800^oC) the formation of deep oxidation products i.e., COx is more favorable as compared to ethylene. Although the new oxide catalysts can reduce the methane activation temperature, the process is highly exothermic and the reaction temperature increases rapidly due to the reaction enthalpy. Increased reaction temperatures eventually lead to total or complete oxidation. Fast reaction kinetics make it difficult to control the reaction temperature causing hot sport formation. To combat the reaction exotherm, the OCM processes operates at the stoichiometric CH_4/O_2 ratio. Reduced O_2 concentration limits the reaction exotherm, but also results in low CH_4 conversion and high COx selectivity. This hampers the yield of the OCM process [1, 3, 45-47]. Currently, the yield of the process is in the vicinity of 20% and is the biggest hurdle in achieving its industrial viability [3, 48-53].

Similarly, a CH_4 conversion of at least 30% and C_2 selectivity of more than 80% are suggested for the industrial deployment of OCM [53, 54]. A higher C_2 selectivity can be achieved at a lower cost and temperature and results in lower COx emissions compared to higher CH_4 conversions and is therefore, preferred over high CH_4 conversion rates. The methane conversion can also be controlled by O_2 content in the feed and the reaction temperature.

2.1.2. Approaches for Industrial Viability of OCM

Overall, there have been five approaches to improve the OCM performance and bring about its industrial viability.

1. The first approach is to find a suitable catalyst and improve its performance by analyzing its yield, selectivity and stability [1, 9, 21, 55, 56].
2. The second approach is to combine the downstream OCM process with another system such as a chemical reaction system to produce valuable products or integration with a power plant [57-60].
3. The third approach is based on different types and configurations of reactors such as packed bed reactors, fluidized bed reactors, membrane reactors, dual reactors and circulating reactors [9, 21, 55, 59, 61].
4. The fourth approach involves the usage of different oxidants to improve the CH_4 activation [21].
5. The fifth approach is to optimize the downstream processes and structures based on system level analysis approach [9] and to utilize the process heat to improve the energy integration [58].

Recently, oxygen membrane reactors have shown a yield of more than 35% [4, 50, 62, 63]. By controlling the oxygen feed through a membrane, the design aims to control the reaction exotherm and process temperature to reduce COx [5]. However, the oxygen membrane reactors have increased complexity with some drawbacks and are still not suitable for the industrial deployment of OCM. These drawbacks include the damage caused by cracking or leakages and consequently, increasing the capital cost for replacement of the

membranes [4]. Membrane catalyst interaction is also a problem which alters the catalytic properties [5].

The following sections of this chapter use detailed chemical kinetics to represent the OCM process and understand the interconnected nature of heat, mass transport and C_2 yield. Moreover, they aim to review various promising results reported in the literature in the context of multiple approaches mentioned above and their combinations. Comprehensive reviews of the OCM technology are already found in the literature [1, 4, 6, 17, 21, 32, 49]. The review in this dissertation differs from these reviews in that it focuses more on the results that are close to the industrially required limits or ones that increase the OCM performance significantly.

Moreover, a novel concept is shown which integrates the OCM technology with the CO_2-H_2O splitting technology in a CL reactor design. The chemical looping design allows efficient energy utilization by integrating the exothermic OCM and CO_2-H_2O splitting processes. The heat rejected from the OCM process is used to drive the CO_2-H_2O splitting and vice versa thereby, improving the thermal efficiency, reducing the external energy inputs and also ensuring minimal heat losses to the environment. This collaboration of chemical processes transforms methane to value added ethylene while simultaneously producing syngas which is a feedstock for many synthetic fuels and also a medium for hydrogen storage. Therefore, the proposed technology serves as a means for efficient energy conversion and chemical energy storage.

2.1.3. OCM Process

In the conventional OCM process, the preheated methane and oxygen gases are fed to the OCM reactor. The heat from the product gases of the OCM reaction are used to generate high pressure steam and then cooled [60, 64]. The steam generated here can generally be used for power generation or for process utilities [64, 65]. These gases are then compressed before entering the CO_2 removal section.

The product gases then go through the CO_2 removal section where they are further cooled, and the CO_2 is captured. Conventional CO_2 capture processes use solvent-based adsorption techniques; monoethanolamine (MEA) is a commonly used absorbent. The saturated solvent is then regenerated in a stripper column [21, 60]. The remaining gases then go through the cryogenic distillation columns. The first column is the demethanizer tower and the second one is called the C_2-splitter [60].

In the demethanizer column, the unreacted methane is removed with traces of H_2 and CO and recycled back to the OCM reactor. After this stage, there are only ethane and ethylene present in the stream. Following the demethanizer, the remaining gases enter the C_2-splitter where ethane and ethylene are separated [21, 58, 64]. Ethylene appears on top of the C_2-splitter column with a molar purity of 99.9% whereas, ethane appears on the bottom and is separately sold as a byproduct [60]. It should be noted that the methane recycled from the demethanizer is not entirely recycled and is mostly used for electricity generation or steam production for process utilities [60]. Figure 6 shows the process flow diagram of a conventional OCM plant [58]. Apart from the steps mentioned before, there is an optional step of methanation where CO and H_2 present in the recycled stream are converted to

methane and water. This step improves the chances of getting higher yields from the OCM process as the presence of the recycled CO and H_2 in the feed can result in reactions with O_2 and reduce its availability for CH_4 activation [64].

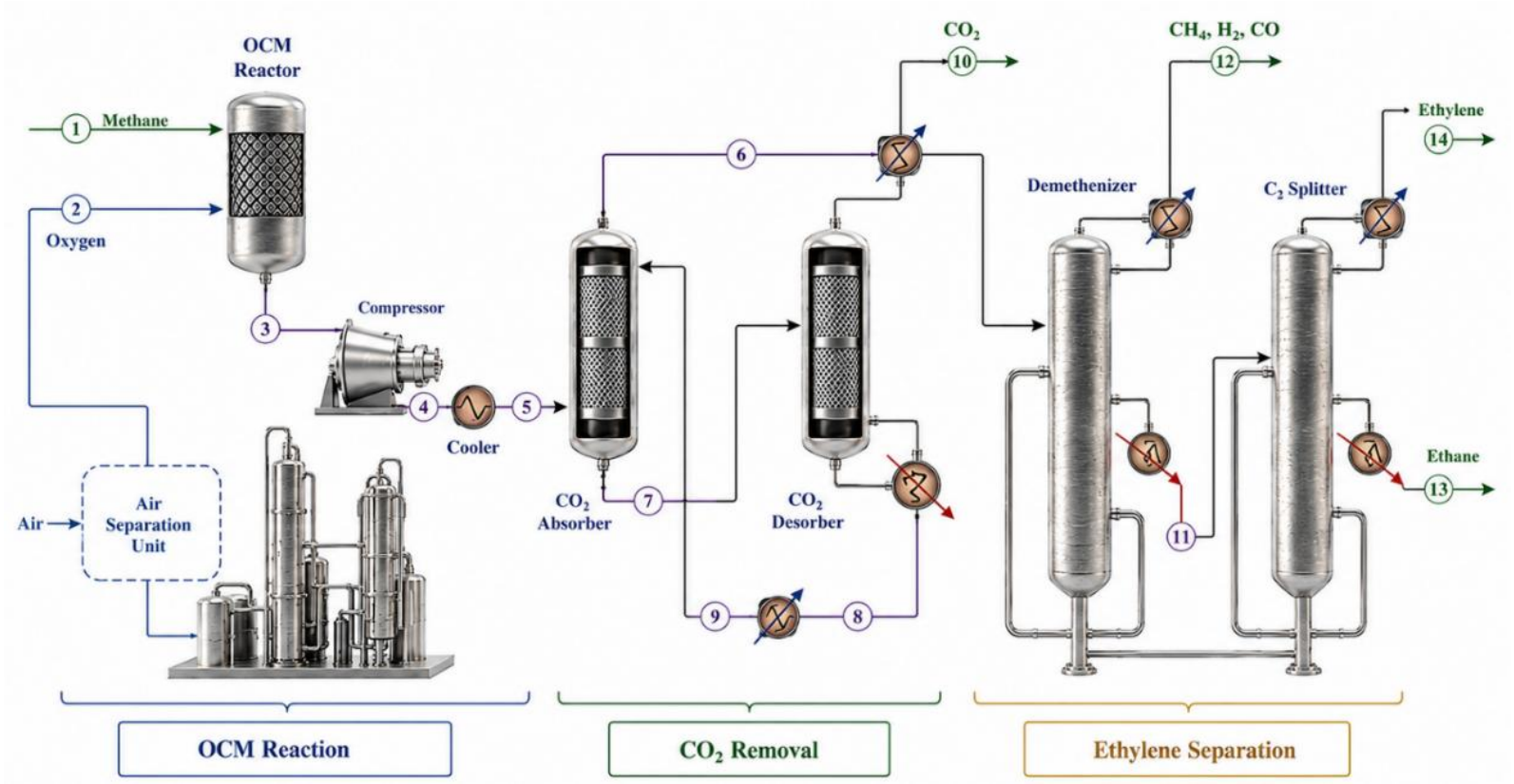

Figure 6. Conventional OCM process.

2.1.3.1. Kinetics of OCM

Although OCM involves predominantly heterogeneous reactions, there are some homogeneous reactions that occur within the gases as well. Even at temperatures above 600°C, the methane can be converted to ethane and ethylene without the catalyst [32]. The contribution of homogeneous reactions can be significant depending on the residence time, pressure and CH_4/O_2 ratio of the inlet stream [32, 66]. Moreover, the gas-phase methyl-radicals affect the C_2 products formation rates strongly [67, 68]. At high temperatures and pressures, the formation rate of methyl radicals increases and becomes the dominant pathway, thus the contribution of the catalyst becomes negligible. However, at low pressures, the formation rate of methyl radicals depends more strongly on the type of catalyst and weakly on temperature [32]. A schematic diagram of the reaction pathways for OCM proposed by Simon et al. [69] is shown in Figure 7.

There is a general agreement in literature that at high temperatures, the methane activation to form methyl radicals is the rate determining step as given below [21, 32]. Moreover, there can also be a $H^{\cdot}$ radical attack [21].

$$CH_4 + (s) \rightarrow CH_4(s) \qquad (2)$$

$$CH_4(s) \rightarrow CH_3^{\cdot} + H(s) \qquad (3)$$

or

$$CH_4 + O(s) \rightarrow CH_3^{\cdot} + OH(s) \qquad (4)$$

$$CH_4 + H^{\cdot} \rightarrow CH_3^{\cdot} + H_2 \qquad (5)$$

Here, (s) indicates adsorption on surface. Moreover, $OH^{\cdot}$ radical induced methane activation is possible as shown below [21, 70].

$$H_2O + O(s) \rightarrow OH^{\cdot} + OH(s) \quad (6)$$

$$2H_2O + O_2 \rightarrow 4OH \quad (7)$$

$$CH_4 + OH^{\cdot} \rightarrow CH_3^{\cdot} + H_2O \quad (8)$$

Consequently, the formation of ethane occurs as a result of coupling of the methyl radicals in the gas phase as shown by an extensive study conducted by Lunsford et al. [71-74].

$$CH_3^{\cdot} + CH_3^{\cdot} + M \rightarrow C_2H_6 + M \quad (9)$$

Here, M represents a gas-phase third body. The ethane is then dehydrogenated to form ethylene. The formation of CO occurs due to homogenous reaction whereas CO_2 and H_2O form heterogeneously and then desorb. There is also a possibility of heterogeneous formation of CO as well [75, 76]. Moreover, there can also be homogeneous chemistry between methane and oxygen as shown below [21, 77].

$$CH_4 + O_3 \rightarrow CH_3^{\cdot} + HO_2 \quad (10)$$

$$CH_4 + O_3 \rightarrow HCHO + OH \quad (11)$$

$$CH_4 + O^{\cdot} \rightarrow CH_3^{\cdot} + OH \quad (12)$$

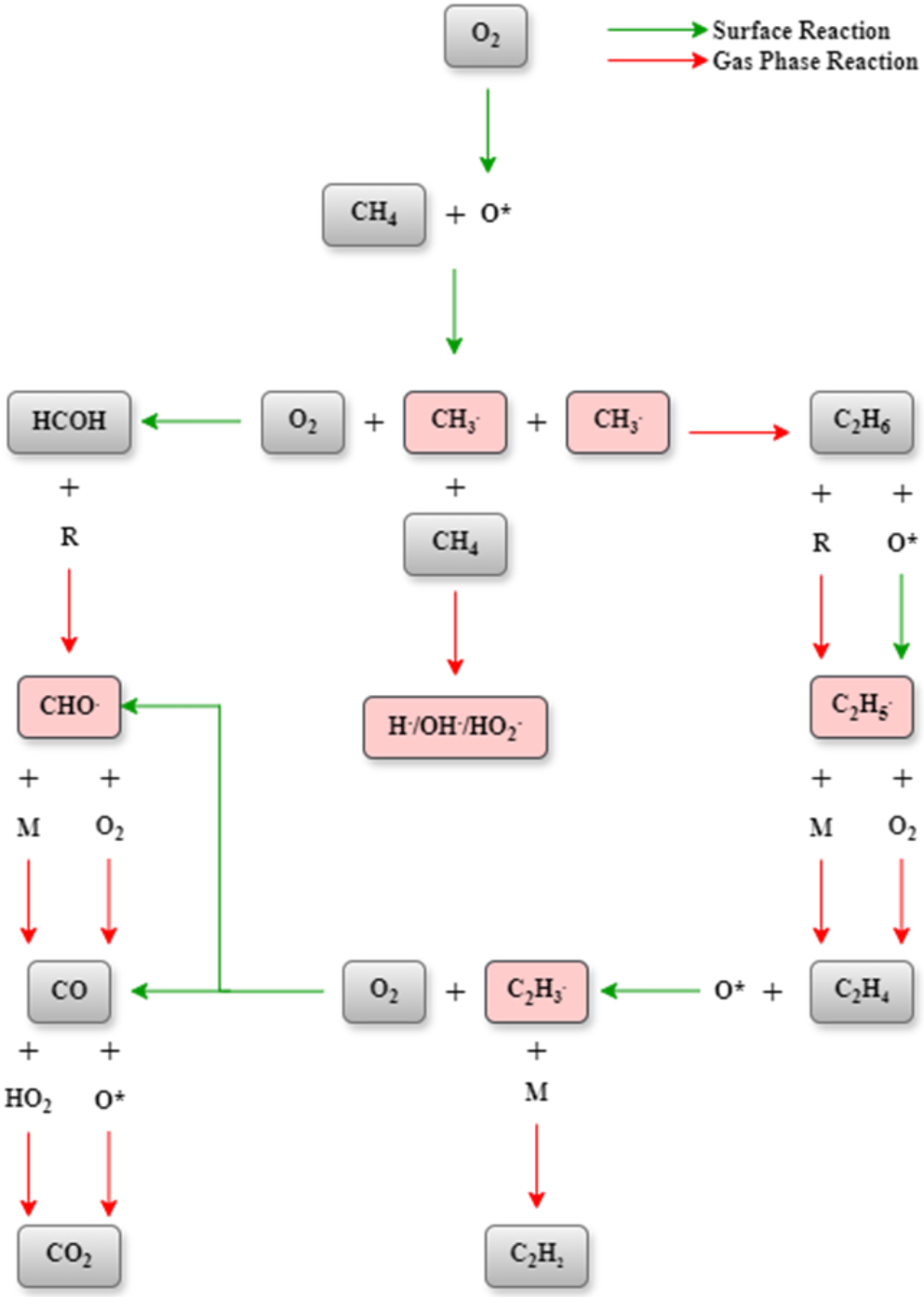

Figure 7. Pathways of OCM reaction [53, 67].

Numerous studies have been conducted for different catalysts on the kinetics and reaction engineering of the OCM process [78-92]. Overall, the desired OCM reaction goes through the steps given below [1].

- The adsorption of gas-phase species on the catalyst surface.
- Activation of CH_4 molecule by heterogeneous reaction with catalyst surface resulting in methyl radicals ($CH_3^{\cdot}$).
- Coupling of ($CH_3^{\cdot}$) radicals resulting in ethane (C_2H_6).
- Dehydrogenation of C_2H_6 to C_2H_4 by O_2.

However, there is occurrence of undesirable deep oxidation and combustion reactions by methane, ethane and ethylene resulting in COx products. In addition to different reaction pathways reported in literature, there have been global reactions reported for multiple catalysts that consider all reactions in homogeneous phases. These reactions can be used to estimate rate equation parameters empirically [32]. Since these kinetic parameters are determined empirically, the kinetic model needs to be fine-tuned at different operating conditions before they can be used for predictions of reactor behavior and assist in reactor design.

The overall/global reaction schemes, as reported for different catalysts in literature, are listed in Table 1. The corresponding references and catalysts (in parentheses) are also mentioned in the Table 1. From these global kinetic models, the model developed by Stansch et al. [63] has been proven to be the most widely used and delivers more accurate results [21, 32, 58, 89, 93]. A schematic of the model is shown in Figure 8.

Table 1. Global OCM kinetic models for different catalysts.

Reactions		Stansch et al. [63] (La_2O_3/CaO)	Olsbye et al. [78] ($BaCO_3/La_2O_n(CO_3)_{3-n}$)	Mleczko and Baerns [79] (La_2O_3/CaO)	Traykova et al. [80] (La_2O_3/MgO)	Lacombe et al. [81] (La_2O_3)	Shahri et al. [75] ($Mn/Na_2WO_4/SiO_2$)	Sohrabi et al. [82] (perovskite titanate)	Vatani et al. [94] (Li/MgO)	Tiemersma et al. [83] ($Mn/Na_2WO_4/SiO_2$)	Petrov et al. [95] (SrO-La_2O_3)	Daneshpayeh et al. [93] ($Mn/Na_2WO_4/SiO_2$)
1.	$2CH_4 + 0.5O_2 \rightarrow C_2H_6 + H_2O$	■	■	■	■	■	■		■	■	■	■
2.	$CH_4 + O_2 \rightarrow CO + H_2O + H_2$	■	■	■					■			■
3.	$CH_4 + 1.5O_2 \rightarrow CO + 2H_2O$				■		■					
4.	$CH_4 + 2O_2 \rightarrow CO_2 + 2H_2O$	■	■	■		■	■		■	■	■	■
5.	$2CH_4 + O_2 \rightarrow C_2H_4 + 2H_2O$											
6.	$CO + 0.5O_2 \rightarrow CO_2$	■		■		■			■			■
7.	$C_2H_6 + 0.5O_2 \rightarrow C_2H_4 + H_2O$	■		■	■	■	■		■	■	■	■
8.	$C_2H_6 + O_2 \rightarrow 2CO + 3H_2$					■						
9.	$C_2H_6 + 2.5O_2 \rightarrow 2CO + 3H_2O$		■									
10.	$C_2H_6 + 3.5O_2 \rightarrow 2CO_2 + 3H_2O$		■			■				■	■	
11.	$C_2H_6 \rightarrow C_2H_4 + H_2$	■	■	■	■				■		■	■
12.	$C_2H_4 + O_2 \rightarrow 2CO + 2H_2$					■					■	

13.	$C_2H_4 + 2O_2 \rightarrow 2CO + 2H_2O$	■	■	■		■	■		■		
14.	$C_2H_4 + 3O_2 \rightarrow 2CO_2 + 2H_2O$		■					■			
15.	$C_2H_4 + 2H_2O \rightarrow 2CO + 4H_2$	■		■			■		■		
16.	$CO_2 + H_2 \rightarrow CO + H_2O$	■			■	■	■		■		
17.	$CO + H_2O \rightarrow CO_2 + H_2$	■		■	■	■	■		■		
18.	$CH_4 + 0.5O_2 \rightarrow CO + 2H_2$										
19.	$C_2H_6 + 0.5O_2 \rightarrow 0.667C_3H_6 + H_2O$						■				
20.	$C_3H_6 + 3O_2 \rightarrow 3CO + 3H_2O$						■				
21.	$C_3H_6 + 3H_2O \rightarrow 3CO + 6H_2$						■				
22.	$C_2H_6 + 0.167O_2 \rightarrow 0.667C_3H_8 + 0.33H_2O$						■				
23.	$C_3H_8 + 3.5O_2 \rightarrow 3CO + 4H_2O$						■				
24.	$C_3H_8 + 3H_2O \rightarrow 3CO + 7H_2$						■				

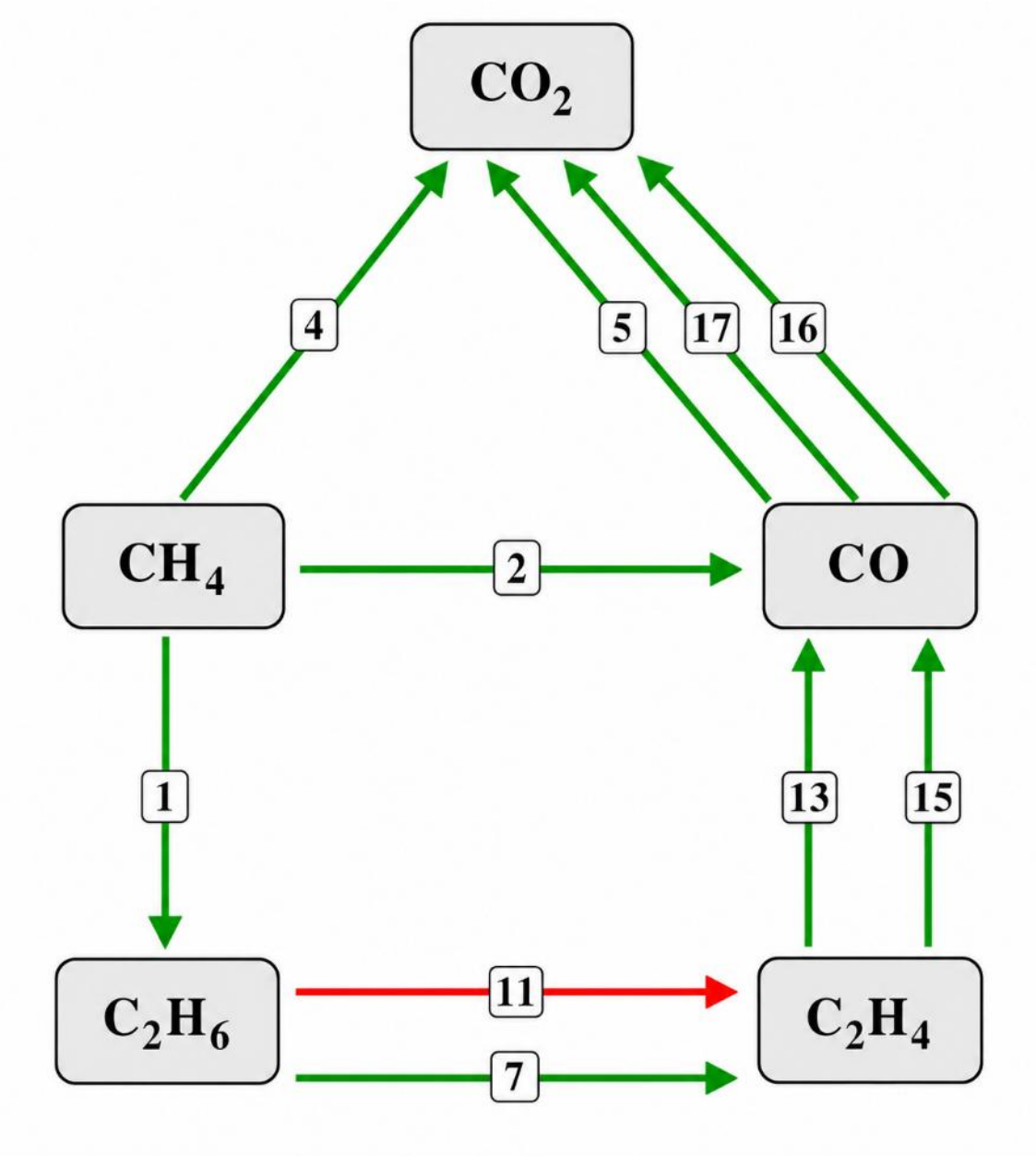

Figure 8. Global OCM reaction scheme [1, 63].

Apart from global kinetic models, Sun et al. [76], Ahari et al. [90] and Karakaya et al [46, 47] developed micro-kinetic models based on both the heterogeneous and homogenous reactions. Sun et al. had 14 surface reactions and 39 gas-phase reactions in their model. The model was validated against experimental data obtained from a fixed bed reactor as reported by [27]. They adsorbed methane on three catalysts (Pr_2O_3, Eu_2O_3, Yb_2O_3) at room temperature, elevated temperatures up to 260ºC, 1.2atm pressure for about an hour and analyzed the Fourier Transform Infrared (FTIR) spectrum of each catalyst. They divided the infrared spectrum in five different regions and reported contributions of different reactions in each region. The reported contributions from free and hydrogen bonded OH and H_2O groups, symmetrical and asymmetrical (C-H) stretches from the $-CH_3$ and $-CH_2$ and carbonyl groups within 4000-3000 cm^{-1} region. Moreover, they showed possibility of CO_2, CO, surface carbon and oxygen formation from dissociation of alkoxy group groups within 2500-2000 cm^{-1} region. Additionally, in the 1800-1100 cm^{-1} range, many absorption bands of compounds and structures appeared including oxalates, carbonates, nitrates, aldehydes, ketones, alcohols and aromatic hydrocarbons. Overall, their results showed that the OCM reaction begins with extraction of hydrogen from CH_4 in gas phase by the activated oxygen from catalyst surface resulting in methyl radicals ($CH_3\cdot$). Then, ethylene could be formed by reaction of $CH_3^{\cdot}$ radicals with surface to form carbon radicals which then combine to form ethylene.

Similarly, Ahari et al. [90] included 11 catalytic reactions and 39 gas-phase reactions in their model. The model was validated against experimental data received from an isothermal fixed bed micro-reactor at atmospheric pressure, 1048-1123K temperature, gas

hourly space velocity (GHSV) of 4000-8000 h^{-1} and CH_4/O_2 ratios of 2-6. They used $Mn/Na_2WO_4/SiO_2$ catalyst for their study. Their proposed model can predict CH_4 conversion, C_2 and COx selectivity with average deviations within 10.1-12.3% range.

Karakaya et al. [46] developed a micro kinetics model for La_2O_3/CeO_2 nanofabric catalyst. The model includes 52 reactions and involves 11 surface species and 16 gas-phase species all of which participate in the gas-phase reactions as well. The surface reactions were irreversible while the gas-phase reactions were reversible. Apart from the general OCM steps, the reaction pathways included the reaction of surface oxygen with $CH_3^{\cdot}$ radicals, C_2H_4 and C_2H_6 that prompted the formation of undesired COx and H_2O.

2.1.3.2. Thermodynamics of OCM

Table 2 summarizes net reaction enthalpies of 10 global reactions in OCM process highlighted by Liu et al. [21]. Reactions 2 and 4 represent partial and complete oxidation of methane. Both reactions are exothermic however, reaction 4 is much more exothermic and favorable compared to reaction 2 [21]. The coupling of methyl radicals and consequent dehydrogenation of ethane has an enthalpy in the vicinity of reaction 2. This indicates that the formation of ethylene is less favored compared to complete oxidation of methane i.e., reaction 4. Due to this reason, there has been emphasis on improving the C_2 selectivity of the OCM process [21].

The thermodynamic calculation by minimizing the Gibbs free energy of the OCM system performed by [21] showed that at a fixed CH_4/O_2 ratio of 5:1, increasing the temperature enhanced the methane conversion rate but also facilitated CO formation as

compared to CO_2. However, the overall C_2 selectivity and COx selectivity remains the same. At a fixed temperature, increasing the CH_4/O_2 ratio decreased the CO_2 selectivity but increased the coke formation. The CO selectivity also decreased with increasing CH_4/O_2 ratios. Regarding the C_{2+} products, variations in temperature and CH_4/O_2 ratio do not affect the C_{2+} selectivity. This again substantiates the appeal to develop a highly selective catalyst for C_{2+} products that can achieve a C_{2+} selectivity above 80%.

Table 2. Energies released for each OCM reaction [21].

	Reaction	ΔH (kJ/mol$_{CH4}$)
1	$2CH_4 + 0.5O_2 \rightarrow C_2H_6 + H_2O$	−177
2	$CH_4 + O_2 \rightarrow CO + H_2 + H_2O$	−278
3	$CH_4 + 0.5O_2 \rightarrow CO + 2H_2$	−36
4	$CH_4 + 2O_2 \rightarrow CO_2 + 2H_2O$	−802
5	$2CH_4 + O_2 \rightarrow C_2H_4 + 2H_2O$	−282
7	$C_2H_6 + 0.5O_2 \rightarrow C_2H_4 + H_2O$	−105
11	$C_2H_6 \rightarrow C_2H_4 + H_2$	137
13	$C_2H_4 + 2O_2 \rightarrow 2CO + 2H_2O$	−757
15	$C_2H_4 + 2H_2O \rightarrow 2CO + 4H_2$	210
16	$CO_2 + H_2 \rightleftharpoons CO + H_2O$	41

In summary, the biggest challenges in the practicability of OCM technology are listed below [1].

1. Kinetic limitations:

a. The formation of COx compounds occurs faster than the selective production of C_2 hydrocarbons.
b. The higher reaction orders with respect to oxygen partial pressure for COx compounds when compared to C_2 hydrocarbons.
c. The rate-determining step of the OCM kinetic is the activation of the highly stable methane molecule.

2. Thermodynamic limitations:
    a. The catalysts used for CH_4 activation also result in energetically favorable reactions which results in products such as COx [1, 4, 5, 96]. These COx products are formed either by a parallel combustion of CH_4 and molecular oxygen (O_2) or deep oxidation of C_2 products [5].
    b. The OCM reactions, especially deep oxidation reactions, are highly exothermic, which may result in increasing the local temperatures by 150-300 ^oC (hot spots formation) and reactor temperature runaway even in a lab-scale reactor at GHSV of <80000 h^{-1} [97].
    c. High temperatures required to activate methane also favor deep oxidation reactions.

Given these limitations, a higher C_2 selectivity and hot spots based investigations should be the main focus of the research moving forward. Lab-scale and pilot-scale demonstrations can be utilized to find highly selective catalysts whereas high fidelity computational models and scale-up methods can be utilized to address hot spot formation in an industrial scale reactor.

2.1.4. OCM Metrics

The performance of an OCM reactor is assessed based on the parameters shown in Equations 13, 14 and 15 [49, 98]. Here C_k is the number of carbon atoms (which is 2 for C_2H_4 and C_2H_6).

2.1.4.1. Methane Conversion

The conversion of CH_4 indicates how much quantity of the CH_4 feed has been converted to other compounds. These compounds include ethane, ethylene, CO, CO_2 and traces of other compounds. A high value of CH_4 conversion results in high quantity of C_2 compounds but also results in high COx compounds and therefore, a value of 30% is acceptable for the CH_4 conversion.

$$\text{CH4 conversion (\%)} = \frac{\text{molar flux of CH4 introduced} - \text{molar flux of CH4 in products}}{\text{molar flux of CH4 introduced}} \quad (13)$$

2.1.4.2. C_2 Selectivity

The C_2 selectivity is the percentage of C_2 compounds (ethane and ethylene etc.) out of all the CH_4 that has been converted in the reactor. This parameter highly depends on the type of catalyst. A high C_2 selectivity indicates low COx compounds while maintaining the same quantity of C_2 compounds and therefore, high values i.e., almost 80% are expected for the C_2 selectivity.

$$\text{C2 selectivity (\%)} = \frac{C_k * \text{molar flux of (C2H6+C2H4)}}{\text{molar flux of (CH4 introduced} - \text{CH4 in products)}} \quad (14)$$

2.1.4.3. C_2 Yield

The C_2 yield is the ratio of C_2 compounds in the products and CH_4 feed. It indicates how much quantity of CH_4 has been converted to valuable chemicals i.e., ethane and ethylene and represents the overall performance of the reactor. A high single pass C_2 yield (almost 30%) results in lower costs of energy and equipment for downstream separation and splitting units.

$$\text{C2 yield (\%)} = \frac{C_k * \text{molar flux of (C2H6+C2H4) in products}}{\text{molar flux of CH4 introduced}} \quad (15)$$

2.2. Strategies to Improve OCM Performance

There have been five strategies to improve the performance of OCM. Briefly, these are:

1. Selection of a suitable catalyst
2. Integration of OCM with another chemical reaction system
3. Reactor types and configuration
4. Alternate oxidants
5. Process heat utilization to optimize energy integration

Out of these strategies the catalyst type, integration of OCM with another chemical reaction system and use of alternate oxidants are described in detail in this section. The notable attempts in terms of C_2 yield and selectivity as reported in literature are the main focus of this section. From the third strategy, i.e., the reactor types, the membrane reactors have shown promising yields (up to 35%). However, the main drawback of the membrane

integration is the mechanical and chemical integrity of the membranes. High temperature causes cracking or leakages of membranes which increases the cost. At high temperatures the membranes react with the catalyst and alter its properties resulting in a reduced C_2 yield. Moreover, the membranes reduce the O_2 flux and consequently the CH_4 conversion. The fifth approach to improve the OCM process (i.e., the utilization of process heat to optimize energy integration) can be achieved by using commercial tools such as ASPEN Plus [49].

2.2.1. Catalysts for OCM

In the early phases of OCM research, from 1980 to 1995, the most of the research was focused on finding an effective OCM catalyst [99]. The desired industrially relevant catalyst should activate the CH_4 molecule while avoiding combustion or deep oxidation reactions. There have been four different types of catalysts being studied for the OCM process which are mentioned below [52, 86, 99].

1. Reducible metal oxides
2. Irreducible metal oxides
3. Halogen-containing oxide materials
4. Solid electrolytes.

Apparently, there have been hundreds of different catalyst composition reported in literature which include metal oxides (single or doped), mixed metal oxides and perovskite [100-110]. An in-depth review of the catalyst performances and effects of dopants has been presented by Ortiz-Bravo et al. [1]. This study highlights only the significant OCM catalysts with relatively high C_2 yield, since the discovery of OCM. For the reducible metal oxide

catalysts, the process starts with reduction of catalyst by periodic streams of methane, and then oxidized by oxygen present in air. This mode of operation, also termed as chemical looping method, excludes the expensive separation of oxygen from air and the chances of deep oxidation and combustion reactions [86].

However, this operation requires frequent stops to the OCM reaction for the oxidizing of catalyst. The irreducible metal oxide catalysts (second group) perform well with co-feed operation mode where methane and oxygen are fed simultaneously. For this operation, Zeng et al. [111] achieved a yield of 27%, selectivity of 62% using $Bi_{1.5}Y_{0.3}Sm_{0.2}O_{3-\delta}$ (BYS) in a packed bed reactor made with dense alumina tube of 0.63cm internal diameter and 56cm length. However, this high yield was achieved at a relatively higher temperature of 950ºC.

Othman et al. [50] used a $Bi_{1.5}Y_{0.3}Sm_{0.2}O_{3-\delta}$ (BYS) catalyst for a hollow fiber membrane microreactor and achieved C_{2+} selectivity of 79% and yield of 39% at high temperatures of 900ºC. Halogen-containing oxide materials improve the C_2 selectivity at high CH_4 conversion rates.

Otsuka et al. [112], in 1986, utilized oxides of Mn and Ni with LiCl and obtained ethylene selectivity of 60% and C_{2+} yield of 27% at a temperature of 750ºC. This high yield at a reasonably low temperature pushed the doping of metal oxides with halogen in years to come [86]. Moreover, a C_2 yield of 31.6% was achieved over a $SrCe_{0.9}Yb_{0.1}O_{3-\delta}$ solid electrolyte in the 1980s at a temperature of 750 ºC [86].

Liu et al. [61] used Mn-Ce-Na_2WO_4/SiO_2 catalyst in a solid oxide fuel cell (SOFC) tubular membrane reactor and achieved a 60.7% CH_4 conversion, 41.6% C_{2+} selectivity and 19.4% ethylene yield. Moreover, for their conventional fixed bed reactor design, they achieved a 36.8% CH_4 conversion, 57.4% C_{2+} selectivity and 12.6% ethylene yield. Among the state-of-the-art catalysts, Mn–Na_2WO_4/SiO_2 is considered an outstanding catalyst as it can produce C_2 yield of 26.4%, C_2 selectivity of 80%, CH_4 conversion of 33% at a temperature of 750 ^oC and is stable for over 500h [1, 52]. Mn/Na_2WO_4/SiO_2 is a mixed oxide catalyst that can produce high C_2 yield and is also more stable. It is, however, very complex in terms of structural and chemical properties which makes the catalyst optimization difficult to achieve [21, 32]. The required temperature for this catalyst based OCM processes is 800 ^oC and above.

In a study conducted by Hiyoshi and Ikeda [113], an ethylene yield of 31% was achieved at 750 ^oC in a packed bed reactor by mixing the Mn/Na_2WO_4/SiO_2 catalyst with alkali chlorides. However, further analysis in terms of the catalyst stability needs to be conducted. Moreover,

Mehmodi et al. [114] also reported a C_2 yield of 31.6% at 775 ^oC in a packed bed reactor using M/Na/Mn/SiO_2-based nanocatalysts. They used different metals represented by “M” in the catalyst notation. However, the catalyst deactivated after 9h.

Zarrinpashne et al. [115] demonstrated a C_2 yield of 27.24% at 850 ^oC in a fixed bed reactor. Palermo et al. [52] reported an ethylene yield of greater than 17% at a CH_4 conversion rate of 33% and impressive C_2 selectivity of 80% over Mn/Na_2WO_4/SiO_2 at 850 ^oC and CH_4/O_2 ratio of 4.5 in a quartz reactor.

Recently, Kim et al. [116] obtained a C_2 yield of 25.9% over $Mn/Na_2WO_4/TiO$ catalyst in a fixed bed reactor at 775 ^oC and CH_4/O_2 ratio of 2. The corresponding CH_4 conversion and C_2 selectivity were 46% and 54.5% respectively.

Perovskite catalysts have shown high stability and activity under harsh conditions. The general formula for the perovskites is of the form ABO_3 where A is a rare earth metal and B is a transition metal [117-120]. Bostan et al. [117] applied a perovskite catalyst i.e., $SrMnO_3$ and its derivatives experimentally on a quartz tube OCM reactor (internal diameter and length of 25mm and 25cm respectively) and concluded that co-containing catalysts produced better catalytic activity and higher selectivity yields. Their results showed that for SrNaKCo, at a temperature of 750 ^oC , a yield of 20% was possible.

Similarly, Pyatnitskii et al. [118] achieved a C_{2+} yield of almost 23% at 973K using a perovskite catalyst i.e., SrNiLi.

Bagherzadhe et al. [121] reported an ethylene yield of 29% using a 24mm outer diameter quartz reactor for a perovskite catalyst $Ba_{(1-0.5x)}TiO_3$ + $0.05xSnCl_2$ and at low temperatures i.e., 600-800^oC. However, their ethylene selectivity was low i.e., 44% and the catalyst performance declined due to loss of chlorine. It has been shown that the addition of Na to $LaMnO_3$ catalyst results in a significant improvement in the C_2 yield in a chemical looping design for OCM reactor [122].

Jiang et al. [98] showed that C_2 yield can be increased by 744% by proper doping of $LaMnO_3$ catalyst with Na in a chemical looping design. Addition of Na led to higher molar ratio of Mn^{4+}/Mn^{3+} and produced more oxygen vacancies which increased the performance

of the catalyst. Moreover, tests showed that the surface oxygen was the active center for methane activation. They achieved a methane conversion of 30%, C_2 selectivity and yield of 55% and 20% respectively. Additionally, the Na doped $LaMnO_3$ catalyst showed stable regenerability for 20 consecutive cyclic redox tests.

Apart from the catalysts mentioned above, some other potentially beneficial catalysts include Li/MgO and La_2O_3. Li/MgO, developed by Ito et al. [123], is an alkaline earth metal-based oxide doped with Li [21]. It produced a yield of almost 12% which was considered effective in the mid-80s. Li/MgO has a comparatively simpler microstructure and only one active center which makes its development and theoretical studies convenient [32]. However, its yield was still far from the target yield of 30% for industrial viability. Studies have revealed that Li/MgO undergoes morphological or structural changes at high temperatures required for OCM which results in catalyst stability issues [123-127].

Hou et al. [128] reported a C_{2+} yield of 18% with CH_4 conversion and C_{2+} selectivity of 27.3% and 65.2% respectively over a Li-ZnO/La_2O_3 catalyst.

Recently, Zhao et al. [129] reported a C_2 yield of 19% at a remarkably low temperature of 550 ^oC over a Sr-doped flower-like La_2O_3 microspheres with hierarchically porous structures ($Sr_{0.1}LaO_x$-H). However, the catalyst deactivated within 30h but the addition of Zr improved its stability. Noon et al. [130] tested La_2O_3-CeO_2 nanofibers as catalysts and obtained C_2 yield of up to 20% at temperatures below 450 ^oC but at low C_2 selectivity of about 58%.

Amongst the above mentioned results, the results of Jiang et al. [98] show that perovskite catalyst i.e., Na doped $LaMnO_3$ may have the potential to cross the 30% C_2 yield barrier with proper investigation of the dopant induced oxygen vacancies of the catalyst and system level optimization of the chemical looping OCM. Perovskite type catalysts are suitable for chemical looping process because of their stable structure and high oxygen releasing/acquiring ability.

2.2.2. Integration of OCM with another Process

Promising results have been shown in terms of making OCM a profitable process and improving its yield by integrating it with another process such as a chemical reaction system or a power plant.

Godini et al. [58] integrated the OCM process with methane reforming process to produce valuable syngas from unreacted methane from OCM. An OCM model calibrated against experimental data obtained from a UniCat mini plant scale OCM facility established in Berlin Institute of Technology was simulated in Aspen Plus software to optimize the integrated system. The economic analysis of the plant was conducted by Aspen Economic Analyzer. The OCM facility incorporated fluidized, membrane and fixed bed reactors over LA_2O_3/CaO catalyst. The integration scheme derived from the process proposed by Godini et al. [58] is highlighted in Figure 9. As shown in the Figure, the heat generated from OCM can be used for the endothermic dry methane reforming process. Moreover, the methane and trace amounts of CO and H_2 from the demethanizer can be fed to the methane reforming reactor. Similarly, CO_2 obtained from the OCM can be used as a reactant for the methane

reforming (dry reforming). Their results indicated a C_2 yield of 35%, methane conversion of 60% (15% higher than conventional OCM), a 40% improvement in heat integration and a 90% CO_2 recovery. Moreover, they reported lower energy consumption for the integrated system compared to the conventional OCM.

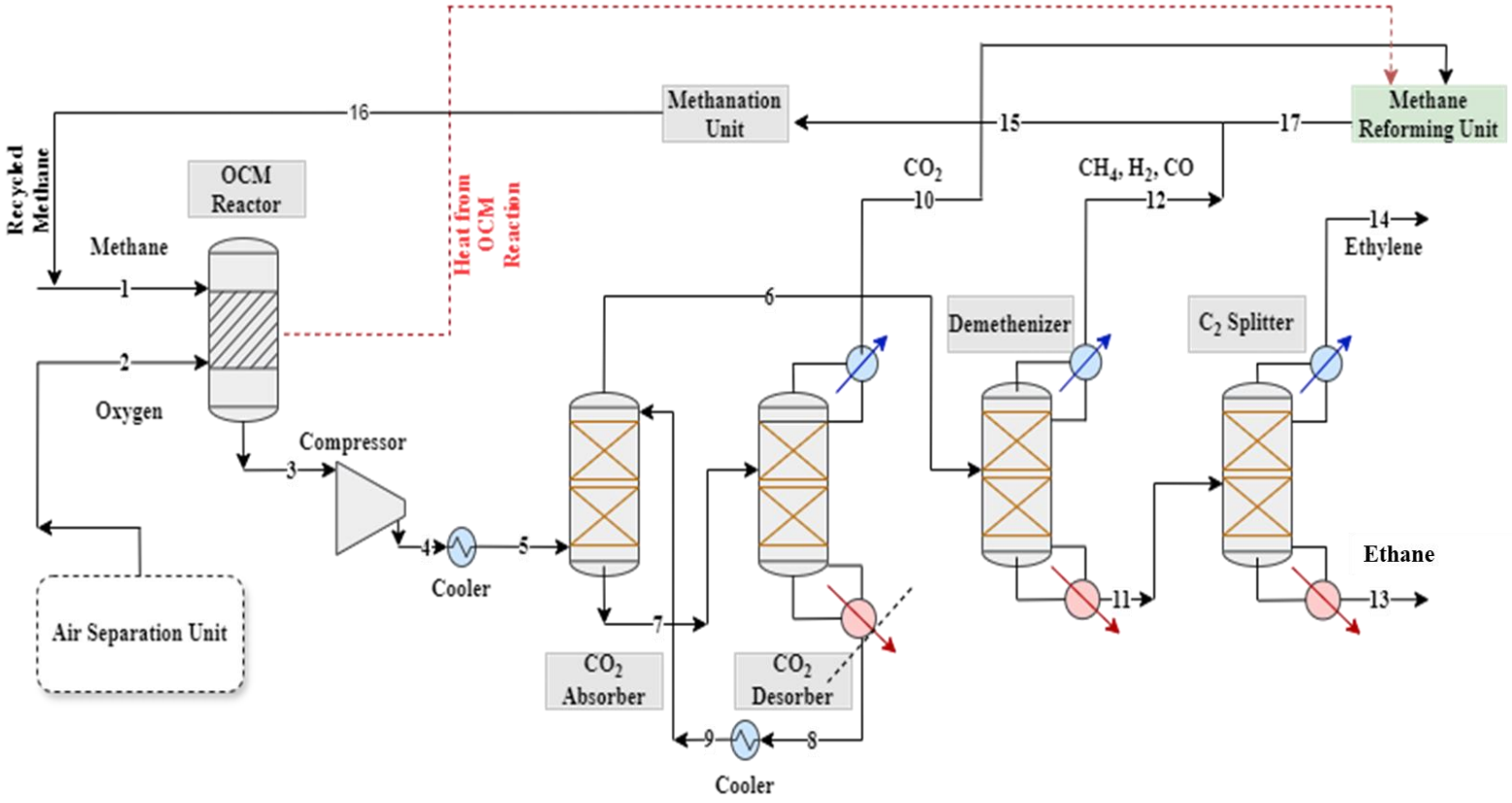

Figure 9. Integration of OCM with methane reforming unit.

Penteado et al. [60] integrated a biogas treatment plant with OCM and performed techno-economic analysis (TEA). The biogas treatment plant was used to produce methane feed for the OCM reaction. The biogas treatment plant related costs were estimated based on literature data whereas the OCM process was simulated in Aspen Plus. A packed bed reactor was used for this study. They presented their results in terms of net positive value (NPV) and discounted payback period (DPP) in years. A positive NPV indicates the project is feasible. They concluded that for a large-scale biogas-based OCM plant the NPV was 741 million USD and DPP was 5 years indicating that the approach can be attractive as the integrated process can yield profits within 5 years.

Ashour [57] integrated the OCM process with a power plant simplified to gas and steam turbines and performed TEA of the integrated plant. The study was conducted using Aspen Plus simulations and assuming 100% methane conversion. The reactor used for the OCM process was a fluidized bed reactor and heat integration techniques were incorporated to ensure efficient use of heat. The motivation was to eliminate the costly methane recycling process and decreases the associated energy consumption. The economic analysis of the plant was conducted by Aspen Economic Analyzer. Ashour's analysis showed that the losses in stand-alone OCM plants can be brought down from 11.6 USD/GJ of methane to 0.84 USD/GJ of methane which shows 93% reduction in losses for OCM as a stand-alone process.

Hugill et al. [64] also applied the idea of co-generation where an OCM plant (106 kt/y ethylene) was integrated with a 44 MW power plant. The OCM plant employed a fluidized bed reactor as recommended by Swanenberg [65]. It was concluded that co-generation did not help with profitability of the integrated system and energy savings were

also not prominent. The internal rate of return was 18.82 percentage points less than the naphtha cracking plant. However, their life cycle analysis (LCA) showed that a significant improvement was found in terms of a reduction in CO_2 emissions i.e., 29 t/h for the cogeneration plant compared to 45 t/h for naphtha cracker plant with electricity production.

Rosner et al. [59] conducted a system level analysis on a stand-alone electrochemical OCM plant. They evaluated various scenarios where an OCM plant operated with air as an oxidant, with steam as an oxidant (H_2 co-production) and an OCM plant with steam oxidant and CO_2 utilization. Their results indicated that the cost of ethylene and CO_2 emissions could not be brought down to comparable levels of industrially deployed ethylene production technologies such as ethane steam cracker plant.

2.2.3. Oxidants for OCM

To overcome the tendency of O_2 for deep oxidation reactions, multiple oxidants have been tried which have less tendency towards COx formation. Zhu et al. [97] applied gaseous sulfur (S) as an oxidant over multiple catalysts experimentally and through density functional theory (DFT) and found that the sulfur and catalyst surface bond weakness directly increased the methane conversion rate. Whereas, for the C_2 selectivity, an opposite trend was observed. Overall, they recommended that a high CH_4/S ratio and short contact time improved the selectivity of OCM reaction. However, their results reported modest CH_4 conversions and C_2 selectivity. Özdemir et al. [106] applied N_2O as an oxidant on Sm_2O_3 catalyst and found an ethylene yield of 8.2%. They found that N_2O was more selective than

O_2 and enhanced the ethylene formation. However, the yield reported was still too small for commercial application.

Similarly, Liu [131] applied N_2O oxidant on chlorinated perovskite oxide catalyst in a packed bed reactor and observed that a slightly higher C_2 selectivity and yield were achieved when using N_2O instead of O_2. Zhang et al. [132] used CO_2 as an oxidant over a CaO-based catalyst with Na and Cl and reported yields of about 6.6% at 950^oC. Using alternative oxidants can improve the OCM performance, however, none of the reported yields are significant enough for industrial viability. Moreover, the alternative oxidants can be costly compared to oxygen which is readily available.

2.3. OCM in a CL Design

The idea of chemical looping or reduction-oxidation (redox) OCM is appealing since it allows for activation of methane through lattice oxygen instead of the molecular oxygen which avoids deep oxidation and combustion reactions and improves the selectivity of OCM process [98, 122, 133, 134]. By employing the chemical looping method, the C_2 yield can be increased by one order of magnitude compared to a conventional co-feed OCM reactor where both the methane and the oxygen are fed simultaneously to the reactor [122].

It is to be noted that the lattice oxygen alone is not sufficient to activate methane, and a bulk oxygen is required to account for methane activation which is restored periodically as revealed by Keller and Bhasin [36]. A schematic diagram of the OCM process in chemical looping is shown in Figure 10. In the chemical looping concept, both methane and oxygen are not fed simultaneously but instead, separate cycles of methane and oxygen/air are fed

periodically. The catalyst is reduced in the reducing reactor (OCM reactor) and oxidized in an oxidizing reactor.

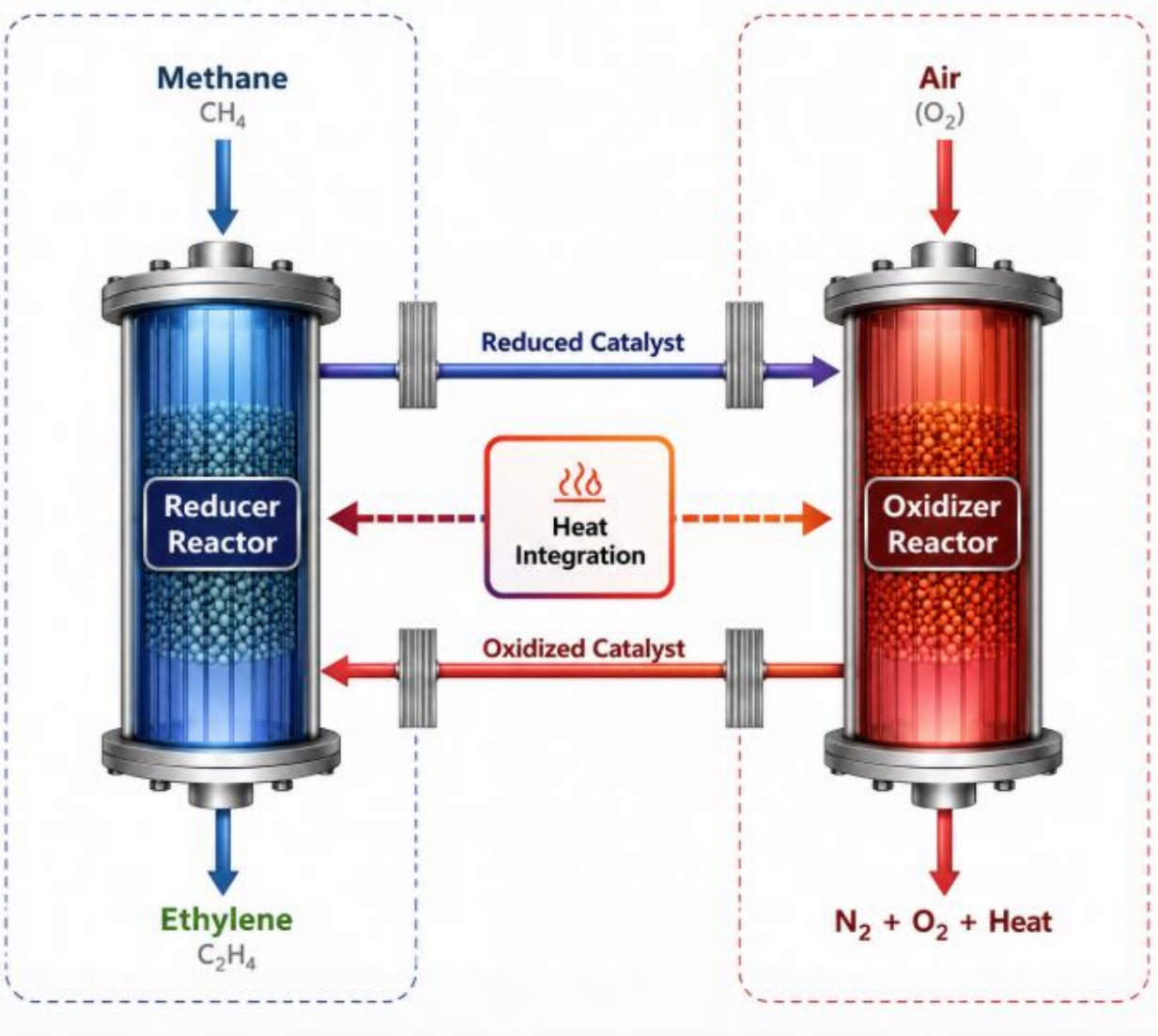

Figure 10. OCM in a CL reactor design.

Figure 10 represents a conceptual diagram for the working of OCM in chemical looping design. As evident from Figure 10, the reducing reactor, i.e., the OCM reactor, does not involve molecular oxygen while methane is fed to this reactor. Another advantage of

chemical looping is that the OCM reaction can occur at lower temperatures compared to conventional co-feed OCM reaction and absence of the direct mixture of methane and molecular oxygen prevents combustion [36, 98, 122]. Additionally, there is no need for a costly and energy consuming air separation unit for oxygen feed as in a co-feed OCM reactor [133]. Since there is no oxygen feed, the catalyst for the chemical looping OCM should have high oxygen carrying capacity, highly stable regenerability and high C_2 selectivity [133].

2.4. CL CO_2-H_2O Splitting

The CL splitting of CO_2-H_2O, also known as thermochemical splitting of CO_2-H_2O, is obtained in a cyclic manner which involves redox reactions periodically. The oxygen carrier (catalyst) is reduced separately during the reduction cycle and is oxidized by the CO_2-H_2O splitting. As a result of these reactions, oxygen and syngas (H_2 and CO) are produced [40, 135]. The CL splitting of CO_2-H_2O requires much lower temperatures i.e., almost 1073K (800^{o}C) compared to high temperatures required by direct thermal dissociation of CO_2-H_2O (thermolysis) which are in the vicinity of 3500K [136]. Moreover, CL cycles do not require separation of oxygen and syngas as required by thermolysis [40]. Additionally, the catalyst remains in solid form and there is no need for a separation process for catalyst particles in the gases [137]. The reactions which occur during the thermochemical CO_2-H_2O splitting in a cerium-based oxide catalyst are shown in Equations 16 &17 [138, 139].

$$CeO_{2-\delta} + \delta H_2O \rightarrow CeO_2 + \delta H_2 \qquad (16)$$

$$CeO_{2-\delta} + \delta CO_2 \rightarrow CeO_2 + \delta CO \qquad (17)$$

Conventionally, the temperature swing process requires high temperature shifts from 750 ºC for the oxidation cycle to 1200-1600 ºC for the reduction cycle of the CL CO_2-H_2O splitting [140]. The high temperature shifts require solid-solid recuperating during the redox cycles and causes thermal stresses, fatigue on the catalyst and also there is downtime required for increasing/decreasing the temperatures [141, 142]. This can be avoided by reducing the catalyst isothermally, i.e., at the same temperature, or near isothermal temperatures. However, there are some challenges faced by the isothermal splitting of CO_2-H_2O. These include higher partial pressures required for CO_2 and H_2O for the process to occur and lower thermodynamic fuel capacity yield compared to the non-isothermal CO_2-H_2O splitting. Moreover, there are challenges associated with gas-gas heat exchange at the outlet for heat recovery [135]. Both CO_2 and H_2O can be co-split or streams of CO_2 and H_2O can be split separately to better control the quality or ratio of syngas [143].

Solar driven chemical looping CO_2-H_2O splitting has been extensively studied to utilize concentrated renewable energy source to carry out the reduction cycle [144-150]. The key indicator for economic feasibility of solar driven catalytic processes is the solar-to-fuel conversion efficiency which is defined as the ratio of heating value of the fuel produced to the input solar energy. Currently, the maximum solar-to-fuel efficiency reported so far is below 10% [138]. As reported in literature, the maximum solar-to-fuel efficiency on a lab scale is 5.25% [138] and on a pilot scale without heat integration is 4.1% [139].

2.4.1. Catalysts for CL CO_2-H_2O Splitting

The catalyst chosen for the isothermal or near isothermal CL CO_2-H_2O splitting should have following qualities [39].

- High number of oxygen vacancies.
- Fast reaction kinetics.
- High solar-to-fuel conversion efficiency.
- High stability.

Many volatile/non-volatile and stoichiometric/non-stoichiometric catalysts has been studied for CO_2-H_2O splitting process including ZnO, SnO_2, ceria (cerium oxide), ferrites and perovskites [39]. One of the promising catalyst for CO_2-H_2O splitting, as reported in literature, is cerium oxide because of its abundant oxygen vacancies and interfaces effects with other phases [151, 152]. Cerium oxide is characterized by its fast kinetics and low fuel productivity. Additionally, ferrite/zirconia composite is also studied as a catalyst and is shown to have slow kinetics but high fuel productivity compared to cerium oxide [135, 148].

Marxer et al. [138] achieved 100% selectivity, 83% molar conversion and 5.25% solar-to-fuel conversion efficiency for thermochemical CO_2 splitting using a ceria catalyst and temperature swing mode. Their next goal was to achieve an efficiency of 15%. Similarly, in a recent press release from SUN-to-LIQUID II, it was mentioned that a solar-to-fuel conversion efficiency of 15% was targeted for thermochemical splitting of CO_2-H_2O using effective radiative absorption through 3D -printed redox materials with optimized structure and by recovering sensible heat during temperature swing process [153].

Zoller et al. [139] developed a pilot scale solar driven reactor using ceria catalyst for thermochemical splitting of CO_2-H_2O. The 50kW solar tower utilized a mean solar flux concentration of 2500 suns and achieved a solar-to-fuel conversion efficiency of 4.1%.

Remo et al. [143] performed experimental parametric study on solar driven thermochemical CO_2/H_2O splitting using ceria catalyst and reported a maximum CO_2 conversion rate of 80.1%. They also reported that the conversion of CO_2 has a trade-off with the yield. Their results showed a syngas yield of 5L for a 4kW reactor.

Robert et al. [154] performed isothermal thermochemical splitting of CO_2 using ceria catalyst and packed bed reactor at 1500^oC. They performed gas flow rates and oxidation/reduction duration optimizations to enhance the process efficiency. They used a solar reactor operating at 3000 suns concentration and 90% sensible heat of gases recovered. Their results showed a stable average rate of CO production i.e., 0.079 μmol/(s.g) and a projected reactor efficiency of 4%.

Chen et al. [133] performed chemical looping CO_2/H_2O splitting using CeO_2 dopped $LaFeO_3$ catalyst and methane partial oxidation as the reduction cycle and showed that almost 100% CO_2 conversion to CO was possible. They recommended that for the desired composition of syngas, the syngenetic effect and competing reaction between CO_2 and H_2O splitting over the reduced catalyst are key factors. They highlighted that the perovskite type catalysts provide a versatile material class for solar-to-fuel thermochemical splitting process due to their elemental composition in a wide range that allows optimization of reducibility, oxygen vacancies, oxygen exchange characteristics, catalytic surfaces and regenerability.

Dey et al. [155] compared the performances of cerium oxide and perovskite type catalysts $La_{1-x}Ca_xMnO_3$ and $La_{1-x}Sr_xMnO_3$ and concluded that the $La_{1-x}Ca_xMnO_3$ produced 1.6 and 5 times greater amounts of O_2 and CO compared to $La_{1-x}Sr_xMnO_3$ and cerium oxide respectively.

Abanades and Le Gal [140] investigated the CO_2 splitting reaction using ceria-zirconia solid ($Zr_xCe_{1-x}O_2$) in a temperature swing mode. The reduction occurred at 1400 ºC and oxidation in the range (700-1200ºC). They concluded that the lower amounts of Zr increased the CO production and enhanced catalyst regenerability.

Abanades and Le Gal [140] reported that both the CO production and the reaction rate increased as the temperature increased from 900 ºC to 1100 ºC for the catalyst $Ce_{0.75}Zr_{0.25}O_{2-\delta}$. However, outside this temperature range, the amount of CO produced and reaction rates dropped (i.e., at 700 ºC and withing 1100-1400 ºC). They concluded that the oxidation and reduction reactions start competing with each other at elevated temperatures above 1200 ºC.

Takalkar et al. [39] analyzed the effect of dopants on CO production ability of the $LaMO_3$ (where M=Co, Fe, Mn, Ni, Al, Cr, Sr). Their results indicated that $LaMnO_3$ had the highest O_2 delivered during the reduction cycle at 1400 ºC compared to other dopants. The average O_2 delivered by $LaMnO_3$ was 184 (µmol/g) whereas the second best average O_2 delivered was almost 100 (µmol/g) by $LaSrO_3$. In terms of CO production, $LaSrO_3$ was the most capable candidate with CO production of 124 (µmol/g).

2.5. CL OCM and CL CO_2-H_2O Splitting

A novel OCM technology integrated with CO_2-H_2O splitting in a CL reactor design is presented in Figure 11. The CO_2 and H_2O are fed in the oxidizing reactor of the integrated design to co-produce valuable syngas. The oxidation of the catalyst by CO_2-H_2O is referred to as thermochemical splitting of CO_2-H_2O. The CO_2-H_2O splitting directly converts CO_2 to CO and H_2O to H_2. The process generally occurs at high temperatures (above 1000^oC) which can be avoided by the proposed chemical looping design [131]. Since both OCM and CO_2-H_2O splitting processes are exothermic, the CL design allows efficient energy utilization. The heat rejected from the OCM process is used to drive the CO_2-H_2O splitting thereby, improving the thermal efficiency, reducing the external energy inputs and also ensuring minimal heat losses to the environment. These integrated chemical processes convert methane to ethylene while simultaneously producing syngas, a feedstock for many synthetic fuels and also a medium for hydrogen storage. Based on the extensive review presented in the paper, it is proposed that a Na-doped $LaMnO_3$ catalyst in CL OCM design using packed bed reactors has the potential to overcome the benchmarks for industrial deployment of OCM with further optimization of downstream processes [96].

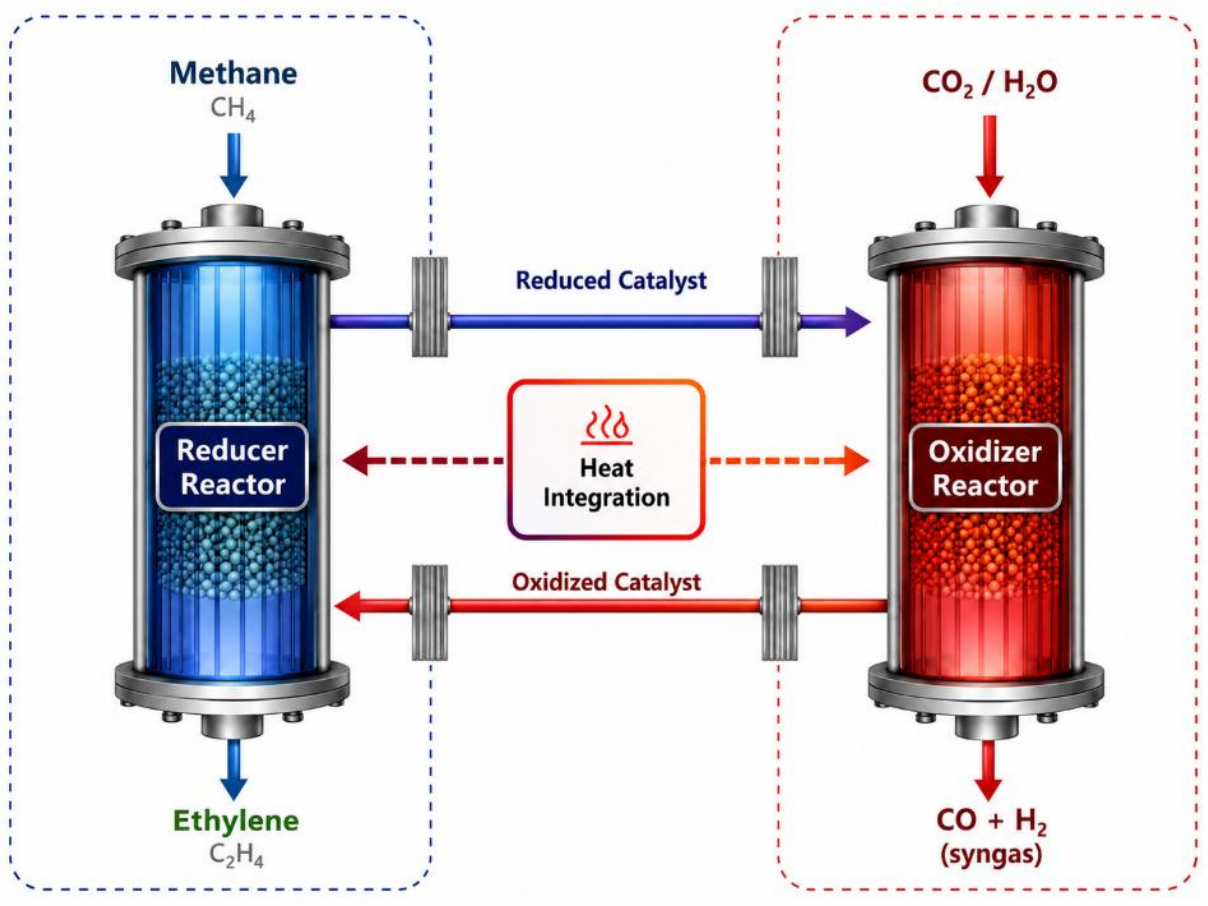

Figure 11. CL OCM integrated with CL CO_2-H_2O splitting.

2.6. Opportunities with CL Splitting of CO_2-H_2O and CL OCM

Some opportunities for the industry associated with the CO_2 and CH_4 conversion are given below [42].

- Building public image as a contributor to the GHG emissions reduction.
- Cost reduction is also associated with CO_2 and CH_4 disposal.

- Acquiring emission reduction credits can benefit companies.
- Feedstock of low or negative value can be manipulated for generating revenue and gaining market share.
- Fuels and chemicals can be produced that integrate with the existing infrastructure for easy transportation.
- Cost intensive air separation unit can be avoided which is required for conventional OCM process since in the chemical looping OCM the feed oxygen is replaced by catalyst surface oxygen.

Chapter 3. Evaluation of the Chemical Looping OCM and CO_2-H_2O Splitting

3.1. Prior Research Contributions from the Sustainable Energy and Carbon Management Center (SECM) at OU

Previous work from Kazempoor et al. [29, 156, 157] focused on evaluations of different advanced technologies. The TEA performed by the group included the evaluation of several membrane based carbon capture and storage (CCS) systems to investigate the feasibility of such systems as a flexible CCS technology for integrating into the future low carbon power plants [158, 159]. These efficient CCS systems can decrease the energy input required for CO_2 removal section of the OCM process.

Jolaoso et al. [29, 157] performed TEA and LCA of an integrated system where a solid oxide electrolytic cell (SOEC) is integrated with fossil fuel assets and water resources such as waste water. The results showed that the carbon footprint can be reduced by 28% in the system. Moreover, they performed techno-economic analysis of a solar energy powered plant level SOEC in a water-energy nexus system for hydrogen production. Through a comparative evaluation of a solar PV, coal and other energy feedstock, they showed that a $2.99/kgH2 or lower levelized cost of hydrogen was achievable.

Similarly, Asadi et al. [156] performed economic and operational assessment of a solar assisted hybrid carbon capture system for combined cycle power plant using Thermoflex and Aspen Plus for natural gas combined cycle power plant and amine-based

CCS system, system advisor model from National Renewable Energy Laboratory for solar PTC field and Aspen Custom Modeler for membrane-based CCS. The proposed hybrid membrane-amine CCS system led to 19.4% higher power output and 10.3% lower carbon intensity. Moreover, the hybrid system reduced the specific reboiler duty and packing volume by 6.9 and 44% respectively. According to the criteria presented in Table 3, it is crucial to perform system level analysis in terms of OCM performance, economics and LCA to develop confidence in the technology and bring about its industrial viability.

In this Chapter, the criteria is first presented which sets a desired end-state for the industrial deployment of chemical looping OCM and CO_2-H_2O splitting. Then a designing process (modeling framework) and different phases of the design are highlighted. Each design phase will be explained in detail in Subsequent sections and the process of coupling each phase will be described.

3.2. Criteria for CL OCM and CO_2-H_2O Splitting for Industrial Deployment

Despite the extensive research conducted on OCM and promising results reported over a period of more than four decades, the OCM process still has not been able to achieve industrial application. The prominent reason is that amongst these promising results, the comprehensive or inclusive metrics for the desired end-state of OCM have not been presented. One exception was the OCM plant of the Siluria Technologies in La Porte, Texas, USA which claimed industrial viability in the year 2015. In 2019, Siluria Technologies was acquired by McDermott International and despite the Siluria's initial success with the OCM

plant, there have been no further full-scale commercial OCM plants or new projects announced. This section presents a reliable end-state requirement which would bring about the industrial viability of OCM.

A thorough process design criterion is developed and presented to evaluate the state-of-the-art OCM technologies and assess the desired end-state for technology deployment which is missing in the previous articles. The end-state is based on required reactor outputs reported in literature (e.g., C_2 yield and selectivity) and on a comparison of cost and reaction temperature with commercial ethylene production technologies such as ethane/naphtha cracking plants. Table 3 represents the initial and end-states for different parameters as reported in the literature. The initial state corresponds to the state of the art or existing state of the technology and the end-state corresponds to the required state for industrial deployment of OCM. The end-state approach, also known as "Technology development road map" or "Target state architecture", is a structured planning methodology for desired targets (end-state) based on a clear long-term vision. It involves defining the initial and end-states for a novel technology and then working backward to identify the required steps and milestones to achieve the end-state. It has been deployed by many companies, including Shell and NASA.

Moreover, the United States Department of Energy (DOE) also developed an end-state Contract Model (ESCM) that utilizes the end-state approach for a clear vision and targets for a project. Shell has used the technology road mapping extensively in its energy transition strategies. By introducing end-states such as net-zero emissions, Shell develops pathways that guide research, development and pilot projects.

Similarly, NASA employs end-state approach for its space exploration programs. An example includes NASA's use of Technology Readiness Levels (TRLs) which is a framework that defines the maturity of a novel technology from TRL 1 to TRL 9. TRL 1 defines the early concept and basic principles observed whereas TRL 9 defines the deployment in the operational environments. In summary, the end-state approach provides a clear vision, structured methodology/milestones and measurable outcomes for the realization of industrial deployment of a novel technology. A packed bed reactor is chosen instead of a membrane reactor because of the complexity and high capital costs associated with membrane reactors as highlighted in Section 1. Moreover, since the chemical looping design does not always involve feed oxygen, there is no requirement of reduced feed oxygen flux and therefore, membranes. The cost of ethylene, CO_2 emissions and reaction temperature are proposed based on a comparison between the OCM process and industrially deployed ethylene production processes such as naphtha/ethane steam cracking plants.

Table 3. Criteria for industrial deployment of OCM.

Parameter	Initial State (Experimental) (Model Prediction)	Reported End-state	Proposed End-state	Comments
C_2 Yield	20-27% [50-52, 111] 25% [3, 49]	30% [1, 3, 49, 99, 122]	**30%**	Agreed in literature for industrial viability.
Stability (hours)	9-500 [1, 160-163]	-	**100**	Catalyst activity (CH_4 conversion, C_2 selectivity, and yield) should remain constant over extended periods.
C_2 selectivity (%)	20-82% [50-52, 99] 67.3% [49]	80-88% [122]	**80%**	Trade-off with CH_4 conversion; higher selectivity reduces cost and can be achieved at lower temperatures.

CH_4 conversion rate (%)	37-49% [50-52, 99] 64% [49]	60% [164], 35-60% [59, 165]	**30-60%**	This is optional and can be compromised over higher C_2 selectivity.
Cost/price of Ethylene (USD per metric tonne of Ethylene)	800-1500 [3, 17, 49, 164]	840-1000 [3, 17, 49]	**1000**	Should be comparable to Ethane/Naphtha steam cracking costs.
CO_2 emissions ($ton_{CO2}/ton_{ethylene}$)	0.4-1 [17, 49]	0.2-3 [17, 49, 164, 166-168]	**1**	Mostly indirect (electricity) and the process CO_2 is captured during separation. Therefore, this number is also flexible.
Temperature (°C)	650-900 [17, 50-52, 99, 164] 800 [49]	600-900 [164, 167, 168]	**800**	Lower temperatures reduce costs and improve catalyst stability.

3.3. Modeling Framework for Integrated CL OCM/CO_2-H_2O Splitting

The modeling framework is shown in Figure 12. First, the packed bed reactor is modeled using a CFD commercial tool (COMSOL Multiphysics v6.4). The CFD model's integrated chemistry is calibrated against experimental data. The calibrated model is then used for a parametric study (sensitivity analysis) at a lab-scale reactor to find out optimum operating conditions for the reactor. The model is then coupled with Aspen HYSYS for system-level model development and consequent techno-economic analysis (TEA) on an industrial scale. The system analysis provides the costs and CO_2 emissions from the plant. In the final phase of the modeling process, the life cycle assessment (LCA) will include the raw material and energy requirement for the plant and corresponding CO_2 emissions for each stage (inputs, plant operation and outputs) using commercial tool SimaPro.

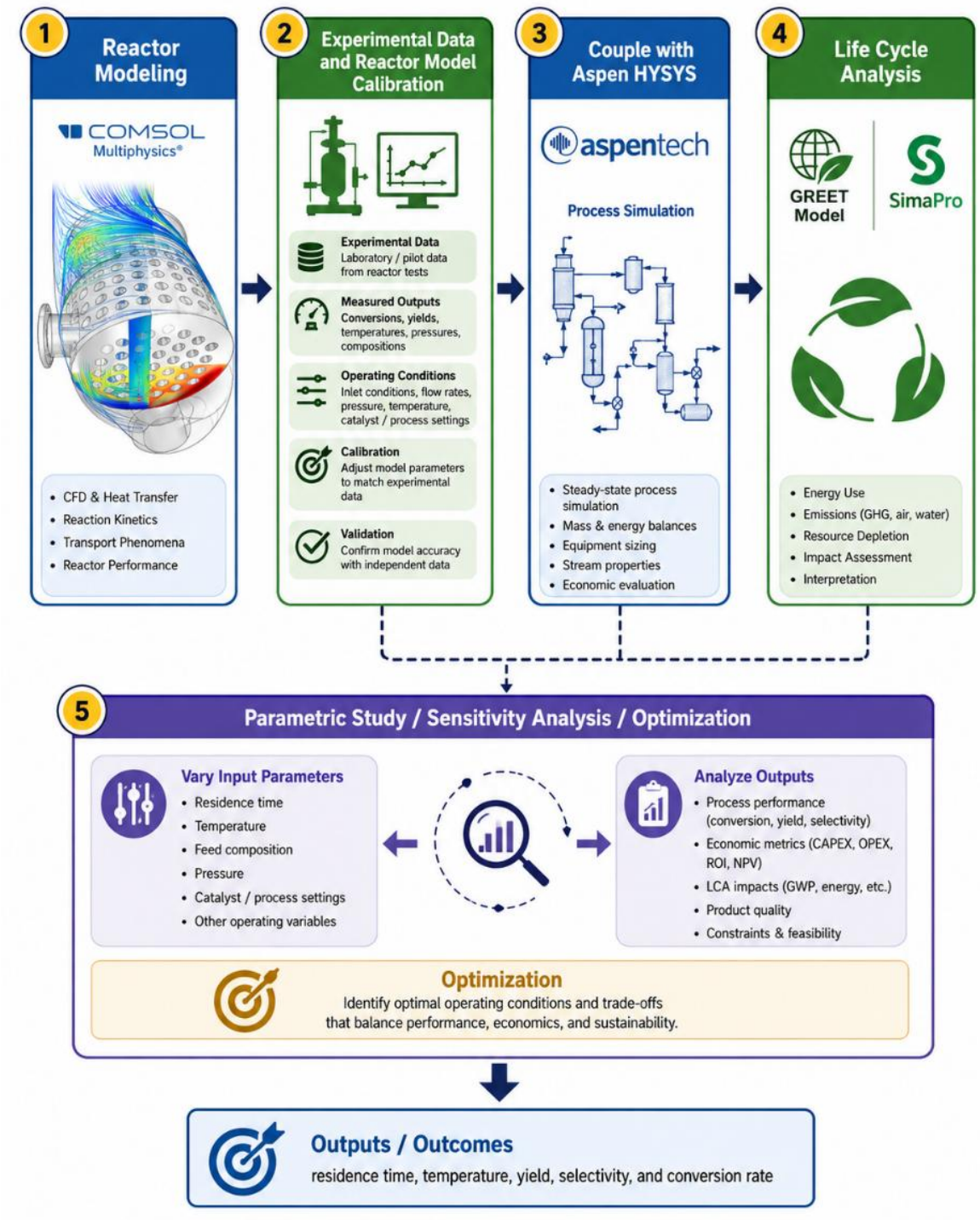

Figure 12. Modeling approach for the assessment of CL OCM/CO_2-H_2O splitting.

Chapter 4. CFD Model

4.1. Background and Literature Review

In Chapter 2, an integrated CL OCM/CO_2-H_2O splitting technology to improve OCM performance is introduced. In this integrated technology, the reactor is operated in a reduction oxidation (redox) cycle where the catalyst (oxygen carrier) is first reduced by the OCM process and then oxidized by the CO_2-H_2O splitting process. Moreover, Chapter 3 presents comprehensive industrial criteria and the technology evaluation method based on the end-state approach for industrial deployment of OCM. This chapter presents the next step which is the lab-scale Computational Fluid Dynamics (CFD) reactor model development. In the second step, the kinetic model used in the CFD model is calibrated against real data before the model can be scaled up to industrial scale.

There have been multiple studies on the OCM using CFD commercial tools. Maghrebi et al. [169] investigated the single pellet catalyst scale OCM process using a steady state CFD modeling approach utilizing the commercial tool FLUENT 6.3. The modeled catalyst was titanate perovskite. Both intra-particle temperature and concentration gradients were considered. They obtained detailed rate and temperature profiles through the porous catalyst considering the competition of reactions, diffusion and heat transfer. The simulation results were validated against experimental data. They found that the temperature variation within the pellet is less than 2 K due to reaction exotherm. Moreover, they highlighted that the exothermic reactions occur prior to the endothermic coupling reaction

within the pellet. Additionally, they indicated that the reactions are dominant at the front of the pellet whereas, diffusion becomes dominant at the back of the pellet (downstream).

Fontoura et al. [170] developed a pellet scale CFD model using ANSYS v19.1 including the heat and mass transfer within the pellet and the gas-solid phases. Moreover, sensitivity analysis was performed to analyze the impact of pellet arrangement and feed conditions on the concentration and temperature gradients. Their results indicated that a high CH_4/O_2 ratio increases the ethylene yield. Moreover, they also reported that a temperature difference of more than 100 ºC instigates the auto-ignition behavior of the catalyst.

Zhang et al. [171] developed a 3D geometric model of a packed-bed reactor loaded with Na_2WO_4-Mn/SiO_2 catalyst using FLUENT software. They validated their results against experimental data. Their results indicated an increase in total moles and speed while a decrease in the density of the mixture from the inlet to outlet. The exact increase in velocity is 0.007 m/s and decrease in density was 0.06 kg/m^3. Moreover, they reported that the reaction rates were maximum near the inlet which resulted in higher heat generation and ultimately, higher heat loss from the reactor walls close to the inlet.

Alturkistani [172] developed a steady state 3D CFD model (using ANSYS FLUENT 2021 R1) of a packed-bed reactor with La_2O_3-based catalysts. They tested three different reactor configurations including isothermal, adiabatic and autothermal approaches. The simulation results were validated against experimental data. The chemical reactions were modeled using a global (lumped) reaction model. Their results indicated a 300 ºC increase in bed temperature in case of isothermal wall temperature. Moreover, adiabatic configuration resulted in a temperature difference of over 500 ºC with a peak temperature of 1340 ºC.

Finally, the autothermal configuration resulted in a peak bed temperature much less than other configurations i.e., 960 ^{o}C.

The previous CFD analysis of OCM are either limited to pellet scale or conducted for conventional OCM where the oxidant (oxygen) is introduced at the inlet. By contrast, CL systems do not require oxygen in the inlet stream, instead, the oxygen is supplied by oxygen carrier i.e., the catalyst. As a result, an approximately constant concentration of oxygen is maintained across the reactor length. Similarly, a CFD model related to Na-$LaMnO_3$ is missing from the literature. The current dissertation focuses on development of a lab-scale, packed-bed reactor's CFD model with integrated chemical kinetics relevant to Na-$LaMnO_3$ for the CL OCM process with a constant concentration of oxygen across the reactor. The present study models only the methane reduction step (OCM step) of the CL process and does not include the oxidation cycle with CO_2-H_2O splitting. This is done because the CO_2-H_2O splitting technology does not face the selectivity issues similar to OCM. The chemical kinetic model is calibrated against experimental results obtained with Na-$LaMnO_3$ catalyst and the calibrated kinetic parameters are listed in detail. Moreover, the concentration gradients are analyzed across the length of the reactor. The purpose of the model development and calibration is to utilize it for parametric study and industrial scale production of ethylene through CL OCM [48, 49].

4.2. Model Description

The representation of the CL OCM process is shown in Figure 13. The Figure shows a cylindrical reactor packed with catalyst pellets. The feed gas i.e., CH_4 enters from the inlet,

passes through the porous catalyst causing chemical reactions and exits the reactor from the outlet. An inert gas i.e., N_2 is also included in the inlet feed.

The mole fraction of CH_4 at inlet is 0.38. When a pressure drop is applied across the reactor, the fluid flow and convection is initiated in the bed whereas the species transport inside the catalyst pellets is dominated by the diffusion.

The multiscale, 2D axisymmetric, packed bed reactor model is developed using a commercial CFD tool i.e., COMSOL Multiphysics v6.4. The reactor's design includes a column filled with porous catalyst particles. The multiscale modeling of a packed bed reactor involves macroscale modeling for the interstitial spaces (macropores) between catalyst pellets and microscale modeling within the pores (micropores) of individual pellets [173]. The multiscale approach not only does not simplify the particle geometry or assume a rate limiting step, unlike the conventional effectiveness factor method, but also reduces the computational times significantly enabling the model scale-up and analysis on an industrial scale [174].

The bed porosity (macroscale) and pellet porosity (microscale) are two important porosities which are considered in the model. For this reason, sometimes this type of model is referred to as the double-porosity model. The material properties such as heat capacity, pellet density for the catalyst, reactor geometry and GHSVs are derived from the previous works [98, 175]. Due to unavailability of complete reactor and pellet dimensions, a combination of the microscopic properties of individual pellets and reactor dimensions are estimated to meet the reported GHSVs from Jiang et al. [98]. The different properties of pellet and bed are listed in Table 4.

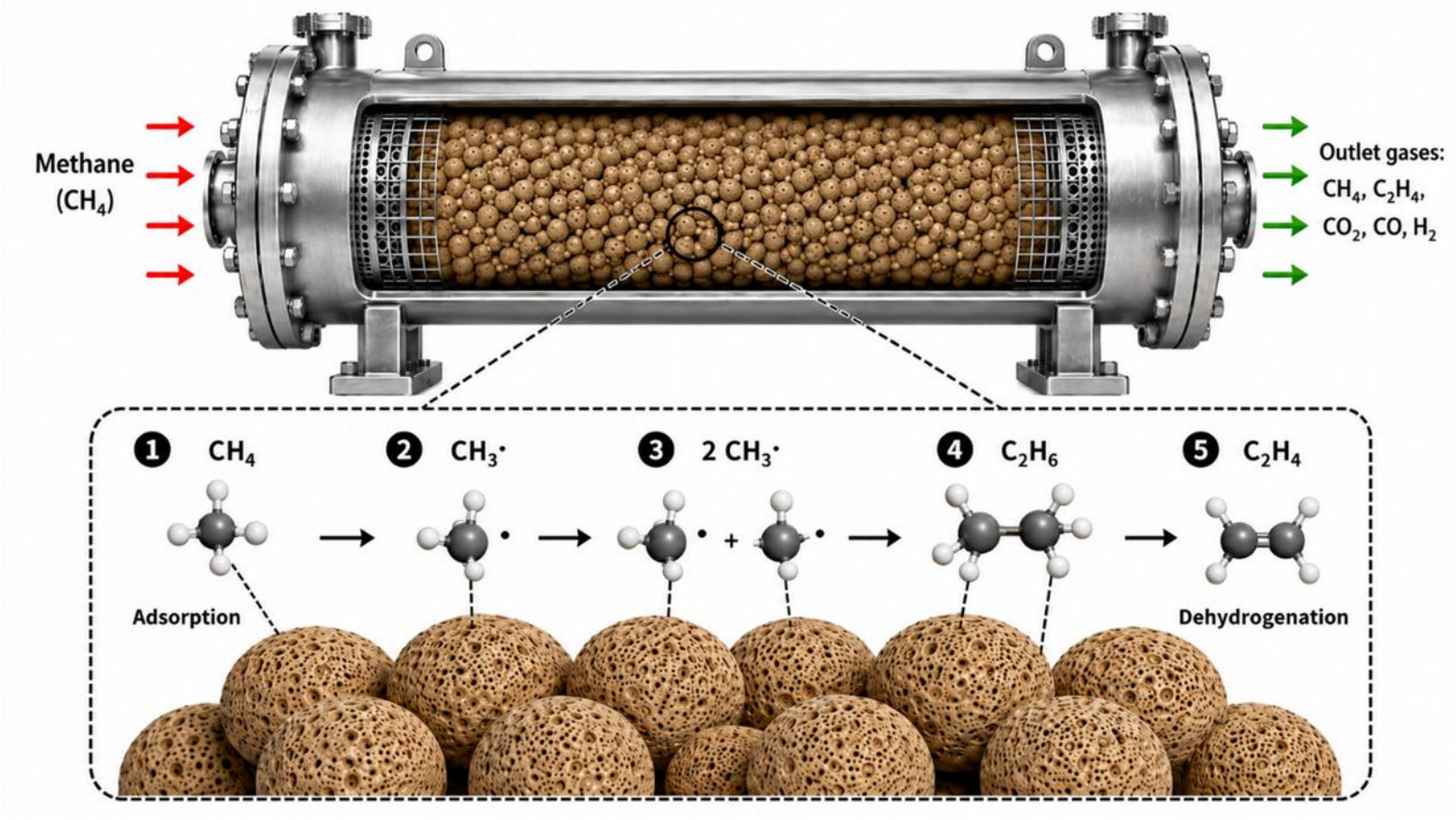

Figure 13. CL OCM packed-bed reactor schematic diagram.

Table 4. Reactor Material and Geometry Parameters [98, 176].

Property	Value	Unit
Bed Porosity	0.45	
Pellet Porosity	0.5	
Reactor Length	0.025	m
Pellet Shape	spherical	
Pellet Radius	0.125	mm
Reactor Radius [53]	0.002	m
Reactor Volume [53]	3.142×10^{-7}	m^3
Reactor Cross Sectional Area [53]	1.257×10^{-5}	m^2
Catalyst Weight [53]	0.0008	kg

The model includes several simplifying kinetic assumptions. These include the following.

- Oxygen availability is maintained along the reactor length through an imposed oxygen-generation mechanism.
- The reaction rates are represented using a global kinetic scheme.
- Possible local limitations due to oxygen depletion, site heterogeneity and transport resistances are neglected.

These assumptions were adopted to enable controllable reactor analysis and to capture the overall behavior of the reactor. The model uses the Ideal gas law to calculate

thermodynamic properties of all species and Kinetic theory for gas thermal conductivity. A fine sized triangular mesh is generated for the model with a boundary layer mesh for the reactor wall. A mesh independence test is conducted to ensure that the results are free from the mesh resolution. Both time-dependent and stationary solvers are included in the model. The stationary solver is used for the Darcy's Law interface whereas, the time-dependent solver for the chemistry, mass and heat transfer. The reactor temperature is swept from 700 ^{o}C to 900 ^{o}C and the CH_4 conversion, C_2 selectivity and C_2 yield are compared with the results of Jiang et al. [98].

The bed porosity is estimated using Equation 18.

$$\varepsilon_b = 1 - \frac{\rho_b}{\rho_{pe}} \qquad (18)$$

Here, ρ_b is the bed density and ρ_{pe} is the pellet density.

4.2.1. Kinetic Model

The global kinetic model of Stansch et al. [63] is employed for the OCM reactions using the Chemistry interface of COMSOL software. The Stansch model includes 10 gas phase reactions and captures the trends in conversion and selectively accurately. Moreover, it provides different routes to capture multiple reactions such as total and partial oxidation of methane, deep oxidation and steam reforming of C_2 products, oxidation of CO, water-gas and reverse water-gas shift, coupling and dehydrogenation of ethane. The model is useful for reactor scaling due to low number of reactions compared to other models. The use of a co-feed global gas-phase mechanism in chemical looping mode captures reactor-scale trends

but may not fully resolve catalyst-specific surface chemistry. The complete set of 10 reactions by Stansch et al. and their corresponding reaction rate equations are displayed in Table 5.

Table 5. OCM Reactions by Stansch et al. [63].

Reaction	Rate Expression
$CH_4 + 2O_2 \rightarrow CO_2 + 2H_2O$	$r_j = \frac{k_{0,j} e^{-E_{a,j}/RT} p_{CH_4}^{m_j} p_{O_2}^{n_j}}{\left(1 + K_{j,CO_2} e^{-\Delta H_{ad,CO_2}/RT} p_{CO_2}\right)^2}$
$2CH_4 + 1/2O_2 \rightarrow C_2H_6 + H_2O$	$r_2 = \frac{k_{0,2} e^{-\frac{E_{a,j}}{RT}} (K_{0,O_2} e^{-\frac{\Delta H_{ad,O_2}}{RT}} p_{O_2})^{n_2} p_{CH_4}^{m_2}}{\left(1 + (K_{0,O_2} e^{-\frac{\Delta H_{ad,O_2}}{RT}} p_{O_2})^{n_2} + K_{j,CO_2} e^{-\Delta H_{ad,CO_2}/RT} p_{CO_2}\right)^2}$
$CH_4 + O_2 \rightarrow CO + H_2 + H_2O$	$r_j = \frac{k_{0,j} e^{-E_{a,j}/RT} p_{CH_4}^{m_j} p_{O_2}^{n_j}}{\left(1 + K_{j,CO_2} e^{-\Delta H_{ad,CO_2}/RT} p_{CO_2}\right)^2}$
$CO + 1/2O_2 \rightarrow CO_2$	$r_j = \frac{k_{0,j} e^{-E_{a,j}/RT} p_{CO}^{m_j} p_{O_2}^{n_j}}{\left(1 + K_{j,CO_2} e^{-\Delta H_{ad,CO_2}/RT} p_{CO_2}\right)^2}$
$C_2H_6 + 1/2O_2 \rightarrow C_2H_4 + H_2O$	$r_j = \frac{k_{0,j} e^{-E_{a,j}/RT} p_{C_2H_6}^{m_j} p_{O_2}^{n_j}}{\left(1 + K_{j,CO_2} e^{-\Delta H_{ad,CO_2}/RT} p_{CO_2}\right)^2}$
$C_2H_4 + 2O_2 \rightarrow 2CO + 2H_2O$	$r_j = \frac{k_{0,j} e^{-E_{a,j}/RT} p_{C_2H_4}^{m_j} p_{O_2}^{n_j}}{\left(1 + K_{j,CO_2} e^{-\Delta H_{ad,CO_2}/RT} p_{CO_2}\right)^2}$
$C_2H_6 \rightarrow C_2H_4 + H_2$	$r_7 = k_{0,7} e^{-E_{a,7}/RT} p_{C_2H_6}^{n_7}$
$C_2H_4 + 2H_2O \rightarrow 2CO + 4H_2$	$r_8 = k_{0,8} e^{-E_{a,8}/RT} p_{C_2H_4}^{m_8} p_{H_2O}^{n_8}$
$CO + H_2O \rightarrow CO_2 + H_2$	$r_9 = k_{0,9} e^{-E_{a,9}/RT} p_{CO}^{m_9} p_{H_2O}^{n_9}$
$CO_2 + H_2 \rightarrow CO + H_2O$	$r_{10} = k_{0,10} e^{-E_{a,10}/RT} p_{CO_2}^{m_{10}} p_{H_2}^{n_{10}}$

Built-in Arrhenius type expressions are used to calculate rate constants as shown in Equation 19 [177].

$$k = A\left(\frac{T}{T_{ref}}\right)^{n^f} e^{\left(\frac{-E}{RT}\right)} \quad (19)$$

Here, $A = \text{pre} - \text{exponentioal factor } (\frac{1}{s}, \frac{m^3}{mol.s}, \frac{m^6}{mol^2.s}, \frac{m^{12}}{mol^4.s})$, $T =$ temperature (K), $T_{ref} = 1000$ (K), $E = \text{activation energy } \left(\frac{J}{mol}\right)$, $R = \text{gas constant}$.

4.2.2. Mass Transport

The mass transport of the species is modeled using the Transport of Concentrated Species (TCS) interface which accounts for transport due to convection and diffusion. In TCS, the mixture properties depend on the composition and molecular interactions between all species. Moreover, the TCS includes models for multicomponent diffusion depending on the mixture composition, pressure and temperature. The mass balance is modeled using Equation 20. The diffusion model deployed for current simulations is Maxwell-Stefan (MS) model as it allows for multicomponent mass diffusion by considering momentum exchange between different species rather than isolated diffusion values for each species. Even though the MS model is computationally more expensive and complex than simpler models such as the Fick's Law, it provides accurate information about interactions between different species. The mass conservation equation for a species i is shown below.

$$\frac{\partial}{\partial t}(\rho.\omega_i) + \nabla(\rho.\omega_i.u) = -\nabla j_i + R_i \quad (20)$$

Here, ρ = mixture density ($\frac{kg}{m^3}$), ω_i = mass fraction species i, u = velocity field ($\frac{m}{s}$), j_i = relative mass flux vector ($\frac{kg}{m^2.s}$), R_i = reaction source term. The relative mass flux vector when using the Maxwell-Stefan model is given by Equation 21.

$$j_i = -\rho\omega_i \sum_{k=1}^{Q} D_{i,k} d_k - \frac{D_i^T}{T}\nabla T \quad (21)$$

Here, $D_{i,k}$ = multicomponent Fick diffusivities ($\frac{m^2}{s}$), d_k = diffusional driving force ($\frac{1}{m}$), D_i^T = thermal diffusion coefficient ($\frac{kg}{ms}$). The diffusional driving force is calculated by the Equation 22.

$$d_k = \nabla x_k + \frac{1}{p}\left[(x_k - \omega_k)\nabla p - \rho\omega_k g_k + \omega_k \sum_{l=1}^{Q} \rho\omega_l g_l\right] \quad (22)$$

Here, g_k = an external force per unit mass acting on species k.

The Packed Bed feature is added to model for the reactive porous domain of the reactor filled with catalyst pellets. An extra dimension technology of COMSOL software adds an additional radial microscale dimension inside each pellet using the Packed Bed feature. The addition of this feature is accompanied by Fluid and Pellets subnodes which are used to define the physical properties of the corresponding phase. The Pellets node is used to define the gas-phase reactions (by coupling with the Chemistry interface) and can also include surface reactions. The Fluid node is used to specify the mass transport in the fluid phase within the catalyst pores. Here, the binary diffusion coefficients are provided as inputs using the Maxwell-Stefan diffusivities from COMSOL database. The effect of porosity is accounted for by utilizing an effective diffusivity model i.e., Millington and Quirk model

(Equation 23) assuming the catalyst is fully gas-saturated. The Millington and Quirk model captures the tortuosity factor which accounts for the reduced diffusivity due to the fact that the solid pellets impede fluid motion. The model is used as a standard approximation for effective diffusivity in the porous medium. Alternative tortuosity models are not examined and Knudsen diffusion is not explicitly included in the present framework.

$$\tau_F = \varepsilon_{pe}^{-1/3} \tag{23}$$

Here, τ_F is the effective transport factor. The Pellet node within the Packed Bed feature is used to define the intraparticle transport and reactions. For a spherical pellet, following diffusion-reaction equation is used for each species along the pellet radius.

$$\varepsilon_{pe}\rho\frac{\partial\omega_{pe,i}}{\partial t} + \frac{1}{r^2 r_{pe}{}^2}\frac{\partial}{\partial r}(r^2 j_i) + \frac{1}{r_{pe}}\rho u_r\frac{\partial\omega_{pe,i}}{\partial r} = R_{pe,i} + S_{b,react}.R^S_{pe,i} \tag{24}$$

Here, ε_{pe} = pellet porosity, r = dimensionless pellet radius [0 (center) ≤ r ≤ 1 (surface)] , $R_{pe,i}$ = surface reaction rate for species i $\left(\frac{mol}{m^3.s}\right)$, $S_{b,react}$ = reactive specific surface area $\left(\frac{1}{m}\right)$, $R^S_{pe,i}$ = surface reaction rate for bulk species $(\frac{kg}{m^2.s})$

The mass transport properties within the pores of catalyst pellets are kept similar to those defined in the Fluid subnode of Packed Bed feature. The gas-phase reactions are added in the Reaction subnode of the Pellet node by coupling each species' reaction rate with the corresponding reaction rate in the Chemistry interface. A Pellet-Fluid Interface node is used to specify the boundary conditions between fluid and pellet out-surface. For the coupling of pellet's internal region and surrounding fluid, the Film Resistance (Mass Flux) option is chosen where the mass flux across the pellet-fluid interface is assumed to be rate determined

on the bulk fluid side. Equations 25–29 describe the bidirectional local coupling between the bed-scale domain and the pellet extra-dimension domain. The inward flux is given by the following equation [177].

$$N_{i,inward} = h_{D,i}(c_i - c_{pe,i}) \quad (25)$$

Here, $N_{i,inward}$ = inward mass flux $(\frac{mol}{m^2.s})$, $h_{D,i}$ = film mass transfer coefficient $\left(\frac{m}{s}\right)$, c_i, $c_{pe,i}$ = concentration of fluid in bulk and just before pellet pore respectively$(\frac{mol}{m^3})$.

The active species surface area is estimated using the following equation [177].

$$S_b = \frac{3}{r_{pe}}(1 - \varepsilon_{pe}) \quad (26)$$

Here, S_b = active species surface area, r_{pe} = pellet radius, ε_{pe} = pellet porosity. The mass transfer coefficient is calculated by the following equation [177].

$$h_D = \frac{Sh.D}{r_{pe}} \quad (27)$$

Here, h_D = mass transfer coefficient, Sh = Sherwood number. The Sherwood number is computed using the following equation (Frössling Model) [177].

$$Sh = 2 + 0.552Re^{1/2}Sc^{1/3} \quad (28)$$

Here, Re = Reynolds number, Sc = Schmidt number. These numbers are calculated using the expressions below [177].

$$\mathrm{Re} = \frac{r_{pe} U}{\nu}, \mathrm{Sc} = \frac{\nu}{D_{pe}} \quad (29)$$

Here, $U =$ fluid velocity, $\nu =$ fluid kinematic viscossity, $D_{pe} =$ effective diffusion coefficient.

The species flow from the bed to the pellets where they take part in chemical reactions and then flow back to the bed. The reactions within the pellets are solved in an extra dimension. In Equation (25), the gas-phase concentration is represented explicitly by the bulk concentration and the concentration at the pellet surface which together define the driving force for interfacial mass transfer. Although bulk temperature does not appear explicitly in this expression, it affects the flux indirectly through its influence on diffusion and mass-transfer parameters. In this way, the macroscopic bed domain supplies the local bulk concentration and temperature-dependent transport conditions to the pellet-scale model, while the pellet-scale reaction and diffusion results are returned to the bulk domain as interfacial fluxes or source terms.

In this case, a surface reaction is added to form molecular oxygen from the pellet surface which later takes part in gas-phase reactions within the bed and the pellets. The surface reaction rate was modeled as a reversible reaction using the Langmuir-Hinshelwood step for the adsorption/desorption of oxygen as shown in Equation 30 [177]. Equation (30) is used here as an effective representation of oxygen availability rather than a fully validated surface mechanism. Accordingly, θ is treated as an assumed effective surface coverage parameter, and Γ is treated as an effective surface oxygen-capacity parameter appearing in

the surface reaction-rate expression. These parameters were selected to maintain a realistic CH_4/O_2 ratio and reasonable oxygen availability within the reactor.

$$r = k_f \Gamma \theta^2 - k_b c O_2 \Gamma \quad (30)$$

Here k_f, k_b = forward and backword reaction constants $\left(\frac{1}{s}, \frac{m^3}{mol.s}\right)$, $\Gamma = 3e^{-12}\ \left(\frac{kg}{m^2}\right)$, $\theta = 0.07$.

4.2.3. Heat Transfer

To ensure that the model captures accurate heat transfer by conduction and convection effects within the packed bed reactor, the Heat Transfer in Porous Media (Packed Bed) was added in the model. The equations 31-34 are used for macroscopic bed fluid and microscopic pellet heat transfer [177].

$$\varepsilon_b \rho_f C_{p.f} \frac{\partial T_f}{\partial t} + \rho_f C_{p.f} \mathbf{u}.\nabla T_f + \nabla.\mathbf{q_f} = Q_{pe,f} + \varepsilon_p Q_f \quad (31)$$

$$q_f = -\varepsilon_b k_f \nabla T_f \quad (32)$$

$$\left((1-\varepsilon_{pe})\rho_{pe} C_{p.pe} + \varepsilon_{pe}\rho_f C_{p.f}\right)\frac{\partial T_{pe}}{\partial t} + \frac{1}{(r r_{pe})^2}\frac{\partial}{\partial t}\left(-r^2 k_{pe,eff}\frac{\partial T_{pe}}{\partial t}\right) = Q_{pe} \quad (33)$$

$$k_{pe,eff} = (1-\varepsilon_{pe})k_{pe} + \varepsilon_{pe} k_f \quad (34)$$

Here ρ_f, ρ_{pe} are the fluid and pellet densities (kg/m³), $C_{p.f}$, $C_{p.pe}$ the fluid and pellet heat capacities (J/kg·K), k_f, k_{pe} the fluid and pellet thermal conductivities (W/m·K), **u** the fluid velocity vector (m/s), $Q_{pe,f}$ the pellet-fluid heat exchange term (W/m³·K), $\mathbf{q_f}$ the fluid

conductive heat flux (W/m^2), T_{pe} the temperature along the radial direction of pellet, $k_{pe,eff}$ the effective thermal conductivity of the pellet, and $Q_{f,}$ Q_{pe} any fluid or pellet heat sources (W/m^3).

The packed bed subnode under the porous media node is used to precisely capture the microscale radial heat transfer effects within the pellets. The reactor walls are treated as thermally insulated which means there is no heat flux across the boundary. A heat source is added within the pellets in the form of total heat released from the chemical reactions in the chemistry interface. To couple the macroscopic bed and microscopic pellet heat transfer, both temperatures at the outer surface of the pellet and fluid temperature in bed are assumed equal and the resulting heat flux is applied in the pellets and bed equations. The inlet temperature is defined as the same temperature T intended for the reactor.

4.2.4. Flow Field

The flow field is assumed to be Darcian flow as the expected Reynolds number is very small (<10) and the pressure drop is modeled using the Darcy's Law interface of COMSOL which is used to simulate fluid flow through the interstices in a porous medium [173]. The model equations specified within the porous medium node of the Darcy's Law interface are given below [177].

$$\frac{\partial}{\partial t}\left(\varepsilon_{pe}\rho\right) + \nabla.(\rho u) = Q_m \tag{35}$$

$$u = -\frac{\kappa}{\mu}\nabla p \tag{36}$$

Here, $\mathrm{u} = \text{dynamic viscosity } \left(\frac{\mathrm{kg}}{\mathrm{m.s}}\right), \mathrm{u} = \text{Darcy velocity vector } \left(\frac{\mathrm{m}}{\mathrm{s}}\right), \mathrm{p} =$ pressure (pa), $\mathrm{Q_m} = \text{mass source term } \left(\frac{\mathrm{kg}}{\mathrm{m^3.s}}\right), \kappa = \text{permiability } (\mathrm{m^2})$.

The permeability is calculated by the Kozeny-Carman model. The model is shown in equation 37 and uses the porosity and pellet diameter to describe permeability of the flow through packed beds.

$$\kappa = \frac{d_p^2}{180} \frac{\varepsilon_{pe}^3}{\left(1-\varepsilon_{pe}\right)^2} \tag{37}$$

Here d_p is the average pellet diameter.

The complete boundary conditions are listed in Table 6.

Table 6. Boundary conditions for CL OCM reactor model.

Boundary	Type	Value / Expression
Inlet	Velocity Inlet	u = 0.0203 m/s GHSV = 1125 mL/hg
Outlet	Pressure	p = 1 atm
Walls	No-slip + Adiabatic	-

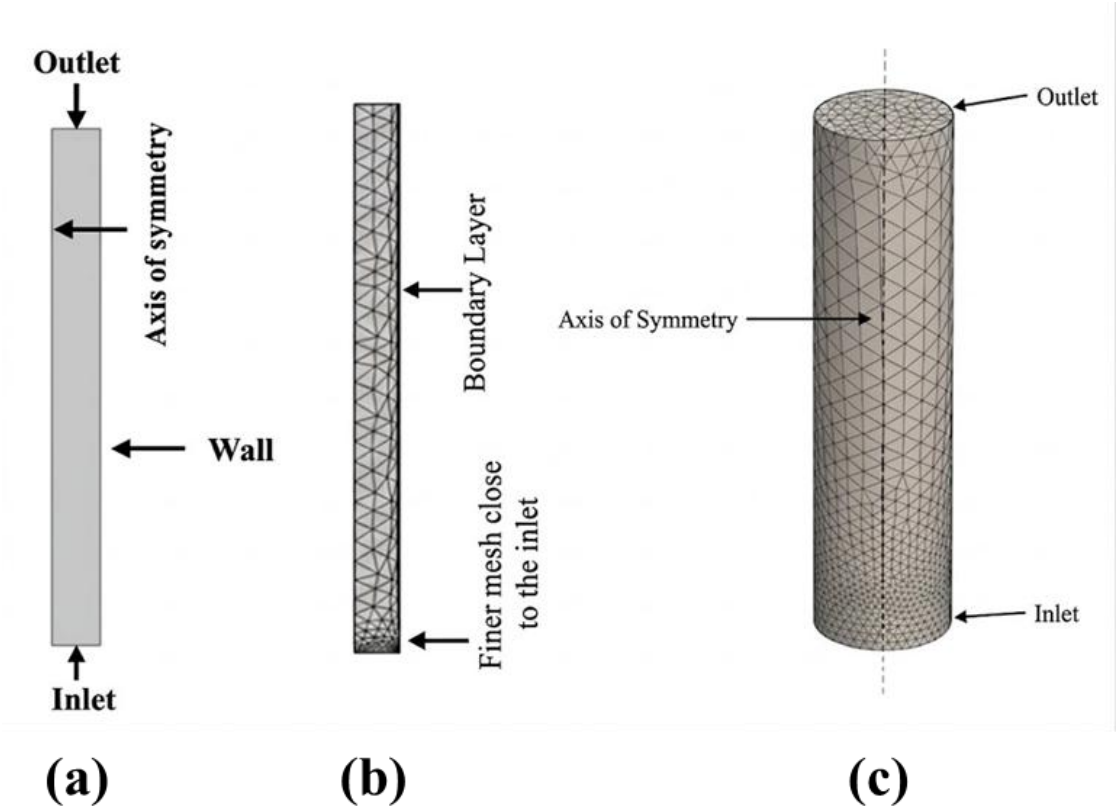

Figure 14. (a) 2D axisymmetric geometry (b) 2D axisymmetric mesh (c) 3D mesh representation.

The mesh and model boundaries are shown in Figure 14. A fine triangular mesh at the inlet which progressively becomes coarser across the reactor length with boundary-layer refinement near the reactor wall was used and mesh independence was confirmed.

A relatively coarser mesh was utilized in the current study because the flow through the packed bed was modeled using Darcy's law rather than by completely solving the full Navier–Stokes equations around individual pellets. In this approach, the packed bed is treated as a porous medium, and the velocity variations are represented through an effective permeability term. The selected mesh provides sufficient resolution to capture the gradients

in species concentration, temperature, velocity and pressure while reducing the computational cost of the multiscale reactor simulations and achieving mesh independence.

Based on the operating conditions considered in this study, the packed-bed Reynolds number was estimated as $Re_p = \rho u_s d_p/\mu \approx 0.02$, using $u_s = 0.0203$ m/s, $\rho = 0.14$ kg/m^3, $d_p = 0.25$ mm, and $\mu = 3.5277 \times 10^{-5}$ Pa.s. Including the bed porosity effect ($\varepsilon_b = 0.45$) through the interstitial velocity gives $Re_{p,i} \approx 0.045$. These values indicate that the flow remains in a creeping-flow where viscous forces dominate, for which Darcy's law is appropriate. However, near-wall effects are not explicitly resolved. The reactor wall is assumed to be thermally insulated (adiabatic), corresponding to a zero heat flux boundary condition. This is a simplification, since in reality, heat exchange with the surroundings may still occur given the exothermic nature of OCM reactions.

4.3. Results and Discussion

The model was run for 30 seconds at each temperature. The model employed a stationary study for the Darcy flow field followed by a time-dependent study for chemistry, mass transport and heat transfer. The results from the calibration of kinetic model are discussed in detail in this section. The fully coupled node was used for both stationary and time-dependent solvers which uses a damped version of the Newton's method and the damping factor is automatically adjusted in each iteration by the solver. Similarly, physics-controlled tolerances ($1x10^{-3}$) are used. The kinetic parameters were calibrated against the experimental data of Jiang et al. by matching CH_4 conversion, C_2 selectivity, and C_2 yield over 700–900 °C. In this section, the model predictions against the experimental data are

presented and the discrepancies between the two are highlighted. Then the spatial concentration gradients of different product gases are analyzed.

4.3.1. Model Calibration and Validation

Figure 15 shows the complete workflow for the calibration process. Here, the kinetic parameters, the pre-exponential factor (A) and the activation energy (E), were iteratively changed and the results (CH_4 conversion, C_2 selectivity/yield) were compared with experimental data until the difference was within an acceptable range i.e., <5% for all values. The complete set of calibrated kinetic parameters from Stansch model are listed in Table 7.

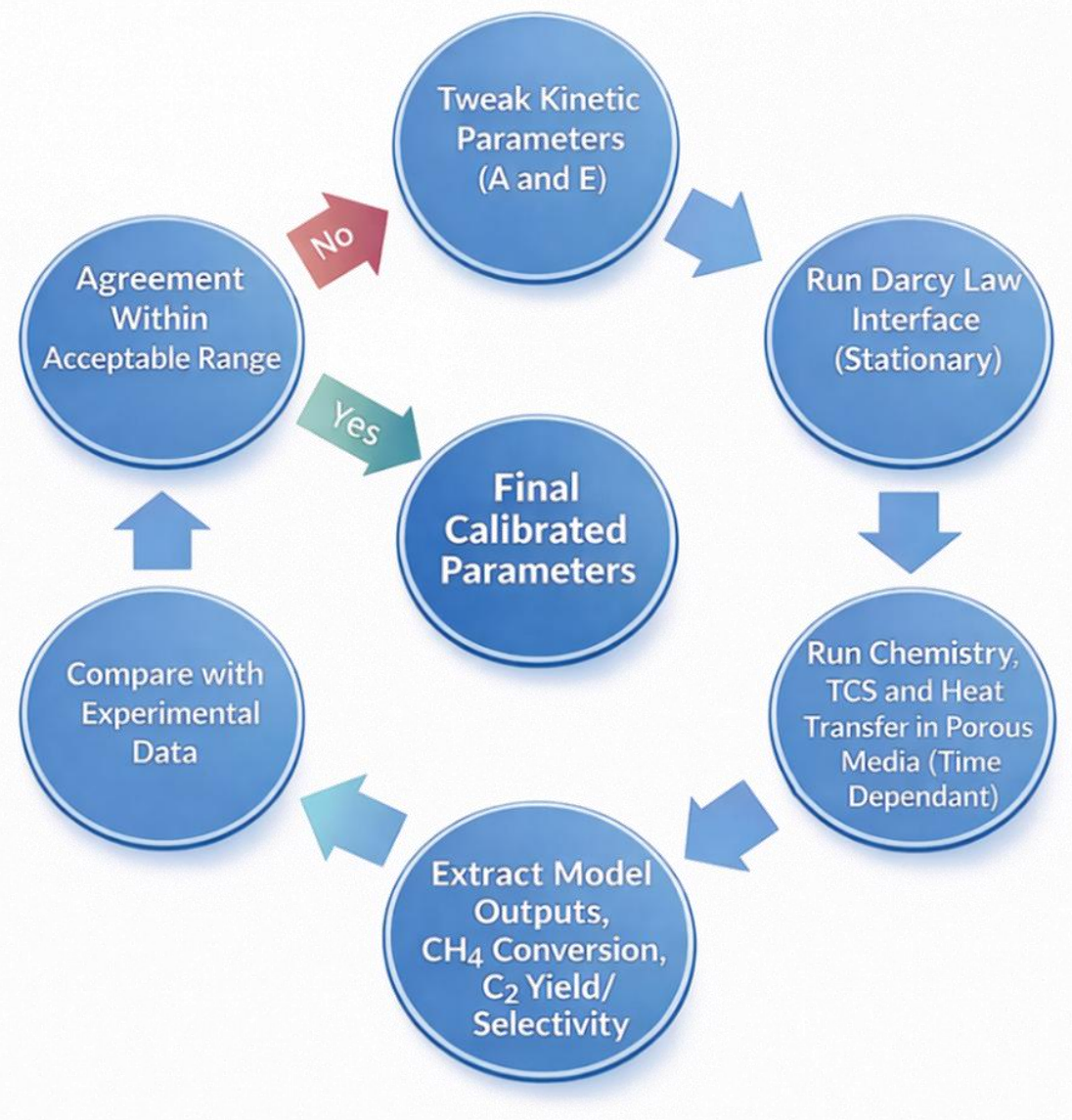

Figure 15. Workflow for CFD model calibration.

Table 7. Kinetic parameters from Stansch model [63].

Reaction Number	Pre-exponential Factor (A) (1/s, m^3/(mol.s))	Activation Energy (E) (kJ/mol)	m_j	n_j
1	9.98×10^{-2} (T)	48	0.24	0.76
2	1.54×10^{6} (T)	182	1	0.4
3	1.21×10^{0} $(T)^{1.42}$	244.8	0.57	0.85
4	7.04×10^{1} $(T)^{1.55}$	936	1	0.55
5	6.01×10^{4} $(T)^{1.32}$	157	0.95	0.37
6	8.38×10^{4} $(T)^{1.96}$	249	1	0.96
7	9.98×10^{7} (T)	226	1	-
8	1.57×10^{10} $(T)^{1.97}$	250	0.97	0
9	3.41×10^{2} $(T)^{2}$	155.7	1	1
10	3.59×10^{3} $(T)^{2}$	286	1	1

Figure 16 shows the calibration plots from 700-900ºC. As evident in the Figure 16, the current model effectively captures the trends in CH_4 conversion, C_2 selectivity and C_2 yield across the temperature range. The C_2 yield rises from nearly 1.5% at 700 ºC to a maximum value at 850 ºC before it starts to drop at 900ºC. The maximum yield is within the 800-850 ºC temperature range which is almost 20% at 825 ºC according to Jiang et al. [98]. The difference in model predicted and experimental C_2 yields remains within ±1.14% across the temperature range. The C_2 selectivity is almost 40% at 700ºC and increases to 60% at 800 ºC. After 800 ºC, the C_2 selectivity starts dropping. The model predicts C_2 selectivities within ±4.35% of the real values. Finally, the CH_4 conversion increases steadily from 700-800 ºC. However, there is a sharp increase in the conversion after 800 ºC and the maximum CH_4 conversion is almost 80% at 900 ºC. The model predictions are within ±3.01% of the experimental values. A decline in C_2 selectivity accompanied by a sharp increase in the CH_4 conversion suggests that the pollutant emissions formation is more favorable at temperatures higher than 800 ºC.

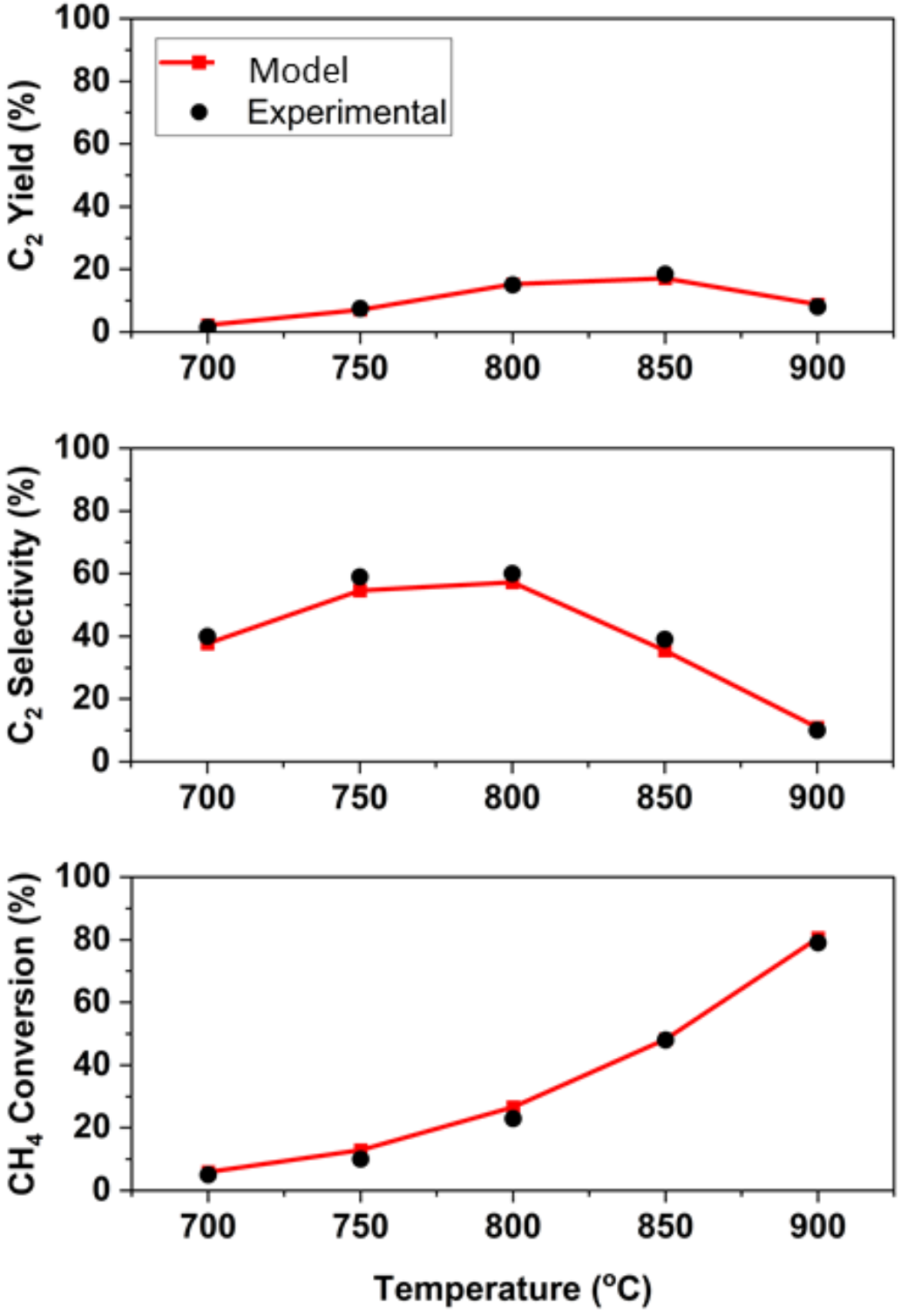

Figure 16. Calibration plots at GHSV = 1125 mL/hg and temperatures 700-900°C.

4.3.2. Spatial Variations

Figure 17-19 show the formation of C_2H_4, C_2H_6 and CO_2 across the length of the reactor at each temperature respectively. As shown in Figure 17, the optimum C_2H_4 concentration is obtained within the 800-850 ºC range. This rise in C_2H_4 concentration or C_2H_4 yield is attributed to enhanced methane activation and methyl radical formation, which promote C_2 coupling. As the temperature increases above 850ºC, deep oxidation reactions begin which facilitate conversion of C_2H_4 to CO and CO_2 and decrease the C_2H_4 selectivity. In case of C_2H_6, as shown in Figure 18, the maximum concentration is observed at 800 ºC. Thereafter, C_2H_6 begins to convert to C_2H_4 at 800 ºC close to the reactor outlet. At 850 ºC, the conversion of C_2H_6 to C_2H_4 begins much earlier in the reactor. The axial concentration profiles further show that the desired C_2 products are formed primarily in the portion of the bed close to the inlet, where reactant availability is the highest, whereas downstream regions increasingly favor the oxidation of the desired C_2 products.

At 900ºC, the overall C_2H_6 concentration drops compared to 800 ºC and 850 ºC because of the more favorable formation of CO_2. The concentration of CO_2 is comparable to C_2 products up to 800 ºC, as shown in Figure 19. After 800ºC, the CO_2 concentration rises sharply. The results show a trade-off between C_2 selectivity and C_2 yield at 800 ºC and 850 ºC. The higher C_2 yield is accompanied by decreased C_2 selectivity or higher pollutant emissions. Higher pollutant emissions increase the cost of operating the downstream CO_2 removal process. This adjudicates further investigation of the downstream processes including CO_2 removal and ethylene purification to optimize the economic aspects of OCM process.

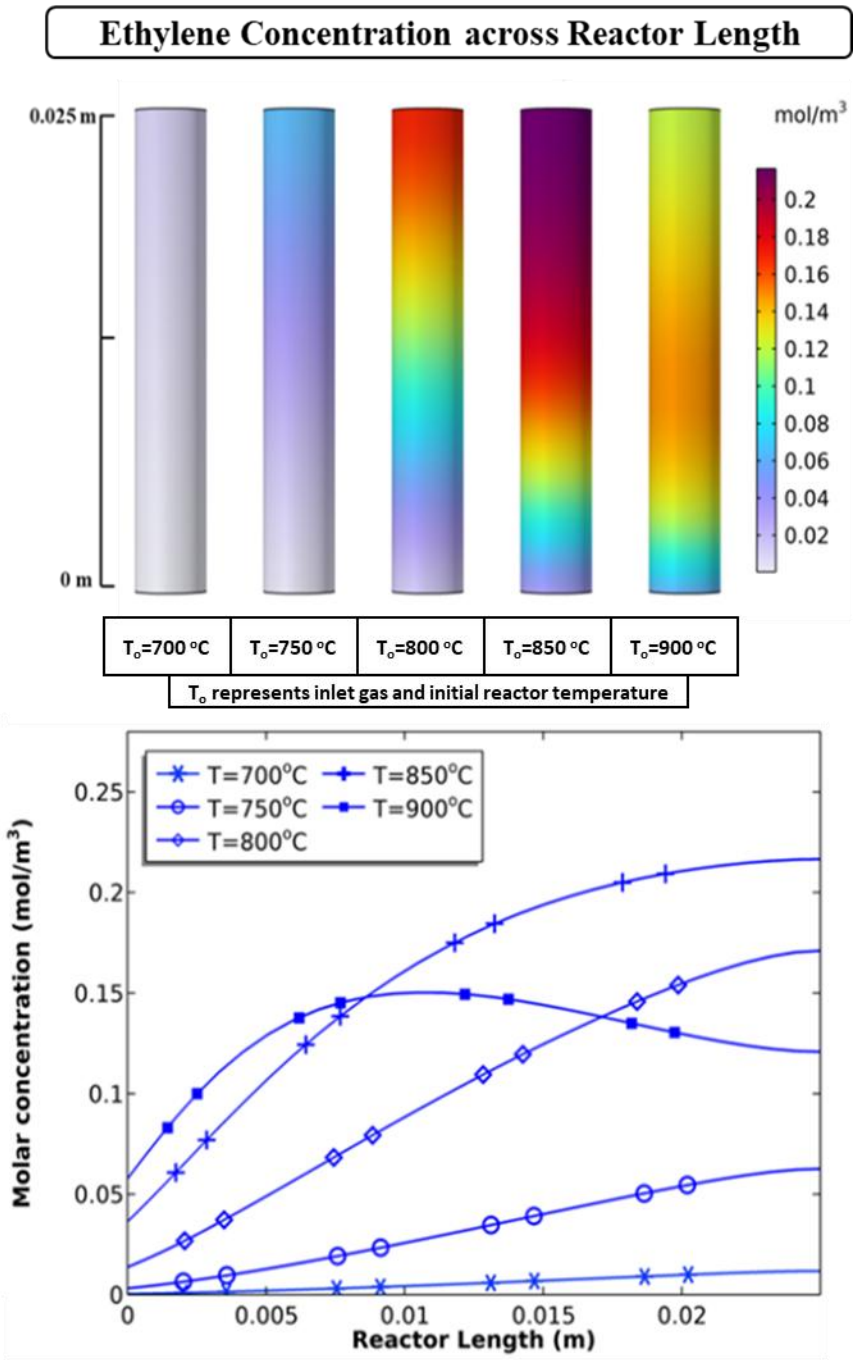

Figure 17. Ethylene concentrations (mol/m^3) across reactor length at GHSV = 1125 mL and temperatures 700-900 °C.

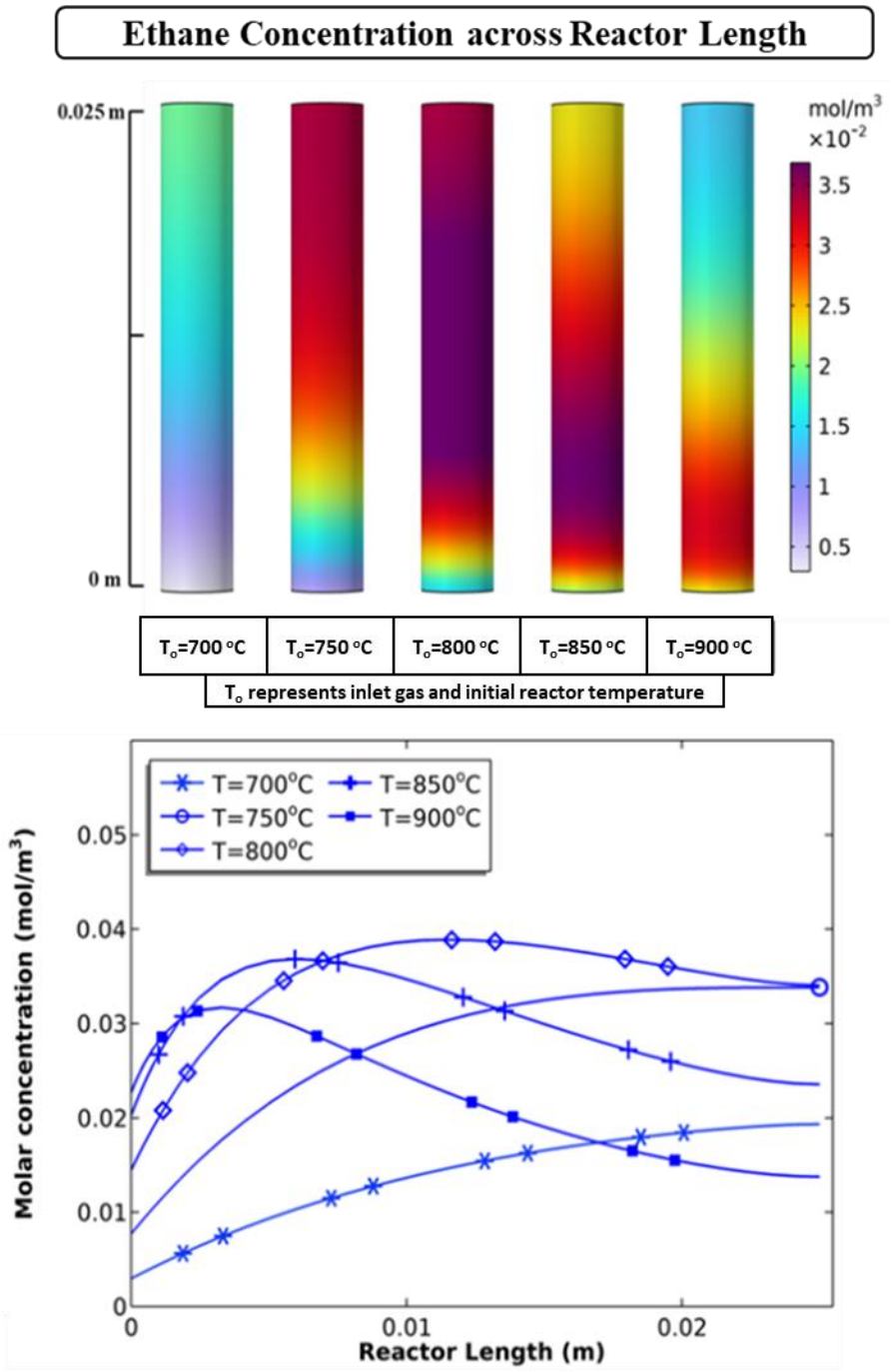

Figure 18. Ethane concentrations (mol/m^3) across reactor length at GHSV = 1125 mL and temperatures 700-900 ºC.

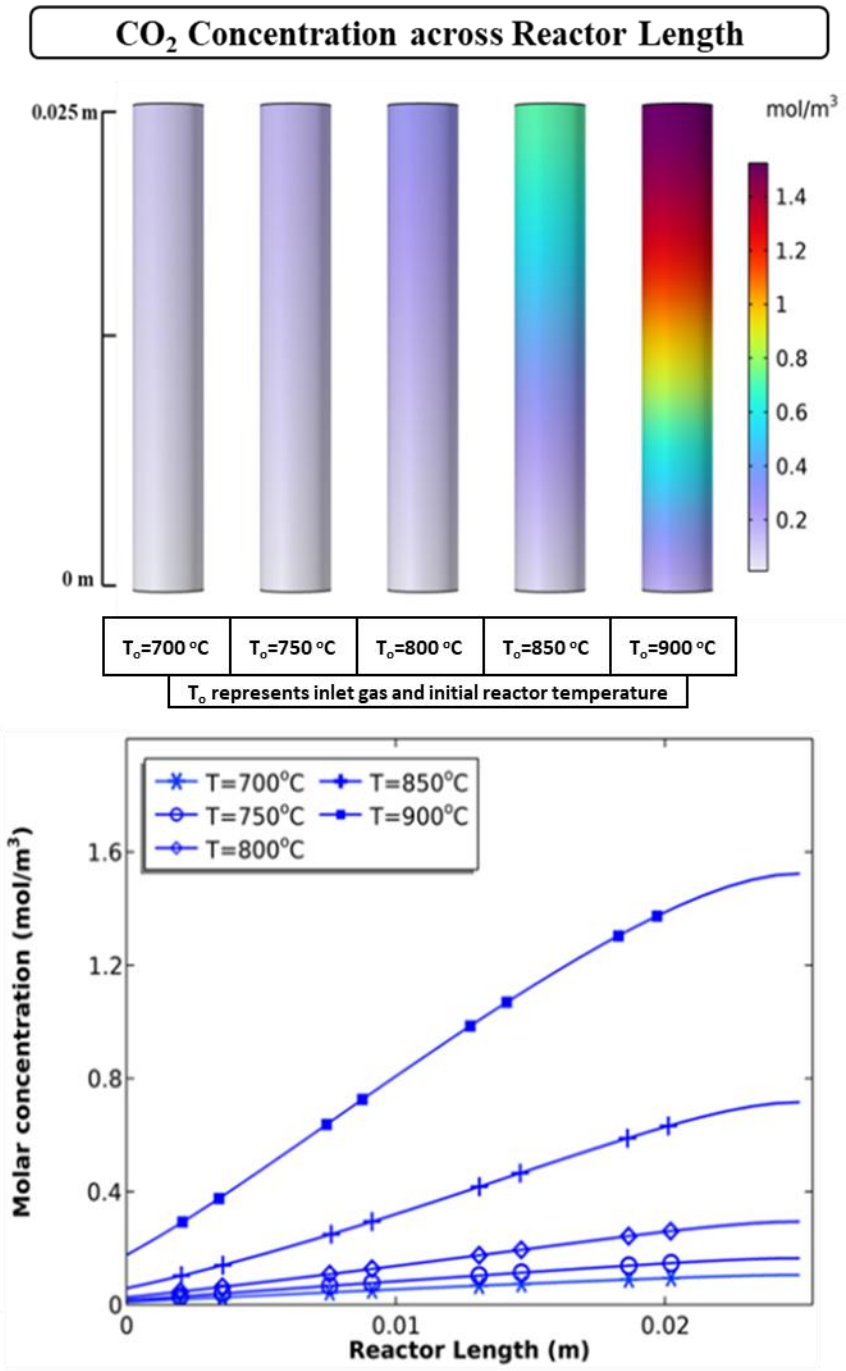

Figure 19. CO_2 concentrations (mol/m^3) across reactor length at GHSV = 1125 mL and temperatures 700-900 ºC.

The exothermic reactions result in a slight increase in reactor temperatures with time. Figure 20 shows temperature gradient across reactor length at T = 1073 K, t = 30 s and Figure 20 shows the reactor temperatures at times 1, 10, 20 and 30 seconds. The temperature increases from 1073 K at t = 1 s to 1077.7 K at t = 30 s at inlet. Moreover, it can be seen from the Figure 20 that the reactor temperature rises slightly close to the inlet and drops back to the inlet temperature value shortly afterwards. This drop in temperature occurs due to the endothermic conversion of C_2H_6 to C_2H_4 and C_2H_4 reaction with H_2O. As shown in Figure 20, the inlet temperature at t = 30 s is 1077.7 K for the 1073 K case however, the maximum temperature is 1078.4 K close to the inlet as highlighted in the Figure. Therefore, it can be concluded that the inclusion of heat transfer model is necessary to accurately predict the reactor behavior. This will be helpful considering scaling up of the model.

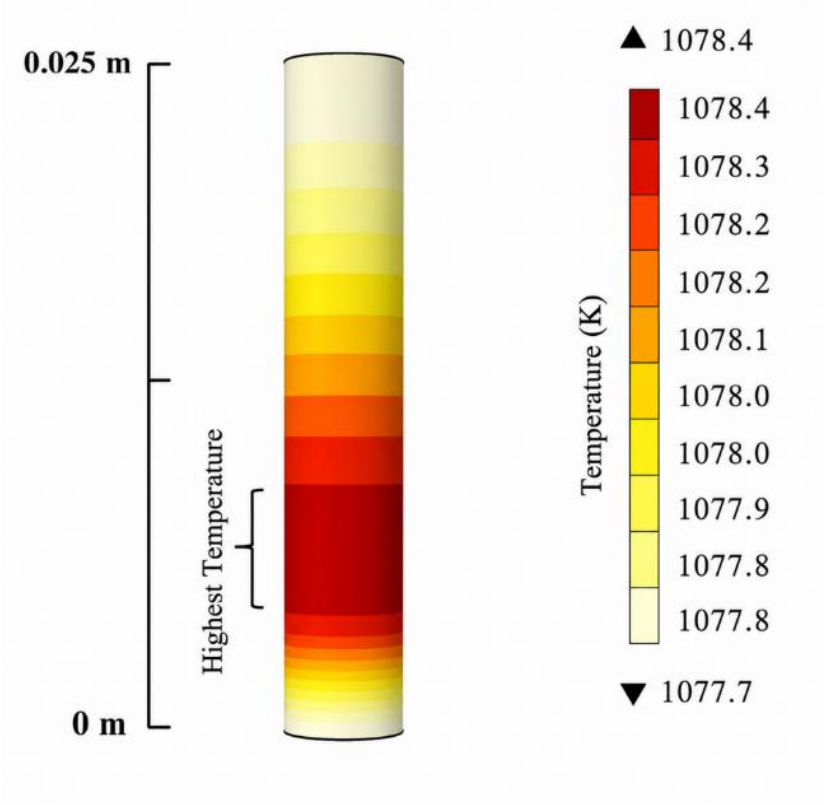

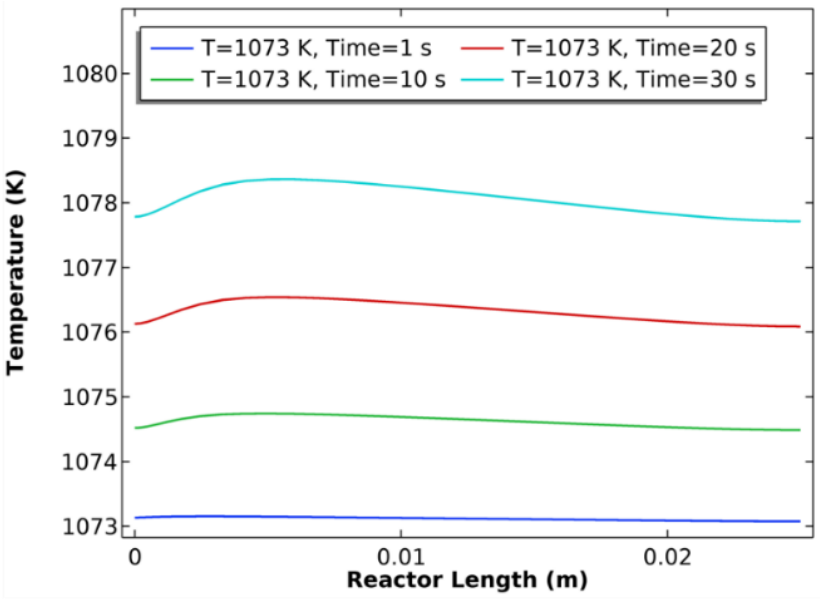

Figure 20. Temperature gradient across reactor length.

4.3.3. Model Robustness

To check the model fidelity and robustness, different parameters such as time step, mesh dependence and pellet diameter are swept to understand how the difference in model predictions and experimental results is impacted with these parameters. The time step is verified from 0.1-5 seconds and the simulations are run for 30 seconds. The model does not show any deviation from the original results even after reducing the time step to 0.01 seconds.

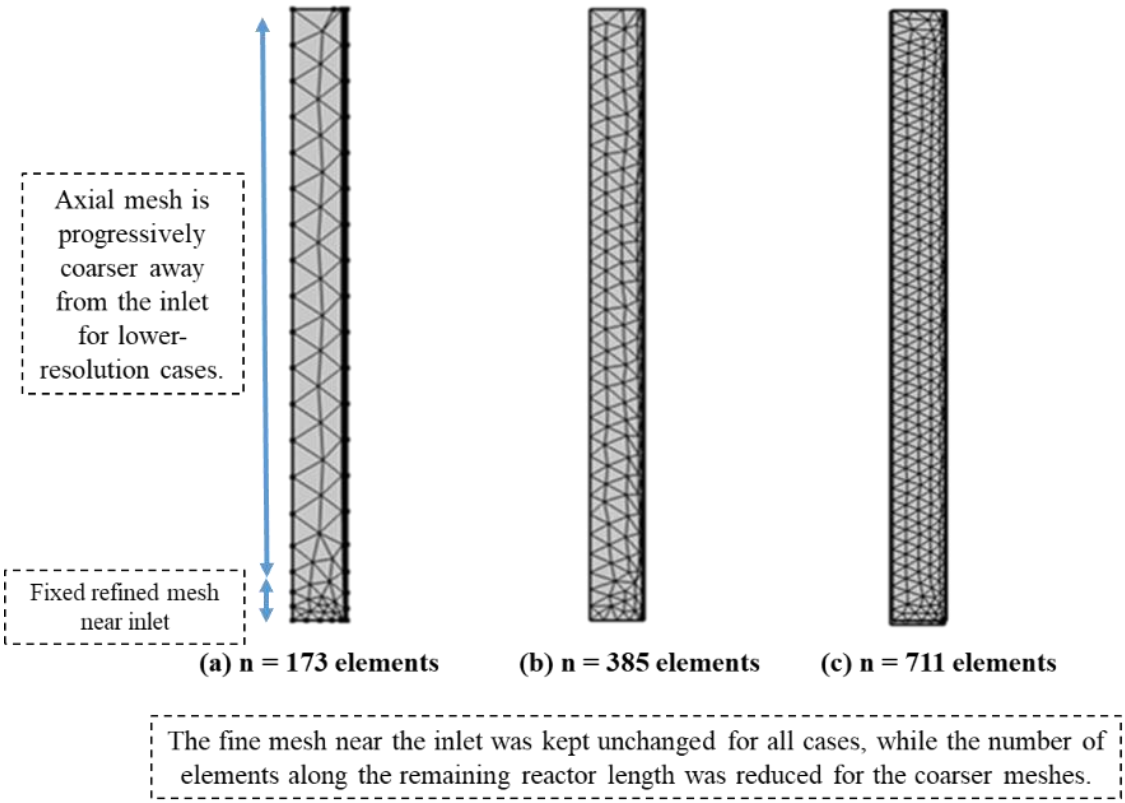

Figure 21. Mesh resolution used for grid-independence analysis.

Three different number of mesh elements (n) are tested i.e., 173, 385 and 711 with 560, 1125 and 1940 degrees of freedoms (DOFs) respectively. The mesh resolution for each n value is shown in Figure 21. To verify the mesh independence of the model, grid convergence index (GCI) was calculated for C_2 yield, selectivity and CH_4 conversion at 800^{o}C. The GCI values were 0.6, 0.1 and 2.5% for C_2 yield, selectivity and CH_4 conversion respectively for n values of 173 and 385. Therefore, considering the low GCI values and negligible deviation in the key performance metrics, the coarser mesh with n = 173 was considered accurate enough for future simulations while reducing computational cost.

4.3.4. Model Verification

The model is verified by observing its predictions at different inlet methane concentrations and GHSVs compared to the ones used for the original model. An increased GHSV reduces the residence time of the gases and hence, reduces the methane conversion but increases C_2 selectivity. Similarly, an increased inlet methane concentration decreases the methane conversion and increases the C_2 selectivity.

Figure 22 shows CH_4 conversion, C_2 selectivity and yield at the original inlet methane mass flow rate (J_{in}) and also at two other mass flow rates i.e., half and 1.5 times of the original methane mass flow rate keeping the GHSV constant. It is evident from the Figure 22 that the reduced methane inlet concentration increases the CH_4 conversion but decreases the C_2 selectivity and vice versa. C_2 yield seems to increase slightly with lower J_{in} at 850 ^{o}C and 900 ^{o}C. These results are in agreement with previous work of Karakaya et al. [47] which shows that a decreased Ch_4/O_2 ratio increases methane conversion.

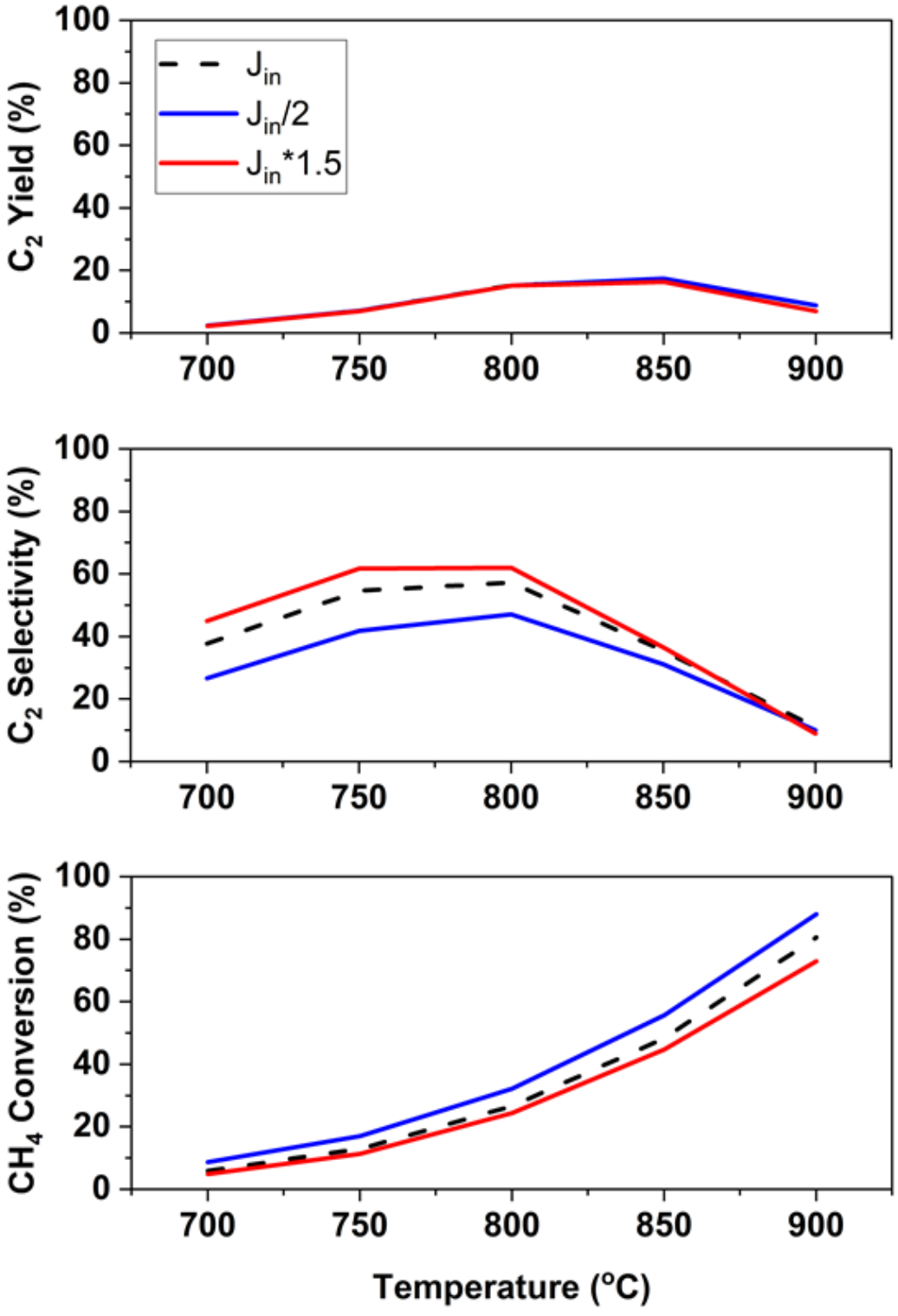

Figure 22. CH_4 conversion, C_2 selectivity & yield at different inlet methane flow rates.

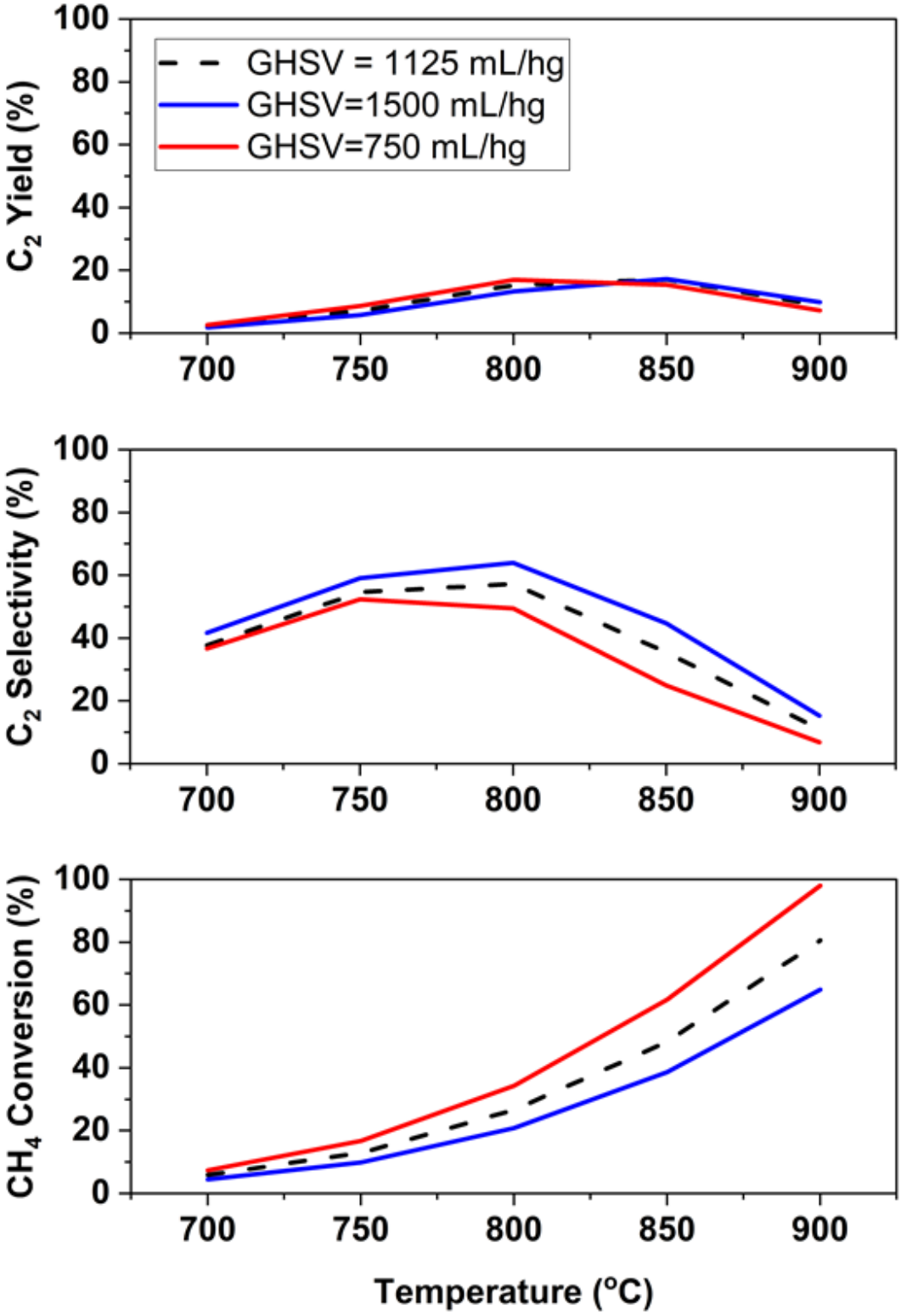

Figure 23. CH_4 conversion, C_2 selectivity and yield at different GHSVs.

Similarly, the work of Jiang et al [98] shows that the methane conversion declines with higher GHSVs whereas, C_2 selectivities are increased and vice versa. The effect of GHSVs is shown in Figure 23. Since the model predictions are aligned with the experimental results reported in literature, the model is physically verified.

4.3.5. Radial and Axial Gradients

Figures 24-27 show the 2D axisymmetric gradients for CH_4, C_2H_4, CO_2 concentrations and the temperature gradients respectively for the 1173 K inlet gas temperature case. The 2D contours indicate that CH_4, C_2H_2, CO_2 and temperature initially exhibit minor localized gradients near the inlet region (both radial and axial) as the gas flow and reaction front begin to establish. The early-time radial gradients close to the inlet, visible between 0.01 and 0.02 s, include limited radial variations caused by transient heat and mass transfer across the bed radius. With increasing time, the concentration and temperature profiles become more developed and the radial gradients diminish, becoming nearly negligible after about 0.03 s. This suggests that, under the selected operating conditions, radial gradients only appear initially, while the later reactor behavior is dominated by axial gradients along the bed length. The weak radial gradients at longer times also support the assumption that the packed-bed reactor approaches a more uniform radial state as it moves toward steady operation. Radial gradients will become important in larger diameter reactor or with strong wall heat loss or external heating/cooling or non-uniform flow distribution such as inclusion of a mixer.

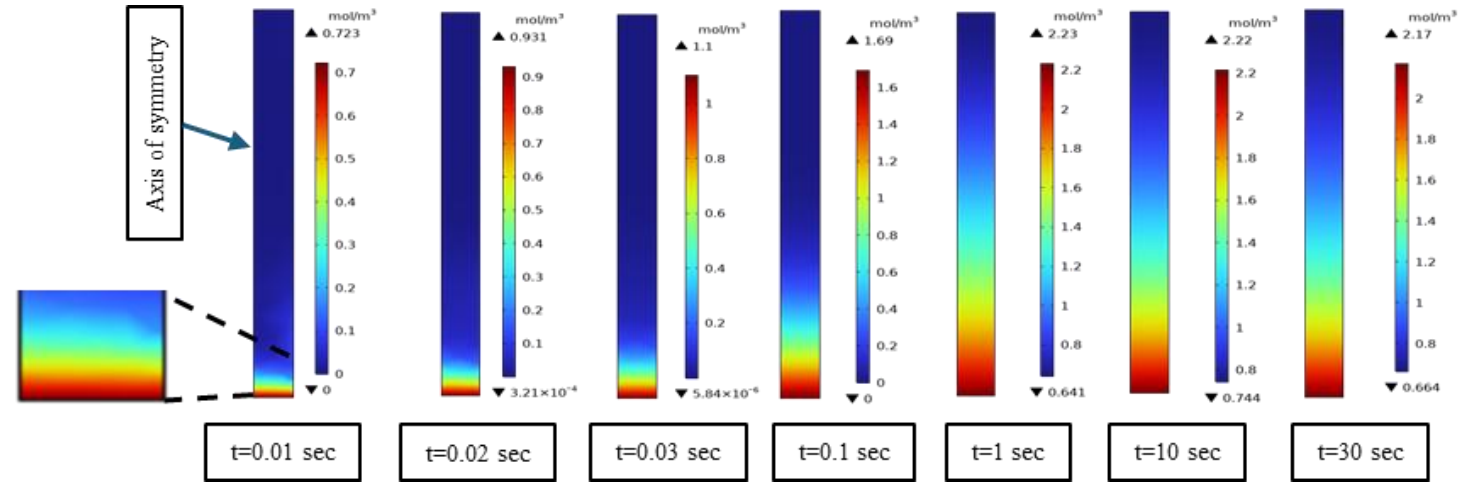

Figure 24. Transient 2D axisymmetric CH_4 concentration contour profiles

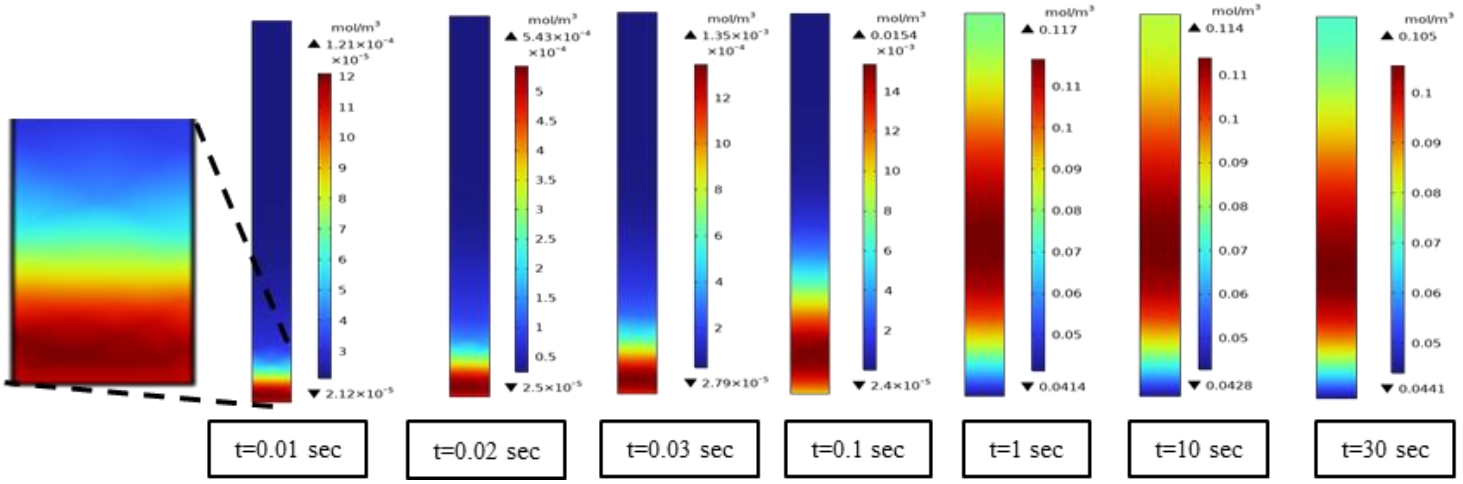

Figure 25. Transient 2D axisymmetric C2H4 concentration contour profiles

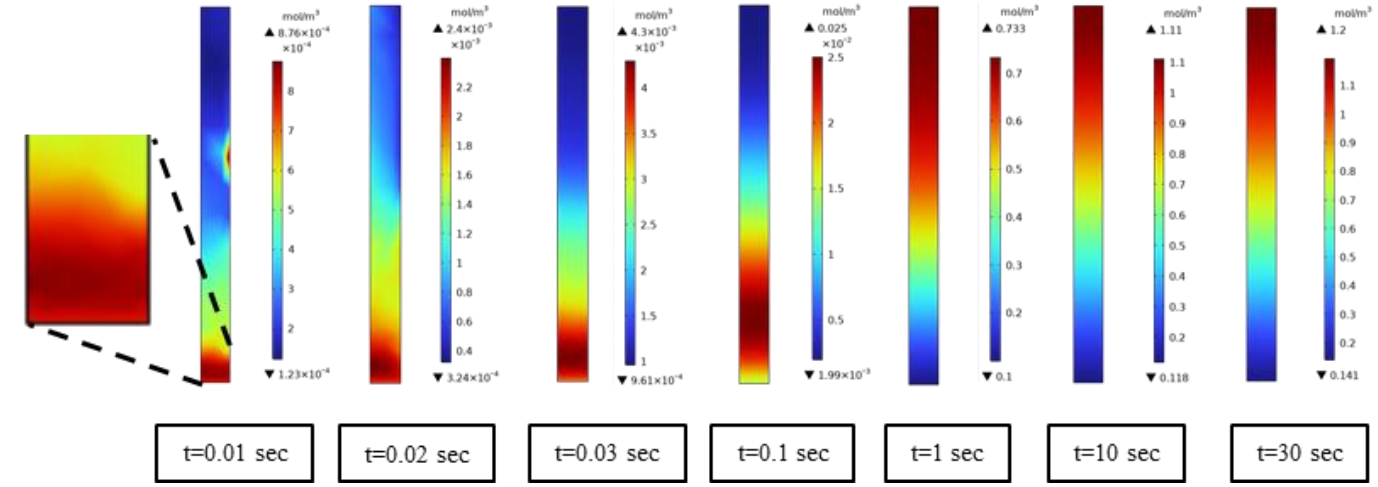

Figure 26. Transient 2D axisymmetric CO_2 concentration contour profiles

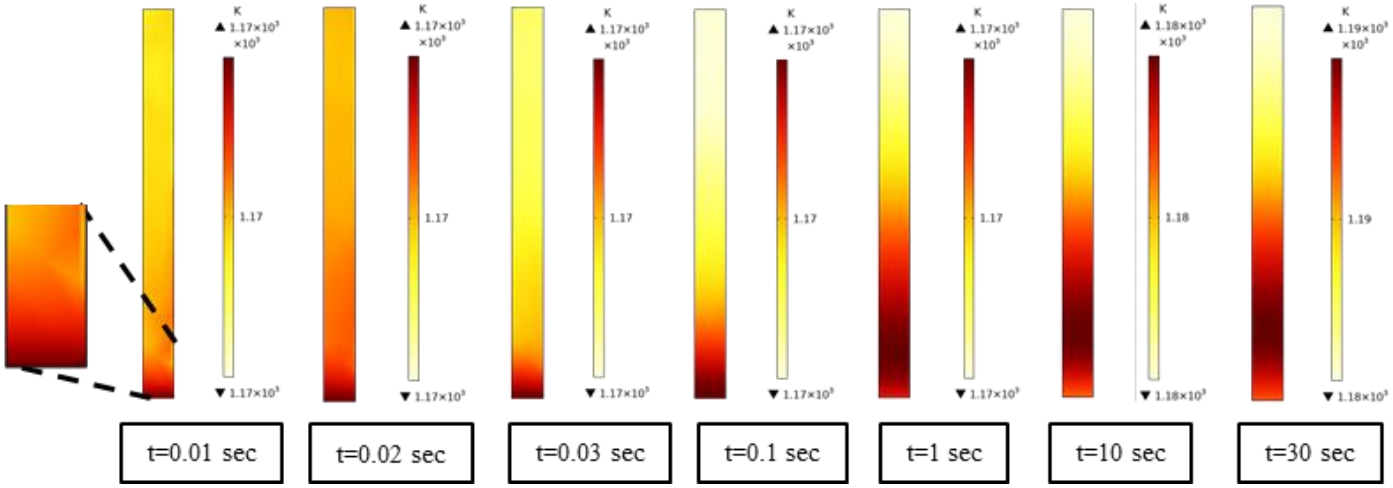

Figure 27. Transient 2D axisymmetric temperature contour profiles

4.3.6. Model Limitations and Applicability

In this section, the effects of several simplifications or assumptions made for the model are discussed, along with their implications and potential directions for future work. The model captures the key multiscale transport and reaction behavior; however, the diffusion model does not explicitly include the Knudsen diffusion or the pore-wall interactions, which may become important for extremely small pore sizes (e.g., $\sim<1\mu m$) and could affect internal mass transfer and local species distributions. Future work will explicitly address these effects and evaluate their significance through sensitivity analysis. Similarly, the adiabatic wall assumption neglects heat losses to the surroundings and may lead to higher predicted internal temperatures and altered reaction behavior at larger scales. Therefore, thermal boundary conditions need to be adjusted accordingly before utilizing the model at an extended scale (pilot or industrial scale).

Gravitational effects were not explicitly included in the CFD model. This assumption is reasonable because the flow is primarily driven by the imposed inlet conditions through the packed bed. However, gravitational effects may become more relevant at larger scales or under conditions closer to practical reactor operation. The gas density and viscosity were also assumed to be constant to simplify the coupled flow and heat-transfer calculations. Therefore, small variations in flow behavior caused by local temperature changes may not be fully captured. This limitation may become more important at larger scales and should be addressed in future scale-up studies.

The applicability of the present model is the strongest mainly under the conditions, reactor geometry and catalyst material/properties considered in this study. Predictions outside these conditions should be treated with caution as changes in scale, oxygen availability, inlet stream composition and transport behavior may affect the results and should be supported by further experimental validation. Therefore, the predictions of the current model should be considered indicative rather than absolute.

Chapter 5. CFD Parametric Study

In the previous chapters, the criteria for CL OCM/CO_2-H_2O industrial deployment and a multiscale, CFD, packed bed reactor model for chemical looping OCM were developed based on experimental results from Jiang et al. [98]. The current chapter presents a parametric study beyond what was reported in Jiang's paper utilizing the CFD reactor model. The study discusses the effect of wide ranges of multiple parameters such as the GHSVs, inlet CH_4/O_2 ratios, oxygen availability and reactor shape on the process performance in terms of C_2 yield, selectivity, methane conversion and temperature gradients.

This following section describes some of the previous parametric studies performed on the OCM reactor and results achieved by systematically performing parametric sweeps on the CFD model developed for the current study.

5.1. Background and Literature Review

Multiple studies can be found in the literature regarding parametric analysis of the OCM technology conducted both by experiments and simulations. Jiang et al. [98] utilized a Na-$LaMnO_3$ catalyst in a lab-scale packed bed reactor for CL OCM process. They performed parametric study to analyze the effects of temperature and GHSV on the CL OCM process. In general, their results showed a decreasing methane conversion and increasing C_2 selectivity with increasing GHSVs. Conversely, increasing temperatures increased methane conversion and decreased C_2 selectivity. C_2 yield had a non-monotonic trend in terms of

temperature and GHSV. Their results showed a maximum C_2 yield of ~20% and selectivity of ~58% at 825 ^oC and GHSV of 1125 mL/hg.

Karsten et al. [178] analyzed three different reactor concepts for OCM on a mini-plant scale. They performed parametric studies for temperature and GHSV. They analyzed a co-feed packed bed reactor, chemical looping packed bed reactor and a membrane reactor. Their results highlighted that a chemical looping reactor resulted in C_2 selectivity of up to 90%. However, their C_2 yields were low (~3%) at the maximum selectivity point. They further showed that the yield can be improved up to 7% by adding more oxygen carrier but this leads to a deterioration of the C_2 selectivity to around 70%. They also showed that increasing temperatures increased the methane conversion but decreased C_2 selectivity.

Fontoura et al. [170] developed a single pellet size CFD model using ANSYS v19.1 including the heat and mass transfer within the pellet and the gas-solid phases. Moreover, they performed sensitivity analysis to analyze the impact of pellet arrangement and feed conditions (i.e., CH_4/O_2 ratios up to 10) on the concentration and temperature gradients. Their results indicated that a high CH_4/O_2 ratio increases the ethylene yield and selectivity. However, the methane conversion rate drops at higher CH_4/O_2 ratio. Moreover, they also reported that a temperature difference of more than 100 ^oC instigates the auto-ignition behavior of the catalyst.

Micale et al. [179] performed a coupled micro-kinetic and Eulerian-Eulerian CFD simulations for lab scale and industrial fluidized bed reactors for OCM using La_2O_3/CaO. The lab scale model was validated against experiments and deviations were below 10%. Their study included a sensitivity analysis of catalyst specific surface area (via particle size)

on reactor performance, helping to identify how changes in catalyst morphology or scale impact methane conversion and C_2 selectivities in fluidized systems. They also highlighted that reactor performance was more sensitive to hydrodynamic parameters than to kinetic uncertainties at large scale.

Kim et al. [180] developed a 1D packed-bed reactor model, validated with experimental data that incorporates detailed reaction kinetics and transport correlations. They varied operating conditions such as the CH_4/O_2 ratio, feed flow rate, dilution and temperature. Their results showed that CH_4/O_2 ratio strongly affected the C_2/COx trade-off. However, the most influential parameter for methane conversion and C_2 selectivity was the temperature.

5.2. Results

In this section, the results from multiple stages of parametric sweeps are discussed in detail. The model was run for 30 seconds at each condition. The model employed a stationary study for the Darcy flow field followed by a time-dependent study for chemistry, mass transport and heat transfer. The fully coupled node was used for both stationery and time-dependent solvers which uses a damped version of the Newton's method and the damping factor is automatically adjusted in each iteration by the solver. Similarly, physics-controlled tolerances ($1x10^{-3}$) are used.

Two stages of simulations are performed. In the first stage, broad sweeps including multiple parameters such as the GHSV, inlet methane concentration, oxygen concentration and reactor diameter are performed across a temperature range of 700-900 ^oC and the results

are analyzed. These parameters are selected as they directly control the physical and chemical processes and hence the reactor performance. For example, increasing the GHSV decreases the residence time and can limit the methane conversion while avoiding deep oxidation reactions occurring at later stages of the reactor. Lower temperatures can have similar impacts on the process, i.e., limiting the conversion and avoiding deep oxidations while promoting C_2 selectivity. However, lower methane conversion could lead to lower process yields as well and therefore, an optimum temperature and GHSV should be found for the process. Inlet methane and oxygen concentrations impact the reaction kinetics. A higher CH_4/O_2 ratio leads to a methane rich environment where oxygen availability for methane combustion and deep oxidation reactions is reduced, resulting in dominant C_2 formation compared to COx compounds. Similarly, reactor diameter affects flow distribution, heat accumulation and radial transport behavior. During these simulations, only one parameter is swept across 700-900 ^oC while every other parameter is kept the same as the baseline case.

From the first round of simulations, the range for most suitable operating conditions is narrowed down and second round of simulations are then performed for CH_4/O_2 ratios and GHSVs across a temperature range of 800-850 ^oC. The baseline operating condition is the one obtained from calibrated model i.e., a GHSV of 1125 mL/hg, temperatures 800-850 ^oC and CH_4/O_2 ratios within 3-3.3.

5.2.1. First Stage of Simulations

5.2.1.1. GHSV Sweep

A GHSV sweep is performed from 300-1800 mL/hg (milliliters per hour per gram of catalyst). Figure 28 shows the effect of GHSV on C_2 yield, selectivity and CH_4 conversion rate at a temperature range of 700-900ºC. At lower temperatures, low GHSVs (500, 750 mL/hg) produce higher yields compared to the original GHSV of 1125 mL/hg. This increase in yield is explained by higher methane conversions caused by increased residence times as shown in Figure 28. However, the yields are very small (<12%) until 750 ºC and become equal to the original case for 300 mL/hg at 800 ºC and drop lower after 800 ºC for 750 mL/hg. These results show a clear advantage of low GHSVs in terms of higher yields at lower temperatures. However, this is outshined by much lower C_2 selectivities as well compared to the original case as shown in Figure 28, indicating increased CO_2 production.

For higher GHSVs i.e., 1125 and 1400 mL/hg, maximum C_2 yields are achieved at 850 ºC. These yields are slightly higher than the yield achieved by the 750 mL/hg at a lower temperature of 800ºC. However, the C_2 selectivities for 1125 and 1400 mL/hg cases are much higher than 750 mL/hg at 800ºC. This shows that the higher GHSVs offer higher C_2 selectivities compared to lower GHSVs at a fixed temperature. At higher GHSVs, the residence time for gases is lower which results in higher number of C_2 molecules quickly escaping the reactor without taking part in deep oxidation reactions. This lowers the conversion of C_2 products to CO_2 or CO and increases the C_2 selectivity of the process.

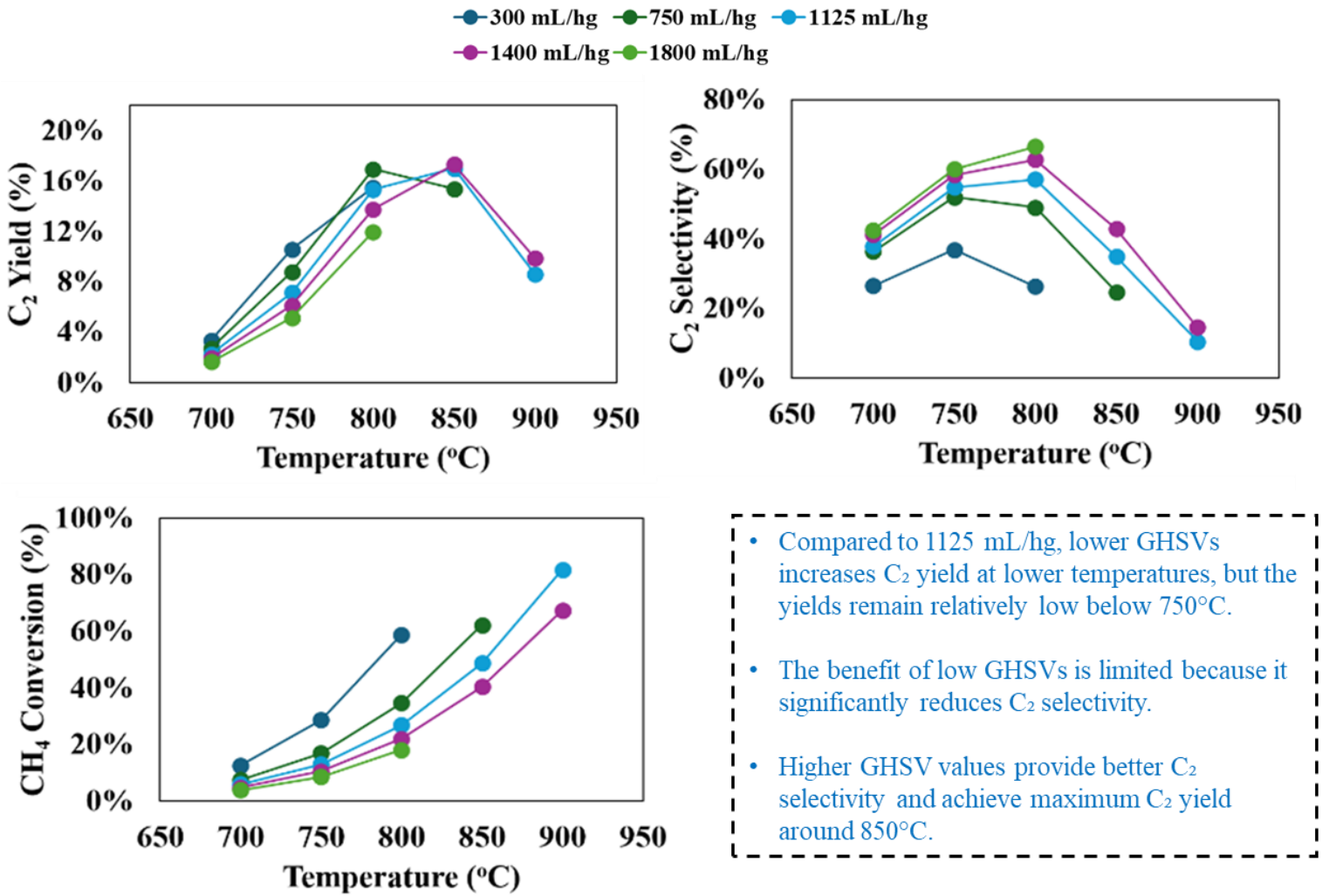

Figure 28. C_2 yield, selectivity and CH_4 conversion for the GHSV sweep.

Furthermore, higher GHSVs serve to increase the convective heat removal as shown in Figure 29. For low GHSV case i.e., 300 mL/hg, the maximum temperature is close to the inlet and the different in maximum temperature and outlet temperature is 1K. However, at higher GHSV i.e., 1400 mL/hg, the maximum temperature moves away from the inlet and the difference in maximum temperature and outlet temperature is only 0.4K. This shows that the heat is less likely to be trapped inside the reactor for high GHSVs reducing the chances for hot spot formation.

Overall, the results are aligned with the parametric study conducted by Jiang et al. [98] showing that the methane conversion declines with higher GHSVs whereas, C_2 selectivities are increased and vice versa. The results support the reactor operation at higher GHSVs where comparable C_2 yields and higher C_2 selectivities are achievable compared to the original case within the temperature range of 800-850^{o}C. Lower GHSVs do provide comparable yields at lower temperatures but the selectivities are significantly low.

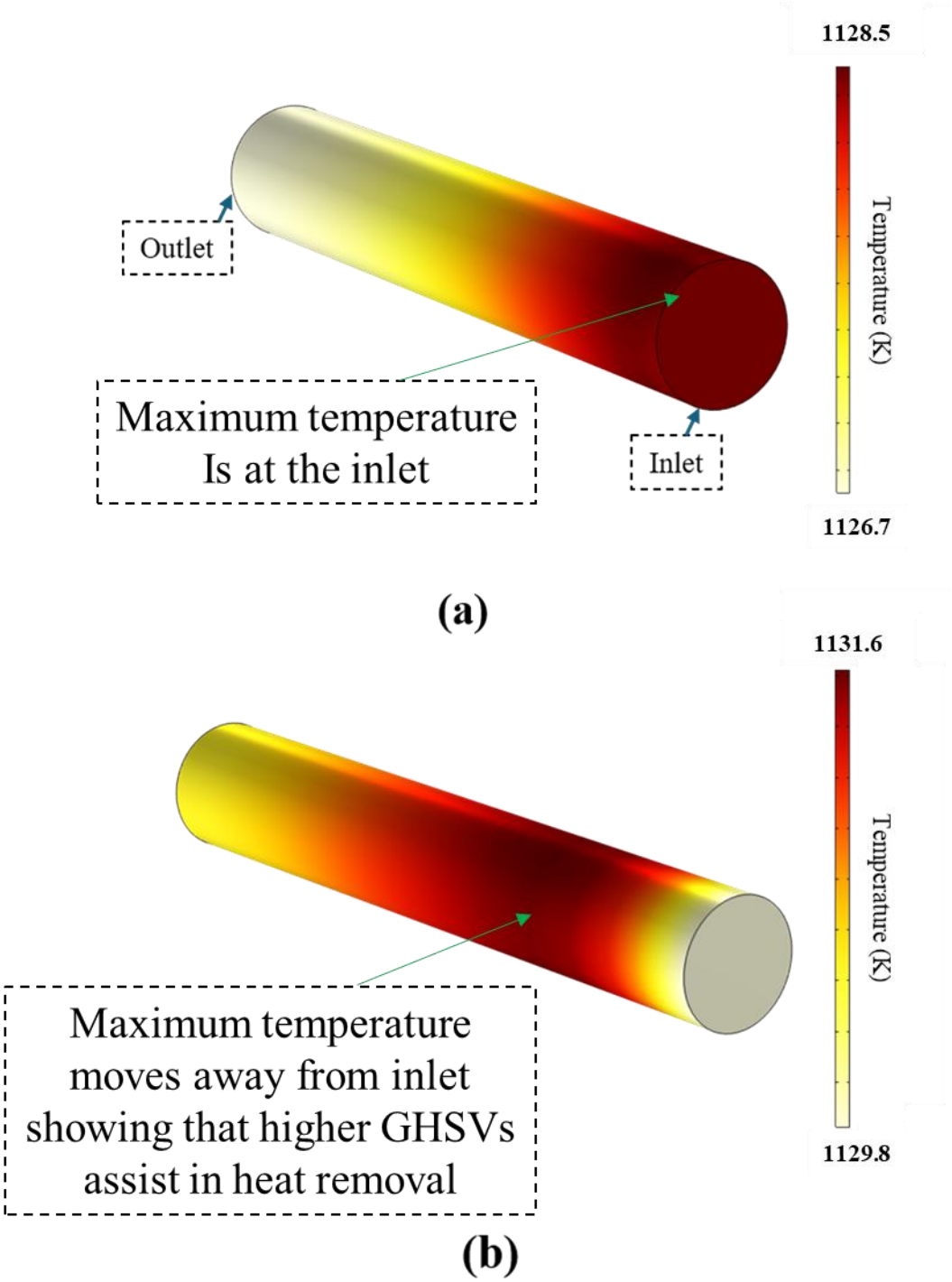

Figure 29. Temperature gradients for GHSVs (a) 300 mL/hg (b) 1400 mL/hg at 800ºC.

5.2.1.2. Inlet Methane Concentration Sweep

Inlet methane concentration sweep is performed to analyze the effect of CH_4/O_2 ratio. Figure 30 shows the C_2 yield, selectivity and CH_4 conversion rate at varies inlet methane mass flow rates. The original/baseline mass flow rate is represented as J_{in}, while the mass flow rate is multiplied by a factor to change the flow rate. A lower methane inlet mass flow rate ($0.8*J_{in}$) results in a slight increase in the C_2 yield i.e., 0.027 percentage points from the original case.

The main benefit of increased inlet methane concentration is the higher selectivity which is more significantly improved at low temperatures. Methane conversion drops at higher inlet methane flow rates. These results suggest an advantage of increasing the inlet methane concentration as the original C_2 yield is preserved while improving C_2 selectivity. Increased methane concentration increases the CH_4/O_2 ratio, resulting in a more fuel-rich operating condition for the reactor. Under the rich condition, the availability of oxygen becomes lower, which is essential for CO_2 and CO formation therefore, the C_2 selectivity of the process increases. Furthermore, lower oxygen availability increases the chances of coupling of the methyl radicals i.e., CH_3-CH_3 compared to the combustion of methane which also contributes to higher C_2 selectivity.

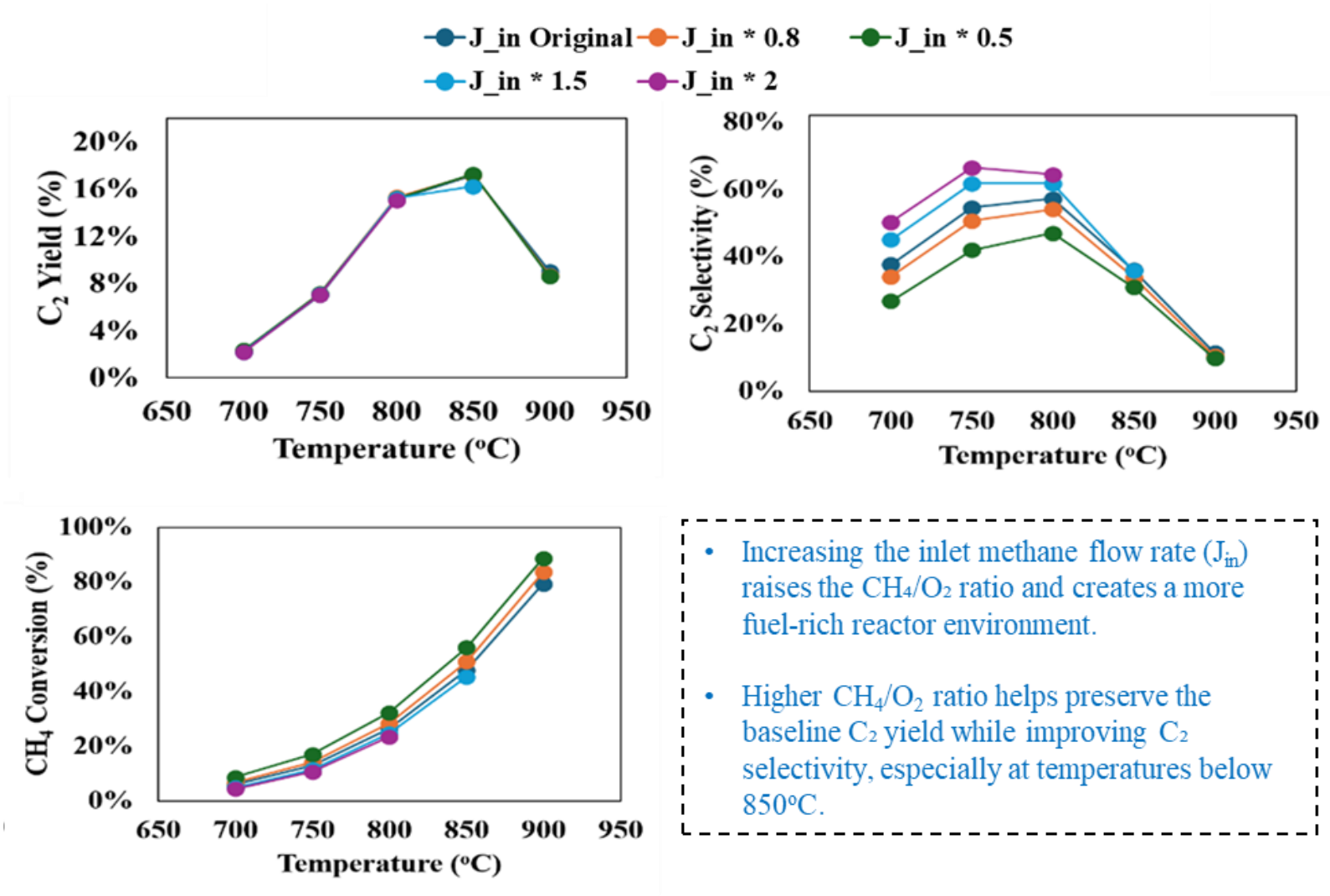

Figure 30. C_2 yield, selectivity and CH_4 conversion for inlet methane concentration sweep.

5.2.1.3. Surface O_2 Concentration Sweep

An O_2 concentration sweep is performed by varying the O_2 formation rate (forward pre-exponential factor A) from the surface reaction as shown in Equation 19. The purpose of the sweep is to study the effect of increased O_2 availability for reactions. Figure 31 shows the effect of increased O_2 formation rate on the C_2 yield, selectivity and CH_4 conversion rate. The original O_2 formation rate is 2.5E9. The increased O_2 results in higher C_2 yields compared to the original case. The overall gain in yield is 1.7 percentage points when O_2 formation rate is doubled. However, the selectivity drops at this rate and the methane conversion increases indicating an increased CO_2 formation. Even though increased oxygen availability decreases the C_2 selectivity, it increases methane conversion which helps increase the C_2 yield as well.

Increased oxygen availability supports the methane activation by increasing the concentration of active oxygen species along the reactor. Increased methane activation promotes methyl radical formation and increases methane conversion. As a result, the total formation of C_2 products increases, resulting in higher C_2 yield. However, excess oxygen also promotes combustion of methane and deep oxidation of C_2 hydrocarbons to COx, which reduces the fraction of converted methane that forms the desired C_2 products.

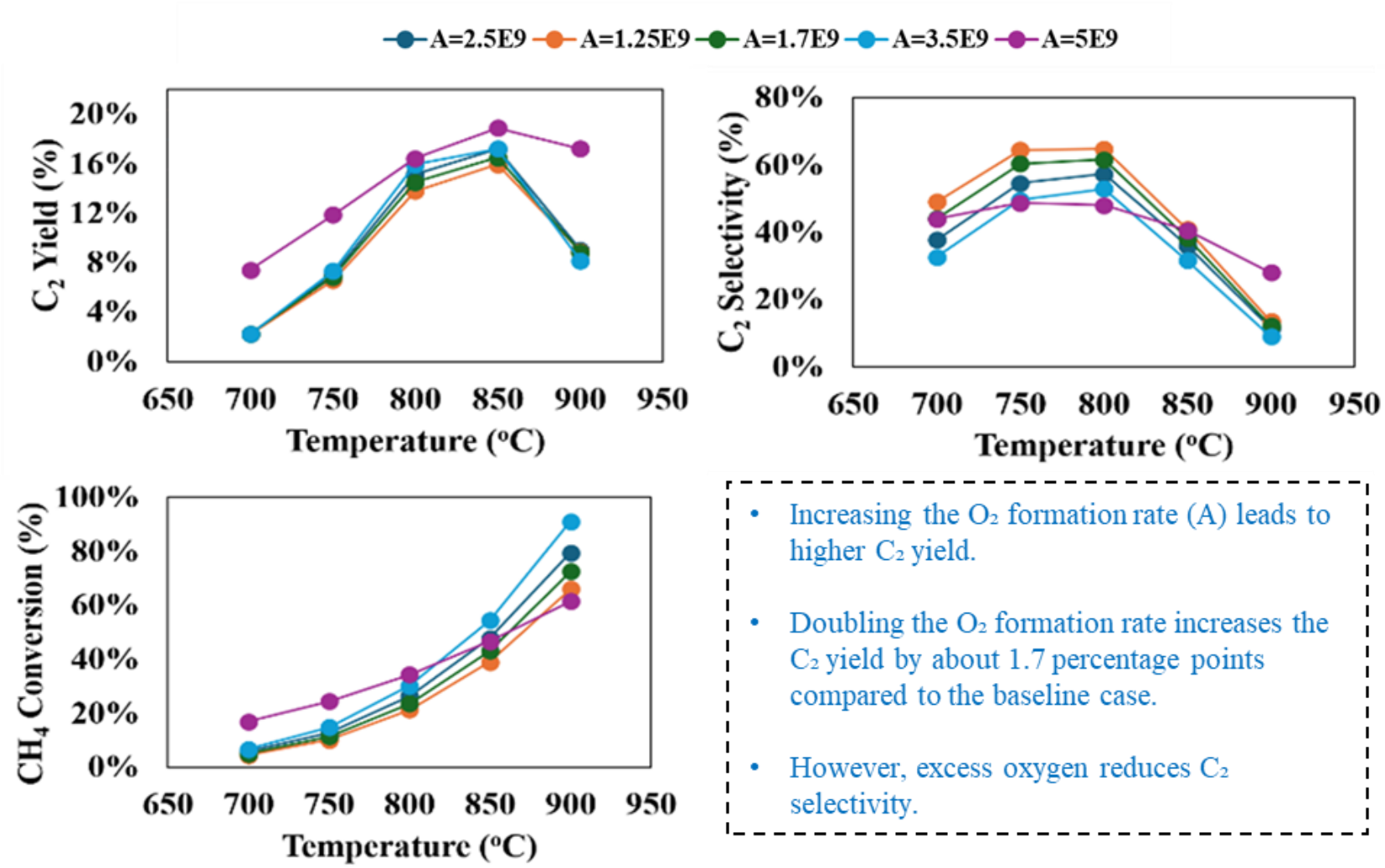

Figure 31. C_2 yield, selectivity and CH_4 conversion for O_2 formation rate sweep.

5.2.1.4. Diameter Sweep at Original Volume

A diameter sweep is performed where diameter of the reactor is increased to two and three times the original diameter, keeping the same volume (3.15E-7 m^3) and GHSV (1125 mL/hg). The purpose is to study the effect of diameter increase on the hot spot formation. The increased diameter does not cause noticeable change in the peak C_2 yield, as shown in Figure 32, as the yield is almost similar at 850 ^oC for all diameters. However, the C_2 selectivity declines and methane conversion increases as the reactor diameter is increased indicating greater CO_2 production.

However, the benefit of larger diameter/length ratio appears in terms of hot spot formation as shown in Figure 33. The highest gas temperature is not trapped closed to the inlet for the largest diameter case as opposed to the original case or with twice the diameter of original case. Increasing the reactor diameter reduces the required bed length for a fixed reactor volume, hence shortening the gas flow path in axial direction and limiting cumulative temperature rise in localized regions. The results suggest a multistage reactor could potentially help in reducing hot spots formation.

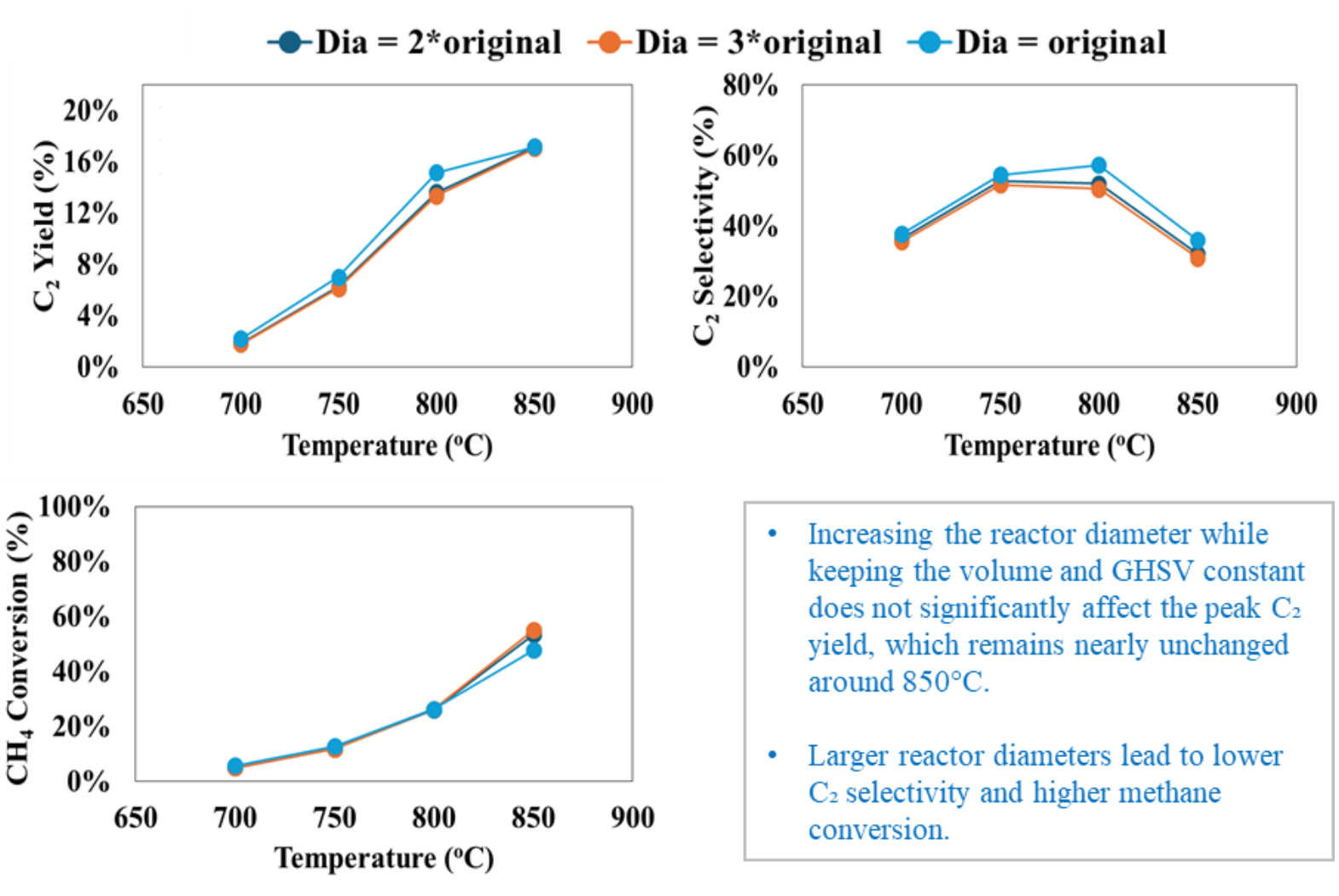

Figure 32. C_2 yield, selectivity and CH_4 conversion for the diameter sweep.

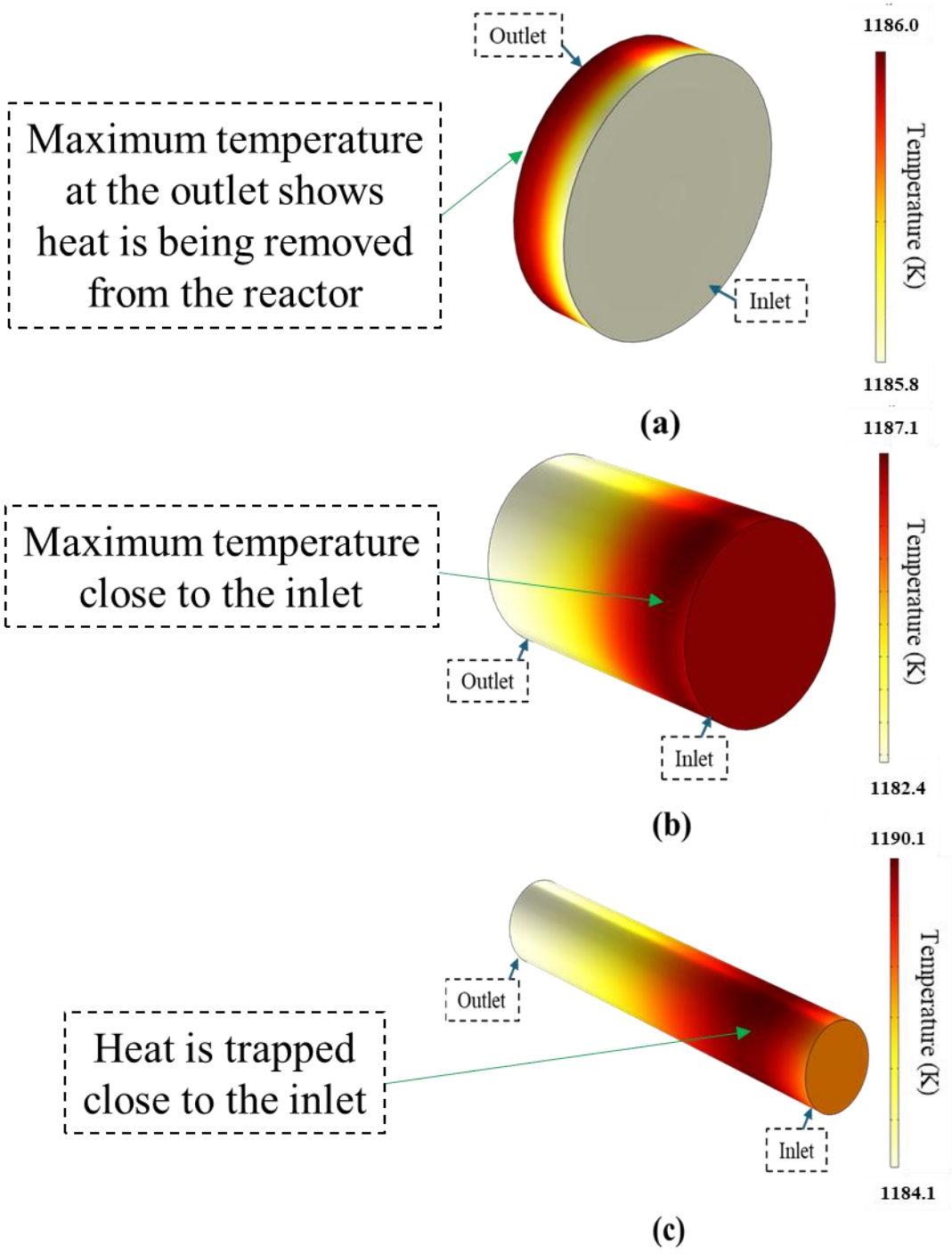

Figure 33. Temperature profile for the diameter sweep (a) Diameter = 3 × original diameter (b) Diameter = 2 × original diameter (c) Diameter = original.

5.2.2. Second Stage of Simulations

The results from 1st stage of simulations suggest that the C_2 yield can be improved by increasing the oxygen availability across the length of the reactor at an expense of decrease C_2 selectivity. However, the C_2 selectivity can be improved by increasing the CH_4/O_2 ratio and GHSV. For this reason, the second round of simulations is conducted mainly focusing on the mole fractions of CH_4, O_2 and N_2 at inlet. Moreover, the temperatures selected for the 2nd round are 800, 825 and 850 ºC as the first round resulted in maximum yields within this range.

Figure 34 shows ternary diagrams across CH_4, O_2 and N_2 mole fractions at inlet for the C_2 yield and selectivity at 800, 825 and 850 ºC temperatures and 1125 mL/hg GHSV. Figure 34a shows that a maximum C_2 yield of 20.4% is achieved at 825 ºC at an inlet CH_4/O_2 ratio of 1.71. This ratio is lower than the original CH_4/O_2 ratio of 3.16 at 825 ºC where the C_2 yield is 19.15%. Therefore, an increase of 1.25 percentage points is observed in the C_2 yield. However, the C_2 selectivity drops to 44.6% at this CH_4/O_2 which is a 7.17 percentage points decline from the original case. The ternary diagrams for the C_2 selectivity are shown in Figure 34b. The maximum C_2 selectivity of 66.7% is observed at a CH_4/O_2 ratio of 6.5 at 800ºC. This is an increase of 7.7% from the original case. However, the C_2 yield at this ratio is 15.72% which is 0.18% less than the original case.

The ternary diagrams indicate two best case scenarios. The first one is the highest C_2 yield point at 825ºC, CH_4/O_2 ratio of 1.71 whereas the second one is the highest C_2 selectivity point at 800 ºC and CH_4/O_2 ratio of 6.5. Further analysis in terms of whether the

highest yield or selectivity point should be adapted for the optimum performance of the OCM reactor at a system level.

Furthermore, ternary diagrams for the 1400 mL/hg GHSV are also plotted and shown in Figure 35. At this GHSV, the maximum C_2 yield is 20.24% at 825 ºC and a CH_4/O_2 ratio of 1.32 as shown in Figure 35a. This C_2 yield is 1.09 percentage points higher than the yield of the original case. The C_2 selectivity at this ratio is 47.53% which is 4.24 percentage points lower than the selectivity of the original case. The highest C_2 selectivity point at 1400 mL/hg GHSV is found at 800 ºC and CH_4/O_2 ratio of 5.94 as shown in Figure 35b. This selectivity is 11.93 percentage points higher than the original case. However, the C_2 yield is 14.41% which is 1.49 percentage points lower than the original case.

Figure 36 shows the ternary diagrams for the 2500 mL/hg GHSVs. At this high GHSV, the maximum C_2 yield of 19.51% is obtained at 850 ºC, as shown in Figure 36a, which is higher than the 1125 and 1400 mL/hg GHSVs where maximum yields were obtained at 825 ºC temperatures. However, at 2500 mL/hg GHSV, the C_2 selectivity at maximum yield point is 52% which is higher than the previous GHSVs. The maximum C_2 yield occurs at a CH_4/O_2 ratio of 2.25. The maximum C_2 selectivity i.e., 76.8% occurs at 800 ºC at a CH_4/O_2 ratio of 8.9 as shown in Figure 36b. However, the C_2 yield at this point is only about 10%. Moreover, a very high CH_4/O_2 ratio of 8.9 poses a likelihood of coke deposition.

Figure 37 shows a comparison of the best case scenarios for GHSVs of 1125, 1400 and 2500 mL/hg. The highest C_2 yields for 1125 and 1400 GHSVs occur at 825 ºC and for 2500 ml/hg at 850ºC. For 1125 mL/hg, the highest C_2 yield occurs at a CH_4/O_2 ratio of 1.71,

for the 1400 mL/hg, the ratio is 1.32 and for the 2500 mL/hg, the ratio is 2.25. The C_2 yields at the highest C_2 yield points are 20.4, 20.24, 19.5% and C_2 selectivities at these points are 44.6%, 47.53, 52% for the 1125, 1400 and 2500 mL/hg GHSVs respectively. At 1400 mL/hg GHSV, the yield drops by a small amount i.e., 0.16 percentage points compared to 1125 mL/hg however, the selectivity improves by ~3%.

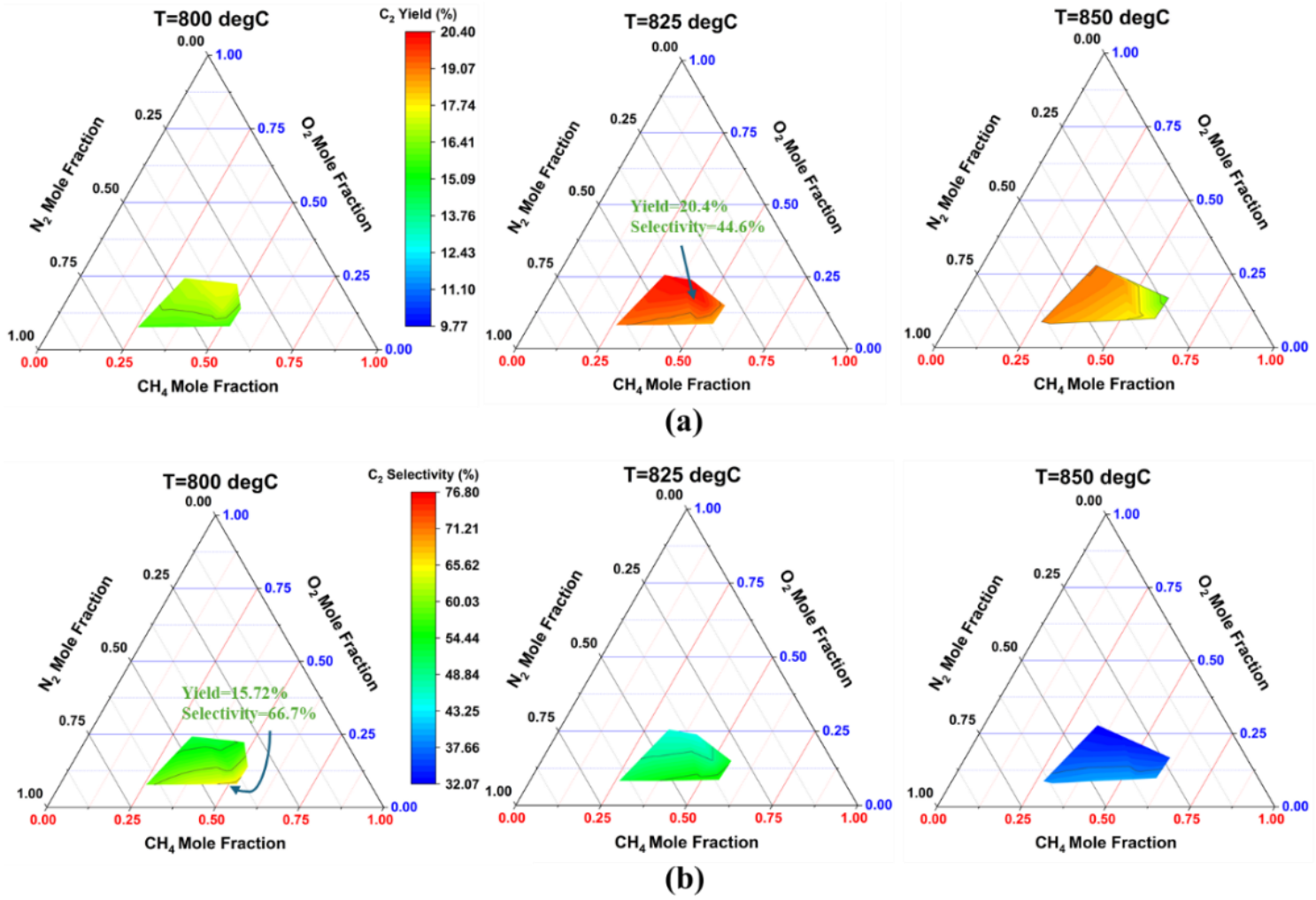

Figure 34. Ternary diagrams for GHSV = 1125 mL/hg (a) C_2 yield (b) C_2 selectivity.

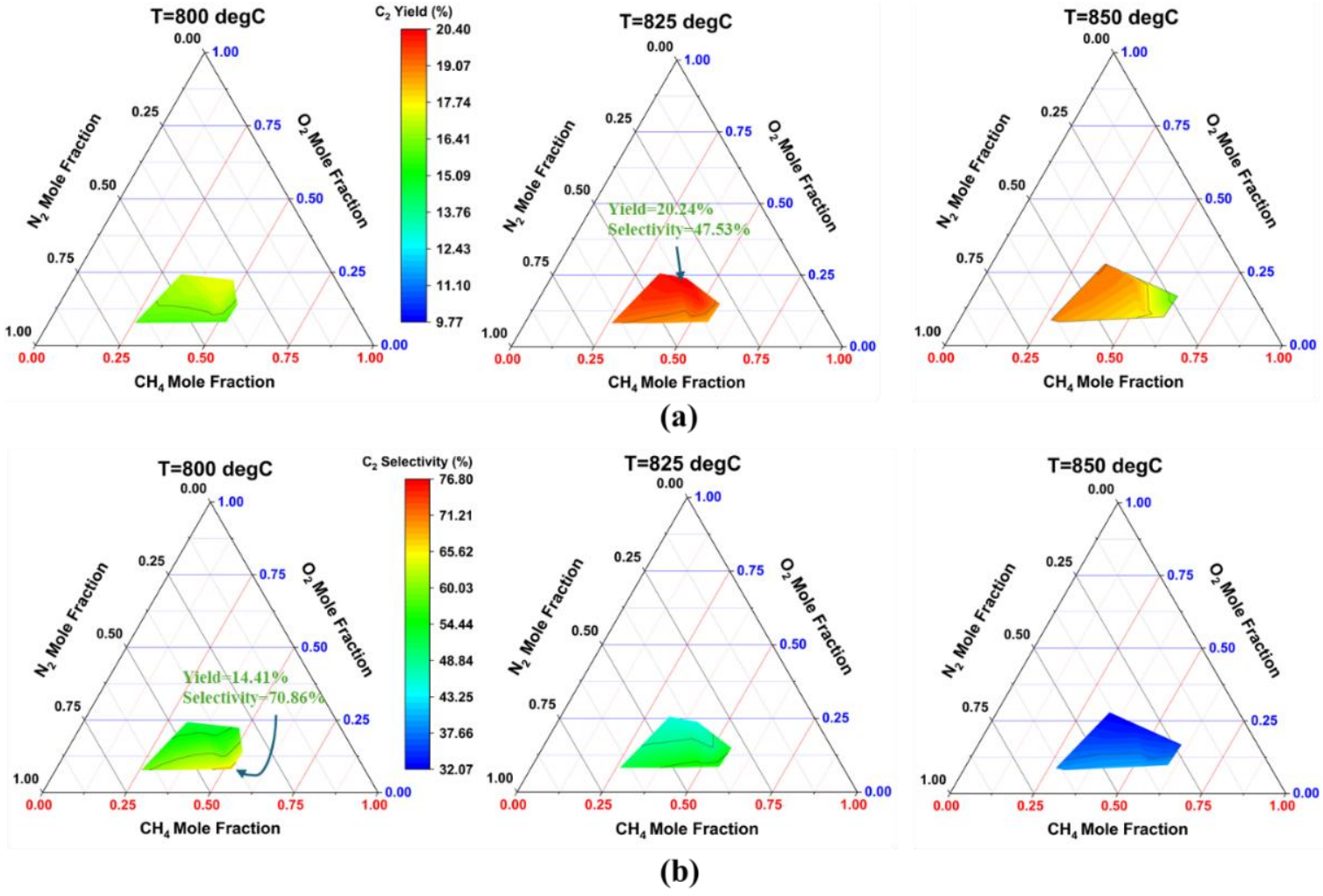

Figure 35. Ternary diagrams for GHSV = 1400 mL/hg (a) C_2 yield (b) C_2 selectivity.

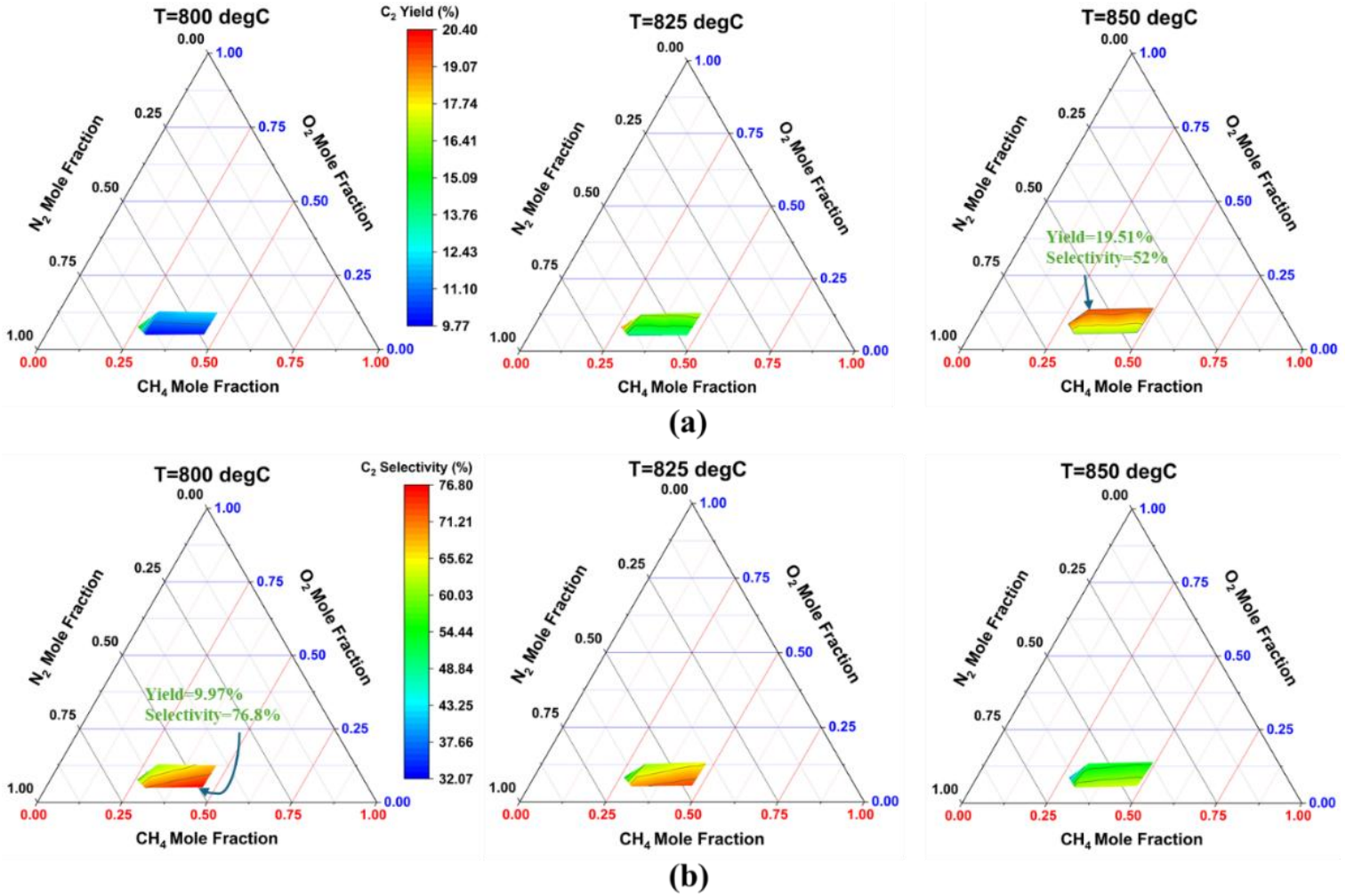

Figure 36. Ternary diagrams for GHSV = 2500 mL/hg (a) C_2 yield (b) C_2 selectivity.

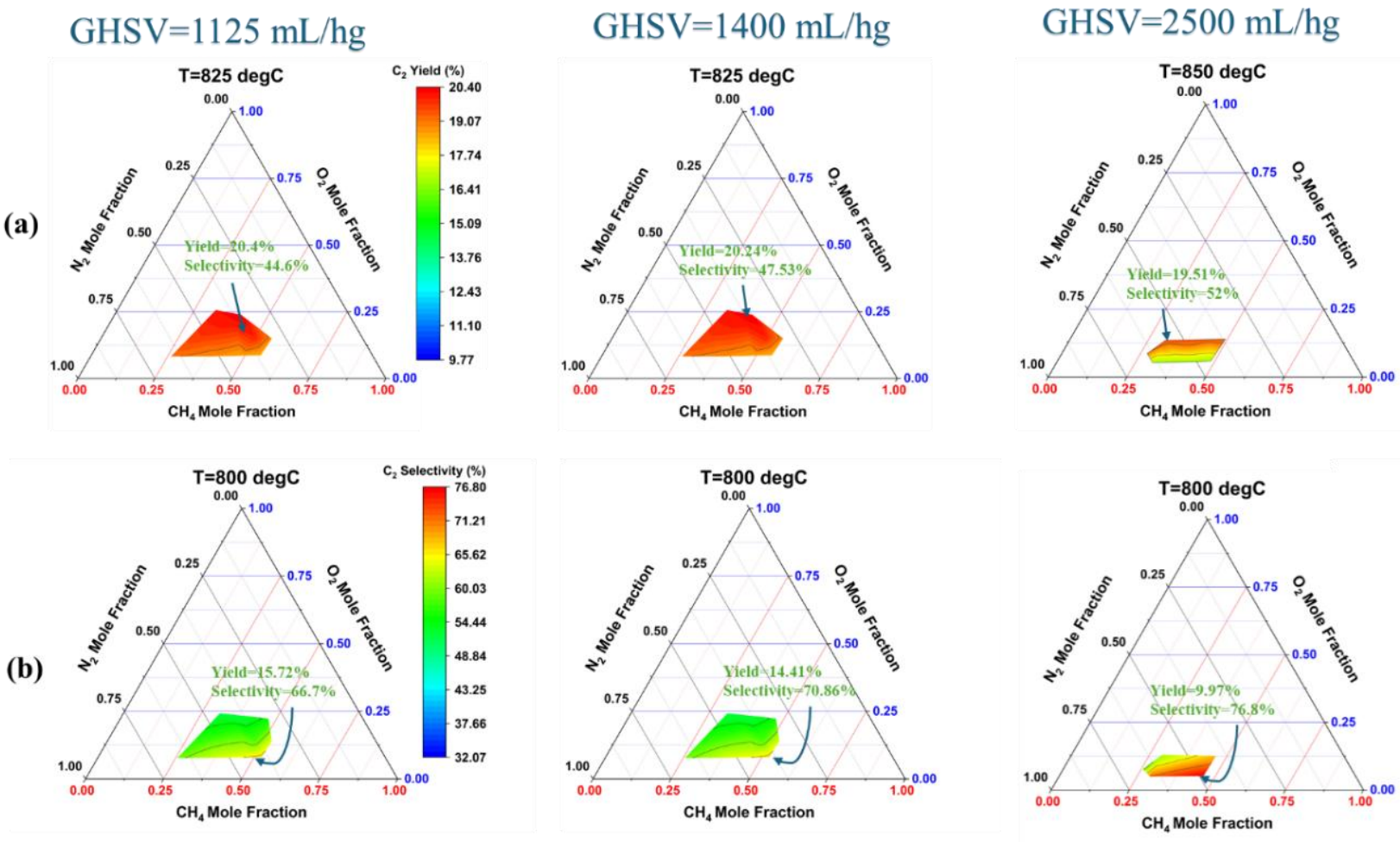

Figure 37. Comparison of the best case scenarios (a) C_2 yield (b) C_2 selectivity.

Chapter 6. System-Level Analysis and Techno-Economic Assessment

This section includes a detailed description of the CL OCM system-level model developed in Aspen HYSYS V14 and the TEA associated with the CL OCM/CO_2-H_2O splitting process. The model includes all major equipment required for the CL OCM process. Moreover, it is assumed that the CO_2-H_2O splitting cycle will not require any additional equipment since the unreacted CO_2 (if any) can be recovered through the CO_2 removal section used for the OCM cycle. A schematic diagram for both the cycles is presented in Figure 38.

At first, a brief literature review is presented regarding the system-level modeling and TEA of the OCM technology. Then the model description, including the model assumptions, are described followed by the TEA methodology and process optimization using methane recycling. A TEA based sensitivity analysis has also been included to show how different parameters can affect the model predictions.

6.1. Background and Literature Review

There have been few TEA studies on OCM in the past mainly comparing the OCM performance with conventional ethylene production technologies such as ethane/naphtha steam cracking. Spallina et al. [17] performed a TEA varying the heat management strategy, syngas dilution, fuel composition, O_2 purity and CH_4/O_2 ratio for the reactor.

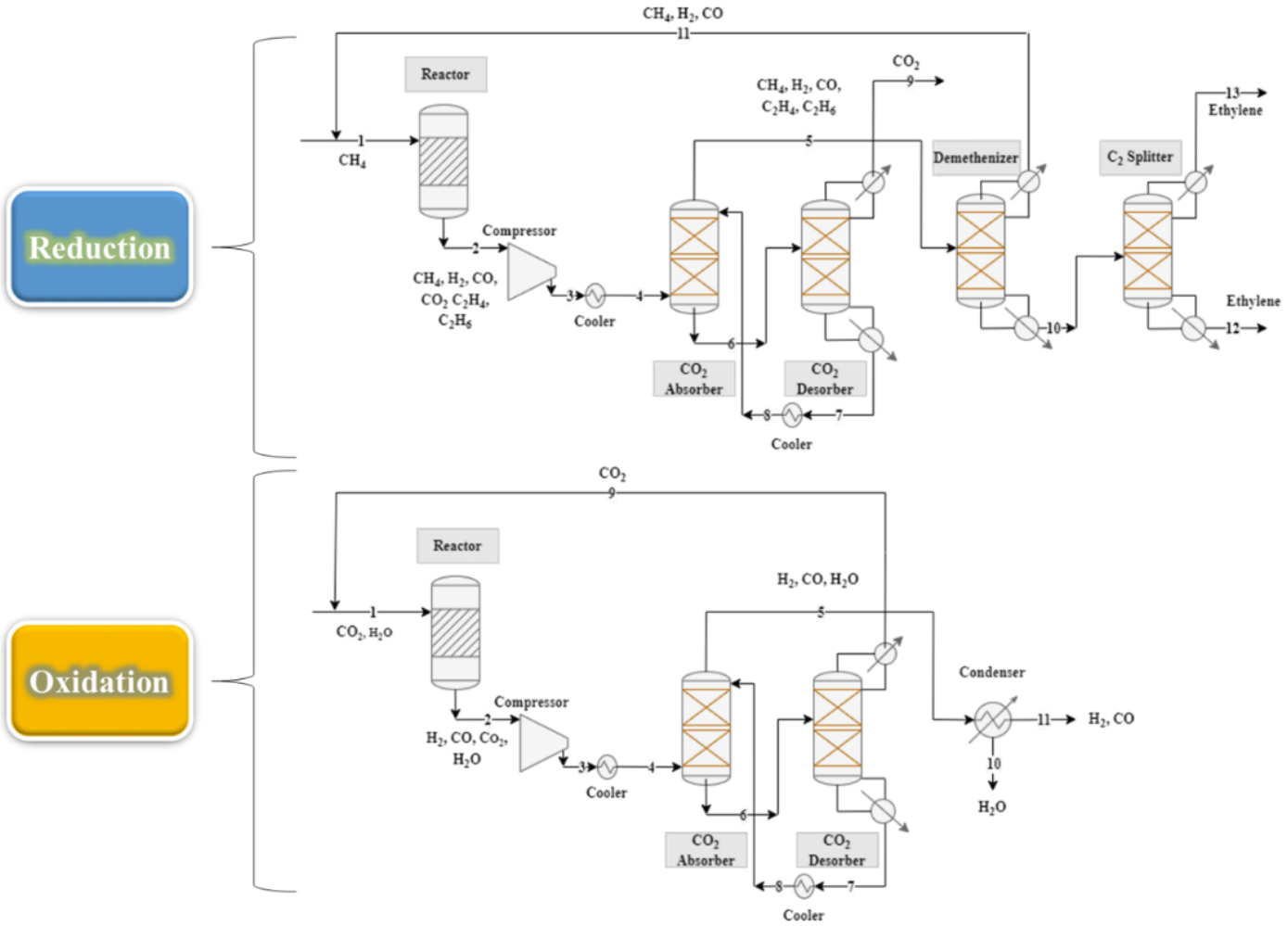

Figure 38. Process flow diagrams for CL OCM/CO_2-H_2O splitting.

They utilized the kinetic model of Stansch et al. [63] validated against experiments using W-Mn/SiO_2 catalyst. Their results showed that the naphtha steam cracking plant performed better than the OCM due to higher yield and lower electricity consumption with OCM only being competitive in areas where natural gas cost was low. They highlighted that the cost of refrigeration, particularly in the demethanizer, was by far the most relevant energy cost. Moreover, they showed that the lower temperature i.e., 650 ^oC or two-stage O_2 distribution led to a 15% decreased cost of ethylene.

Chung et al. [181] performed a TEA with three novel process configurations for the coproduction of ethylene and hydrogen using an isothermal, two-stage reactor compared with a single-staged reactor with methane recycle. They performed system-level simulations using Aspen Plus V12 and analyzed unit production cost, net CO_2-eq emissions, energy efficiency and carbon efficiency. They optimized the CH_4/O_2 ratios, eliminated methane recycle loop and introduced alternative separation schemes. The hydrogen produced during the OCM reactions is recovered after CO_2 removal section using the pressure swing adsorption and the unreacted methane was used in a combined heat and power unit integrated with CO_2 capture. Their results showed that the utilization of methane in the combined heat and power unit with CO_2 capture resulted in 55.9% reduction in ethylene unit production cost compared to the benchmark case with methane recycle. Moreover, the net carbon emissions improved by 66.2%. They also showed that the methane feedstock cost, hydrogen selling price and CH_4/O_2 ratios were the dominant economic drivers.

Ortiz-Espinoza et al. [182] evaluated the profitability and environmental impacts of two methane conversion processes i.e., OCM and Methanol to Olefins (MTO) for ethylene

production using system level model in Aspen Plus. They also performed a sensitivity analysis to analyze the impacts of feedstock and product prices on the profitability of the processes. Their results showed that the MTO had a higher return on investment (ROI) compared to OCM. However, OCM could have an attractive ROI if shale gas prices could be dropped by ~15% and the selectivity of the process could be increased by 5-10%. Moreover, their analysis showed that the heating requirements could be eradicated through proper energy integration and electricity could be produced through co-generation. In terms of environmental impacts, OCM outperformed MTO.

Rosner et al. [59, 164] conducted TEA for OCM and compared it with conventional ethane stream cracker plant. They concluded that the current OCM technology is not competent enough with ethane cracker plant due to its much higher capital and operational costs. However, they recommended that an OCM plant with a single pass conversion of over 60% could become economically viable.

Ashour [57] performed TEA on an integrated OCM plant with a power plant simplified to gas and steam turbines. The study assumed 100% methane conversion and used Aspen Plus simulator for the system-level model. The OCM reactor was a fluidized bed reactor and heat integration techniques were incorporated to ensure efficient energy utilization. The motivation was to eliminate methane recycling and reduce the associated energy consumption. The economic analysis was conducted by Aspen Economic Analyzer. Ashour's results showed that the losses in stand-alone OCM plant can be brought down from 11.6 USD/GJ of methane to 0.84 USD/GJ of methane i.e., 93% reduction in losses associated with OCM as a stand-alone process.

Penteado et al. [60] performed TEA on an integrated OCM plant with a biogas treatment plant. Methane feed was produced by the biogas plant. The cost estimations for the biogas treatment plant were based on literature data whereas the OCM process was simulated in Aspen Plus. A packed bed reactor was used for this study. Their results showed that for a large-scale biogas-based OCM plant the net positive value (NPV) was 741 million USD and discounted payback period (DPP) was 5 years indicating that the approach can be attractive as the integrated process can yield profits within 5 years.

Hugill et al. [64] performed TEA for a co-generation plant where an OCM plant (106 kt/y ethylene) was integrated with a 44 MW power plant. The OCM plant utilized a fluidized bed reactor as recommended by Swanenberg [65]. Their results showed that the co-generation did not help with profitability of the integrated system and energy savings were also not significant. The internal rate of return was 18.82 percentage points less than the conventional naphtha cracking plant. However, the life cycle analysis (LCA) showed that the CO_2 emissions reduced significantly i.e., 29 t/h for the cogeneration plant compared to 45 t/h for naphtha cracker plant with electricity production.

Godini et al. [58] performed TEA on an integrated OCM process with the methane reforming process to produce syngas from unreacted methane of the OCM process. An Aspen Plus OCM model calibrated against experimental data obtained from a UniCat mini plant scale OCM facility established in Berlin Institute of Technology was simulated to optimize the integrated system. The TEA was conducted using Aspen Economic Analyzer. The OCM process used fluidized, membrane and fixed bed reactors over the LA_2O_3/CaO catalyst. The heat generated from OCM can be used for the endothermic dry methane

reforming process. CO_2 obtained from the OCM can be used as a reactant for the methane reforming (dry reforming). Their results indicated a C_2 yield of 35%, methane conversion of 60% (15% higher than conventional OCM), a 40% improvement in heat integration and a 90% CO_2 recovery. Furthermore, they reported lower energy consumption for the integrated system compared to the conventional or stand-alone OCM process.

These studies do suggest that integrating OCM with another chemical reaction system can enhance its performance significantly. However, any of the prior studies do not include TEA analysis specifically for the CL OCM process. The current system-level model and TEA is specifically based on the CL OCM rather than the conventional OCM studies conducted prior. Moreover, the TEA also includes the integrated CL CO_2-H_2O splitting process. In the subsequent sections, the base case is defined first and then further cases are studied based on the percentage of methane recycled. Furthermore, sensitivity analysis is conducted for the feedstock prices and Lang factors to assess the impact of these factors on the suggested economic performance of the integrated CL OCM/CO_2-H_2O splitting technology.

6.2. Base Case (Case 1):

The base case chosen for this study is the highest C_2 selectivity case obtained from the CFD parametric study of the CL OCM reactor. Specifically, the C_2 yield and selectivity for this case are 10% and 76% respectively. The operating temperature and pressure are 800 ^oC and 1.01 bar. However, for the industrial sized reactor, the inlet pressure is assumed to be 15 bar. The CH_4/O_2 ratio of the inlet feed is 8.9. The CH_4/O_2 ratios equal to 9 or even up to 13 have been utilized in many previous studies to improve the C_2 selectivity of OCM,

suggesting that the current CH_4/O_2 ratio is feasible for the CL OCM reactor in terms of coke deposition [58, 172, 183-185].

The kinetic model of Stansch et al. [63] was integrated in Aspen HYSYS V14 and calibrated to achieve C_2 yield and selectivity within ±5% (10.76% and 72%) of the considered case from reactor parametric study. A reactor size of 147 m^3 and C_2 production capacity of 1 million tonne/year are chosen based on previous studies for the industrial scale OCM plant [3, 17, 49]. This production capacity would later be divided in half considering that half of the plant run time would be dedicated to CO_2-H_2O splitting.

The system-level model developed for this study includes all the major equipment shown in the Figure 38 and also includes minor equipment such as heat exchangers, compressors, separators etc. The air separation unit is not included since it is not needed for the CL OCM as oxygen is made available through the catalyst. The integrated CL OCM/CO_2-H_2O splitting process can produce approximately 1 million tonnes of C_2 products and syngas per year considering 50% plant dedication to the CL OCM cycle and 50% to the CL CO_2-H_2O splitting cycle.

The current TEA is based on a system-level simulation of OCM cycle in Aspen HYSYS and a qualitative assessment of the integration of CO_2-H_2O splitting process considering 30% syngas yield. The reason for qualitative assessment of the CO_2-H_2O splitting cycle is that the process does not face selectivity issues similar to the OCM cycle and the CO_2 conversions as close to near-complete are reported in literature [186-188]. Moreover, since OCM is an exothermic process, it can provide the energy demand to keep reactor temperatures suitable for the CO_2-H_2O splitting cycle. Therefore, in the present TEA,

the CO_2-H_2O splitting cycle is considered at a conceptual integration level and its additional capital costs are regarded unnecessary and not explicitly included. The key streams and their relative mass flow rates at representative stages for the base case are shown in the Table 8 and Figure 39. These also list the pressures and temperatures at each stage.

The system-level model developed in this study did not explicitly include detailed utility cycles such as individual cooling-water loops, fired heaters or other auxiliary utility systems and Aspen Economic Analyzer was used for utilities' cost estimation. Furthermore, Aspen Energy Analyzer indicated that further heat integration could potentially improve the process energy performance up to approximately 10%. Therefore, significant reductions in external utility requirements are expected, which would further decrease the LCOP. In addition, CO_2 recycling for the CO_2-H_2O splitting cycle was not considered in the current model. Cycling unconverted CO_2 would further reduce fresh CO_2 demand and contribute to additional LCOP reductions.

The levelized cost of products (LCOP), considering 85% plant capacity, is calculated as the target performance metric for the economic evaluation of the proposed technology [189]. Moreover, the C_2 yield of the process was collected from the parametric study of the reactor model. Since the CL process involves oxidation cycle with CO_2-H_2O splitting process, a qualitative assessment of LCOPs dedicating half of the run time to CO_2-H_2O splitting process and with a syngas yield of 30%, was conducted. The feedstock for CO_2-H_2O splitting also includes recycled CO_2 from the OCM cycle which further reduces the LCOP.

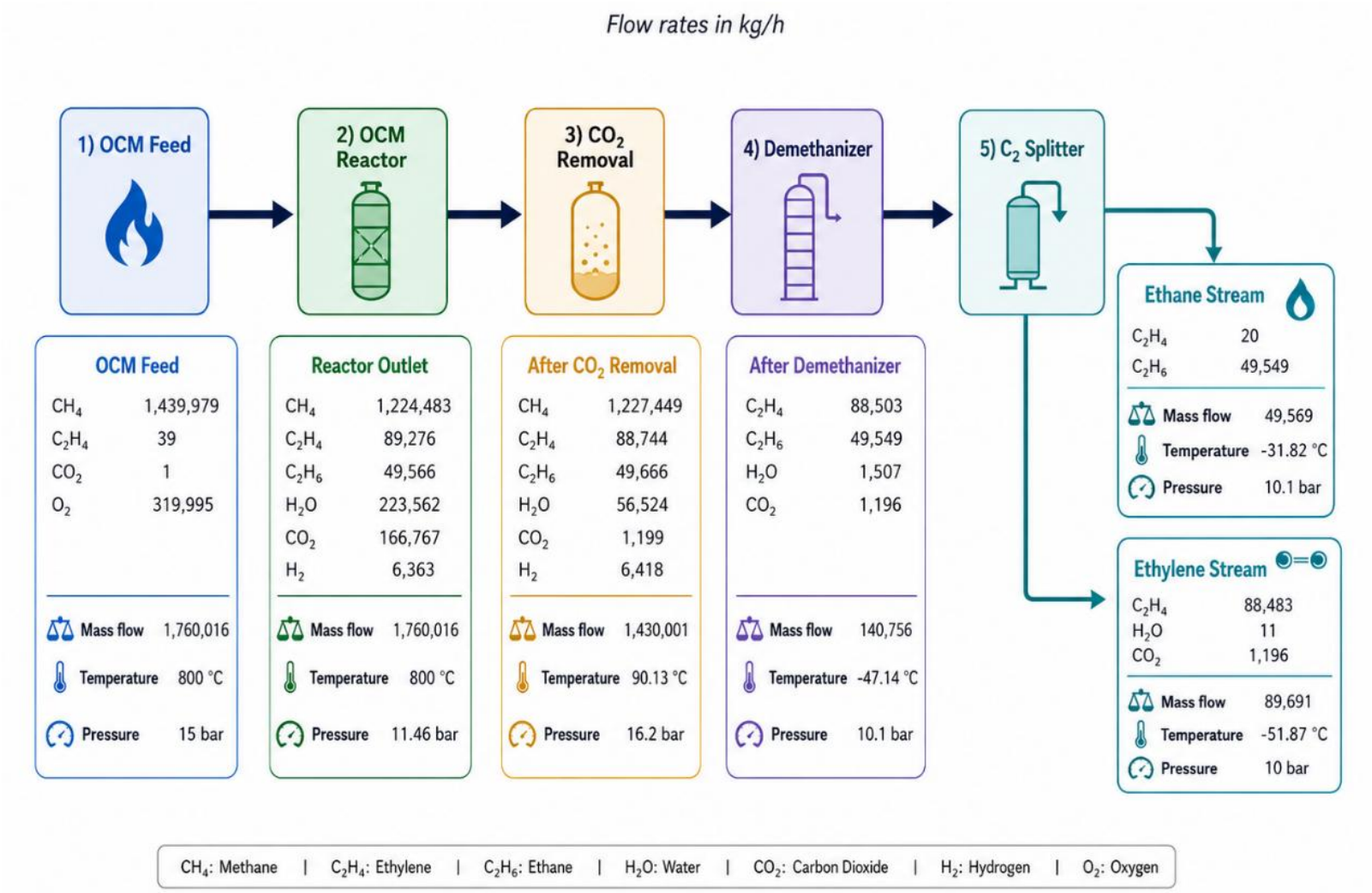

Figure 39. Snapshot of the Aspen HYSYS Model.

Table 8. Key streams for the CL OCM process after major equipment.

Component	Units	OCM Feed	Reactor Outlet	CO_2 Removal	Demethanizer	Ethane	Ethylene
Methane	kg/h	1,439,979	1,224,483	1,227,449	0	0	0
Ethylene	kg/h	39	89,276	88,744	88,503	20	88,483
Ethane	kg/h	0	49,566	49,666	49,549	49,549	0
Water	kg/h	0	223,562	56,524	1,507	0	11
Carbon dioxide	kg/h	1	166,767	1,199	1,196	0	1,196
Carbon monoxide	kg/h	0	0	0	0	0	0
Hydrogen	kg/h	0	6,363	6,418	0	0	0
Oxygen	kg/h	319,995	0	0	0	0	0
Mass Flow	kg/h	1,760,016	1,760,016	1,430,001	140,756	49,569	89,691
Temperature	°C	800	800	90.13	-47.14	-31.82	-51.87
Pressure	Bar	15	11.46	16.2	10.1	10.1	10

6.2.1. Modeling Assumptions

A system-level model is developed to simulate the CL OCM process and establish mass & energy balances. A simplified schematic of the process is shown in Figure 38 and is modeled using Aspen HYSYS V14 software, leveraging existing model libraries and literature for reactors and separation units. A snapshot of the Aspen HYSYS model is shown in Figure 40. Key design assumptions and methods include the following.

- The model is based on a commercial-scale OCM plant designed to produce 1 million tonnes of C_2 products per year considering 7500 operational hours (capacity factor of 85%) of the plant.
- There was mainly one performance configuration utilized as suggested by the parametric study of reactor operation. Specifically, this configuration was a C_2 yield of ~10.7% and selectivity of ~72% in the OCM reactor. This case is selected as it allows for higher methane recycling percentages due to the lower hydrogen accumulation.
- The model assumes natural gas as pure methane and the primary feedstock for OCM. The oxygen presence was simulated using pure oxygen present in the feed instead of using oxygen from catalyst surface for simplicity.
- Aspen Economic Analyzer was used to estimate cost associated with the utility requirements.

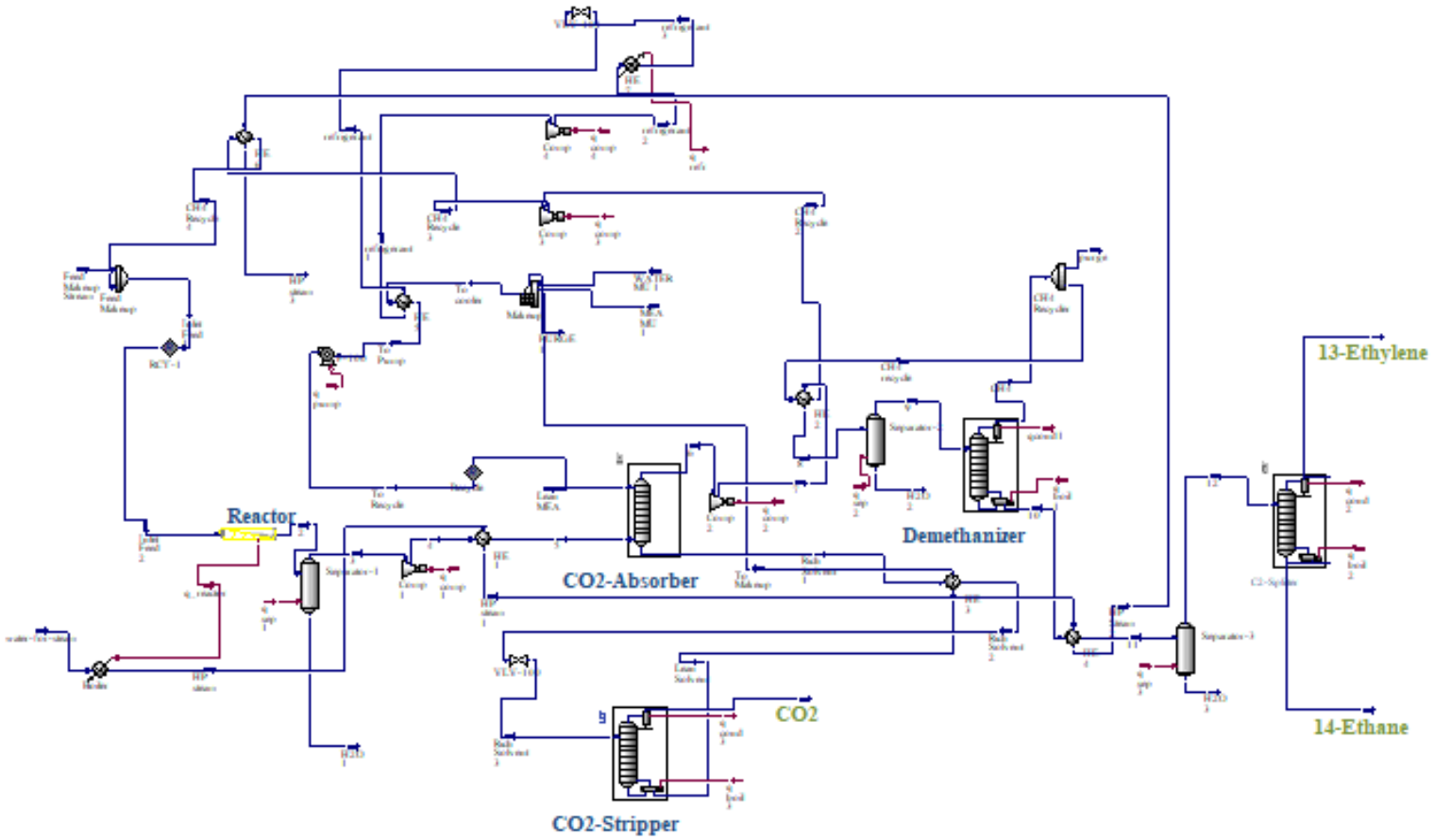

Figure 40. Snapshot of the Aspen HYSYS Model.

6.2.2. Capital Cost Estimation

The total capital cost (CAPEX) or total overnight cost (TOC) for the plant includes all major process equipment (reactor, distillation columns, etc.) and balance of plant (BOP) equipment, installation, indirect costs, contingency, and owner's costs. All costs are expressed in 2026 dollars. The Aspen Economic Analyzer estimations were updated to reflect 2026 pricing [59].

The Lang Factor method was used for fixed capital cost, where the sum of delivered or purchased equipment costs is multiplied by an empirical factor to approximate the capital cost. This approach is commonly used for early-stage process-industry estimates when detailed engineering data are limited. For this study, a Lang Factor of 4.8 is considered [190-193].

The sum of all equipment costs constitutes the Direct Plant Cost (DPC). In addition, Indirect Costs (IC) for engineering, procurement, and construction management services are added. IC is estimated as roughly 14% of DPC based on the United States Department of Energy (US DOE) guidelines [17]. Adding DPC and IC yields the Engineering, Procurement and Construction Cost (EPC) of the project. Contingency and Owner's Costs are included as 15% of EPC to cover both contingency (10%) and owner's (5%) costs [17]. When added to EPC, this gives the Total Overnight Cost (TOC). Financing & Construction Period related assumptions are listed in Table 9 which resulted in a Capital Charge Factor (CCF) of 0.08 [59].

Table 9. Financial assumptions.

Parameter	Value
Operating period	30 years
Capital expenditure period (400,000 MTPY plant)	4 years
Reference construction period (1,500,000 MTPY Pennsylvania plant)	4 years
Distribution of capital expenditure (overnight capital)	Year 1: 20%, Year 2: 35%, Year 3: 25%, Year 4: 20%
Depreciation method	150% declining balance
Depreciation period	20 years
Equity percentage	45%
Debt percentage	55%
Real dollar cost (equity)	7.84%
Real dollar cost (debt)	2.94%
After-tax weighted average cost of capital (WACC)	4.74%
Federal tax rate	21%
State tax rate	6%
Investment tax credits	Not considered
Tax holidays	0 years
Capital Charge Factor (CCF)	0.080

6.2.3. Operating Cost Estimation

Annual operating costs (OPEX) are dominated by the feedstock expense, with additional contributions from utilities (electricity, HP steam, and refrigerant), catalyst & MEA makeup, labor and maintenance. Operating costs (OPEX) are estimated on an annual basis, including both variable costs (feedstock, utilities, and consumables) and fixed costs (labor, maintenance). We assumed a cost of 165 $/tonne (3.5 $/MMBtu) [194]. This cost dominates the OPEX. When including CO_2-H_2O splitting, this feedstock is divided in half by CO_2 which is priced at 50 $/tonne [189]. Furthermore, CO_2 recovered from the OCM cycle is also recycled for the CO_2-H_2O splitting cycle reducing the fresh CO_2 feedstock requirement by ~8% for each case.

Main utilities are electricity, refrigerant (propane) and high pressure (HP) steam. The cost of utilities is estimated on the basis of the Aspen Economic Analyzer provided rates. The catalyst/oxygen carrier (Na-$LaMnO_3$) needs replacement over time and will need periodic makeup. We assumed a carrier lifetime of ~1 year, i.e. the entire inventory (165 tonnes in the reactor) might be replaced every year. This is a rough assumption. If carrier life proves longer (e.g. 2-year life), this cost would become half.

100 full-time operators are considered for this plant capacity based on a number suggested by Rosner et al. [59]. At an average fully burdened rate of $75,000/year + 30% overhead benefits, the annual labor cost is calculated. Maintenance (materials and labor for upkeep) is taken as 4% of the capital cost per year. Administrative overhead at 20% of direct labor to account for plant management, support staff, etc. is also included.

6.2.4. Economic Analysis Metrics

The primary metric is the LCOP, in $/tonne and is calculated by combining the annualized CAPEX and annual OPEX, then dividing by the annual ethylene, ethane and syngas production as shown in Equation 38 [189].

$$\text{LCOP}\left(\frac{\$}{\text{tonne}}\right) = \frac{(\text{CAPEX}+\text{OPEX})_y * 1000}{\text{h} * \dot{m}} \quad (38)$$

Here, the subscript y represents per year, h is the total annual hours of operation i.e., 7500, $\dot{m}$ is the production rate of ethane, ethylene and syngas in kg/h.

6.3. Results

In this section, the effects of methane recycling on the process yield and LCOP are explained in detail specifically with 0%, 30%, 40% and 60% recycled methane. The process yield is calculated only for the OCM cycle whereas the LCOP is calculated for the complete CL OCM/CO_2-H_2O splitting process. Complete details of the effects of each cost component on the LCOP for each case are provided.

6.3.1. Effect of Recycling on LCOP

For the recycling, the methane separated from the product stream after the demethanizer is mixed with a fresh methane stream before being fed to the reactor. One of the drawbacks of the recycled stream is the presence of hydrogen in it, which can accumulate in the reactor as the percentage of recycling increases. In the following sections, each recycling case is discussed in detail.

6.3.1.1. Case 1: 0% Methane Recycled

In this case, the levelized cost is the maximum. The inlet feed does not contain any other gases than methane and oxygen. The LCOP is 1595 $/tonne which is higher than the initial target of 1000 $/tonne of products set up in the Section 3 [195].

It is to be noted that the cost would have been much higher if the OCM was treated as a stand-alone process since the price of CO_2 feedstock is much less compared to methane i.e., approximately 3 times less. The LCOP would be 2140 $/tonne i.e., ~35% higher for the stand-alone OCM process compared with the integrated CL OCM/CO_2-H_2O splitting technology. This cost of ethylene (stand-alone OCM process) is comparable with the previously reported values by Spallina et al. and Rosner et al. [17, 59]. However, a direct comparison is not possible with these studies considering different process yields, conversions and selectivities reported.

The reason for such high cost is the selection of low C_2 yield point i.e., ~10.7% C_2 yield. For the case with 20% C_2 yield, this cost would have been much lower however, methane recycling might not be feasible in this case as opposed to the selected C_2 yield case. The LCOP reduction by integration of CO_2-H_2O splitting substantiates the significance of the novel integrated technology in terms of the profitability. Table 10 summarizes the capital cost breakdown.

Table 10. Capital cost breakdown for the CL OCM/CO_2-H_2O splitting.

Equipment	Total Volume (m^3)	Cost (USD)
BOP Equipment		232,329,893
Reactor	147	12,700,800
Demethanizer (60 stages)	2,651	179,809,920
CO_2 Absorber (35 stages)	4,312	463,747,200
CO_2 Stripper (15 stages)	2,121	207,216,000
C_2 Splitter (90 stages)	3,534	233,658,000
MEA		2,123,863
Direct Plant Cost (DPC)		1,331,585,676
Indirect Cost (IC)		186,421,995
Engineering, Procurement and Construction Cost (EPC)		1,518,007,671
Contingency and Owner's Cost (C&OC)		227,701,151
Total Overnight Cost (TOC)		1,745,708,821
CAPEX/year		**139,656,706**

Figure 41 provides a breakdown and summary of the CAPEX. The annualized CAPEX is ~139.7 Million USD. DPC contributes ~76% to the TOC whereas, for the DPC multiple components contribute to the total amount with the CO2 absorber being the most costly one which contributes ~35% to the total DPC.

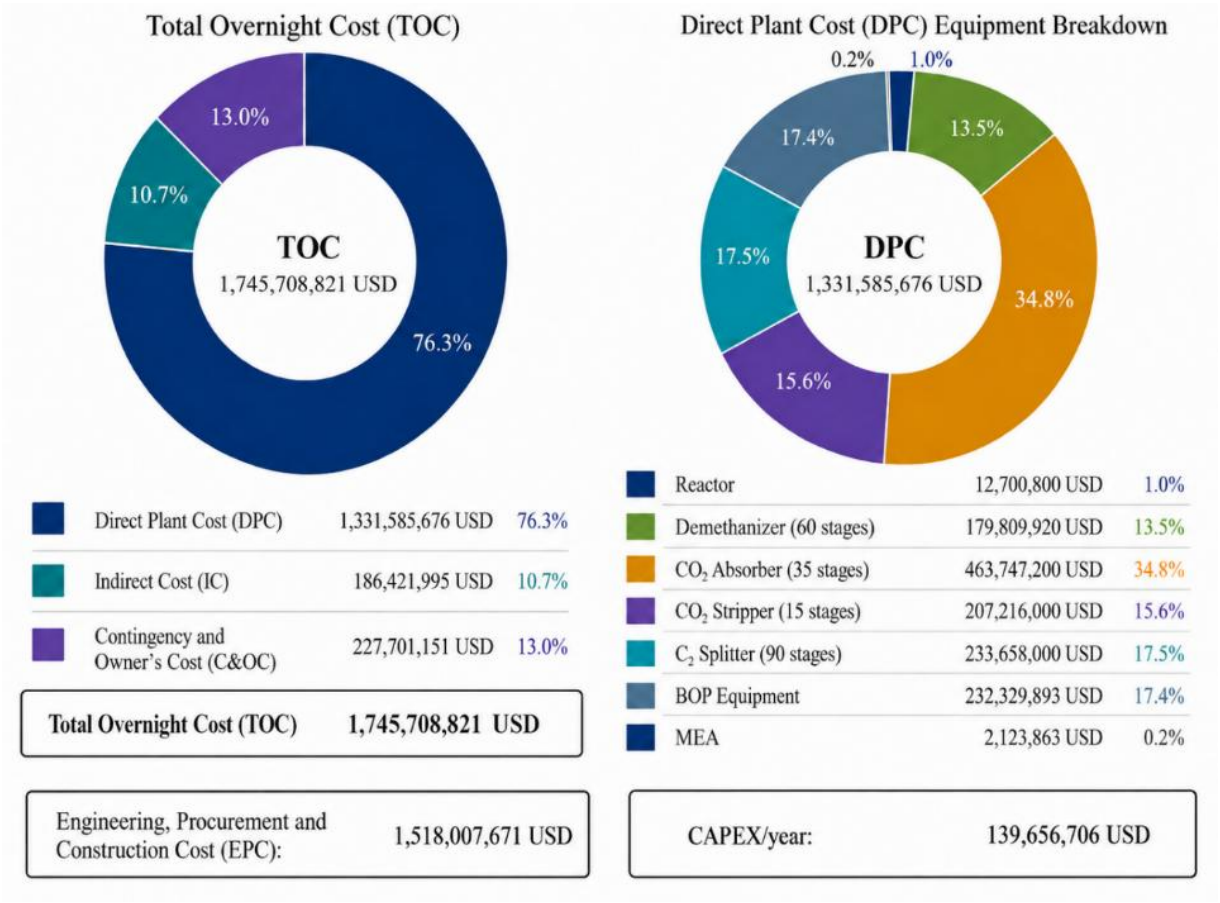

Figure 41. Summary of TOC and DPC for 0% Methane Recycled Case (Case 1) [17, 59].

Table 11. Operational cost breakdown for the CL OCM/CO_2-H_2O splitting.

Category	Rate	Total	Annual Cost (USD)
Feedstock (CO_2)	50 $/tonne	6,333,290 tonne/y	316,664,501
Feedstock (CH_4)	165 $/tonne	5,400,000 tonne/y	891,000,000
Electricity	3,055 $/h	-	22,914,421
HP Steam	16,762 $/h	-	125,713,972
Refrigerant-Propane	12,668 $/h	-	95,013,632
Catalyst replacement	0.3 $/kg	165,375 kg/y	49,613
MEA makeup	1.5 $/kg	6,368,250 kg/y	15,547,500
Labor		-	7,725,000
Maintenance & parts		-	5,586,268
Overhead & admin		-	1,545,000
Total OPEX/year			**1,481,759,907**

Table 11 compiles the operating cost breakdown. Figure 42 provides the breakdown and summary of the OPEX/year. The total OPEX/year is ~1.48 Billion USD which is significantly higher than the CAPEX/year i.e., ~11 times higher. The major cost drivers for the OPEX are methane and CO_2 feedstocks which contribute ~60% and ~21% to the OPEX respectively and 81.5% collectively. Every other cost component contributes to less than

10% of the OPEX with only noticeable contributions of 8.5% and 6.4% by the HP steam and refrigerant. The overall contribution of feedstocks to the OPEX highlights the significance of feedstock prices on the LCOP and given the projected reductions in these prices, LCOP of the CL OCM/CO_2-H_2O splitting technology will reduce further.

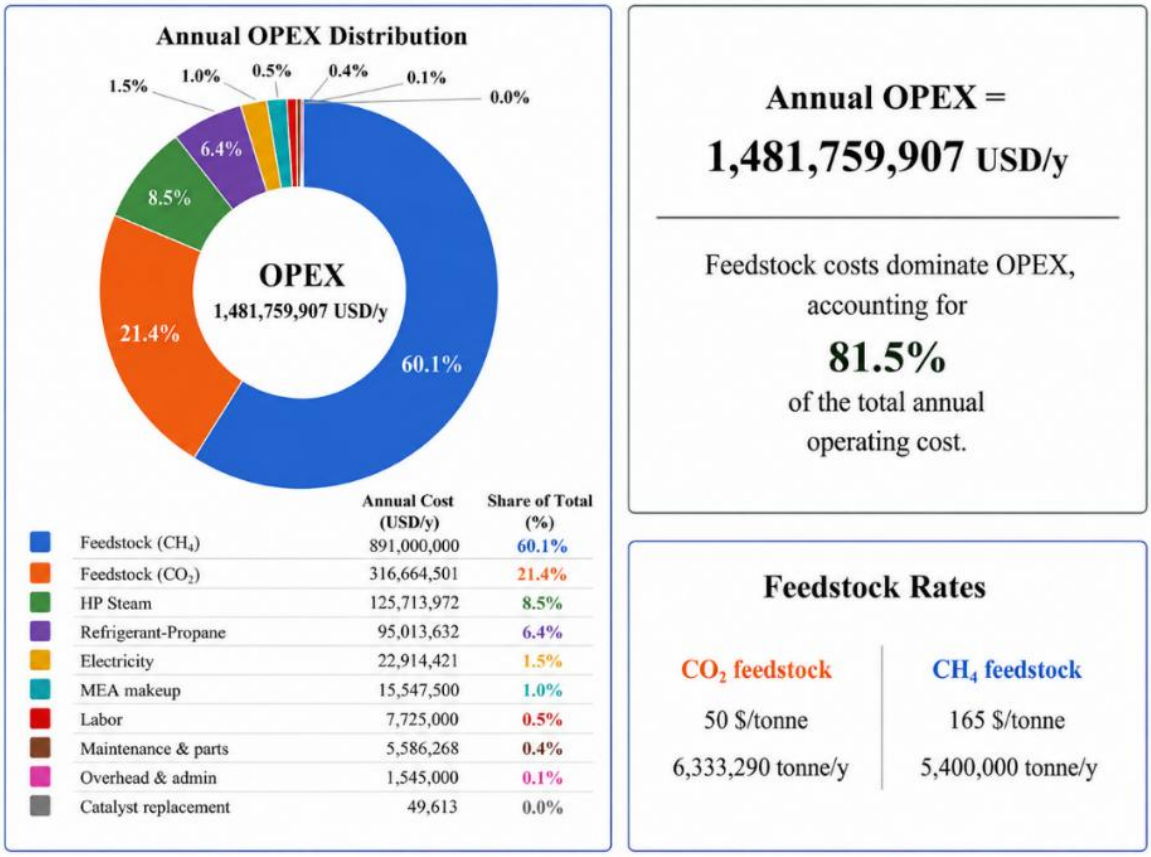

Figure 42. Summary of OPEX for Case 1 [17, 59].

Figure 43 provides the effect of each cost component (including both capital and operational) on the LCOP of the CL OCM/CO_2-H_2O splitting technology. As expected, the LCOP is majorly dependent on the feedstocks with a combined effect of both methane and CO_2 feedstocks contributing to ~74% of the LCOP. Apart from the feedstock costs, the remaining noticeable contributions include annualized CAPEX ~9%, utilities ~15% (HP

steam ~8%, refrigerant-propane ~6% and electricity ~1%). The remaining contributions are less than 1%.

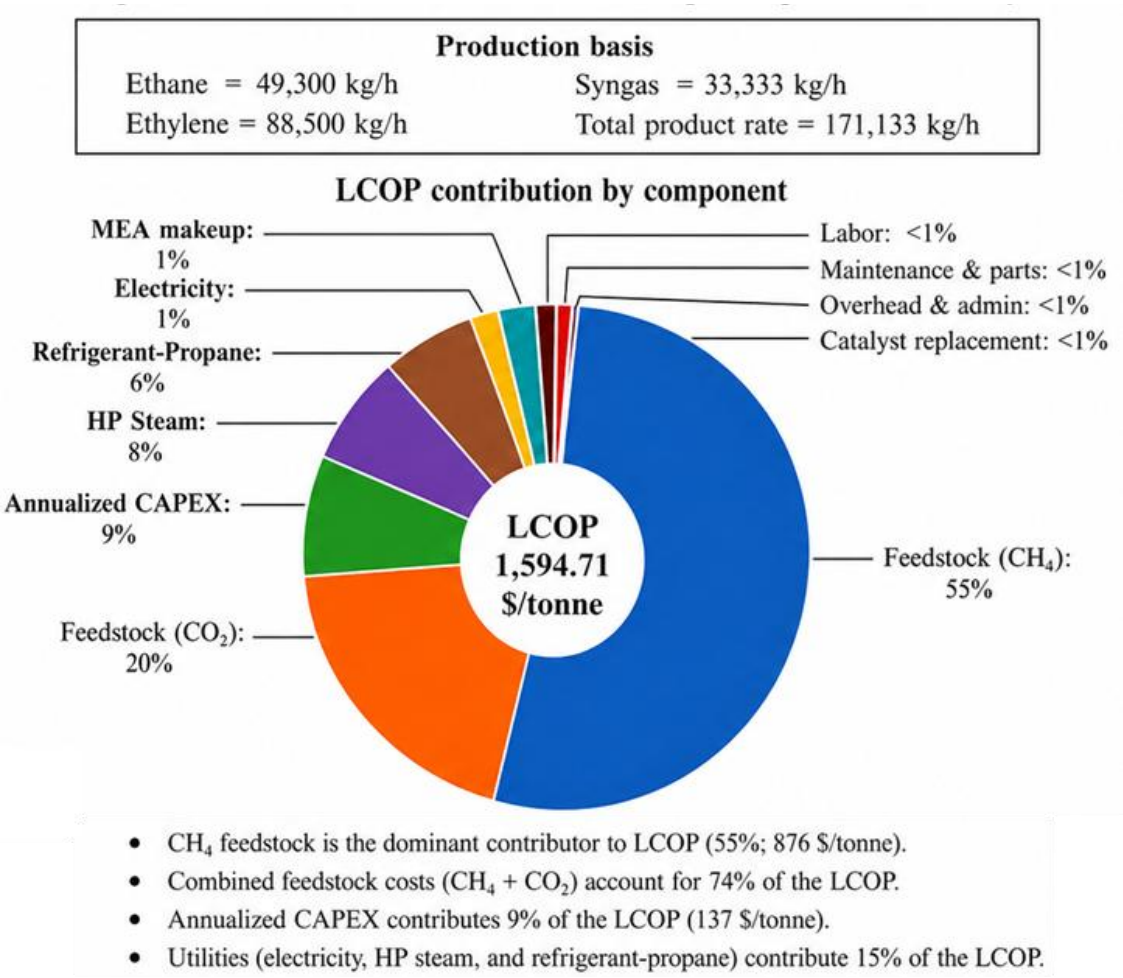

Figure 43. Contribution of cost components to LCOP for Case 1 (0% methane recycled) [17, 59].

6.3.1.2. Case 2: 30% Methane Recycled

In this case, recycled methane is mixed with the inlet feed before being fed to the reactor. The composition of the makeup feed is adjusted to maintain the original CH_4/O_2 ratio and C_2 yield of the reactor. The capital cost is almost similar to the 0% recycle case

with a minor change in the total requirement of the MEA solution. However, the operational cost significantly declines majorly due to the lower requirement of methane feedstock. The LCOP in this case is 1,288 $/tonne of products which is ~19% less than the Case 1.

A breakdown and summary of the LCOP for Case 2 including contributions from all cost components is shown in Figure 44. The feedstocks cost now contributes ~68% of the LCOP which is 6% less than the Case 1. The lower contribution from the feedstocks results in lower overall LCOP. However, the utilities requirements are still comparable with Case 1. Due to a lower LCOP compared to the Case 1, the individual contributions from all cost components are 1-2% higher. Specifically, the annualized CAPEX contribution is ~11% and utilities ~19% (HP steam ~10%, refrigerant-propane ~7% and electricity ~2%). The remaining contributions are either ~1% or lower than 1%.

One drawback of recycling is the accumulation of hydrogen. Since there is 5.7% hydrogen in the recycled stream, it results in lower CH_4/O_2 ratios in the reactor feed. However, this is dealt with by adjusting the makeup feed composition so the CH_4/O_2 ratio is kept in the vicinity of the original value. This resulted in 1.54% hydrogen concentration in the reactor feed. Higher concentrations of hydrogen in the reactor feed can also hinder the process yield by thermodynamically opposing the ethane dehydrogenation to ethylene. Furthermore, hydrogen combustion can occur at hydrogen concentrations close to 4% [196].

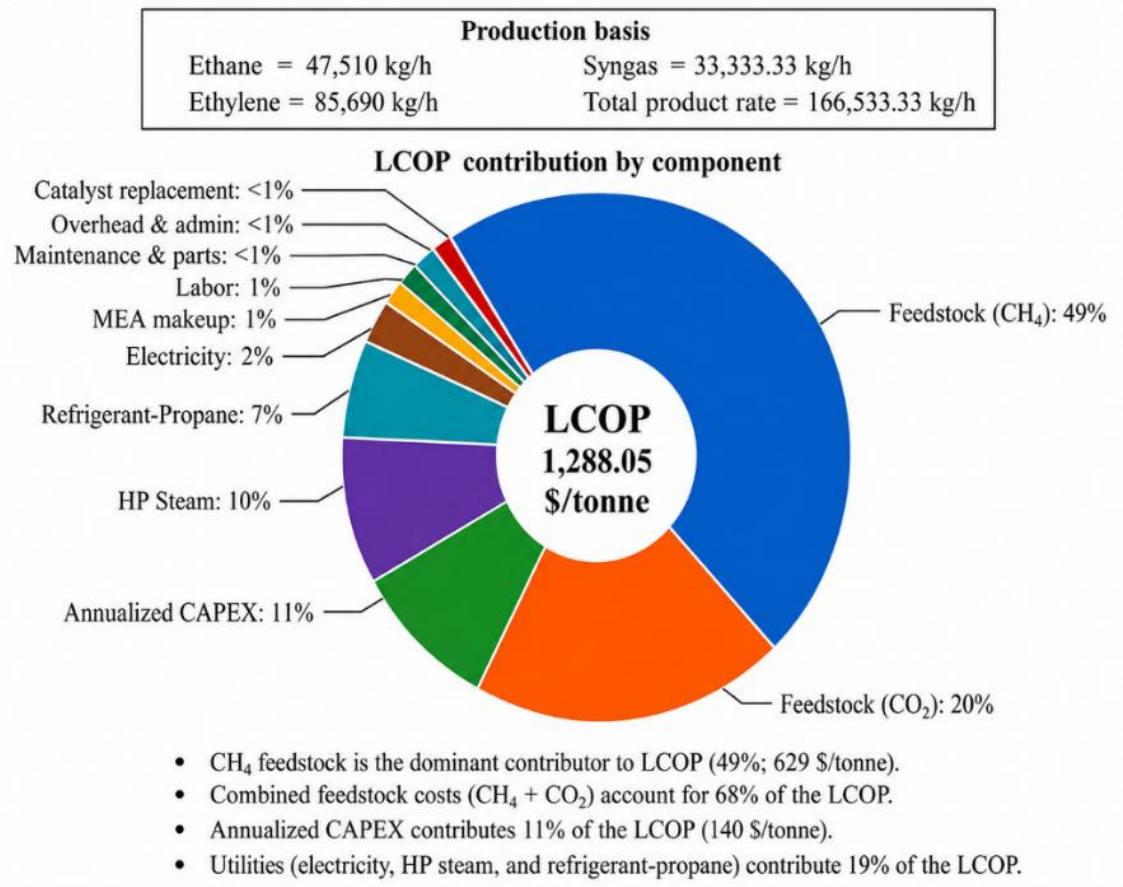

Figure 44. Contribution of cost components to LCOP for Case 2 (30% methane recycled) [17, 59].

6.3.1.3. Case 3: 40% Methane Recycled

For the 40% methane recycled case, the LCOP is 1,138 $/tonne which is ~12% and ~19% less than Case 2 and 1 respectively. The hydrogen concentration in the recycled stream is 7.97% and in the reactor feed is 3.2%. The hydrogen concentration in the reactor feed is still below the flammability limit of hydrogen i.e., 0.8 percentage points lower than 4%. This suggests that a recycled percent slightly higher than 40% can further reduce the LCOP and also ensure process safety. A breakdown and summary of the LCOP for Case 3 is shown in Figure 45. The feedstocks cost now contributes ~64% of the LCOP which is 4% less than

the Case 2 and 10% less than Case 1. There is a slight increase in the individual contributions of annualized CAPEX and utilities. However, the utilities requirements are still comparable with Case 1 and 2. Specifically, the annualized CAPEX contribution is ~12% and utilities ~21% (HP steam ~11%, refrigerant-propane ~8% and electricity ~2%). The remaining contributions are again either ~1% or lower than 1%.

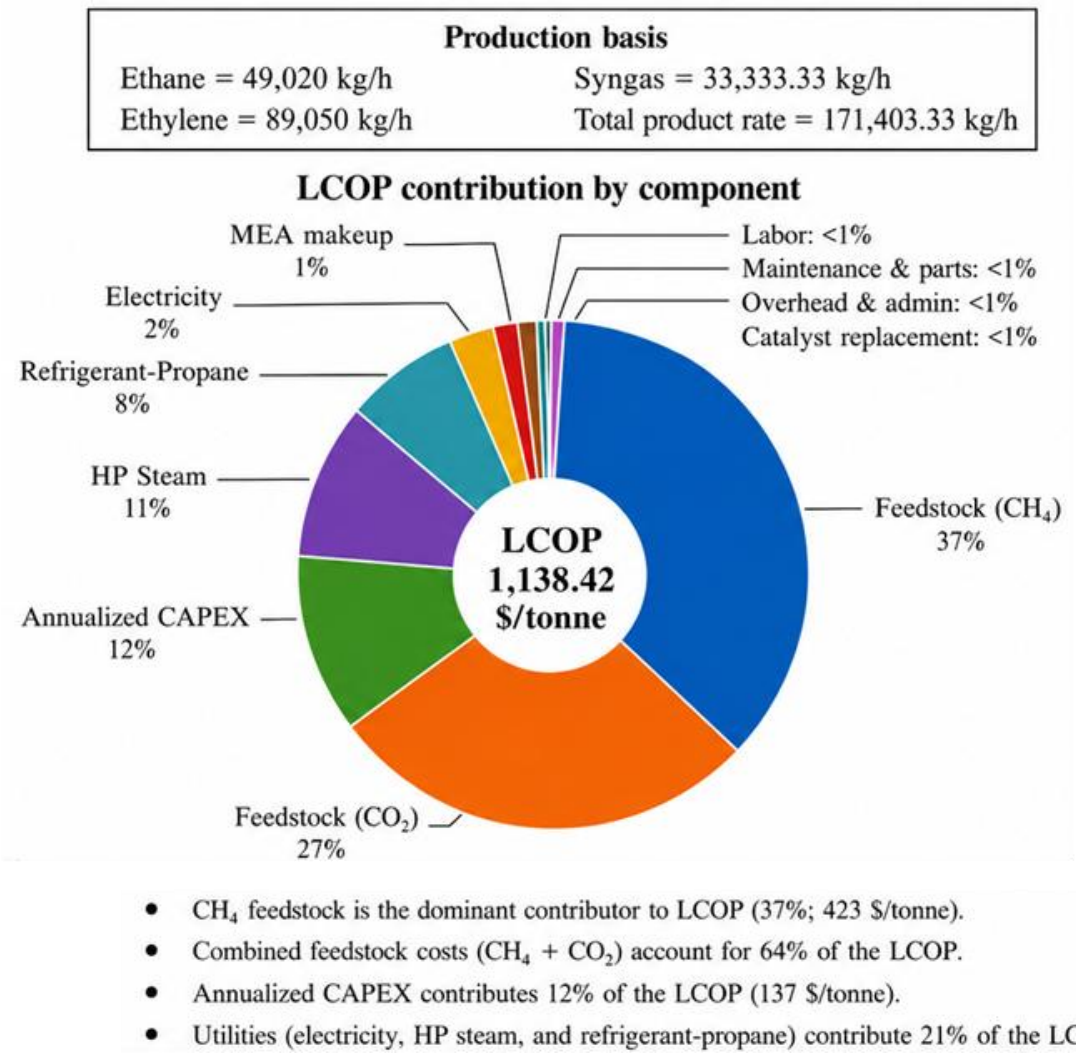

Figure 45. Contribution of cost components to LCOP for Case 3 (40% methane recycled) [17, 59].

6.3.1.4. Case 4: 60% Methane Recycled

The 60% methane recycle case displayed the minimum LCOP i.e., only 1006 $/tonne of products which is ~12% less than Case 3 and ~37% less than Case 1. The hydrogen concentration in the recycled stream is 12.3% which is reduced to 7% at the reactor inlet by the makeup feed. However, since the lower flammability limit of hydrogen is 4%, a concentration of 7% can potentially create safety issues which renders this case impractical for the real life scenario.

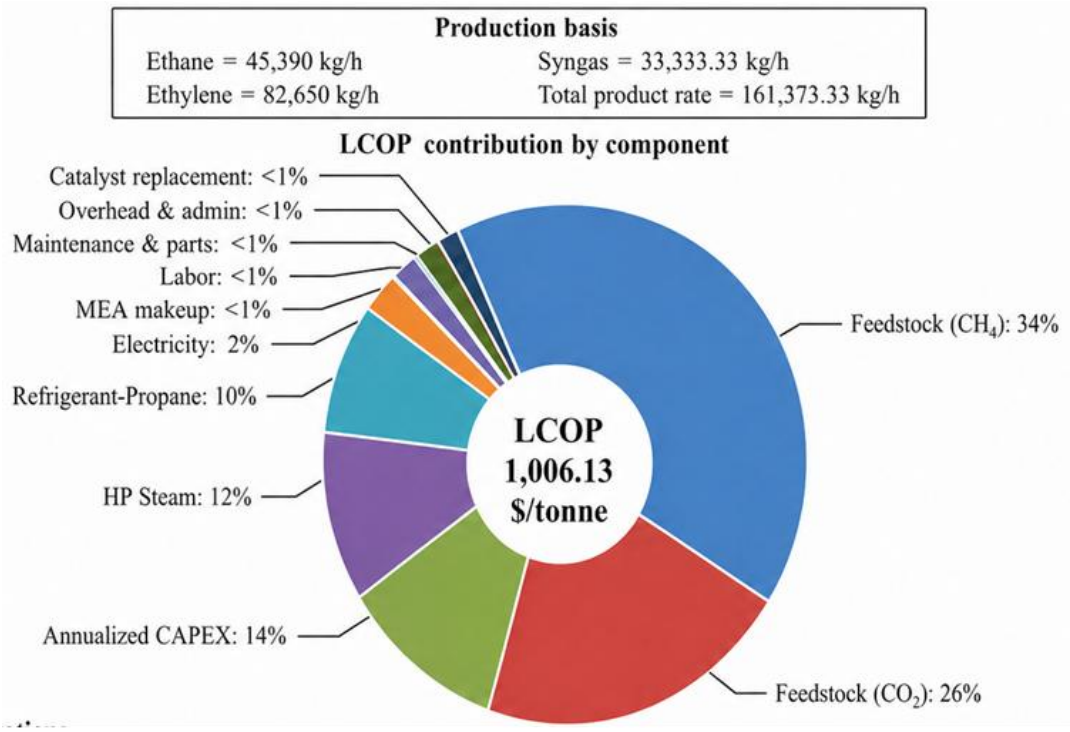

- CH_4 feedstock is the dominant contributor to LCOP (34%; 339 $/tonne).
- Combined feedstock costs (CH_4 + CO_2) account for 59% of the LCOP.
- Annualized CAPEX contributes 14% of the LCOP (142 $/tonne).
- Utilities (electricity, HP steam, and refrigerant-propane) contribute 24% of the LCOP.

Figure 46. Contribution of cost components to LCOP for Case 4 (60% methane recycled) [17, 59].

A breakdown and summary of the LCOP for Case 4 is shown in Figure 46. The feedstocks cost now contributes ~59% of the LCOP which is 15%, 9% and 5% less than the Case 1, 2 and 3 respectively. The annualized CAPEX and utilities increase slightly again with the annualized CAPEX contribution now ~14% and utilities ~24% (HP steam ~12%, refrigerant-propane ~10% and electricity ~2%). The remaining contributions are again either ~1% or lower than 1%.

Figure 47 shows the effect of methane recycling on the LCOP of CL OCM/CO_2-H_2O splitting. The LCOP drops from 1594 $/tonne to 1006 $/tonne as the percentage of recycled methane is increased from 0% to 60%. From 0 to 30% recycling, there is a ~19% reduction in LCOP. At 40% methane recycling, the reduction is ~29% and at the 60% methane recycling, the reduction is ~37%. This shows a significant improvement in the economics of the CL OCM/CO_2-H_2O splitting technology with the recycling of methane. However, at higher methane recycling percentages such as 60%, the high hydrogen content of the reactor inlet feed becomes an issue. Therefore, for the 60% or higher methane recycling, it is necessary to deploy hydrogen separation units to decrease the hydrogen content of the recycled stream before it can be introduced to the reactor inlet.

Moreover, as mentioned earlier, the current TEA does not include CO_2 recycling for the CO_2-H_2O splitting cycle and significant LCOP reduction is expected if CO_2 recycling is considered. Even recycling only 50% of the unconverted CO_2 from the CO_2-H_2O splitting cycle of Case 3 (40% Methane Recycled) would significantly reduce the LCOP from 1,138 to ~988 $/tonne, corresponding to about a 13.2% reduction. With CO_2 recycling, the LCOP can be reduced below 1000 $/tonne without recycling over 60% methane.

6.3.2. Effect of Recycling on C_2 Yield

Figure 48 shows the effect of recycling on the C_2 yield of the OCM cycle. The C_2 yield considered for the OCM cycle of base case (Case 1) is 10.63%. For Case 2, the C_2 yield increases to 14.58% which is 3.95 percentage points higher than the Case 1. This shows significant improvement in the OCM cycle performance. For Cases 3 & 4, the yield becomes 19.21% and 26.50%, respectively resulting in an overall increase of 15.87 percentage points relative to Case 1. The higher yields with higher recycling occur due to the reduced requirement of fresh methane feedstock. In general, a 30% C_2 yield is recommended for the OCM process to make the technology industrially feasible and compatible with existing ethylene production technologies. However, in this integrated CL OCM/CO_2-H_2O splitting design, the LCOPs are not only feasible but also lower than conventional ethylene production technologies. The reason for lower LCOPs even at a C_2 yield of ~19% is that the CO_2 feedstock, which is much cheaper than the methane feedstock, replaces the methane feedstock for half of the plant's operation time.

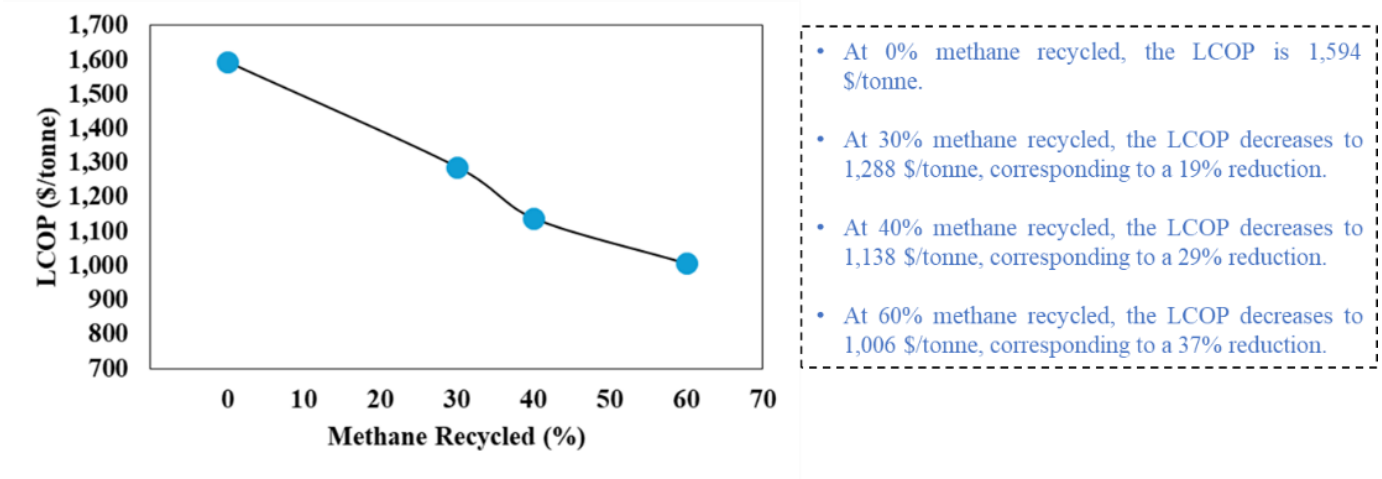

Figure 47. Effect of methane recycling on LCOP.

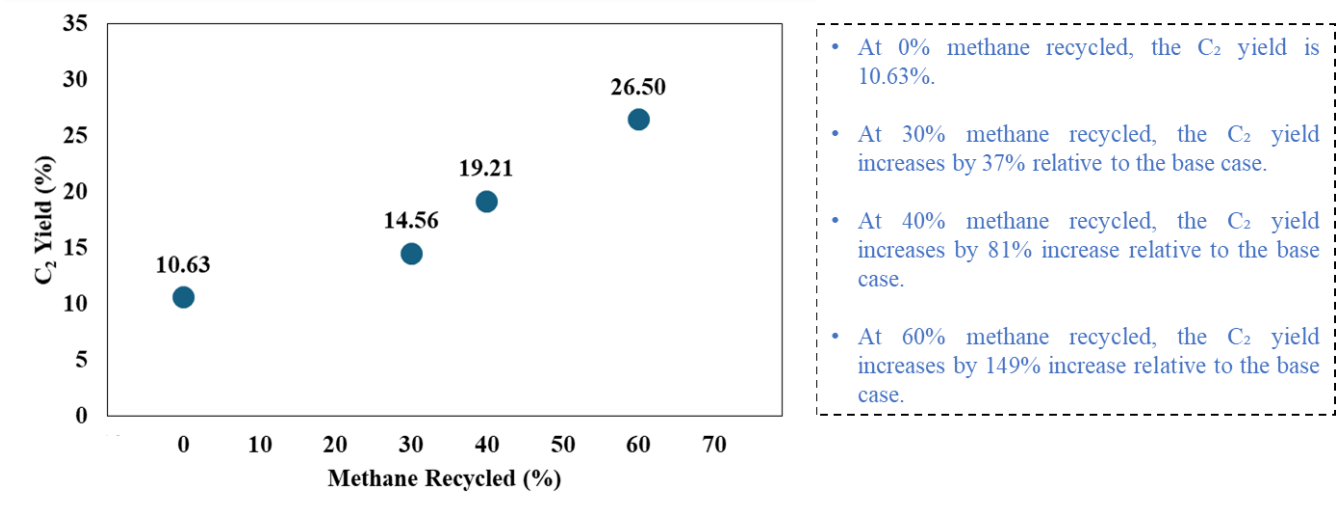

Figure 48. Effect of methane recycling on C_2 yield of OCM cycle.

6.3.3. Sensitivity Analysis

6.3.3.1. Effect of Feedstock Prices

A sensitivity analysis is conducted to analyze the impact of feedstock prices on the LCOP. This analysis is conducted for Case 3 since it is the most practical case in terms of both profitability and safety. Figure 49 shows the effects of feedstock price on the LCOP. The original prices for methane and CO_2 considered for the TEA are 165 and 50 $/tonne respectively.

The price of methane is varied from 130-190 $/tonne at an increment of 10 $/tonne while keeping the price of CO_2 constant at 50 $/tonne. The minimum LCOP is 1054 $/tonne at 130 $/tonne methane price which reaches 1209 $/tonne at 190 $/tonne methane. With each 10 $/tonne increment the LCOP varies by ~2%. This shows that even though the LCOP is heavily dependent on the methane feedstock prices, it still remains competitive with conventional ethylene production technologies even at prices as high as 190 $/tonne.

The CO_2 price is varied from 20-80 $/tonne at an increment of 10 $/tonne while keeping the price of methane constant at 165 $/tonne. As evident in the Figure 49, the LCOP drops to 956 $/tonne at a CO_2 price of 20 $/tonne. However, the LCOP increases over 1000 $/tonne at higher CO_2 prices. The LCOP varies by ~5-7% with each 10 $/tonne increase in the CO_2 price showing that the LCOP is almost 3 times more sensitive to the CO_2 price compared to the methane price.

This analysis shows that LCOPs are heavily dependent on the feedstock price and even though the current configuration shows that a minimum of 40-50% methane recycling

may be required to make this integrated technology economically feasible, but this can change given that the prices of methane are projected to decline in coming years as projected in the Short Term Energy Outlook, 2026 [194]. With lower prices of methane, LCOPs below 1000 $/tonne may be achieved with methane recycling percentages less than 35%. It is also worth noting that the LCOP drops to 863 $/tonne considering minimum prices for both methane and CO_2, i.e., 130 and 20 $/tonne respectively.

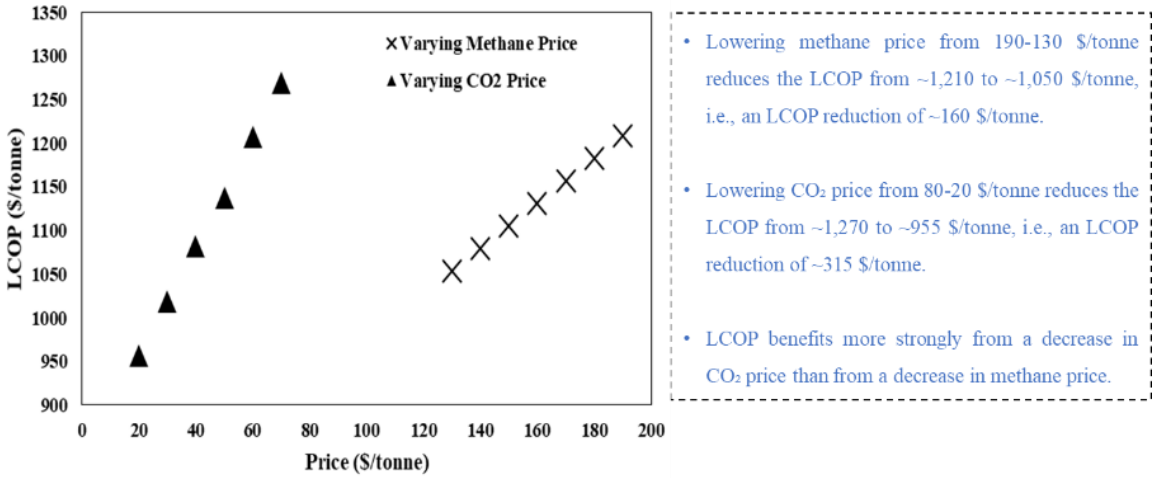

Figure 49. Effect of feedstock prices on LCOP.

6.3.3.2. Effect of Lang Factor

Figure 50 shows the effect of varying Lang Factor for the equipment capital cost i.e., reactor, CO_2 absorber/stripper, demethanizer and C_2 splitter, on the LCOP for Case 3. The Lang Factor is varied from 3.5-6 at an increment of 0.5. As evident in the Figure 50, the LCOP is barely affected even by varying the Lang factor by an increment of 0.5. The variation in LCOP is ~1% at each increment. Since the capital cost is heavily dependent on the Lang Factor, this analysis shows that the overall capital cost has much lower impact on the LCOP compared to the feedstock price variation and substantiates improved performance

of the process accompanied by lower feedstock prices for the technology's economic viability.

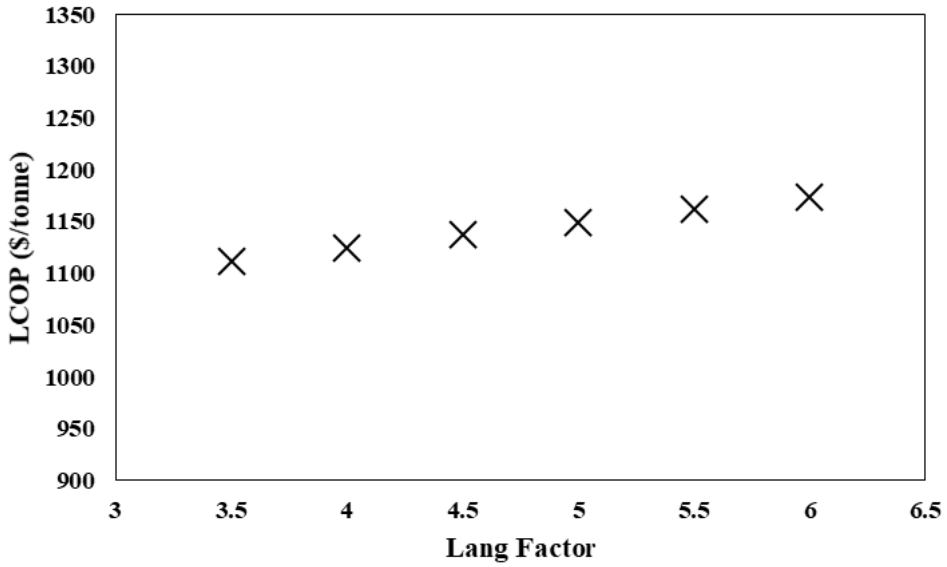

Figure 50. Effect of Lang Factor on LCOP.

6.3.4. Scale-Dependent LCOP Reduction

This analysis evaluates how plant capacity affects the LCOP for the CL OCM/CO_2-H_2O process through the economies of scale method [197-199]. The analysis is based on the Case 3 (40% methane recycled case). The CAPEX is scaled using the six-tenths rule (0.6 rule). The CAPEX (TOC) is estimated using the following formulation.

$$C_2=C_1\cdot(S_2/S_1)\text{^}0.6 \qquad (39)$$

Here, C_2 is the new CAPEX, C_1 is the original CAPEX, S_1 is the original plant capacity (i.e., 1 Million tonne/year) and S_2 is the new capacity. Consequently, the annualized CAPEX is calculated using the CCF. Operating costs are separated into variable and fixed

components, with variable costs scaled linearly with production capacity and fixed costs scaled using a 0.6 exponent to account for economies of scale. The formulations are listed below.

$$\text{Variable OPEX } (VO_2) = VO_1 \cdot (S_2/S_1)^{\wedge}1 \quad (40)$$

$$\text{Fixed OPEX } (FO_2) = FO_1 \cdot (S_2/S_1)^{\wedge}0.6 \quad (41)$$

$$\text{Annual OPEX } (AO_2) = VO_2 + FO_2 \quad (42)$$

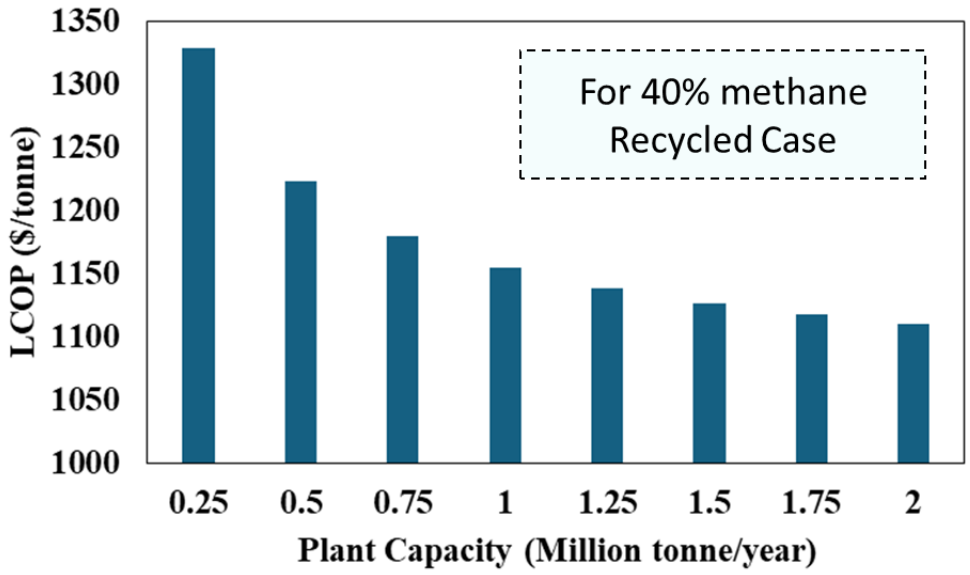

Figure 51. LCOP at different plant scales

Here, VO1 and FO1 include the original variable and fixed operating costs for the 1 Million tonne/year plant capacity. The effects of Scaling are shown in Figure 51. As plant capacity increases, the LCOP decreases because capital and fixed operating costs are extended to a larger annual production rate. However, the reduction becomes less significant

at larger capacities and LCOP starts leveling out, indicating diminishing economic benefits from scaling up beyond a certain point.

Chapter 7. Life Cycle Assessment (LCA)

The final stage of the modeling-based analysis of the proposed CL OCM/CO_2-H_2O splitting technology includes the LCA to account for cradle-to-gate (CtG) environmental impacts generated through the process. The integrated CL OCM/CO_2-H_2O splitting technology is compared with conventional ethylene production routes such as ethane/naphtha steam cracking in terms of carbon footprint, fossil resource consumption, water usage and toxic emissions.

The LCA is an advanced tool for government and non-government organizations to enhance the decision-making process in terms of sustainable management, strategic planning, priority setting, design or redesign of resources and products while analyzing innovative technologies [29, 200]. Moreover, LCA also assists in selection of relevant parameters for assessing the environmental impact and measurement techniques. Additionally, it helps in marketing e.g., implementing an ecolabelling scheme, making environmental claims or producing an environmental product declaration [200]. LCA is a modeling approach to quantify the entire lifetime environmental and net-energy impact of a system.

7.1. LCA Methodology

7.1.1. Principles of LCA

The LCA method has been defined by International Organization for Standardization (ISO) standards 14040 and 14044 [200, 201]. The principles of LCA include the following [201].

- The LCA begins with the extraction and acquisition of raw materials, their transformations in manufacturing process and operations including energy production, marketing, usage and re-usage of the product, maintenance, recycling and waste.
- LCA includes only the environmental aspects and the economic and social aspects are usually not included in LCA.
- LCA is a relative approach in which a functional unit is first defined. All the subsequent analyses are then relative to that functional unit including all the inputs and outputs to the life cycle impact assessment (LCIA).
- LCA is also an iterative approach where individual phases of LCA use results of other phases which leads to a more comprehensive and consistent set of results.
- Since LCA is a complex method, transparency is a vital principle to properly interpretate the results.
- LCA addresses all attributes of natural environment, human health and resources comprehensively so that the potential trade-offs can be identified in a single study.
- The decisions in LCA study are preferably based on natural science. If not possible, other scientific approaches, international conventions or value choices can be referred to as well in the respective order.

7.1.2. Phases of LCA

There are four phases of an LCA study.

[1] The goal and scope definition: The scope includes the subject and intended use of the study. This includes the system boundary and the level of detail.

[2] The inventory analysis: The inventory analysis occurs during the life cycle impact (LCI) phase. It involves the collection of input/output data with regards to the system boundary to achieve the LCA goals.

[3] The impact assessment: The impact assessment or LCIA includes additional information to the LCI to better understand the environmental significance of the proposed system.

[4] The interpretation: In the interpretation phase, the results of LCI and LCIA are summarized and discussed. Moreover, conclusions and recommendations regarding the decision-making are presented to meet the goals and scope of the study.

7.1.3. Goal and Scope

The scope of the study is CtG including the extraction of the feedstock such as natural gas, biogas and flare gas, CL OCM process including the separation and purification stages and associated energy and utility requirements, as shown in Figure 52. The downstream usage and disposal of end product (ethylene) is not included since it is the same for all the processes.

7.1.4. Functional Unit

The functional unit is 1 tonne of ethylene at the plant gate. This functional unit is chosen as it allows for consistent comparison across all different processes considered for this study.

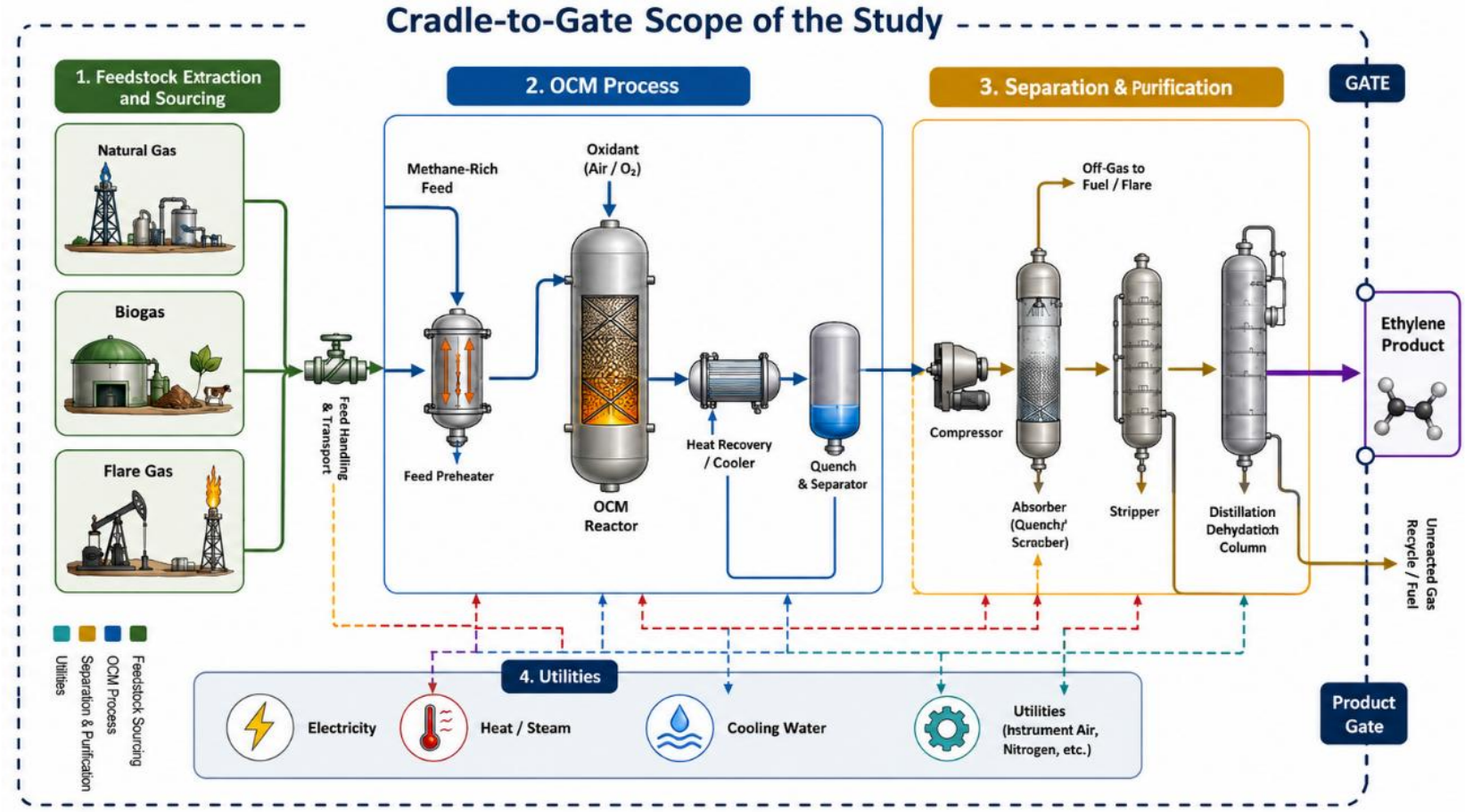

Figure 52. CtG scope of LCA study.

7.1.5. Impact Categories and Assessment Method

Key impact categories selected for the LCIA are Global Warming Potential (GWP), Acidification Potential (AP), Human Toxicity (HT), Water Depletion (WD), and Fossil Resource Depletion (FRD). These categories are chosen based on their relevance to the environmental burdens typically associated with petrochemical production and the specific challenges linked to methane-based ethylene production processes.

For impact assessment, the ReCiPe Midpoint (H) 2016 method is employed as it comprehensively covers both the emissions and resource use impacts [202-204]. Background data for energy inputs, material production, and emissions are sourced from the Ecoinvent v3.6 database and supplemented with process-specific data where necessary. SimaPro 8.1 software is used for the simulations which enables detailed process mapping, scenario analysis, and impact quantification.

7.1.1. Model Assumptions

Methane conversion is set at 30% and a C_2 yield of ~20% for the base case driven from the results of Jiang et al. [98]. The comparison includes an emerging technology (CL OCM/CO_2-H_2O splitting) modeled using lab-driven performance metrics and integration assumptions with steam cracking routes that represent mature, industrially optimized technologies supported by commercial operating data. Therefore, the results are presented as a prospective benchmark that highlights potential environmental benefits for the proposed technology.

The traditional ethane steam cracking and naphtha cracking processes are modeled based on published literature and industrial data [205, 206], considering the steam-to-feed ratio, reaction temperatures, energy consumption (in terms of high-temperature steam and electricity), and associated byproducts like propane, butadiene, and hydrogen. Emissions, particularly CO_2, are calculated using emission factors derived from the combustion of hydrocarbons, energy use, and production of byproducts. The environmental impacts of each process are evaluated using the ReCiPe 2016 method [202], focusing on key indicators of midpoint and endpoint categories.

7.1.2. System boundary

CtG boundary is applied to all cases. Under this boundary, the inventory includes the core process units (main reaction/conversion), in-plant utilities and energy requirements (thermal and electricity), and product recovery/separation up to the ethylene plant gate. Upstream feedstock extraction, refining, and supply-chain processing are excluded from this specific comparison because including upstream stages in the technology comparison can conceal technology-driven differences attributable to reactor design, heat integration, separations, and the chemical looping configuration.

For the CL OCM/CO_2-H_2O splitting (Figure 53), the boundary starts at the plant gate feed input of methane and includes the OCM reactor operated at 800 °C, oxygen-carrier/catalyst oxidation and regeneration with CO_2 and H_2O in a chemical looping configuration, and downstream separation and purification required to recover 99.9% ethylene from unreacted methane and by-products, including recycle handling.

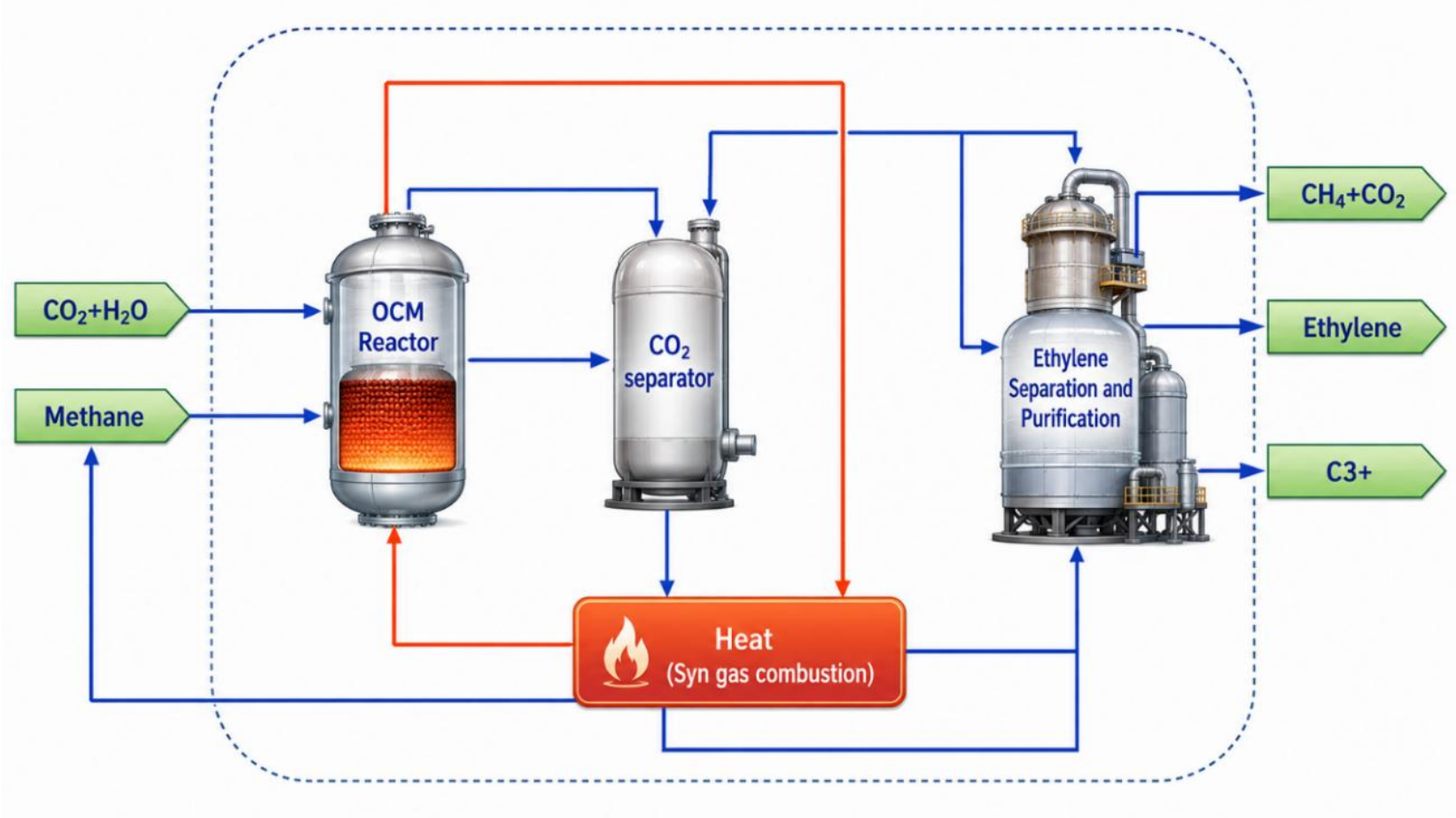

Figure 53. System boundary of CL OCM/CO_2-H_2O splitting.

For ethane and naphtha steam cracking (Figure 54 & 55), the boundary starts with the delivered hydrocarbon feed at the cracker inlet and includes feed preheating, steam generation, high-temperature cracking furnaces (typically ~850–950 °C), quenching, compression, and multi-stage separation and purification to obtain ethylene at the plant gate.

Across all pathways, direct emissions, utility consumption, and energy inputs are included, while capital equipment/infrastructure, construction, distribution beyond the plant gate, use phase, and end-of-life are excluded in line with the gate-to-gate scope of this comparison.

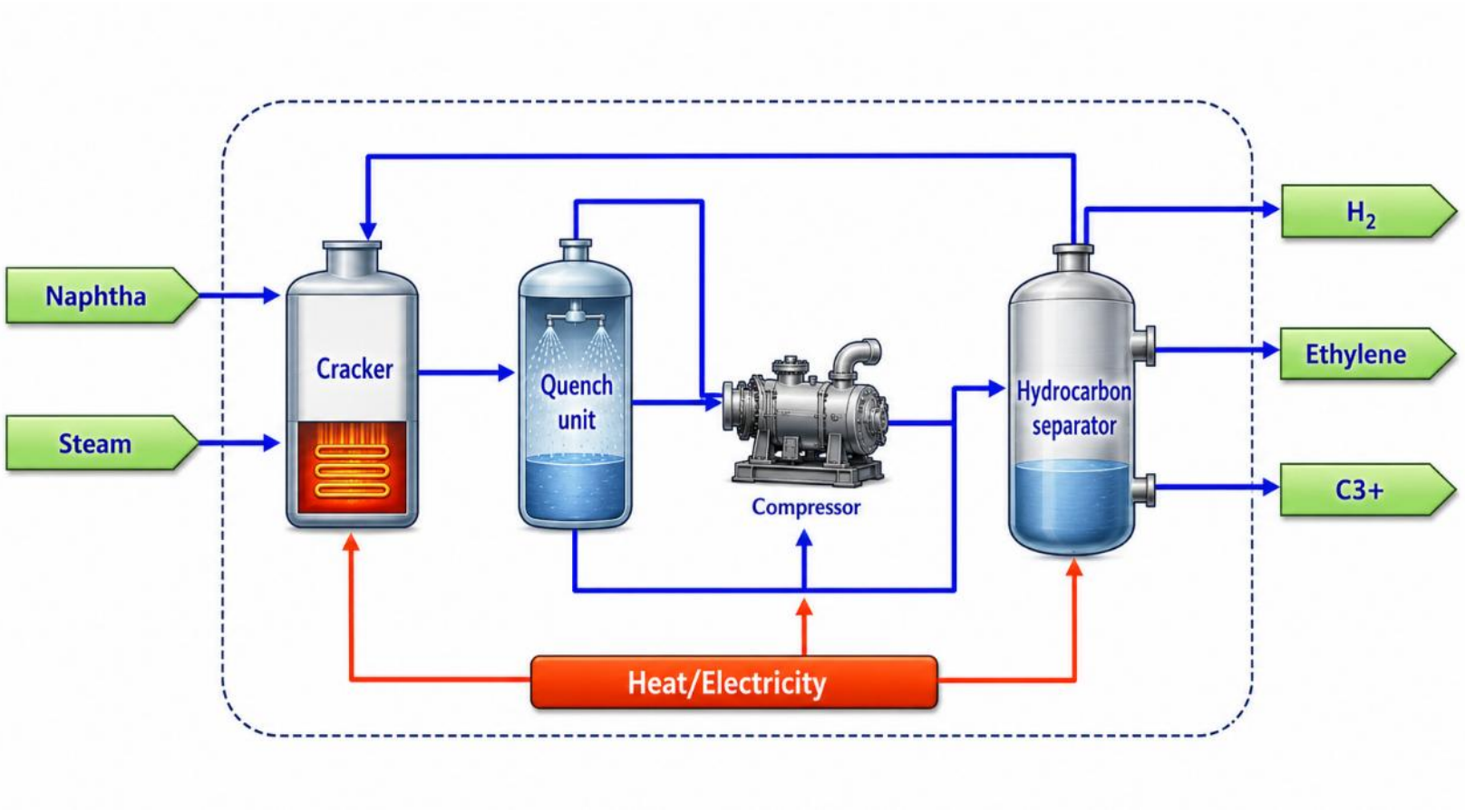

Figure 54. System boundary of Naphtha cracking.

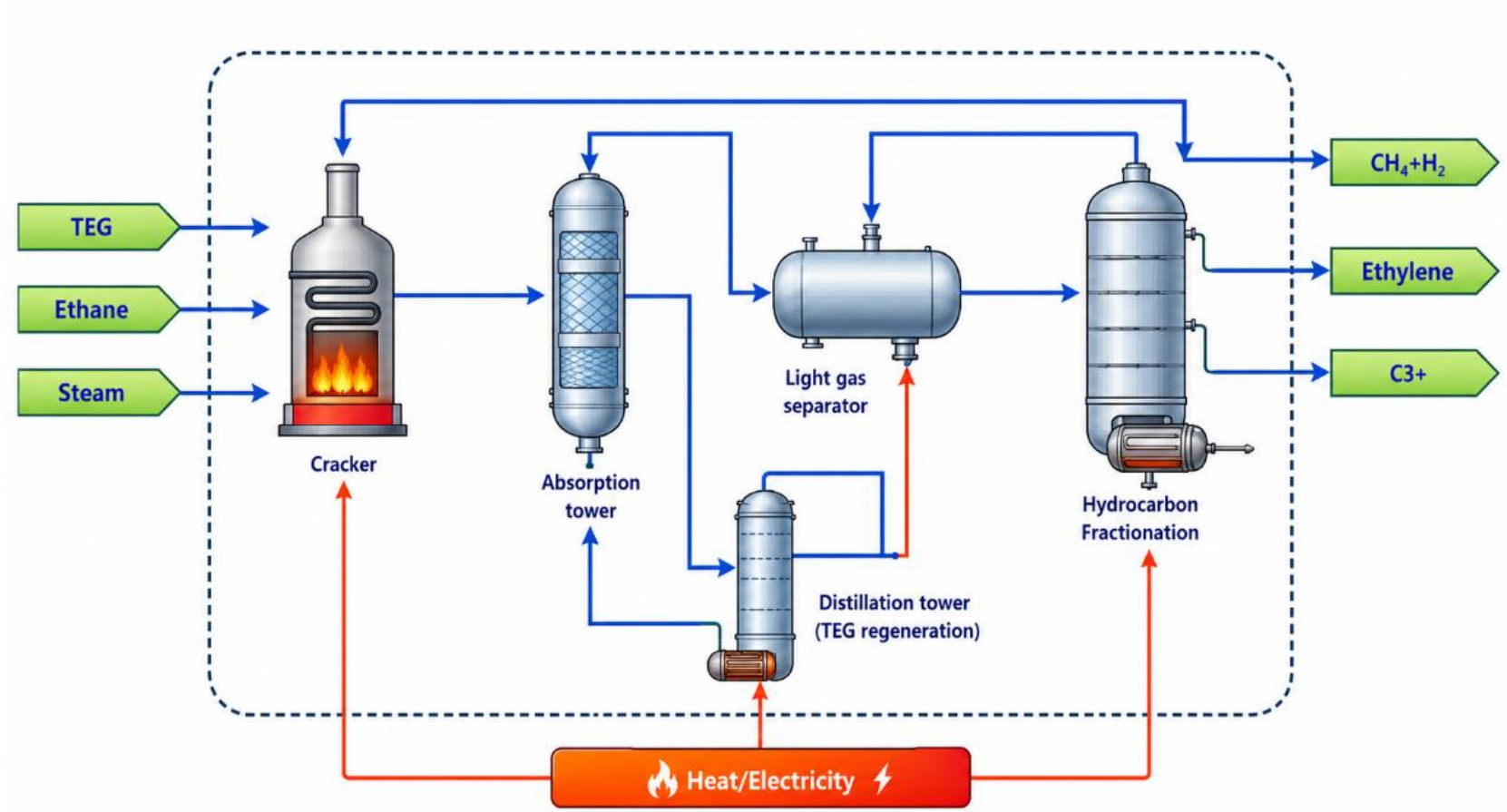

Figure 55. System boundary of Ethane cracking.

7.1.3. Life Cycle Inventory (LCI)

The LCI phase of this study involved compiling all relevant inputs and outputs associated with the production of one metric ton (tonne) of ethylene using the CL OCM/CO_2-H_2O splitting process and conventional processes. The inventory data specifically covers the energy and material requirements for the reactor operation and the subsequent downstream processing of the product flow. The output inventory includes the main products, co-products and emissions generated across all the technologies. Table 12 provides a summary of the inputs and outputs for each process.

The 30% methane conversion and 20% C_2 yield at 800°C directly influence the methane feedstock requirement and are derived from experiments by Jiang et al. [98]. Similarly, the 80% ethylene selectivity for ethane cracking, also from a peer-reviewed source, critically determines the yields of the main product versus co-products, impacting overall process efficiency. Moreover, the reaction energy (ΔH kJ/molCH_4), derived from literature and calculations, is fundamental for accurately modeling the thermal balance and associated energy demands or credits of the OCM reactor [195].

Table 12. The summary of inputs and outputs of CL OCM/CO_2-H_2O splitting and Ethane/Naphtha cracking for LCA in SimaPro.

Category	Naphtha Cracking (950 °C)		Ethane Cracking (950 °C)		Chemical Looping OCM (800 °C)	
Inputs	**Component**	**Amount**	**Component**	**Amount**	**Component**	**Amount**
	Naphtha	2,941 kg	Ethane	1282 kg	Methane	3810 kg
	Steam	1,177 kg	Steam	424 kg	Cooling water	7 m^3
	Natural Gas (heating)	27,000 MJ	Natural gas (heating)	23000 MJ	Natural gas (heating)	1635 MJ
	Electricity (Mix. Grid)	250 kWh	Electricity	250 kWh	Electricity	25 kWh
	-	-	-	-	CO_2+H_2O (to oxidize catalyst)	225MJ
Outputs	Ethylene (C_2H_4)	1,000 kg	Ethylene (C_2H_4)	1,000 kg	Ethylene (C_2H_4)	1,000 kg
	Propylene (C_3H_6)	450 kg	Propylene (C_3H_6)	500 kg	Water vapor	810 kg
	Butadiene (C_4H_6)	58 kg	Butadiene (C_4H_6)	150 kg	Carbon dioxide	250 kg
	Methane (CH_4)	40 kg	Methane (CH_4)	40 kg	Carbon monoxide	80 kg
	Hydrogen (H_2)	66 kg	Hydrogen (H_2)	125 kg	Ethane (C_2H_6)	120 kg
	Coke	60 kg	Coke	60 kg	-	-
Emission	Carbon dioxide (CO_2)	1344 kg	Carbon dioxide (CO_2)	1621	-	-

For natural gas, the methane content is assumed to be between 85–95% with minimal CO_2 content (1–3%) requiring minimal pre-treatment. Catalyst manufacture is initially excluded from the base inventory because the Na–$LaMnO_3$ perovskite catalyst is expected to be long-lived relative to the ethylene throughput the life-cycle of the reactor. Because a specific Ecoinvent process for Na–$LaMnO_{3-\delta}$ is not available, catalyst manufacture is approximated using a ceramic/perovskite proxy based on precursor oxides/salts (La-, Mn-, and Na-containing materials) and calcination energy; to remain conservative, a high bounding GWP intensity is applied for catalyst production of 10 kg CO_2-eq per kg catalyst (upper-bound proxy for calcined ceramic materials).

7.2. Results

The Figure 56 represents a comparative analysis of the GWP of all the technologies, expressed in kg CO_2-eq / kg of ethylene produced. As evident from the Figure, CL OCM/CO_2-H_2O splitting performs better than ethane/naphtha cracking technologies. The GWP for OCM/CO_2-H_2O splitting is 0.38 kg CO_2 eq/kg ethylene. In contrast, ethylene from ethane cracking at 950°C results in a significantly higher GWP of 1.93 kg CO_2 eq, while naphtha steam cracking performs the worst among the three, with a GWP of 2.84 kg CO_2 eq/kg ethylene.

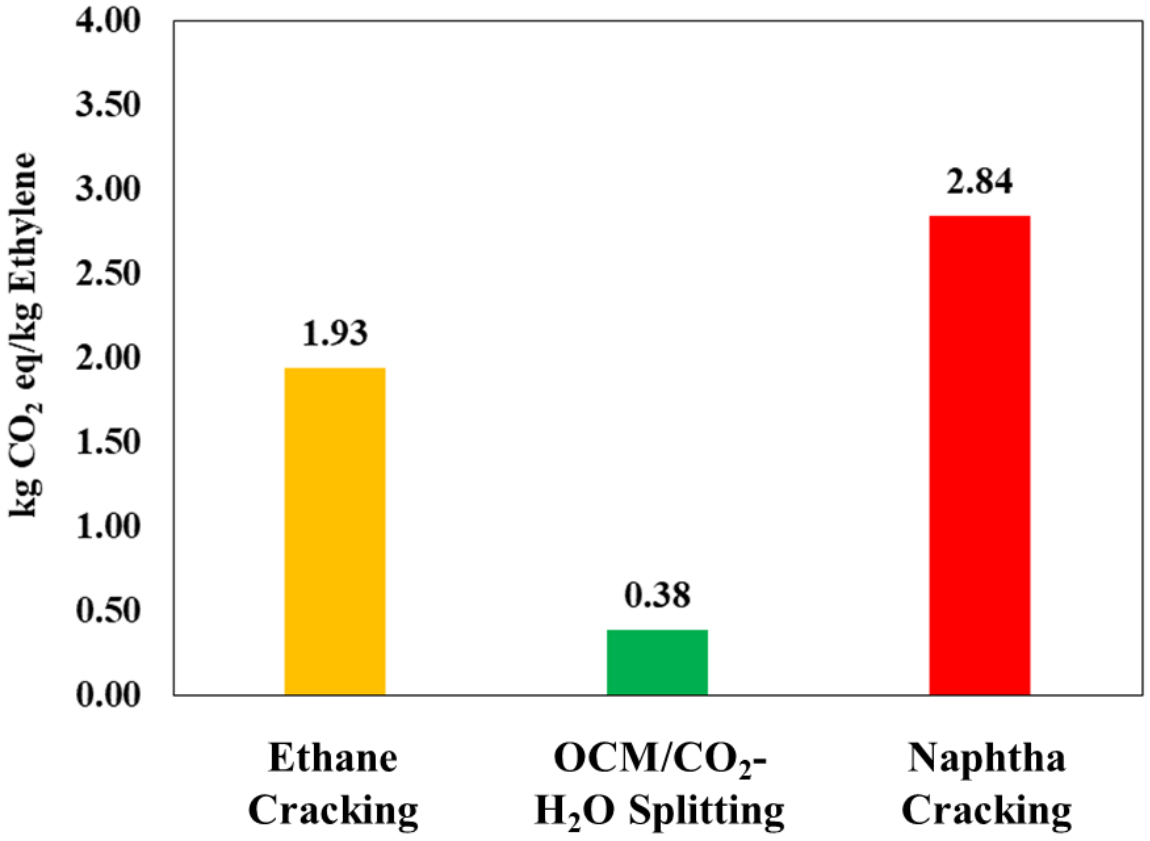

Figure 56. GWP comparison of ethylene production pathways expressed in kg CO_2-eq / kg ethylene produced.

These results substantiate the potential of CL OCM/CO_2-H_2O splitting as a low-carbon ethylene and syngas production technology, especially when combined with renewable or low-carbon electricity and optimized methane sources such as biogas or flare gas.

7.2.1. Environmental Trade-offs/ Midpoints Categories

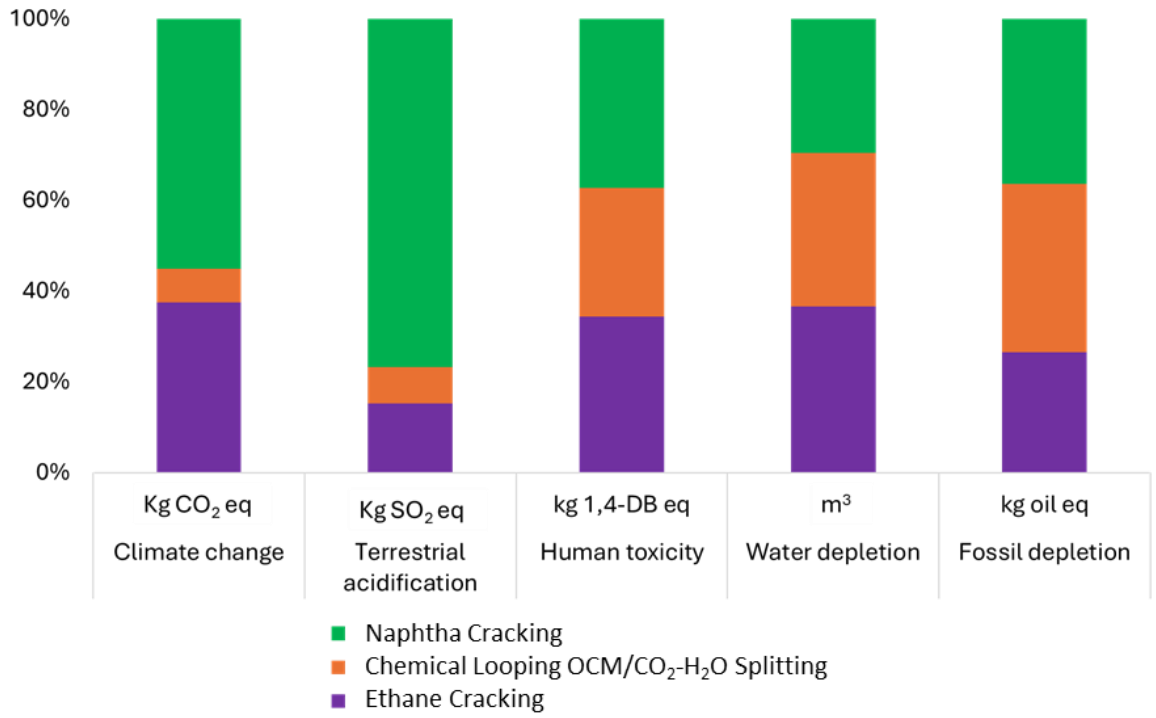

Figure 57. Environmental burden distribution (%) of three ethylene production pathways.

Figure 57 shows the environmental performance profiles of the three ethylene production technologies i.e., naphtha cracking, ethane cracking and CL OCM./CO_2-H_2O splitting. Naphtha cracking consistently results in the highest contributions to climate change and terrestrial acidification, while ethane cracking performs moderately across most categories. In contrast, CL OCM/CO_2-H_2O splitting demonstrates comparatively lower climate change and acidification impacts but exhibits significantly higher water depletion and fossil resource use.

7.2.2. Impacts on endpoints categories

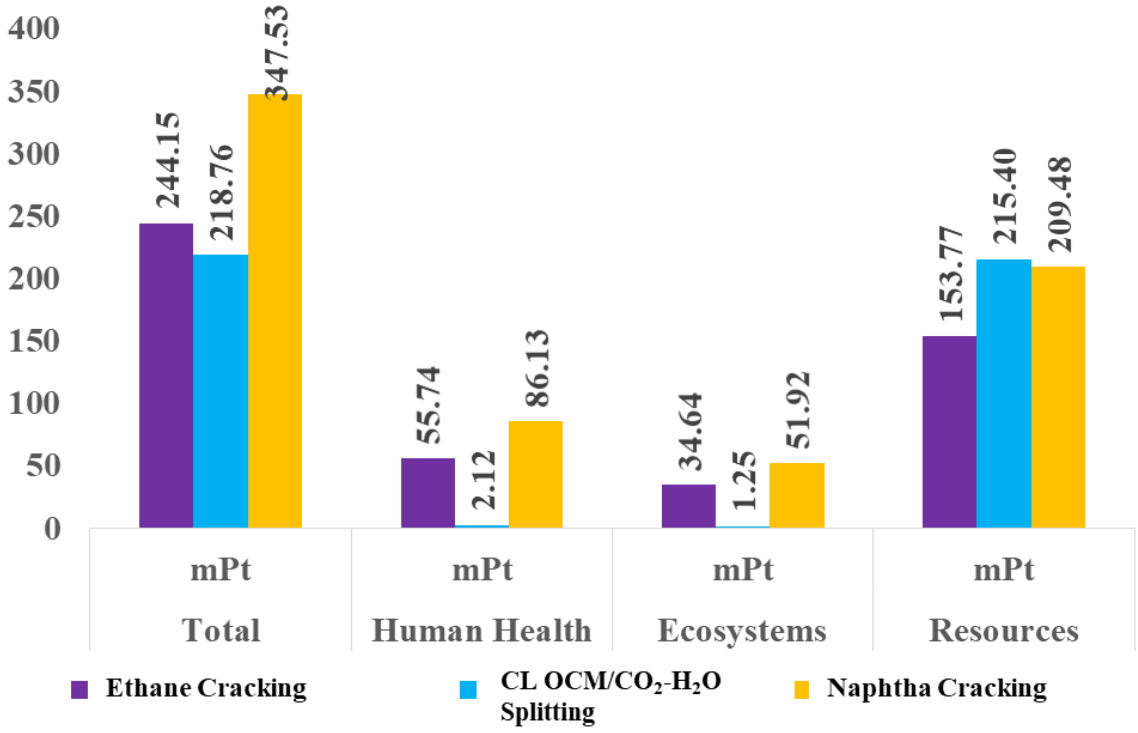

Figure 58. Life cycle endpoint impact scores for ethylene produced showing trade-offs across environmental categories.

The Figure 58 shows the environmental impacts of the three technologies based on endpoint indicators expressed in millipoints (mPt). 1 mPt = 0.001 Pt = 0.1% of a person's average yearly environmental burden. The results show that naphtha cracking has the highest overall environmental burden, with a total score of 347.53 mPt followed by ethane-steam cracking (244.15 mPt) and CL OCM/CO_2-H_2O splitting (218.76 mPt), indicating that the CL OCM/CO_2-H_2O splitting route offers the lowest total environmental impact among the three technologies assessed.

In the human health category, CL OCM/CO_2-H_2O splitting performs significantly better, with an impact of only 2.12 mPt compared to 55.74 mPt for ethane cracking and a significantly high 86.13 mPt for naphtha cracking. Similarly, for ecosystem impacts, CL OCM/CO_2-H_2O splitting shows excellent environmental performance with only 1.25 mPt, while ethane and naphtha cracking show 34.64 mPt and 51.92 mPt, respectively.

However, in the resource depletion category, CL OCM/CO_2-H_2O splitting exhibits the highest impact at 215.40 mPt exceeding slightly the naphtha cracking (209.48 mPt) and significantly the ethane cracking (153.77 mPt). The results suggest that while the CL OCM/CO_2-H_2O splitting pathway offers considerable advantages in terms of reducing health and ecosystem-related impacts, it still faces challenges in terms of resource sustainability.

Chapter 8. Conclusion and Future Work

OCM technology is of high interest as it converts methane directly into ethylene which is a highly valuable chemical in petrochemical industry. On the other hand, chemical looping CO_2-H_2O splitting technology converts CO_2 (the most abundant greenhouse gas) to syngas. A review of the wide-ranging research done on the both of these technologies was presented in this dissertation especially highlighting some of the notable achievements in terms of C_2 yield and selectivity of OCM technology. The detailed kinetic and thermodynamic mechanisms of the OCM reaction were described as well. Moreover, the dissertation highlighted results in terms of various catalysts for OCM, the potential benefits of integrating the OCM technology with other processes and utilizing alternative oxidants instead of oxygen. For the CO_2-H_2O splitting technology, the challenges associated with regenerability of the catalyst are mainly discussed as the process does not face selectivity issues such as OCM. Some key points from the conducted review can be summarized below.

- The CL method for OCM can improve the C_2 yield and selectivity, reduce cost of CO_2 removal and also eliminate expensive air separation unit compared to the co-feed method for OCM.
- Perovskite catalysts are highly stable and can achieve high C_2 yields at lower temperatures. Moreover, doping with alkali metals can improve the C_2 yield by several orders of magnitude.
- The integration of OCM technology with another process such as a chemical reaction system or a power generation system can significantly improve its C_2 yield, lower

CO_2 emissions and improve its chances of being profitable. One such technology can be the chemical looping CO_2-H_2O technology which can complete the oxidation cycle of the chemical looping OCM.

Despite its attractive possibilities and potentially low environmental impact, the OCM technology still has not found industrial application due to lack of comprehensibility in the reported data in literature. To overcome this inadequacy, a criteria was presented for the industrial viability of OCM integrated with CO_2-H_2O splitting. The criteria can be met utilizing TEA and LCA assessments to build confidence in the proposed ideas for OCM. The proposed criteria includes C_2 yield, C_2 selectivity, and CH_4 conversion, the levelized-cost of ethylene, CO_2 emissions and reaction temperature. Moreover, a novel integrated OCM/CO_2-H_2O splitting technology in CL design was introduced to optimize the energy utilization and minimize heat rejection to the environment.

Furthermore, a multiscale packed bed reactor is modeled and calibrated for a CL OCM process based on the experiments of Jiang et al. [98]. The model includes 10 gas-phase reactions from Stansch et al. [63], to which a surface reaction was added to simulate the oxygen formation from the oxygen carrier (the catalyst). The model included mass and heat transfer with integrated chemistry and effectively captured trends in CH_4 conversion, C_2 selectivity and C_2 yield within ±1.40%, ±4.35% and ±3.66% respectively across a temperature range of 700-900^{o}C. The model helped visualize the concentration and temperature gradients across the reactor length. The mapping of concentration gradients plays a critical part in determining the optimum reactor size, shape and other features such as GHSVs.

A parametric study is performed with the CFD reactor model to find optimum operating conditions for C_2 yield and selectivity. The study included multiple sweeps for different operating parameters such as the GHSV, inlet methane concentration, oxygen availability and reactor diameter across a temperature range of 700-900ºC. Furthermore, a second set of focused sweeps for CH_4/O_2 ratio were also conducted across a temperature range of 800-850 ºC and GHSVs, 1125, 1400 and 2500 mL/hg. The results from the parametric study show that oxygen availability plays an important role in controlling the conversion-selectivity tradeoff. Higher oxygen availability increased methane conversion and improved C_2 yield, but it also reduced C_2 selectivity by enhancing deep oxidation reactions. In contrast, higher GHSVs and higher CH_4/O_2 ratios improved C_2 selectivity by reducing deep oxidation and caused by high oxygen availability and residence time, but these conditions also reduced overall C_2 yield because of lower methane conversion.

- The highest C_2 yield was 20.4% at the CH_4/O_2 ratio of 1.71, 1125 mL/hg GHSV and 825ºC. The C_2 selectivity was 44.6% at this point.
- The highest C_2 selectivity of 76.8% was achieved at a CH_4/O_2 ratio of 8.9, 2500 mL/hg GHSV and 800ºC. The C_2 yield at this point was ~10%.

The reactor geometry also had a significant effect on thermal behavior as it was shown that increasing the diameter of the reactor, while keeping the same volume, decreased the chances of hot spots formation while maintaining the C_2 yield. Similar trends in hot spots were observed for higher GHSVs as well, where shorter residence time reduced excessive heat accumulation and assisted in heat removal from the reactor.

Overall, the parametric study provides a CFD-based framework for identifying the most suitable operating windows for chemical looping OCM in terms of tackling challenges in C_2 yield, selectivity and hot-spot formation.

Based on the reactor parametric study, a system-level model was developed in Aspen HYSYS V14 and subsequent TEA was conducted at industrial scale for CL OCM/CO_2-H_2O Splitting to produce ethylene and syngas. The LCOP was calculated for the integrated technology under different configurations for methane recycling, including 0%, 30%, 40% and 60% methane recycled. The C_2 yield and selectivity of the reactor OCM cycle were 10.76% and 72% respectively for the base case of no recycling. Moreover, a sensitivity analysis was conducted to analyze the impacts of feedstock prices and capital costs on the LCOP. The results indicate that the integrated technology performed as well as or better than the conventional ethylene production technologies at 40% recycled methane. Furthermore, projected lower methane feedstock prices will further reduce this LCOP making the integrated technology economically attractive in terms of ethylene production and methane conversion. The C_2 yield of the OCM cycle can be increased from 10.63% to 26.50% with 60% methane recycled however, at this high recycling percentage the increased hydrogen accumulation can initiate combustion as the hydrogen concentration crosses its flammability limit. Overall, the integrated technology shows competitive LCOP at 40% recycled methane and slightly higher methane recycling can still ensure safe conditions considering hydrogen accumulation.

CL OCM/CO_2-H_2O splitting is also favorable in terms of environmental impacts, especially CO_2-eq emissions, compared to conventional ethylene production technologies.

A LCA is conducted to further substantiate the importance of this novel integrated technology as an alternative to methane conversion and ethylene production technologies. The results show that CL OCM/CO_2-H_2O splitting achieves the lowest GWP (0.38 kg CO_2-eq/kg C_2H_4) relative to ethane steam cracking (1.93 kg CO_2-eq/kg C_2H_4) and naphtha steam cracking (2.84 kg CO_2-eq/kg C_2H_4). Endpoint indicators also indicate better performance by CL OCM/CO_2-H_2O, with major reductions in human health and ecosystem damage compared to conventional technologies, although resource depletion remains slightly higher.

Overall, this dissertation shows that the integrated CL OCM/CO_2-H_2O technology has the potential to not only be competitive to ethane/naphtha steam cracking processes in terms of economic performance but can also outperform these technologies because of its lower environmental impact. The integrated technology also offers potential solutions for methane and CO_2 emissions conversion. In particular, the technology may offer an attractive route for utilizing methane emissions that are otherwise difficult to convert on site.

Despite these advantages, further research is required to advance the technology toward industrial deployment. One important direction for future work is the scale-up of the CL OCM reactor, since maintaining lab-scale performance at industrial scales requires careful control of hot-spot formation, mass transfer limitations, combustion/deep oxidation reactions and oxygen availability within the reactor. Although such studies may require significant computational resources. In addition, future LCA studies should evaluate the effect of methane recycle, feedstock source, heat integration and process configuration in greater detail to further clarify and strengthen the environmental performance of the integrated system.

References

1. Ortiz-Bravo, C.A., C.A. Chagas, and F.S. Toniolo, *Oxidative coupling of methane (OCM): An overview of the challenges and opportunities for developing new technologies.* Journal of Natural Gas Science and Engineering, 2021. **96**: p. 104254.
2. Taifan, W. and J. Baltrusaitis, *CH4 conversion to value added products: Potential, limitations and extensions of a single step heterogeneous catalysis.* Applied Catalysis B: Environmental, 2016. **198**: p. 525-547.
3. Cruellas, A., et al., *Techno-economic analysis of oxidative coupling of methane: Current state of the art and future perspectives.* Energy Conversion and Management, 2019. **198**: p. 111789.
4. Gambo, Y., et al., *Recent advances and future prospect in catalysts for oxidative coupling of methane to ethylene: A review.* Journal of industrial and engineering chemistry, 2018. **59**: p. 218-229.
5. Farrell, B.L. and S. Linic, *Oxidative coupling of methane over mixed oxide catalysts designed for solid oxide membrane reactors.* Catalysis Science & Technology, 2016. **6**(12): p. 4370-4376.
6. Schwach, P., X. Pan, and X. Bao, *Direct conversion of methane to value-added chemicals over heterogeneous catalysts: challenges and prospects.* Chemical reviews, 2017. **117**(13): p. 8497-8520.
7. Farsi, A. and S.S. Mansouri, *Influence of nanocatalyst on oxidative coupling, steam and dry reforming of methane: A short review.* Arabian Journal of Chemistry, 2016. **9**: p. S28-S34.
8. Horn, R. and R. Schlögl, *Methane activation by heterogeneous catalysis.* Catalysis Letters, 2015. **145**: p. 23-39.

9. Kondratenko, E.V. and U. Rodemerck, *A Dual-Reactor Concept for the High-Yielding Conversion of Methane into Higher Hydrocarbons.* ChemCatChem, 2013. **5**(3): p. 697-700.

10. Deng, J., et al., *Advances in oxidative coupling of methane.* Atmosphere, 2023. **14**(10): p. 1538.

11. WBG. *Global Flaring and Methane Reduction Partnership (GFMR)*. 2023; Available from: https://www.worldbank.org/en/programs/gasflaringreduction/global-flaring-data.

12. GECF. *Monetisation of natural gas through the development of value-added petrochemicals* 2023; Available from: https://www.gecf.org/_resources/files/events/expert-commentary---monetisation-of-natural-gas-through-the-development-of-value-added-petrochemical/monetisation-of-natural-gas-through-the-development-of-value-added-petrochemicals.pdf.

13. Dimensions. Available from: https://www.dimensions.ai/.

14. SUSlick, K.S., *Kirk-Othmer encyclopedia of chemical technology.* J. Wiley & Sons: New York, 1998. **26**: p. 517-541.

15. Penteado, A., et al., *Design and assessment of a membrane and absorption based carbon dioxide removal process for oxidative coupling of methane.* Industrial & Engineering Chemistry Research, 2016. **55**(27): p. 7473-7483.

16. Leonzio, G., B. Chachuat, and N. Shah, *Towards ethylene production from carbon dioxide: Economic and global warming potential assessment.* Sustainable Production and Consumption, 2023. **43**: p. 124-139.

17. Spallina, V., et al., *Techno-economic assessment of different routes for olefins production through the oxidative coupling of methane (OCM): Advances in benchmark technologies.* Energy Conversion and Management, 2017. **154**: p. 244-261.

18. Thiruvenkataswamy, P., et al., *Safety and techno-economic analysis of ethylene technologies.* Journal of Loss Prevention in the Process Industries, 2016. **39**: p. 74-84.

19. NASA. *SEH 4.0 System Design Processes*. 2019; Available from: https://www.nasa.gov/reference/4-0-system-design-processes/.

20. NASA, *NASA Technology Roadmap Update Overview.* 2014.

21. Liu, J., et al., *From fundamentals to chemical engineering on oxidative coupling of methane for ethylene production: A review.* Carbon Resources Conversion, 2022. **5**(1): p. 1-14.

22. Lavoie, J.-M., *Review on dry reforming of methane, a potentially more environmentally-friendly approach to the increasing natural gas exploitation.* Frontiers in chemistry, 2014. **2**: p. 81.

23. Li, X., et al., *Dry reforming of methane over Ni/La2O3 nanorod catalysts with stabilized Ni nanoparticles.* Applied Catalysis B: Environmental, 2017. **202**: p. 683-694.

24. Amghizar, I., et al., *New trends in olefin production.* Engineering, 2017. **3**(2): p. 171-178.

25. Rafique, H.A., et al., *Oxidative coupling of methane implementations for olefin production*. 2016, Google Patents.

26. LAKHAPATRI, G.R.A.R.V.C.S.M.C.P., *Efficient oxidative coupling of methane processes and systems*. 2015, Lummus Technology LLC.

27. Couwenberg, P.M., Q. Chen, and G.B. Marin, *Kinetics of a gas-phase chain reaction catalyzed by a solid: The oxidative coupling of methane over Li/MgO-based catalysts.* Industrial & engineering chemistry research, 1996. **35**(11): p. 3999-4011.

28. Tung, W.Y. and L.L. Lobban, *Oxidative coupling of methane over lithium/magnesia: kinetics and mechanisms.* Industrial & Engineering Chemistry Research, 1992. **31**(7): p. 1621-1625.

29. Jolaoso, L.A., C. Duan, and P. Kazempoor, *Life cycle analysis of a hydrogen production system based on solid oxide electrolysis cells integrated with different energy and wastewater sources.* International Journal of Hydrogen Energy, 2024. **52**: p. 485-501.

30. Chen, Y., et al., *Catalytic conversion of methane at low temperatures: A critical review.* Energy Technology, 2020. **8**(8): p. 1900750.

31. Lunsford, J.H., *Catalytic conversion of methane to more useful chemicals and fuels: a challenge for the 21st century.* Catalysis today, 2000. **63**(2-4): p. 165-174.

32. Karakaya, C. and R.J. Kee, *Progress in the direct catalytic conversion of methane to fuels and chemicals.* Progress in Energy and Combustion Science, 2016. **55**: p. 60-97.

33. Guo, X., et al., *Direct, nonoxidative conversion of methane to ethylene, aromatics, and hydrogen.* science, 2014. **344**(6184): p. 616-619.

34. Rytter, E. and A. Holmen, *Deactivation and regeneration of commercial type Fischer-Tropsch Co-catalysts—A mini-review.* Catalysts, 2015. **5**(2): p. 478-499.

35. Jang, W.-J., et al., *A review on dry reforming of methane in aspect of catalytic properties.* Catalysis Today, 2019. 324: p. 15-26.

36. Keller, G. and M. Bhasin, *Synthesis of ethylene via oxidative coupling of methane: I. Determination of active catalysts.* Journal of Catalysis, 1982. **73**(1): p. 9-19.

37. Zhang, Q., et al., *Comparatively high yield methanol production from gas phase partial oxidation of methane.* Applied Catalysis A: General, 2002. **224**(1-2): p. 201-207.

38. Zakaria, Z. and S.K. Kamarudin, *Direct conversion technologies of methane to methanol: An overview.* Renewable and Sustainable Energy Reviews, 2016. **65**: p. 250-261.

39. Takalkar, G., et al., *Thermochemical splitting of CO2 using solution combustion synthesized LaMO3 (where, M= Co, Fe, Mn, Ni, Al, Cr, Sr).* Applied Surface Science, 2020. **509**: p. 144908.

40. Hao, Y., J. Jin, and H. Jin, *Thermodynamic analysis of isothermal CO2 splitting and CO2-H2O co-splitting for solar fuel production.* Applied Thermal Engineering, 2020. **166**: p. 113600.

41. Dimitrakis, D.A., et al., *On kinetic modelling for solar redox thermochemical H 2 O and CO 2 splitting over NiFe 2 O 4 for H 2, CO and syngas production.* Physical Chemistry Chemical Physics, 2017. **19**(39): p. 26776-26786.

42. Centi, G. and S. Perathoner, *Opportunities and prospects in the chemical recycling of carbon dioxide to fuels.* Catalysis Today, 2009. **148**(3-4): p. 191-205.

43. Beck, B., et al., *Oxidative coupling of methane—A complex surface/gas phase mechanism with strong impact on the reaction engineering.* Catalysis Today, 2014. **228**: p. 212-218.

44. Lomonosov, V. and M.Y. Sinev, *Oxidative coupling of methane: Mechanism and kinetics.* Kinetics and Catalysis, 2016. **57**: p. 647-676.

45. Fleischer, V., et al., *Chemical looping as reactor concept for the oxidative coupling of methane over a Na2WO4/Mn/SiO2 catalyst.* Chemical Engineering Journal, 2016. **306**: p. 646-654.

46. Karakaya, C., et al., *Detailed reaction mechanisms for the oxidative coupling of methane over La2O3/CeO2 nanofiber fabric catalysts.* ChemCatChem, 2017. **9**(24): p. 4538-4551.

47. Karakaya, C., et al., *A detailed reaction mechanism for oxidative coupling of methane over Mn/Na2WO4/SiO2 catalyst for non-isothermal conditions.* Catalysis today, 2018. **312**: p. 10-22.

48. Kondratenko, E.V., et al., *Methane conversion into different hydrocarbons or oxygenates: current status and future perspectives in catalyst development and reactor operation.* Catalysis Science & Technology, 2017. **7**(2): p. 366-381.

49. Cruellas, A., et al., *Oxidative coupling of methane in membrane reactors; a techno-economic assessment.* Processes, 2020. **8**(3): p. 274.

50. Othman, N.H., Z. Wu, and K. Li, *An oxygen permeable membrane microreactor with an in-situ deposited Bi1. 5Y0. 3Sm0. 2O3− δ catalyst for oxidative coupling of methane.* Journal of Membrane Science, 2015. **488**: p. 182-193.

51. Song, J., et al., *Monodisperse Sr–La 2 O 3 hybrid nanofibers for oxidative coupling of methane to synthesize C 2 hydrocarbons.* Nanoscale, 2015. **7**(6): p. 2260-2264.

52. Palermo, A., et al., *Critical influence of the amorphous silica-to-cristobalite phase transition on the performance of Mn/Na2WO4/SiO2 catalysts for the oxidative coupling of methane.* Journal of Catalysis, 1998. **177**(2): p. 259-266.

53. Hayek, N.S., et al., *Effect of reaction conditions on the oxidative coupling of methane over doped MnOx-Na2WO4/SiO2 catalyst.* Journal of Catalysis, 2019. **376**: p. 25-31.

54. Gradassi, M.J. and N.W. Green, *Economics of natural gas conversion processes.* Fuel Processing Technology, 1995. **42**(2-3): p. 65-83.

55. Albrecht, M., U. Rodemerck, and E.V. Kondratenko, *Higher hydrocarbon production through oxidative coupling of methane combined with hydrogenation of carbon oxides.* Chemie Ingenieur Technik, 2014. **86**(11): p. 1894-1900.

56. Ito, T. and J.H. Lunsford, *Synthesis of ethylene and ethane by partial oxidation of methane over lithium-doped magnesium oxide.* Nature, 1985. **314**(6013): p. 721-722.

57. Ashour, F.M., *Economic Profiling on Oxidative Coupling of Methane and Opportunities for Integration*. 2023.

58. Godini, H.R., et al., *Techno-economic analysis of integrating the methane oxidative coupling and methane reforming processes.* Fuel processing technology, 2013. **106**: p. 684-694.

59. Rosner, F., et al., *Prospects of hydrogen cogeneration and carbon dioxide utilization in electrochemical refineries for ethylene production via oxidative coupling of methane: A techno-economic assessment*. 2024: United States. p. Medium: ED; Size: 64 p.

60. Penteado, A.T., et al., *Techno-economic evaluation of a biogas-based oxidative coupling of methane process for ethylene production.* Frontiers of Chemical Science and Engineering, 2018. **12**: p. 598-618.

61. Liu, K., et al., *Oxidative coupling of methane in solid oxide fuel cell tubular membrane reactor with high ethylene yield.* Catalysis Communications, 2017. **96**: p. 23-27.

62. Bhatia, S., C.Y. Thien, and A.R. Mohamed, *Oxidative coupling of methane (OCM) in a catalytic membrane reactor and comparison of its performance with other catalytic reactors.* Chemical engineering journal, 2009. **148**(2-3): p. 525-532.

63. Stansch, Z., L. Mleczko, and M. Baerns, *Comprehensive kinetics of oxidative coupling of methane over the La2O3/CaO catalyst.* Industrial & engineering chemistry research, 1997. **36**(7): p. 2568-2579.

64. Hugill, J., et al., *Feasibility study on the co-generation of ethylene and electricity through oxidative coupling of methane.* Applied Thermal Engineering, 2005. **25**(8-9): p. 1259-1271.

65. Swanenberg, G., *Cogeneration of ethylene and electricity with oxidative methane coupling: study of technical feasibility and economic merit.* 1998.

66. Otsuka, K., Y. Uragami, and M. Hatano, *The oxidative coupling of methane in the presence and absence of catalyst.* Catalysis today, 1992. **13**(2-3): p. 291-300.

67. Campbell, K., H. Zhang, and J. Lunsford, *Methane activation by the lanthanide oxides.* The Journal of Physical Chemistry, 1988. **92**(3): p. 750-753.

68. Luo, L., et al., *Methyl radicals in oxidative coupling of methane directly confirmed by synchrotron VUV photoionization mass spectroscopy.* Scientific reports, 2013. **3**(1): p. 1625.

69. Simon, Y., et al., *Detailed mechanism of the oxidative coupling of methane*, in *Studies in surface science and catalysis*. 2004, Elsevier. p. 571-576.

70. Takanabe, K. and E. Iglesia, *Rate and selectivity enhancements mediated by OH radicals in the oxidative coupling of methane catalyzed by Mn/Na2WO4/SiO2.* Angewandte Chemie, 2008. **120**(40): p. 7803-7807.

71. Xu, M. and J.H. Lunsford, *Effect of temperature on methyl radical generation over Sr/La 2 O 3 catalysts.* Catalysis letters, 1991. **11**: p. 295-300.

72. Campbell, K.D. and J.H. Lunsford, *Contribution of gas-phase radical coupling in the catalytic oxidation of methane.* The Journal of Physical Chemistry, 1988. **92**(20): p. 5792-5796.

73. Tong, Y., M.P. Rosynek, and J.H. Lunsford, *Secondary reactions of methyl radicals with lanthanide oxides: their role in the selective oxidation of methane.* The Journal of Physical Chemistry, 1989. **93**(8): p. 2896-2898.

74. Lunsford, J.H., *The catalytic oxidative coupling of methane.* Angewandte Chemie International Edition in English, 1995. **34**(9): p. 970-980.

75. Shahri, S.M.K. and S.M. Alavi, *Kinetic studies of the oxidative coupling of methane over the Mn/Na2WO4/SiO2 catalyst.* Journal of Natural Gas Chemistry, 2009. **18**(1): p. 25-34.

76. Sun, J., J.W. Thybaut, and G.B. Marin, *Microkinetics of methane oxidative coupling.* Catalysis today, 2008. **137**(1): p. 90-102.

77. Reyes, S.C., E. Iglesia, and C. Kelkar, *Kinetic-transport models of bimodal reaction sequences—I. Homogeneous and heterogeneous pathways in oxidative coupling of methane.* Chemical engineering science, 1993. **48**(14): p. 2643-2661.

78. Olsbye, U., et al., *A kinetic study of the oxidative coupling of methane over a BaCO3/La2On (CO3) 3-n catalyst: I. Determination of a global reaction scheme and the influence of heterogeneous and homogeneous reactions.* Catalysis today, 1992. **13**(2-3): p. 209-218.

79. Mleczko, L. and M. Baerns, *Catalytic oxidative coupling of methane—reaction engineering aspects and process schemes.* Fuel Processing Technology, 1995. **42**(2-3): p. 217-248.

80. Traykova, M., et al., *Oxidative coupling of methane–the transition from reaction to transport control over La2O3/MgO catalyst.* Applied Catalysis A: General, 1998. **169**(2): p. 237-247.

81. Lacombe, S., et al., *Kinetic modelling of the oxidative coupling of methane over lanthanum oxide in connection with mechanistic studies.* Chemical Engineering & Technology: Industrial Chemistry-Plant Equipment-Process Engineering-Biotechnology, 1995. **18**(3): p. 216-223.

82. Sohrabi, M., et al., *Some aspects of kinetics and mechanism of the oxidative coupling of methane.* Journal of Chemical Technology & Biotechnology: International Research in Process, Environmental AND Clean Technology, 1996. **67**(1): p. 15-20.

83. Tiemersma, T., et al., *A kinetics study for the oxidative coupling of methane on a Mn/Na2WO4/SiO2 catalyst.* Applied Catalysis A: General, 2012. **433**: p. 96-108.

84. Labinger, J.A. and K.C. Ott, *Mechanistic studies on the oxidative coupling of methane.* Journal of Physical Chemistry, 1987. **91**(11): p. 2682-2684.

85. Sinev, M.Y., et al., *Kinetics of oxidative coupling of methane: Bridging the gap between comprehension and description.* Journal of natural gas chemistry, 2009. **18**(3): p. 273-287.

86. Baerns, M. and E.V. Kondratenko, *Oxidative coupling of methane*, in *Handbook of heterogeneous catalysis*. 2008, Wiley-VCH. p. 3010-3023.

87. Zanthoff, H. and M. Baerns, *Oxidative coupling of methane in the gas phase. Kinetic simulation and experimental verification.* Industrial & engineering chemistry research, 1990. **29**(1): p. 2-10.

88. Kim, M., et al., *Reaction engineering of oxidative coupling of methane: experimental observations and analysis of the impacts of operating parameters.* Chemical Engineering Research and Design, 2021. **172**: p. 84-98.

89. Mohammadi, Y. and A. Penlidis, *"Optimulation" in Chemical Reaction Engineering: Oxidative Coupling of Methane as a Case Study.* Industrial & Engineering Chemistry Research, 2018. **57**(26): p. 8664-8678.

90. Ahari, J.S., S. Zarrinpashne, and M.T. Sadeghi, *Micro-kinetic modeling of OCM reactions over Mn/Na2WO4/SiO2 catalyst.* Fuel processing technology, 2013. **115**: p. 79-87.

91. Chen, Q., J.H. Hoebink, and G.B. Marin, *Kinetics of the oxidative coupling of methane at atmospheric pressure in the absence of catalyst.* Industrial & engineering chemistry research, 1991. **30**(9): p. 2088-2097.

92. Chen, Q., P. Couwenberg, and G. Marin, *Effect of pressure on the oxidative coupling of methane in the absence of catalyst.* AIChE journal, 1994. **40**(3): p. 521-535.

93. Daneshpayeh, M., et al., *Kinetic modeling of oxidative coupling of methane over Mn/Na2WO4/SiO2 catalyst.* Fuel Processing Technology, 2009. **90**(3): p. 403-410.

94. Vatani, A., et al., *Kinetic modeling of oxidative coupling of methane over Li/MgO catalyst by genetic algorithm.* Journal of Natural Gas Science and Engineering, 2014. **20**: p. 347-356.

95. Petrov, R., S. Reshetnikov, and Y. Ivanova, *Study of the oxidative methane coupling over SrO-La2O3 catalyst: Experiment and kinetic modeling.* Fuel Processing Technology, 2021. **213**: p. 106667.

96. Arndt, S., et al., *A critical assessment of Li/MgO-based catalysts for the oxidative coupling of methane.* Catalysis Reviews, 2011. **53**(4): p. 424-514.

97. Zhu, Q., et al., *Sulfur as a selective 'soft'oxidant for catalytic methane conversion probed by experiment and theory.* Nature chemistry, 2013. **5**(2): p. 104-109.

98. Jiang, S., et al., *Enhanced Chemical looping oxidative coupling of methane by Na-doped LaMnO3 redox catalysts.* Fuel, 2021. **299**: p. 120932.

99. Zavyalova, U., et al., *Statistical analysis of past catalytic data on oxidative methane coupling for new insights into the composition of high-performance catalysts.* ChemCatChem, 2011. **3**(12): p. 1935-1947.

100. Pacheco Filho, J., J.G. Eon, and M. Schmal, *Oxidative coupling of methane on Ce/Na/CaO catalysts.* Catalysis letters, 2000. **68**: p. 197-202.

101. Olivier, L., et al., *High-temperature parallel screening of catalysts for the oxidative coupling of methane.* Catalysis today, 2008. **137**(1): p. 80-89.

102. Garrone, E., A. Zecchina, and F.S. Stone, *Anionic intermediates in surface processes leading to O2− formation on magnesium oxide.* Journal of Catalysis, 1980. **62**(2): p. 396-400.

103. Choudhary, V.R., V.H. Rane, and M.Y. Pandit, *Comparison of alkali metal promoted MgO catalysts for their surface acidity/basicity and catalytic activity/selectivity in the oxidative coupling of methane.* Journal of Chemical Technology & Biotechnology: International Research in Process, Environmental AND Clean Technology, 1997. **68**(2): p. 177-186.

104. Korf, S., et al., *The selective oxidation of methane to ethane and ethylene over doped and un-doped rare earth oxides.* Catalysis today, 1989. **4**(3-4): p. 279-292.

105. Papa, F., et al., *Acid–base properties of the active sites responsible for C2+ and CO2 formation over MO–Sm2O3 (M= Zn, Mg, Ca and Sr) mixed oxides in OCM reaction.* Journal of Molecular Catalysis A: Chemical, 2011. **346**(1-2): p. 46-54.

106. Özdemir, H., M.F. Öksüzömer, and M. Ali Gürkaynak, *Studies on oxidative coupling of methane using Sm2O3-based catalysts.* Chemical Engineering Communications, 2019. **206**(1): p. 48-60.

107. Jones, A.S., et al., *Effects of low molar concentrations of low-valence dopants on samarium oxide xerogels in the oxidative coupling of methane.* Catalysis Today, 2021. **365**: p. 58-70.

108. Jones, A.S., et al., *Doped samarium oxide xerogels for oxidative coupling of methane—Effects of high-valence dopants at very low concentrations.* Catalysis Today, 2021. **365**: p. 46-57.

109. Huang, P., et al., *Exploiting shape effects of La 2 O 3 nanocatalysts for oxidative coupling of methane reaction.* Nanoscale, 2013. **5**(22): p. 10844-10848.

110. Jiang, T., et al., *La 2 O 3 catalysts with diverse spatial dimensionality for oxidative coupling of methane to produce ethylene and ethane.* RSC advances, 2016. **6**(41): p. 34872-34876.

111. Zeng, Y., F. Akin, and Y. Lin, *Oxidative coupling of methane on fluorite-structured samarium–yttrium–bismuth oxide.* Applied Catalysis A: General, 2001. **213**(1): p. 33-45.

112. Otsuka, K., et al., *Synthesis of ethylene by partial oxidation of methane over the oxides of transition elements with LiCl.* Chemistry Letters, 1986. **15**(6): p. 903-906.

113. Hiyoshi, N. and T. Ikeda, *Oxidative coupling of methane over alkali chloride–Mn–Na2WO4/SiO2 catalysts: Promoting effect of molten alkali chloride.* Fuel Processing Technology, 2015. **133**: p. 29-34.

114. Mahmoodi, S., M. Ehsani, and S. Ghoreishi, *Effect of promoter in the oxidative coupling of methane over synthesized Mn/SiO2 nanocatalysts via incipient wetness impregnation.* Journal of Industrial and Engineering Chemistry, 2010. **16**(6): p. 923-928.

115. Zarrinpashne, S., R. Ahmadi, and S.M. Zekordi, *Catalyst direct conversion of methane to ethane and ethylene*. 2011, Google Patents.

116. Kim, G.J., J.T. Ausenbaugh, and H.T. Hwang, *Effect of TiO2 on the performance of Mn/Na2WO4 catalysts in oxidative coupling of methane.* Industrial & Engineering Chemistry Research, 2021. **60**(10): p. 3914-3921.

117. Bostan, A., et al., *Influence of the composition of perovskites based on SrMnO 3 on their catalytic properties in the oxidative coupling of methane.* Theoretical and Experimental Chemistry, 2005. **41**: p. 32-36.

118. Pyatnitskii, Y.I., et al., *Effect of the composition of Mn-, Co-and Ni-containing perovskites on their catalytic properties in the oxidative coupling of methane.* Theoretical and Experimental Chemistry, 2005. **41**: p. 117-121.

119. Spinicci, R., et al., *Catalytic properties of stoichiometric and non-stoichiometric LaFeO3 perovskite for total oxidation of methane.* Materials Chemistry and Physics, 2002. **76**(1): p. 20-25.

120. O'Connell, M., et al., *Catalytic oxidation over lanthanum-transition metal perovskite materials.* Catalysis Today, 1999. **47**(1-4): p. 123-132.

121. Bagherzadeh, E., A. Hassan, and A. Hassan, *Preparation of catalyst and use for high yield conversion of methane to ethylene*. 2007, Google Patents.

122. Damasceno, S., et al., *Oxidative coupling of methane in chemical looping design.* Fuel Processing Technology, 2022. **231**: p. 107255.

123. Ito, T., et al., *Oxidative dimerization of methane over a lithium-promoted magnesium oxide catalyst.* Journal of the American Chemical Society, 1985. **107**(18): p. 5062-5068.

124. Myrach, P., et al., *Temperature-dependent morphology, magnetic and optical properties of Li-doped MgO.* ChemCatChem, 2010. **2**(7): p. 854-862.

125. Driscoll, D.J., et al., *Formation of gas-phase methyl radicals over magnesium oxide.* Journal of the American Chemical Society, 1985. **107**(1): p. 58-63.

126. Peng, X., D. Richards, and P. Stair, *Surface composition and reactivity of lithium-doped magnesium oxide catalysts for oxidative coupling of methane.* Journal of Catalysis, 1990. **121**(1): p. 99-109.

127. Kwapien, K., et al., *Sites for methane activation on lithium-doped magnesium oxide surfaces.* Angewandte Chemie International Edition, 2014. **53**(33): p. 8774-8778.

128. Hou, S., Y. Kou, and L. Liu, *Li-ZnO/La~ 2O~ 3 Catalyst for the Oxidation Coupling of Methane at Low Temperature.* ACTA PHYSICOCHIMICA SINICA, 2006. **22**(8): p. 1040.

129. Zhao, M., et al., *Flower-like Sr-La2O3 microspheres with hierarchically porous structures for oxidative coupling of methane.* Industrial & Engineering Chemistry Research, 2019. **58**(51): p. 22847-22856.

130. Noon, D., A. Seubsai, and S. Senkan, *Oxidative Coupling of Methane by Nanofiber Catalysts.* ChemCatChem, 2013. **5**(1).

131. Liu, H., et al., *Oxidative Coupling of Methane with High C2 Yield by using Chlorinated Perovskite Ba0. 5Sr0. 5Fe0. 2Co0. 8O3− δ as Catalyst and N2O as Oxidant.* ChemCatChem, 2010. **2**(12): p. 1539-1542.

132. Zhang, Y., et al., *CO2 oxidative coupling of methane using an earth-abundant CaO-based catalyst.* Scientific Reports, 2019. **9**(1): p. 15454.

133. Chen, Y., et al., *Chemical looping Co-splitting of H2O–CO2 for efficient generation of syngas.* ACS Sustainable Chemistry & Engineering, 2019. **7**(18): p. 15452-15462.

134. Cheng, Z., et al., *C2 selectivity enhancement in chemical looping oxidative coupling of methane over a Mg–Mn composite oxygen carrier by Li-doping-induced oxygen vacancies.* ACS Energy Letters, 2018. **3**(7): p. 1730-1736.

135. Al-Shankiti, I., B.D. Ehrhart, and A.W. Weimer, *Isothermal redox for H2O and CO2 splitting–A review and perspective.* Solar Energy, 2017. **156**: p. 21-29.

136. Roeb, M., et al., *Materials-related aspects of thermochemical water and carbon dioxide splitting: a review.* Materials, 2012. **5**(11): p. 2015-2054.

137. Bader, R., et al., *Thermodynamic analysis of isothermal redox cycling of ceria for solar fuel production.* Energy & Fuels, 2013. **27**(9): p. 5533-5544.

138. Marxer, D., et al., *Solar thermochemical splitting of CO 2 into separate streams of CO and O 2 with high selectivity, stability, conversion, and efficiency.* Energy & Environmental Science, 2017. **10**(5): p. 1142-1149.

139. Zoller, S., et al., *A solar tower fuel plant for the thermochemical production of kerosene from H2O and CO2.* Joule, 2022. **6**(7): p. 1606-1616.

140. Abanades, S. and A. Le Gal, *CO2 splitting by thermo-chemical looping based on ZrxCe1− xO2 oxygen carriers for synthetic fuel generation.* Fuel, 2012. **102**: p. 180-186.

141. Hao, Y., C.-K. Yang, and S.M. Haile, *High-temperature isothermal chemical cycling for solar-driven fuel production.* Physical Chemistry Chemical Physics, 2013. **15**(40): p. 17084-17092.

142. Hathaway, B.J., et al., *Effect of flow rates on operation of a solar thermochemical reactor for splitting CO2 via the isothermal ceria redox cycle.* Journal of solar energy engineering, 2016. **138**(1): p. 011007.

143. Schappi, R., V. Hüsler, and A. Steinfeld, *Solar Thermochemical Production of Syngas from H2O and CO2─ Experimental Parametric Study, Control, and Automation.* Industrial & Engineering Chemistry Research, 2024. **63**(8): p. 3563-3575.

144. Bulfin, B., et al., *Thermodynamics of CeO2 thermochemical fuel production.* Energy & Fuels, 2015. **29**(2): p. 1001-1009.

145. Ermanoski, I., J. Miller, and M. Allendorf, *Efficiency maximization in solar-thermochemical fuel production: challenging the concept of isothermal water splitting.* Physical Chemistry Chemical Physics, 2014. **16**(18): p. 8418-8427.

146. Ehrhart, B.D., et al., *System efficiency for two-step metal oxide solar thermochemical hydrogen production–Part 2: Impact of gas heat recuperation and separation temperatures.* International Journal of Hydrogen Energy, 2016. **41**(44): p. 19894-19903.

147. Ehrhart, B.D., et al., *System efficiency for two-step metal oxide solar thermochemical hydrogen production–Part 3: Various methods for achieving low oxygen partial pressures in the reduction reaction.* International Journal of Hydrogen Energy, 2016. **41**(44): p. 19904-19914.

148. Ehrhart, B.D., et al., *System efficiency for two-step metal oxide solar thermochemical hydrogen production–Part 1: Thermodynamic model and impact of oxidation kinetics.* International Journal of Hydrogen Energy, 2016. **41**(44): p. 19881-19893.

149. Jarrett, C., et al., *Critical limitations on the efficiency of two-step thermochemical cycles.* Solar energy, 2016. **123**: p. 57-73.

150. Krenzke, P.T. and J.H. Davidson, *On the efficiency of solar H2 and CO production via the thermochemical cerium oxide redox cycle: the option of inert-swept reduction.* Energy & Fuels, 2015. **29**(2): p. 1045-1054.

151. Lapp, J., J.H. Davidson, and W. Lipiński, *Efficiency of two-step solar thermochemical non-stoichiometric redox cycles with heat recovery.* Energy, 2012. **37**(1): p. 591-600.

152. Siegel, N.P., et al., *Factors affecting the efficiency of solar driven metal oxide thermochemical cycles.* Industrial & Engineering Chemistry Research, 2013. **52**(9): p. 3276-3286.

153. *SUN-to-LIQUID II project initial press release*. 2024; Available from: https://zenodo.org/records/10620233.

154. De Smith Robert, M. and H. Yong, *Efficient Splitting of CO2 in an Isothermal Redox Cycle Based on Ceria.* 2014.

155. Dey, S., et al., *Noteworthy performance of La 1− x Ca x MnO 3 perovskites in generating H 2 and CO by the thermochemical splitting of H 2 O and CO 2.* Physical Chemistry Chemical Physics, 2015. **17**(1): p. 122-125.

156. Asadi, J. and P. Kazempoor, *Economic and operational assessment of solar-assisted hybrid carbon capture system for combined cycle power plants.* Energy, 2024: p. 131861.

157. Jolaoso, L.A., et al., *A novel green hydrogen production using water-energy nexus framework.* Energy Conversion and Management, 2023. **276**: p. 116344.

158. Asadi, J. and P. Kazempoor, *Sustainability Enhancement of Fossil-Fueled Power Plants by Optimal Design and Operation of Membrane-Based CO2 Capture Process.* Atmosphere, 2022. **13**(10): p. 1620.

159. Asadi, J., L. Jolaoso, and P. Kazempoor. *Efficiency and flexibility improvement of amine-based post combustion CO2 capturing system (CCS) in full and partial loads*. in *Energy Sustainability*. 2022. American Society of Mechanical Engineers.

160. Wang, P., et al., *MnTiO3-driven low-temperature oxidative coupling of methane over TiO2-doped Mn2O3-Na2WO4/SiO2 catalyst.* Science advances, 2017. **3**(6): p. e1603180.

161. Elkins, T.W. and H.E. Hagelin-Weaver, *Characterization of Mn–Na2WO4/SiO2 and Mn–Na2WO4/MgO catalysts for the oxidative coupling of methane.* Applied Catalysis A: General, 2015. **497**: p. 96-106.

162. Mirodatos, C., et al., *Deactivation of alkali promoted magnesia in oxidative coupling of methane*, in *Studies in Surface Science and Catalysis*. 1987, Elsevier. p. 183-195.

163. Li, Z., et al., *Intelligent Optimization of Na− Mn− W/SiO2 Catalysts for the Oxidative Coupling of Methane.* ChemNanoMat, 2018. **4**(5): p. 487-495.

164. Rosner, F., et al., *Techno-Economic Analysis of Electrochemical Refineries Using Solid Oxide Cells for Oxidative Coupling of Methane.* ECS Transactions, 2023. **111**(6): p. 2049.

165. Li, X., C. Wang, and J. Tang, *Methane transformation by photocatalysis.* Nature Reviews Materials, 2022. **7**(8): p. 617-632.

166. Flores-Granobles, M. and M. Saeys, *Quantitative analysis of CO 2 emissions reduction potential of alternative light olefins production processes.* Green Chemistry, 2023. **25**(16): p. 6459-6471.

167. Luongo, G., et al., *Highly selective oxidative dehydrogenation of ethane to ethylene via chemical looping with oxygen uncoupling through structural engineering of the oxygen carrier.* Advanced Energy Materials, 2022. **12**(23): p. 2200405.

168. Zhang, P., J. Tong, and K. Huang, *Role of CO2 in catalytic ethane-to-ethylene conversion using a high-temperature CO2 transport membrane reactor.* ACS Sustainable Chemistry & Engineering, 2019. **7**(7): p. 6889-6897.

169. Maghrebi, R., et al., *CFD modeling of catalyst pellet for oxidative coupling of methane: Heat transfer and reaction.* Particuology, 2013. **11**(5): p. 506-513.

170. Fontoura, T.B., N.J. De Jesus, and J.C. Pinto, *Modeling of Oxidative Coupling of Methane for Manufacture of Olefins—Part I: CFD Simulations.* Processes, 2023. **11**(8): p. 2505.

171. Zhang, Z., Z. Guo, and S. Ji, *Numerical simulation of packed-bed reactor for oxidative coupling of methane.* Journal of Energy Chemistry, 2015. **24**(1): p. 23-30.

172. Alturkistani, S., et al., *Importance of Process Variables and Their Optimization for Oxidative Coupling of Methane (OCM).* ACS omega, 2023. **8**(23): p. 21223-21236.

173. George, G.R., et al., *Multiscale characterization, modeling and simulation of packed bed reactor for direct conversion of syngas to dimethyl ether.* RSC Sustainability, 2025.

174. Karakaya, C. and H.-Y. Chen, *Model-based optimization strategies for direct hydrogenation of carbon dioxide to dimethyl ether.* Chemical Engineering Journal, 2025. **503**: p. 157448.

175. Jacob, K. and M. Attaluri, *Refinement of thermodynamic data for LaMnO 3.* Journal of Materials Chemistry, 2003. **13**(4): p. 934-942.

176. Hassan, H.A., et al., *A multiscale packed-bed reactor model for sustainable ethylene production via chemical looping oxidative coupling of methane.* Energy Conversion and Management, 2026. **366**: p. 121821.

177. Multiphysics, C. *COMSOL Documentation*. 2024; Available from: https://doc.comsol.com/6.3/docserver/#!/com.comsol.help.comsol/helpdesk/helpdesk.html.

178. Karsten, T., et al., *Performance Evaluation of Different Reactor Concepts for the Oxidative Coupling of Methane on Miniplant Scale.* Methane, 2025. **4**(4): p. 25.

179. Micale, D., et al., *Coupling Euler–Euler and microkinetic modeling for the simulation of fluidized bed reactors: an application to the oxidative coupling of methane.* Industrial & engineering chemistry research, 2021. **60**(18): p. 6687-6697.

180. Kim, M., et al., *Recognition of Oxidative Coupling of Methane Reactor Performance Patterns.* Chemical Engineering & Technology, 2022. **45**(4): p. 694-708.

181. Chung, H., et al., *Co-production of ethylene and hydrogen via oxidative coupling of methane: Improving techno-economics and sustainability under emerging hydrogen markets.* Resources, Environment and Sustainability, 2026: p. 100332.

182. Ortiz-Espinoza, A.P., et al., *Design, simulation and techno-economic analysis of two processes for the conversion of shale gas to ethylene.* Computers & Chemical Engineering, 2017. **107**: p. 237-246.

183. Fujimoto, K., et al., *Oxidative coupling of methane with alkaline earth halide catalysts supported on alkaline earth oxides.* Chemistry Letters, 1987. **16**(11): p. 2157-2160.

184. Alturkistani, S., et al., *High-Throughput Experiments and Kinetic Modeling of Oxidative Coupling of Methane over La2O3/CeO2 Catalyst.* SPE Journal, 2023. **28**(05): p. 2566-2582.

185. Qiu, Z. and Y. Cai, *Optimizing Methane Oxidative Coupling over La2O3: Kinetic and Product Analysis.* Catalysts, 2025. **15**(5): p. 499.

186. Kang, K., et al., *Equilibrium unconstrained low-temperature CO 2 conversion on doped gallium oxides by chemical looping.* Chemical Communications, 2023. **59**(74): p. 11061-11064.

187. Zhang, J., V. Haribal, and F. Li, *Perovskite nanocomposites as effective CO2-splitting agents in a cyclic redox scheme.* Science advances, 2017. **3**(8): p. e1701184.

188. Li, F., S. Iftikhar, and L. Neal, *Sustainable Conversion of Carbon Dioxide and Shale Gas to Green Acetic Acid via a Thermochemical Cyclic Redox Scheme*. 2022, North Carolina State University, Raleigh, NC (United States).

189. United States Department of Energy, N.E.L., *CARBON CONVERSION EXAMPLETECHNO-ECONOMIC ANALYSIS:ELECTROCHEMICAL CONVERSION*. 2024.

190. Lang, H.J., *Simplified approach to preliminary cost estimates.* Chemical Engineering, 1948. **55**(6): p. 112-113.

191. Wain, Y.A., *Updating the Lang Factor and Testing its Accuracy, Reliability and Precision as a Stochastic Cost Estimating Method.* PM World Journal, 2014. **3**(10).

192. Van Amsterdam, M., *Factorial techniques applied in chemical plant cost estimation: A comparative study based on literature and cases.* TU Delft, 1918.

193. Kazi, F.K., et al., *Techno-economic comparison of process technologies for biochemical ethanol production from corn stover.* Fuel, 2010. **89**: p. S20-S28.

194. Administration, U.S.E.I. *Short-Term Energy Outlook*. 2026; Available from: https://www.eia.gov/outlooks/steo/report/natgas.php.

195. Hassan, H.A., et al., *A Review on Advances in Oxidative Coupling of Methane (OCM) for Industrial Use and Prospects of CO2–H2O Splitting Integration.* Gas Science and Engineering, 2025: p. 205834.

196. Rocourt, X., et al. *Flammability limits of hydrogen mixtures diffusing in air*. in *31st Meeting on Combustion-Italian Section of the Combustion Institute: Torino*. 2008.

197. Williams, R., *Six-tenths factor aids in approximating costs.* Chemical Engineering, 1947. **54**(12): p. 124-125.

198. Tribe, M. and R. Alpine, *Scale economies and the "0.6 rule".* Engineering Costs and Production Economics, 1986. **10**(4): p. 271-278.

199. Weber, R.S., J.A. Askander, and J.A. Barclay, *The scaling economics of small unit operations.* Journal of Advanced Manufacturing and Processing, 2021. **3**(1): p. e10074.

200. ISO, *ISO 14040: 2006 Environmental Management-Life Cycle Assessment-Principles and Framework. International Organization for Standardization (ISO).* Geneva, 2006.

201. Finkbeiner, M., et al., *The new international standards for life cycle assessment: ISO 14040 and ISO 14044.* The international journal of life cycle assessment, 2006. **11**: p. 80-85.

202. Singh, A., et al., *Life cycle assessment (LCA) of biodegradable linear low-density polyethylene (LLDPE) manufactured in India.* Journal of Environmental Management, 2024. **372**: p. 123120.

203. Huijbregts, M.A., et al., *ReCiPe2016: a harmonised life cycle impact assessment method at midpoint and endpoint level.* The international journal of life cycle assessment, 2017. **22**(2): p. 138-147.

204. De Pascale, B., et al., *Life cycle assessment of urban pavements: Environmental impact analysis of integrating waste silt in hot mix asphalt.* Science of the Total Environment, 2025. **991**: p. 179931.

205. Yang, M. and F. You, *Comparative techno-economic and environmental analysis of ethylene and propylene manufacturing from wet shale gas and naphtha.* Industrial & Engineering Chemistry Research, 2017. **56**(14): p. 4038-4051.

206. Marcos, J.M., *Modelling of naphtha cracking for olefins production.* Tecnico Lisboa, 2016.